

# **High-Resolution X-ray Ptychography for Magnetic Imaging**

**Von der Fakultät Mathematik und Physik der Universität Stuttgart  
zur Erlangung der Würde eines Doktors der  
Naturwissenschaften (Dr. rer. nat.) genehmigte Abhandlung**

**vorgelegt von**

**Iuliia Bykova**

**geboren am 22.04.1989**

**in Seversk, Russia**

Hauptberichter Prof. Dr. Gisela Schütz  
Mitberichter Prof. Dr. Jörg Wrachtrup

Tag der mündlichen Prüfung: 23. Juli 2018

Max-Planck-Institut für Intelligente Systeme, Stuttgart  
2018



## Abstract

The development of storage rings as highly brilliant X-ray sources in the early 1970s became a breakthrough for X-ray imaging techniques that allowed overcoming the resolution limits of optical microscopy restricted by the wavelength of visible light. Beside the shorter wave length in the nm range, X-rays have higher penetration depth in order of several  $\mu\text{m}$  providing sufficient contrast for  $\mu\text{m}$  and sub- $\mu\text{m}$  objects. In the scope of steady minimalization of material feature sizes for various technological applications, e.g. information storage, biology, medicine, energy and material science, X-ray microscopy has attracted an increasing interest. The use of soft X-rays in microscopy gives not only the advantage of the elemental specificity, but also provides information about chemical and magnetic characteristics based on X-ray absorption spectroscopy (XAS) and X-ray circular dichroism (XMCD). The latter is of special interest, because magnetic features, i.e. magnetic domain walls, vortices or skyrmions, in modern nanomaterials reach sizes below few tens of nanometer.

The resolution in standard X-ray microscopes is limited by the focusing element, e.g. Fresnel Zone Plates (FZP), and stays in the range of 20 nm for highly efficient plates. Diffraction imaging techniques with the use of coherent X-ray radiation potentially can achieve wavelength limited resolution solving so-called “phase problem”. During the last years with steadily increasing computing power, which is necessary for the iterative image reconstructions, these methods became highly efficient for high resolution imaging. Ptychography is the combination of diffraction imaging and scanning transmission microscopy that provides images of extended sample areas utilizing iterative reconstruction algorithm, which gives phase and amplitude information from the studied specimens. The main focus of this thesis is the realization of ptychographic imaging on the samples with different scattering power, as well as the investigation and improvement of the microscopic potential of this method in detailed comparison with conventional STXM imaging. The technique is applied to nanoscale systems of current interest in energy and environmental science and magnetic data processing.

In this work X-ray ptychography was adopted to the scanning transmission X-ray microscope MAXYMUS operated on UE46-1 PGM2 beamline at BESSY II synchrotron (HZB, Berlin, Germany). For the adjustment of the ptychographic setup the main parameters of scanning geometry, i.e. overlap ratio, defocus position, dwell time and degree of spatial coherence, have been thoroughly investigated on the test magnetic and non-magnetic samples and the optimal values have been determined.

The scientific part includes experimental investigation of ptychographic imaging for various research related samples with chemical, magnetic and mixed scattering:

1. Charged/discharged Li battery particles.  $\text{LiFePO}_4$  nanoparticles, which are efficiently used in batteries, have been imaged in lithiated and delithiated states to

---

investigate the capabilities of ptychography for imaging of highly scattering specimen with prominent chemical contrast. The results showed profound resolution improvement on morphological edges as well as on the borders of the regions with different chemical states in comparison with STXM images. It provides important information on the relation of the corresponding phase transitions and the sample sizes and morphologies.

2. Rock varnish samples. Desert varnish specimens consist of ultra-thin (down to few nanometers) altering layers of Mn, Fe, Si and Al and are found as a crust growing on the rock in desert environments. Ptychographic images were used in order to investigate elemental distribution of basic materials in varnish samples with high spatial resolution revealing layers of 10-20 nm that was never observed in STXM studies. The obtained results give intrinsic information about the rock varnish growth mechanism and climate changes in the specific area with the time span of thousands of years.
3. Cu-Ni core shells. The structures of thin magnetic Ni film deposited on the curved 3D Cu crystal possess complex multi domain structure that is determined by the shape of the substrate. Characteristic length scales of magnetic features induced by magneto-chiral effects and topology have been studied in the tens of nanometer regime accessible only by ptychography. In order to understand the magnetization behavior of separate particles micro magnetic simulations were performed for different geometrical shapes. The results showed correspondence to experimental data and predict the magnetization configurations on different particle faces.
4. Magnetic skyrmion systems. Two different sets of skyrmionic samples with different heavy metals and varying thicknesses of ferromagnetic interlayer have been studied using magnetic sensitive ptychography. The extensive measurements of magnetic parameters have been performed using SQUID. The main highlight is the application of ptychography for the study of sub-100 nm sized magnetic object at room temperature identifying clearly their skyrmionic geometry. The high resolution images have been used for analysis of shapes and sizes of skyrmions in dependence on the compound and thicknesses of the used multilayer, also applied bias fields. Based on the obtained data Dzyaloshinskii Moriya interaction (DMI) was estimated and its influence on skyrmion state stabilization was discussed in comparison with recent literature data.

In the thesis the potential of ptychographic imaging was investigated for purely magnetic and non-magnetic systems showing the significant gain of resolution, in some cases limited only by geometrical constraints of the experimental setup. This provides an excellent foundation for the next steps for achieving wavelength limited resolution down to 1 nm and 3D imaging by tomo-ptychography. The progress in advanced new X-ray CCDs,

---

will open new possibilities for time-resolved measurements and 4D spectro-microscopy. Potentially, it will offer an unprecedented combination of nm, meV and ps resolution that can be realized at BESSY II in the forthcoming VSR mode starting from 2021.

---

## Kurzfassung

Die Entwicklung der Speicherringanlagen als hochbrillante Röntgenquellen in den frühen Siebzigern wurde zum Durchbruch für die Röntgenbildgebungsmethoden, die die Auflösungsbegrenzungen der optischen Mikroskopie gegeben durch die Wellenlänge des sichtbaren Lichts überwinden. Neben der kürzeren Wellenlänge im Nanometerbereich bieten die Röntgenstrahlen zusätzlich ein höheres Durchdringungsvermögen - bis zu einigen Mikrometern, das in einem genügenden Kontrast für Objekte im Mikrometer- und Submikrometerbereich resultiert. Im Zusammenhang mit den sich stetig verkleinernden Größen der Materialstrukturen in unterschiedlichen technologischen Anwendungen, z. B. Datenspeicherung, Biologie, Medizin, Energie- und Materialwissenschaften, hat die Röntgenmikroskopie dadurch ein erhöhtes Interesse hervorgerufen. Zusätzlich zur Elementspezifität bieten weiche Röntgenstrahlen auch einen Zugang zur Information über die chemischen und magnetischen Eigenschaften der Materialien, basierend auf Röntgenabsorptionsspektroskopie (XAS) und dem Röntgendichroismus (XMCD). Dies ist von besonderem Interesse, da die magnetischen Strukturen, z. B. magnetischen Domänenwände, Vortices oder Skyrmionen, in modernen Nanomaterialien Größen unter wenigen Zehnteln eines Nanometers erreichen.

Die Auflösung eines Standardröntgenmikroskops ist beschränkt durch das fokussierende Element, z. B. die Fresnelsche Zonenplatte (FZP), und liegt im Bereich von etwa 20 nm für hocheffiziente Platten. Beugungsbasierte Bildgebungsverfahren, die kohärente Röntgenstrahlung nutzen, können theoretisch die Beschränkung der Auflösung durch die Wellenlänge der genutzten Strahlung überwinden, indem sie das sogenannte "Phasenproblem" lösen. In den letzten Jahren hat sich die zur Verfügung stehende Rechenleistung kontinuierlich erhöht, so dass die iterativen Bildrekonstruktionsmethoden, die diese Leistung brauchen, sehr effektiv im Bereich der hochauflösenden Bildgebung geworden sind. Ptychografie ist eine Kombination aus Beugungsbildgebung und Rastertransmissionsmikroskopie, welche Bilder von den ausgedehnten Probenflächen liefert, indem sie sich eines iterativen Rekonstruktionsalgorithmus zur Bestimmung der Phase und Amplitude der untersuchten Probe bedient. Hauptschwerpunkt dieser Arbeit ist die Umsetzung der ptychographischen Bildgebung an unterschiedlichen Proben mit unterschiedlichem Streuvermögen, sowie Untersuchung und Verbesserung des Mikroskopiepotentials dieser Methode im detaillierten Vergleich mit der herkömmlichen STXM Bildgebung. Die Ptychografiemethode wurde auf Nanosysteme im Interessenfokus der modernen Forschung in Bereichen der Energie- und Umweltforschung, sowie der magnetischen Datenverarbeitung angewendet.

Als Teil dieser Arbeit wurde Röntgenptychografie an dem Rasterröntgenmikroskop MAXYMUS, das am UE46-1 PGM2 Strahlrohr am BESSY II Synchrotron (HZB, Berlin)

---

betrieben wird, implementiert. Für die Anpassung des ptychografischen Aufbaus wurden die unterschiedlichen Einstellungen der wichtigsten experimentellen Parameter wie Überlappverhältnis, Defokusposition, Belichtungszeit und Grad der räumlichen Kohärenz an unterschiedlichen magnetischen und nicht-magnetischen Testsystemen eingehend getestet. Dadurch wurden die optimalen Einstellungen der experimentellen Parameter bestimmt.

Der wissenschaftliche Teil der Arbeit beinhaltet experimentelle Untersuchungen der ptychografischen Darstellung unterschiedlicher forschungsrelevanter Proben mit chemischer, magnetischer und gemischter Streuung:

1. Geladene/entladene Li-Batterie-Teilchen:  $\text{LiFePO}_4$  Nanoteilchen, die effektiv in Batterien genutzt werden, wurden in lithiierten und delithiierten Zuständen abgebildet, um die Möglichkeiten der Ptychographie für die Darstellung der stark streuenden Proben mit hohem chemischen Kontrast zu untersuchen. Die Ergebnisse haben eine starke Verbesserung der Auflösung im Vergleich zu STXM an den morphologischen Rändern sowie an den Grenzen der Bereiche der unterschiedlichen chemischen Zustände gezeigt. Die Experimente haben wichtige Informationen über den Zusammenhang des entsprechenden Phasenübergangs und den Probengrößen sowie der Morphologie aufgezeigt.
2. Felsen-Schichtproben: Die Außenschichtproben von Wüstenfelsen bestehen aus ultradünnen (bis zu wenigen Nanometern) abwechselnden Schichten von Mn, Fe, Si und Al und können in Form der Kruste auf den Felsen in der Wüste gefunden werden. Ptychografische Abbildungen wurden benutzt, um die Elementverteilung der Bestandmaterialien in den Außenschichtproben mit hoher örtlicher Auflösung zu untersuchen. Dabei wurden Schichten mit der Dicke von 10 - 20 nm entdeckt, welche nie zuvor mit der herkömmlichen STXM Untersuchungen beobachtet werden konnten. Die Ergebnisse helfen die Wachstumsmechanismen und die Schichtung der äußeren Schicht der Felsen zu verstehen und erlauben dadurch die Erforschung des Klimawechsels in einem bestimmten geographischen Bereich über die Jahrtausende hinweg.
3. Cu-Ni Kern-Schale-Systeme: Die Strukturen der dünnen magnetischen Ni-Filme, die auf dem gewölbten 3D Cu-Kristall aufgetragen worden sind, besitzen komplizierte Multidomänenstrukturen, die durch die Form des Substrats definiert werden. Kennzeichnende Längenskalen der magnetischen Merkmale, die durch magnetochirale Effekte und Topologie erzeugt worden sind, wurden auf der Zehntelnanometerskala untersucht, die nur durch Ptychografie zugänglich ist. Um das Magnetisierungsverhalten der einzelnen Teilchen zu verstehen, wurden mikromagnetische Simulationen für unterschiedliche geometrische Formen durchgeführt. Die Ergebnisse zeigten Übereinstimmung mit den Experimenten und konnten die magnetischen Konfigurationen an den unterschiedlichen Teilchenflächen voraussagen.

- 
4. Magnetische Skymionsysteme: Zwei unterschiedliche Sets der skymionischen Proben mit unterschiedlichen Schwermetallen als Bestandteil und variierenden Dicken der ferromagnetischen Zwischenlage wurden untersucht mithilfe der magnetosensitiven Ptychografie. Die umfassende Messung der magnetischen Parameter wurden an einer SQUID-Anlage durchgeführt. Ein wichtiges Ergebnis ist die Anwendung der ptychografischen Bildgebung für die Untersuchung der sub-100 nm großen Objekte bei Raumtemperatur, wobei ihr skymionisches Profil klar identifiziert werden konnte. Die erhaltenen Daten wurden zur Analyse der Form und Größen der Skymionen in Abhängigkeit von dem Material und der Dicke der benutzten Viellagenschicht, sowie des angelegten Ausrichtungsfeldes untersucht. Die Dzyaloshinskii-Moriya-Wechselwirkung (DMI) wurde auf der Grundlage der gemessenen Daten abgeschätzt und ihre Wirkung auf die Stabilisierung der Skymionenzustände diskutiert im Vergleich mit den Daten aus der Literatur.

Diese Arbeit hat das Potential der ptychografischen Bildgebung für rein-magnetische und nicht-magnetische Systeme aufgezeigt. Ein signifikanter Fortschritt bezüglich der Auflösung wurde erreicht, der in vielen Fällen nur von den geometrischen Einschränkungen des experimentellen Aufbaus limitiert wurde. Dies bietet eine hervorragende Grundlage für die nächsten Schritte, um die wellenlängen-limitierte Auflösung bis zu einem Nanometer und 3D-Bildgebung durch Tomo-Ptychografie zu erreichen. Der Fortschritt im Bereich der neuen modernen Röntgen-CCD-Detektoren, die für kohärente "one shot"-Bildgebung an den FELs entwickelt wird, kann auch neue Möglichkeiten für die zeitaufgelösten Messungen und die 4D-Spektro-Mikroskopie mit vorher noch nie erreichten Kombinationen von nm, meV und ps Auflösung eröffnen. Diese Optionen können am BESSY II im geplanten VSR-Modus ab dem Jahr 2021 realisiert werden.

# Contents

<b>1</b>	<b>Introduction</b>	<b>4</b>
<b>2</b>	<b>Interaction of X-ray radiation with matter</b>	<b>7</b>
2.1	Synchrotron radiation . . . . .	7
2.1.1	Creation and properties of synchrotron radiation . . . . .	8
2.1.2	Undulator radiation . . . . .	10
2.1.3	Coherence of X-Ray sources . . . . .	12
2.2	X-ray absorption in matter . . . . .	14
2.2.1	Fermi's Golden Rule . . . . .	16
2.2.2	X-ray absorption spectroscopy . . . . .	18
2.2.3	XMCD . . . . .	19
2.3	Diffraction . . . . .	23
2.3.1	X-ray scattering . . . . .	25
2.3.2	Resonant X-ray scattering for magnetic materials . . . . .	27
2.4	Relevant basics of magnetism . . . . .	31
2.4.1	Energy in ferromagnetic materials . . . . .	32
<b>3</b>	<b>X-ray Imaging</b>	<b>38</b>
3.1	Background . . . . .	38
3.1.1	Types of X-ray Microscopy . . . . .	39
3.1.2	Scanning Transmission X-ray Microscopy . . . . .	40
3.2	Phase imaging and phase problem . . . . .	43
3.2.1	Holography . . . . .	44
3.2.2	Coherent X-ray diffraction imaging . . . . .	45
3.2.3	Ptychography . . . . .	46
3.2.4	Sampling in diffraction imaging . . . . .	51
3.3	Magnetic microscopy . . . . .	53

---

<b>4</b>	<b>Ptychography at the MAXYMUS microscope</b>	<b>57</b>
4.1	UE46 beamline at BESSY II	57
4.1.1	MAXYMUS end station	59
4.1.2	Coherence at MAXYMUS	62
4.2	Ptychographic imaging implementation in STXM	67
4.2.1	The CCD camera for X-ray detection	69
4.3	FZPs for ptychography	75
4.4	Ptychography resolution	77
4.4.1	Coherence and ptychography	77
4.4.2	Numerical aperture	78
4.4.3	Flux and scattering power	79
4.5	Optimization of diffraction pattern acquisition	82
4.5.1	Overlap ratio of scanning points	82
4.5.2	Defocus scanning	84
4.5.3	Resolving power and dwell time	86
4.6	Conclusion	88
<b>5</b>	<b>Ptychographic chemical and magnetic contrast</b>	<b>90</b>
5.1	Chemical contrast in LiFePO <sub>4</sub> battery nanoparticles	90
5.2	Rock varnish sample	93
5.3	Magnetic ptychography at domain labyrinth structure	99
5.4	Conclusion	102
<b>6</b>	<b>Ptychographic imaging of skyrmions</b>	<b>104</b>
6.1	Basics of skyrmions	104
6.1.1	Methods to determine DMI	106
6.1.2	Skyrmion imaging	108
6.2	Ptychography on skyrmion systems	108
6.2.1	CoFeB based multilayers with different heavy metals: Pd and Pt	108
6.2.2	Skyrmion samples with different thickness of ferromagnetic layer	112
6.3	Comparison of STXM and ptychography for skyrmion imaging	121
6.4	Conclusion	123
<b>7</b>	<b>3D magnetization of Cu-Ni core shell nano particles</b>	<b>126</b>
7.1	Particle shape	127
7.1.1	Cu single crystal	127
7.1.2	Twinned particles	128
7.1.3	Twin boundaries and strain	129
7.2	Ni shell on Cu core grown by epitaxy	130
7.2.1	Ni shell magnetic properties	130

# CONTENTS

---

7.3	Sample preparation . . . . .	131
7.4	Magnetic properties . . . . .	134
7.5	STXM spectroscopy and magnetic contrast of core-shell structures . . . . .	135
7.6	Simulation of 3D magnetization . . . . .	138
7.6.1	Magnetization simulation of icosahedral shape . . . . .	139
7.6.2	Magnetization simulation of pentagonal dipyramid shape . . . . .	141
7.7	Magnetic ptychography on core-shells . . . . .	142
7.8	Conclusion . . . . .	150
<b>8</b>	<b>Summary and outlook</b>	<b>151</b>
<b>A</b>	<b>Ptychographic reconstruction engine at MAXYMUS</b>	<b>156</b>
A.1	Reconstruction software . . . . .	156
A.2	Computing power . . . . .	158
<b>B</b>	<b>Phase imaging and phase information</b>	<b>160</b>
B.1	Interpretation of phase information . . . . .	160
B.2	Artifacts . . . . .	161
<b>C</b>	<b>Methods for resolution evaluation</b>	<b>164</b>
<b>D</b>	<b>Magnetic properties of skyrmion multilayer</b>	<b>166</b>
<b>E</b>	<b>Magnetisation simulation of nanoparticle Ni shell</b>	<b>174</b>
E.1	Cell size of the simulations . . . . .	174
E.2	Icosahedral particle . . . . .	175
E.3	Pentagonal dipyramid particle . . . . .	175
E.4	Simulation with external magnetic field . . . . .	178
	<b>Bibliography</b>	<b>181</b>
	<b>List of Figures</b>	<b>199</b>
	<b>List of Tables</b>	<b>205</b>
	<b>List of publications</b>	<b>206</b>
	<b>Acknowledgments</b>	<b>208</b>

# Chapter 1

## Introduction

High resolution imaging on nanometer scales is essential for many fields of technology and science. Originally microscopy was introduced with the use of visible light with resolution limited by the wavelength to about 300 nm. Nowadays microscopy methods are also extended to more complex and high resolution applications using electrons and X-rays. Electron microscopy provides information on atomic resolution level, however because of the strong interaction of electrons with matter the method is suitable only for imaging of thin samples and their surfaces [1, 2]. X-ray microscopy using synchrotron radiation has been in active development for the last few decades [3]. Beside the shorter wavelength of a few nanometer soft X-rays have high penetration depth up to several  $\mu\text{m}$  in any material that is combined with spectroscopic capabilities providing high chemical and magnetic sensitivity. X-ray light is focused by the special diffraction optics which can be based on diffraction on crystal and gratings, using refractive or reflecting mechanisms. In soft X-ray microscopy, which covers the energy range between 200 and 2000 eV, Fresnel Zone Plates (FZPs) are the most successfully applied focusing devices. FZPs typically have lateral resolution in a range of 20 nm given by the smallest width of the outermost zone. However resolution below few tens of nanometer is still challenging since fabrication of high resolving FZPs is technically very elaborated process and results in low diffraction efficiency of this optics [4].

Ptychography is a lenseless diffraction imaging technique which became a promising method in the field of X-ray microscopy providing phase information and higher spatial resolution than conventional scanning transmission X-ray microscopy (STXM). In this case the spatial resolution is not limited by the used focusing optics theoretically reaching wavelength limited resolution [5]. Ptychography combines all the advantages of STXM for the nondestructive study of sample structure with a resolution that is only limited by the sample scattering strength and the largest scattering angle measured in diffraction image.

This coherent imaging technique enables probing of extended objects with possibility to reconstruct phase image due to over redundant data obtained from the overlap of neighboring scanning points. Iterative phase retrieval algorithm reconstructs the complex-valued transmission function of the sample and provides information about the illumination profile simultaneously.

The fundamental length scales of magnetic features like domain wall width, exchange length or domain pattern can reach sizes below few tens of nanometer. Therefore the application of highly resolved methods for the imaging of modern magnetic materials is of strongly increasing scientific interest. To find a path to magnetic measurements the X-ray magnetic circular and linear dichroism (XMCD and XMLD) effects are utilized. They provide strong magnetic contrast at L and M edges for the 3d and 4f elements which are contained in nearly any magnetic media. These edges are energetically positioned in the soft X-ray range between 350 eV (La  $L_3$ -edge) and 1576 eV (Yb  $M_4$ -edge) [6]. The XMCD effect allows the mapping of magnetic moments inside the observed material with high contrast and the inherent possibility the quantitatively determine spin and orbital moments in specific elements basing on sum rules [7].

The ptychographic set up installation with the following experimental work presented in this thesis was done at MAXYMUS scanning transmission X-ray microscope at BESSY II synchrotron operated by the Helmholtz Zentrum Berlin. For the capturing of the diffraction patterns in reciprocal space a fast and sensitive CCD camera was installed and commissioned. That in combination with specially designed highly efficient FZPs allowed to perform fast and reliable high resolution ptychography imaging.

One of the main points of this thesis was to explore how scattering power of the studied sample influences on the contrast and resolution of ptychographic reconstructions. The scattering strength of pure magnetic samples is reduced in comparison with scattering on morphological and chemical features due to smaller dichroic scattering cross section. It produces certain experimental challenges for magnetic ptychographic imaging. Therefore the wide range of research relevant materials with chemical, pure magnetic and mixed scattering have been imaged and studied:  $\text{LiFePO}_4$  nano batteries, desert varnish and multilayer film with magnetic domains.

Another line of this work was the investigation of non-trivial magnetization configurations, which occur in skyrmionic multilayer systems and magnetic thin films having curved geometry, using soft X-ray magnetic ptychography. Magnetic skyrmions in multilayer thin films are topologically protected local whirls of the spin configuration, which are proposed as possible candidates for spintronic application. These magnetic structures with the size ranging from few nm till  $\mu\text{m}$  can be stabilized in the multilayer and manipulated by external magnetic field or applied current. On the other hand, the magnetization of curved surfaces is under active investigation due to unusual magnetic spin configurations induced by geometry and strain in thin films. The core-shell nano particles with complex 3D shapes have been chosen for this study because thin Ni film shell potentially

can host vortex like magnetic structures and domain walls. The study of sub-100 nm sized skyrmions, vortices and domains allows to explore limitations, advantages and applicability of soft X-ray ptychography for high resolution magnetic imaging.

The thesis is structured as follows. Chapter 2 is a brief introduction of the fundamentals of synchrotron radiation and interaction of X-rays with matter. In particular X-ray absorption and scattering by magnetic materials have been discussed.

Chapter 3 has an overview over existing X-ray imaging methods, their advantages, limitations and application for imaging of magnetic materials. The phase sensitive methods utilizing highly coherent X-ray light, like coherent diffraction imaging (CDI) and ptychography, which solve so-called “phase problem” have been described. The basic concept of diffraction image sampling in CDI and ptychography, as well as iterative phase retrieval algorithm for ptychographic reconstruction are presented.

Chapter 4 describes the realization of ptychography at MAXYMUS microscope. It includes implementation and commissioning of a new in-vacuum CCD camera for soft X-ray detection, also realization of ptychographic reconstruction code at 8 GPUs computing cluster. New FZP optics in-house produced specially for ptychographic use and made out of SiN and Au with improved beam stop have been tested in terms of diffraction efficiency. The detailed analysis of the performance of different ptychographic scanning configurations, e.g. step size, defocus scanning, dwell time, using Au resolution target have been done.

In chapter 5 for the evaluation of image contrast, reconstruction reliability and resolution in dependance on the sample structure and scattering power the ptychographic imaging of various samples with charge and magnetic scattering has been performed. In this chapter reconstructions of  $\text{LiFePO}_4$  nano batteries and desert varnish sample obtained by ptychography are given in comparison with STXM images. Ptychographic phase and amplitude images of magnetic domain sample exhibiting pure magnetic contrast were analyzed in dependance on X-ray energy and magnetic resolution was estimated.

Chapter 6 describes the imaging of magnetization in skyrmion samples. Multilayer skyrmion specimens with different heavy metals and different thicknesses of ferromagnetic layers have been studied using ptychography. The evolution and shape of skyrmions, as well as their sizes were investigated in dependence on sample composition and applied external magnetic field. Basing on the obtained data Dzyaloshinskii Moriya interaction (DMI) was estimated and its influence on skyrmion state stabilization was discussed.

In Chapter 7 the magnetization of Ni shell of 3D shaped core-shell nanoparticles have been studied using STXM and ptychographic imaging. The magnetization of Ni shell was simulated for different shapes, particle sizes, cubic anisotropy, without and with external magnetic field.

## Chapter 2

# Interaction of X-ray radiation with matter

### 2.1 Synchrotron radiation

The X-ray synchrotron radiation was accidentally discovered as a side effect in 1947 [8] at General Electric's synchrotron accelerator designed as a table top device. The further development of highly brilliant synchrotron radiation sources at dedicated large facilities and their optimization for numerous scientific aims produced completely new and significantly improved methods of X-ray analysis. Nowadays the powerful X-ray radiation generated in storage rings has found multiple applications in various scientific fields like materials science, engineering, life science, paleontology and cultural heritage. Synchrotron light has several advantages compared to laboratory or industrial X-ray tubes and modern high-harmonics laser sources, including [9]:

1. a high photon flux, collimation and brightness with natural source sizes in a range from  $\mu\text{m}$  up to mm;
2. a broad energy spectrum that allows spectroscopic measurements;
3. variable polarization;
4. high beam coherence required for diffraction imaging methods;
5. pulsed time structure of synchrotron X-rays allows pump-probe experiments on a picoseconds scale.

### 2.1.1 Creation and properties of synchrotron radiation

Synchrotron light is electromagnetic radiation emitted by relativistic particles which move with radial acceleration. In a synchrotron particles move on a circular trajectory which is conventionally guided by the bending magnets. The emitted spectrum of such radiation is determined by a characteristic energy  $E_c$  as the central energy value of the emitted light:

$$E_c = \hbar\omega_c = \frac{3q\hbar B\gamma^2}{2m_0} \tag{2.1}$$

where  $B$  is the magnetic field of the bending magnet,  $m_0$  - the mass of the particle at rest,  $q$  - charge of the particle,  $\gamma$  is a Lorentz factor. The energy scales reciprocal with mass of the particles, thus heavy particles (ion, proton, etc.) oscillations tend to produce infrared light, whereas electrons used on the modern synchrotrons and storage rings, radiate visible, ultraviolet light and X-rays.

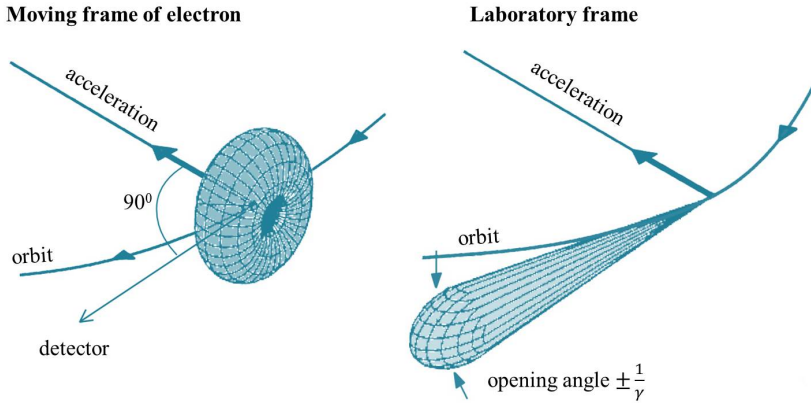


Figure 2.1: The characteristic emission of an electron in the average electron speed and in the laboratory frames. In the electron frame the particle behaves like a Hertzian dipole. The Lorentz transformation in the laboratory system shows the characteristic distortion of the radiation field into the cone in the forward direction with opening angle  $1/\gamma$ . Adapted from [10].

Due to the Doppler effect the relativistic speed will change the observed frequency by the Lorentz factor  $\gamma$ :

$$\gamma = \frac{1}{1 - (v^2/c^2)} = \frac{E}{m_0c^2}, \tag{2.2}$$

where  $E$  is a total energy of the particle. Because of the relativistic Lorentz compression (figure 2.1) in laboratory system the radiation field of the electron is distorted into the cone. The opening angle of this cone, which is emitting perpendicular to the motion direction in

the laboratory system, is inversely proportional to the Lorentz factor:  $1/\gamma$ . For instance, at ESRF synchrotron with the electron energy of 6.04 GeV opening angle is  $\pm 8.4 \cdot 10^{-5}$  rad, while BESSY II provides 1.72 GeV energy with the opening angle of  $\pm 3.0 \cdot 10^{-4}$  rad.

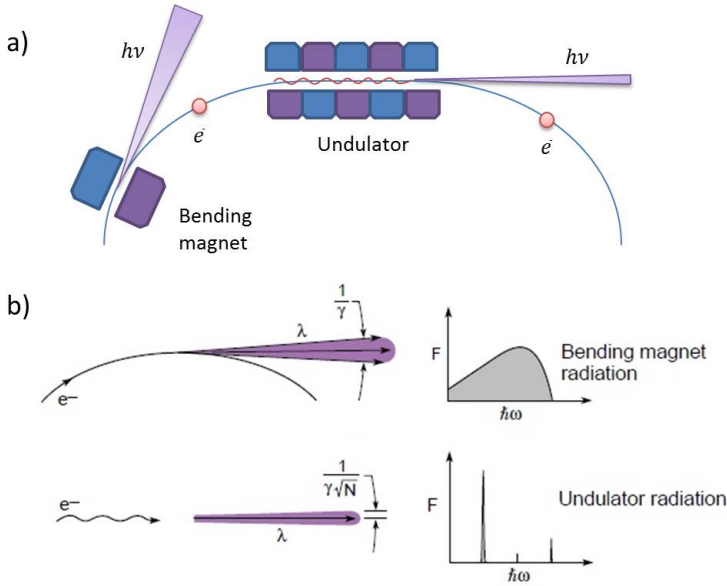


Figure 2.2: Synchrotron radiation from bending magnet and undulator: a) sketch of the storage ring with a bending magnet and an undulator on its straight section; b) radiation cones and energy spectra for bending magnet and undulator. Bending magnets cause single curved trajectory movement, its radiation has a broad spectrum comparable to “white light” of X-ray source. Undulators possess weak periodic magnetic fields that makes characteristic emission angle narrowed by a factor of  $\sqrt{N}$ , where  $N$  is the number of magnetic periods. As a result it produces very bright coherent X-ray light with a narrow emission spectra width. Adapted from [11].

Particles in the storage ring are not spread uniformly on their trajectory, but modulated into “bunches”, which are distributed according to rf-system of the synchrotron. That means that electrons can be held together in particular positions evenly distributed along the storage ring circumference named “buckets”. For instance, BESSY II has a bucket distance of 60 cm that correspond to a bucket frequency [12]:

$$f_{ring} = \frac{c}{60cm} \approx 499.65MHz. \quad (2.3)$$

The duration of one bunch inside of the bucket usually varies from 20 to 100 ps depending

on operation mode [13].

To enhance brilliance insertion devices as undulators, built of a periodic assembly of magnetic dipoles with different polarity and zero integral of resultant magnet field [11, 14], are implemented in the straight sections of the storage ring (figure 2.2 a). The comparison of the radiation properties of bending magnet and undulator is presented in figure 2.2 b).

### 2.1.2 Undulator radiation

X-ray light in undulator is produced by electrons moving through a periodic magnetic structure as it is shown in figure 2.3. The electrons oscillate and create radiation of an energy which can be varied by changing the gap distance between lower and upper rails.

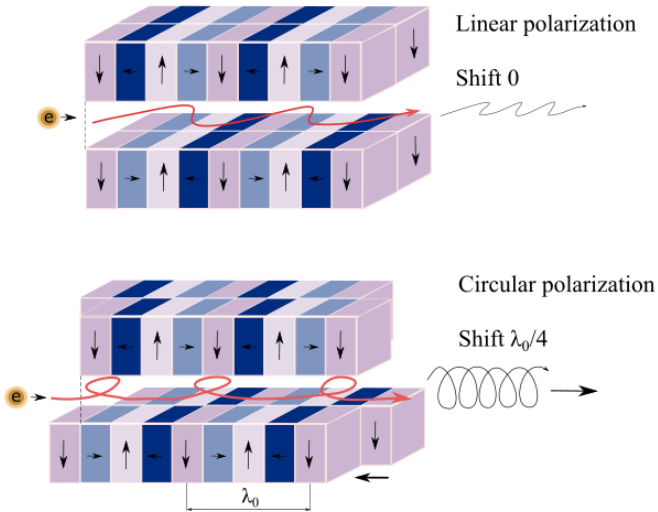


Figure 2.3: Schematic drawing of an APPLE II undulator at different settings. Top image: linear mode without shift which results in horizontally polarized light. Bottom image: circular mode. The shift is set to the position with equal amplitudes of the horizontal and vertical magnetic fields (nearly quarter period of the magnetic structure).

**Parameters and properties** The produced radiation is determined by parameters of magnetic system (length of magnetic period, configuration of magnetic fields, their quantity, etc.), as well as an energy of synchrotron. A K-factor is a dimensionless constant, which generalizes all these parameters characterized by the combination of intensity, an-

gle distribution and polarity of undulator radiation. The K-factor is defined as [15]:

$$K = \frac{qB_0\lambda_0}{2\pi mc} = 0.934B_0\lambda_0 \quad (2.4)$$

with  $\lambda_0$  as a period of magnets in an ID,  $q$  - the charge of electron and  $B_0$  - the deflecting magnetic field. For undulators  $K < 1$  that results in radiation interference, which produces narrow energy bands (figure 2.2).

Electrons emit electromagnetic radiation according to their periodic motions in the undulator, which is determined by its period  $\lambda_0$ . Because of the relativistic Lorentz compression the wavelength period in the frame of electron movement is reduced by a factor  $\gamma$ :

$$\lambda' = \frac{\lambda_0}{\gamma}, \quad (2.5)$$

producing radiation at the frequency:

$$f' = \frac{c}{\lambda'} = \frac{c\gamma}{\lambda_0} \quad (2.6)$$

In the laboratory field of reference (on axis:  $\theta = 0 \rightarrow \cos\theta = 1$ ) a wavelength has the frequency which is Doppler shifted:

$$f = \frac{c}{\lambda_0(1 - \beta)} \quad (2.7)$$

where  $\beta = v/c$  is the velocity of the observer in terms of the speed of light. Considering that  $\gamma \cong \frac{1}{2(1-\beta)}$ , the observed radiation frequency and wavelength respectively are [16]:

$$f = \frac{2\gamma^2 c}{\lambda_0} \Rightarrow \lambda = \frac{\lambda_0}{2\gamma^2} \quad (2.8)$$

Taking into account magnetic tuning through the value  $K$  we can express resulting wavelength for off-axis observation, when  $\theta \neq 0$ , as following:

$$\lambda = \frac{\lambda_0}{2\gamma^2} \left(1 + \frac{K^2}{2} + \gamma^2\theta^2\right), \quad (2.9)$$

where  $\lambda^2\theta^2$  presents the off-axis wavelength variation. This formula is valid only for the first harmonic radiation, but undulators generate higher harmonics as well ([11]-[17]). The odd harmonics are the most prominent with high brightness and narrow spectrum and provide X-rays of higher energies. The observed wavelength is calculated as:

$$\lambda^2 = \frac{1}{n} \frac{\lambda_0}{2\gamma^2} \left(1 + \frac{K^2}{2} + \gamma^2\theta^2\right), n = 1, 3, 5, \dots \quad (2.10)$$

The equation shows that for producing photons with lower energy (with bigger wavelength) stronger magnetic field is needed, that can be done by reducing the gap between magnetic rails.

**Polarization** An APPLE-type undulator is frequently used insertion device. It has rails divided into two, with the ability to shift these rows with regards to each other (figure 2.3). Their relative shifting modifies the magnetic field in the electron path and allows the creation of light which is polarized circularly, elliptically, or linearly in the horizontal and vertical directions.

Normally an electron moving along  $Z$ -axis in an undulator oscillates in  $X$  direction (horizontally). Circular polarization is created by using an undulator with four rows periodic magnets, with two of them placed above the electron orbit plane and other two below. Displacing one of the rails in each pair for one quarter period produces magnetic field which forces the electrons to move on helical trajectory. Also the relative shift of rails is used for creation linear polarized light in arbitrary planes.

### 2.1.3 Coherence of X-Ray sources

A high degree of coherence is required for the most of the X-ray imaging techniques (STXM, holography, diffraction imaging, ptychography, etc.). In practice coherence determines the interference and diffraction behavior of the X-ray light.

Since a real X-ray beam is not a perfect plane and monochromatic wave, the property of coherence is only valid over so called coherence length, which is determined by the features of radiation source. There are two types of coherence [18, 19]:

- Temporal (longitudinal) coherence length  $L_T$ , describes variation of wavelength within a beam as it is shown in figure 2.4 (on the left). Considering two waves traveling in phase from the starting point,  $L_T$  defines the distance that they can travel keeping their components in phase.
- Spatial (transverse) coherence  $L_S$  determines directional relative displacement of two waves coming from the initial point in one phase as it is shown in figure 2.4 (on the right).

The coherence length is the distance when the phase difference between the two waves becomes considerably large, i.e. the minimum of the one wave coincides with the maximum of the other. It means they are out of phase at length  $L_T$  and in phase again after the distance  $2L_T$  because of the periodic structure of wave oscillations. Dividing the distance into  $N$  wavelengths it is possible to conclude that:

$$2L_T = N\lambda = (N + 1)(\lambda - \Delta\lambda), \tag{2.11}$$

where  $\lambda' = \lambda - \Delta\lambda$  is a difference between two wavelengths. Rearranging 2.11 and assuming that  $N \gg 1$  it is easy to calculate the temporal coherence length:

$$L_T = N\lambda = \frac{1}{2} \frac{\lambda^2}{\Delta\lambda}. \tag{2.12}$$

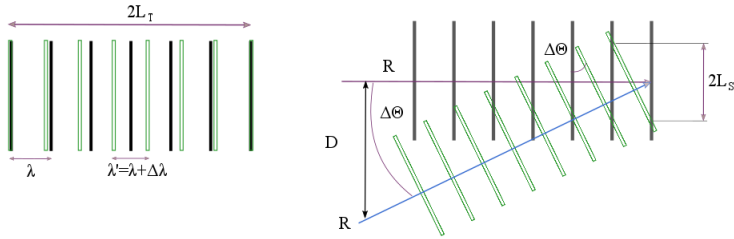


Figure 2.4: Coherence properties of waves: temporal coherence length  $L_T$  (on the left) and spatial coherence  $L_S$  (on the right).

At synchrotron sources temporal coherence is determined by the bandwidth of an undulator and/or the monochromators used for the further decrease of  $\Delta\lambda$ .

A spatial coherence occurs when two wavefronts differ from each other by the propagation direction for a small angle  $\Delta\theta$ . These two waves, emitted in phase from two source points and separated by the distance  $D$ , come in phase again in the distance  $2L_S$ , as for the temporal coherence length. Basing on the trigonometric principles the angle  $\Delta\theta$  can be presented as:

$$\Delta\theta = \frac{\lambda}{2L_S} = \frac{D}{R}, \quad (2.13)$$

where  $R$  is a distance from the source. Solving the 2.13 we can get the formula for  $L_S$ :

$$L_S = \frac{\lambda R}{2D}. \quad (2.14)$$

The equation 2.14 implies that while reducing the source size  $D$  we improve spatial coherence of the source as well as its brightness.

Figure 2.5 shows typical layout of a beamline with elliptical undulator as an insertion device, monochromator and exit slit system. The aperture given by both slits creates the size of a virtual point source. Energy resolution is controlled by the opening of vertical aperture, which results in higher energy resolution with the decrease of the slit gap. The spatial coherence is determined by the opening degree of the horizontal slits which typically a few tens of  $\mu\text{m}$ . The smaller slits opening leads to the higher coherence of the resulting light, but at the same time to significant drop of the beam flux. The relation between coherent flux obtained after spatial and monochromator spectral filtering,  $P_{coh}$ , and initial flux in the center cone of the undulator,  $P_{cen}$ , can be expressed as:

$$P_{coh} \propto \frac{(\lambda/2\pi)^2}{(d_x \Theta_x)(d_y \Theta_y)} \cdot N \frac{\Delta\lambda}{\lambda} \cdot P_{cen}. \quad (2.15)$$

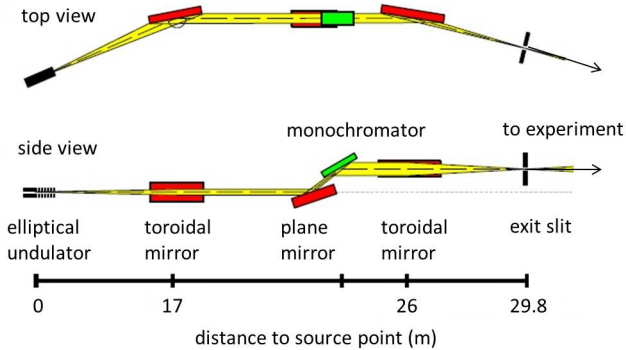


Figure 2.5: Typical beamline components based on layout of UE46 beamline at BESSY II. After leaving the undulator the X-rays are focused onto a grating monochromator using mirrors, which produces a vertical energy dispersion. A further mirror focuses the light on the adjustable exit slit assembly, which creates a source point for experiments and determines monochromaticity and coherence of X-rays. Adapted from [12].

The first factor refers to the spatial filtering, where  $d_x$  and  $d_y$  are horizontal and vertical pinhole (or slits) size respectively, and  $\Theta_x$ ,  $\Theta_y$  describe the beam divergence. The second term is a spectral filtering component.

## 2.2 X-ray absorption in matter

X-ray light with incident intensity  $I_0$  is weakened by passing through matter. The quantitative description of this process is given by the absorption coefficient  $\mu$ . The value  $\mu$  depends on the energy of incident X-ray beam and is characteristic for a specific material. Considering  $z$  as a thickness of a specimen and the attenuation of the incoming X-ray beam through this sheet  $\mu dz$ , we can describe the intensity of the beam in the medium by the equation:

$$\frac{dI(E)}{I(E)} = -\mu(E)dz \quad (2.16)$$

Integrating 2.16, we obtain the intensity of the transmitted beam with initial intensity  $I_0$  after propagation through the sample with thickness  $z$ :

$$I(z) = I_0 e^{-\mu z} \quad (2.17)$$

This formula is an expression of Lambert-Beer's law. For materials with different atomic density  $\rho_a$  in heterogeneous structures, absorption events in layers can also be calculated using total absorption cross-section  $\sigma_a$  of these materials:

$$\mu I(z)dz = \rho_a \sigma_a I(z)dz, \quad (2.18)$$

where

$$\sigma_a = \tau + \sigma_{coh} + \sigma_{incoh} + \kappa_n + \kappa_e + \sigma_{ph} \quad (2.19)$$

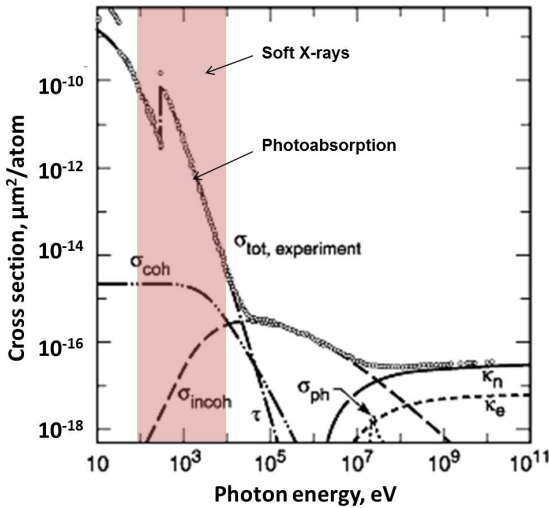


Figure 2.6: Total photon cross section in carbon, as a function of energy, showing the contributions of different processes:  $\tau$ , atomic photo-effect (electron ejection, photon absorption);  $\sigma_{coh}$ , coherent scattering (Rayleigh scattering atom neither ionized nor excited);  $\sigma_{incoh}$ , incoherent scattering (Compton scattering of an electron);  $\kappa_n$ , pair production, nuclear field;  $\kappa_e$ , pair production, electron field;  $\sigma_{ph}$ , photonuclear absorption (nuclear absorption, usually followed by emission of a neutron or other particle). Adapted from [20].

$\sigma_a$  in equation 2.19 includes all X-ray interactions with matter which additively contribute to their attenuation: photoabsorption  $\tau$ , Rayleigh scattering (elastic scattering)  $\sigma_{coh}$ , Compton scattering (inelastic scattering)  $\sigma_{incoh}$ , absorption with forming electron-positron pairs  $\kappa_n$  and  $\kappa_e$ , and photonuclear absorption  $\sigma_{ph}$ . The contribution of X-ray photoabsorption is energy dependent and often increasing with atomic number roughly

Element	Absorption edge	Element	Absorption edge
C	$K$ 184 eV	Co	$L_3$ 777.7 eV
N	$K$ 410 eV	Ni	$L_3$ 852.7 eV
O	$K$ 543 eV	Gd	$M_5$ 1190 eV
Fe	$L_3$ 707.3 eV	Tb	$M_5$ 1241 eV

Table 2.1: Absorption edges of basic elements in soft X-ray range (up to 2000 eV).

proportional to  $Z^4$ . In the range of energies used for soft X-ray microscopy ( $E < 1.2$  keV) the most significant influence on energy attenuation is caused by photo absorption, which is for instance two to three orders higher than Rayleigh scattering that can be neglected (figure 2.6).

In photoabsorption process if an atom absorbs the photon with energy larger than ionization energy of an electron bound to the atomic nucleus it becomes ionized. The emitted electron has a kinetic energy equal to difference of the photon energy and binding energy:

$$E_k = E_{ph} - E_b. \quad (2.20)$$

Figure 2.7 shows the calculated dependence of absorption cross section on photon energy. The presence of the rapid jumps of absorption is connected with sudden possibility of the atoms to get ionized since the photon energy is large enough to eject an inner shell electron. Between these, so called, absorption edges cross section decreases with the increase of photon energy proportionally to  $E^{-3}$ . Observed absorption edges correspond to excitation of 1s electron at K-edge, 2s or 2p electrons at an L-edge, 3s, 3p, 3d - M-edge, and they are specific characteristics for every chemical element of periodic table. Table 2.1 presents energy of absorption edges of different materials.

### 2.2.1 Fermi's Golden Rule

For the description of X-ray photoabsorption it is considered that an X-ray photon with energy  $E = \hbar\omega$  excites a core shell electron from the initial state  $|i\rangle$  to the final state  $|f\rangle$ , which has energy  $E_f = E_i + E$  and density of states  $\rho(E_f)$ . The transition probability  $\Gamma_{i \rightarrow f}$  from initial to final state is described by Fermi's Golden Rule [22]:

$$\Gamma_{i \rightarrow f} = \frac{2\pi}{\hbar} |\langle \Psi_f | H_{int} | \Psi_i \rangle|^2 \rho(E_f), \quad (2.21)$$

where  $|\langle \Psi_f | H_{int} | \Psi_i \rangle|$  - matrix element of magnetic field operator,  $H_{int}$  is a time depended disturbance operator of the Hamiltonian  $H_0$  of the atom and can be expressed as:

$$H_{int} = -\frac{e\hbar}{i2mc} A_0 \epsilon e^{i(kr - \omega t)} \cdot \nabla = -\frac{e\hbar}{i2mc} A_0 \epsilon e^{-i\omega t} (1 - ikr + 1/2(ikr)^2 + \dots), \quad (2.22)$$

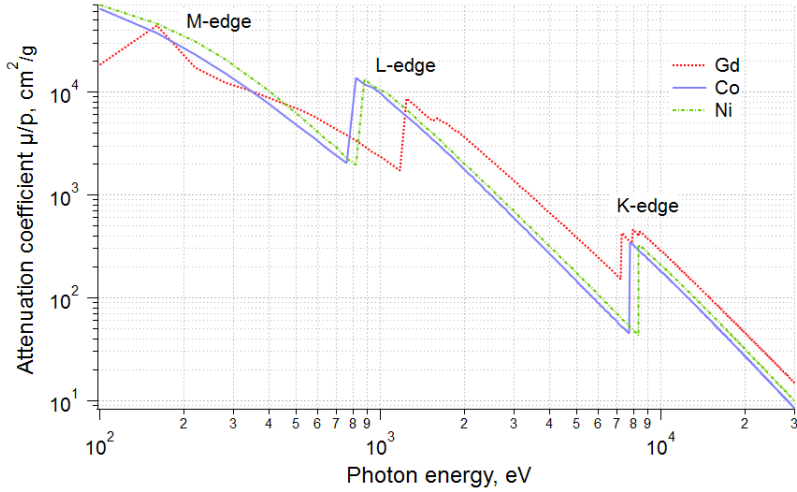


Figure 2.7: Absorption edges of ferromagnetic materials Gd, Co, Ni. Calculations are based on data from [21].

$\epsilon$  - light polarization vector,  $k$  - light propagation vector,  $r$  - electron position coordinates. Since the core function is extremely localized and  $kr \ll 1$  we can apply dipole approximation [23]. In this case all factors of the exponential Fourier series after the first one can be truncated. At this case the absorption cross section for a photon is estimated as:

$$\sigma(E) \sim |\langle \Psi_f | \epsilon \cdot p | \Psi_i \rangle|^2 \rho(E_f), \quad (2.23)$$

where  $p$  - the dipole transition operator. So the transition occurs only when the classic dipole criteria are met. Therefore the following selection rules for excitations have to be consider:

$$\begin{aligned} \text{angular momentum } \Delta l &= \pm 1 \\ \text{magnetic quantum number } \Delta m_l &= 0, \pm 1 \\ \text{total angular momentum } \Delta j &= 0, \pm 1 \end{aligned}$$

For instance, on K- and  $L_1$ -edges, at  $s$  state with  $l = 0$ , transitions occur only to final states which contain  $p$  symmetry. While for  $L_{2,3}$ -edges, at  $p$  states with  $l = 1$ , transitions happen only to final states containing  $s$  or  $d$  symmetry. The dipole transition to the final  $s$  state is mostly neglected because its transition radial matrix element is about two orders of magnitude lower than transition to  $d$  state.

### 2.2.2 X-ray absorption spectroscopy

X-ray absorption spectroscopy (XAS) is a technique which studies the absorption structures of particular elements in the vicinity of an inner-shell edges. There are two regions to be distinguished Near Edge X-ray Absorption Fine Structure (NEXAFS) covering the energy up to about 10 eV above threshold and Extended X-ray Absorption Fine Structure (EXAFS) which relates to the region higher than 30 eV. In EXAFS the outgoing electron can be treated as a nearly free radial wave. The observed oscillation in the absorption results from interference phenomena of the outgoing and back-scattered wave. With their analysis by FT the atomic arrangement, i.e. the distance to the neighboring atoms, can be determined with relative accuracy less than 10 fm. However EXAFS measurements in soft X-ray range are hard to realize due to difficulties in the subtraction of the background and the appearance of overlapping absorption edges.

The interpretation of the NEXAFS is based on the Fermi's Golden Rule. In the simplified form the matrix element can be considered as a constant and thus the absorption profile mirrors the density of the final states, which symmetry is determined by the dipole selection rule. However, in the absorption process a highly excited core hole is created, which decays very rapidly of the time scale of  $10^{-14}$ -  $10^{-15}$  s that results in a natural broadening of the spectra [24].

**Metallic L-absorption spectra** In principle the density of the final state corresponds to the electronic structure in the presence of a core hole. But if the absorbing atom is embedded in a metallic system, there is an efficient screening of the core hole by the conducting electrons and the spectra can be interpreted as a ground state that is applicable for the  $L_{2,3}$  edges in Fe, Co and Ni components in metallic systems. Here the absorption edge exhibits a very intense, resonance-like peak often called "white line". This feature can be ascribed to the large matrix element of the 2p-3d transition due to the local overlap of initial 2p and final 3d bands. The strength of the "white line" is directly correlated to the density of the final states in the unoccupied 3d band at the Fermi level. As shown in figure 2.8 a) for Fe, Co, Ni and Cu  $L_{2,3}$ -edges the line intensities decrease with the decrease of number of empty states in the atomic 3d level.

**Chemical shift** It has been experimentally observed that changes in the different valence states usually result in variations of the XAS "white line positions". Empirically it was found that the peaks are shifted to higher energies with the higher valence [26]. Additionally the absolute shifts depend on the variations of lattice energy in the absorbing atom and also are related to strength of valency vs. ionic bonding [26]. Many electron phenomena, like core-hole interaction and multiplet effects, can also affect the XAS. Since in the final state the core has one electron less present, the outer electrons see an effective core with an increase in positive charge by one. This changes the energy position to the stronger

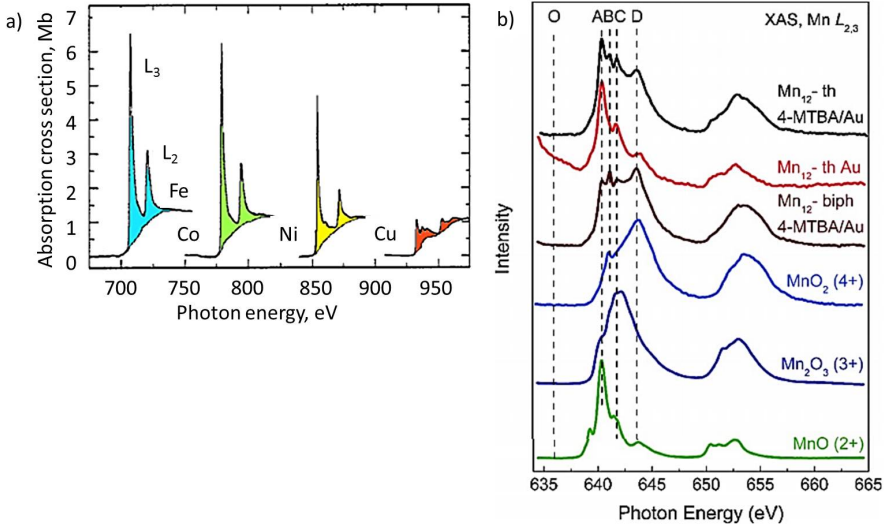


Figure 2.8: X-ray absorption spectroscopy: a) absorption cross sections at  $L_{2,3}$ -edges in Fe, Co, Ni and Cu, b) XAS spectra obtained from  $Mn_{12}$ -th and  $Mn_{12}$ -biph monolayers compared to reference absorption spectra of MnO,  $Mn_2O_3$ , and  $MnO_2$ . Reproduced from [25].

bonding of the outer electrons and varies the final state that can be reached. Due to this shift to higher binding energy, only locally present on the excited atom, other electron states at higher energy can shift down below the energy of occupied states of the neighbouring sites. In most of the cases measurements of suitable reference compounds can be used in order to interpret the XAS data with the possibility of a convolution of reference spectra [27]. This is shown in figure 2.8 b) for Mn compounds with different valencies.

### 2.2.3 XMCD

XMCD (X-ray magnetic circular dichroism) effect was firstly predicted in 1975 by Erskine and Stern [28] and practically discovered in late 1980s [29]. The XMCD describes the different absorption of right and left circular polarized X-ray light by magnetic materials. The important application of the XMCD effect is a unique possibility to determine spin and orbital magnetic moments. These values are of crucial importance to give insights in the anisotropic magnetic properties such as coercivity, magnetostriction, magnetic hysteresis, etc.

In the so-called Stoner model the appearance of magnetism in the transition metals can be described based on the principle that the final 3d states correspond to the unoccupied

d-band at the Fermi level. This band-like structure provides the number of holes which is not an integer number. This also explains that the magnetic moment per atom is  $2.22 \mu_B$  for Fe,  $1.72 \mu_B$  for Co and  $0.62 \mu_B$  for Ni - strongly different from the magnetic moment of the single atoms. Especially the orbital moment contribution of  $0.09 \mu_B$  (Fe),  $0.14 \mu_B$  (Co) and  $0.06 \mu_B$  (Ni) is significantly reduced. This reduction is attributed to the quenching of the orbital moment in the crystal field of the lattice.

In the band structure picture the occurrence of a spin moment is correlated to the exchange splitting of the d-like majority and minority states with respect to the Fermi level as it is shown in figure 2.9 a. It results in a larger amount of empty minority states. Neglecting an orbital contribution the occurrence of XMCD can be explained in a simplified two-step model [30]:

1. In case of  $3d$  transition metal the  $2p$  initial core level splits energetically in a  $j = 3/2$  state ( $L_3$  edge) and  $j = 1/2$  state ( $L_2$  edge). In the first state spin and orbit are coupled parallel ( $l + s$ ), in the second - antiparallel ( $l - s$ ). If the absorbed light has helicity with parallel vector regarding to the  $2p$  orbital moment, it excites the electrons of preferred spin up (down) direction, for antiparallel orientation - spin down (up) electrons in case of  $L_3$  edge ( $L_2$  edge);
2. The excited electrons move to the  $3d$  valence band. All transitions between orbitals follow the so called selection rules, which allows transitions with  $\Delta l = +1$  for positive helicity. Since spin flip of electrons is negligible, they can occupy valence states only with the same spin value. In magnetic materials polarized in beam direction spin-down holes are available in higher number than spin-up holes, polarized photoelectrons see different densities of state, and the XMCD spectrum will display net negative  $L_3$  and positive  $L_2$  peaks.

Using sum rule we can get the separate quantitative estimation of spin and orbital moments from the integrated XMCD signal [7]. It allows determination of moments in a good agreement with experimental data with uncertainty around 10-20%. The spin moment sum rule for  $L_{2,3}$  edges is given by:

$$S_z + \frac{7}{2}T_z = \frac{3}{2}(10 - n) \frac{\int_{L_3} d\omega(\mu^+ - \mu^-) - 2 \int_{L_2} d\omega(\mu^+ - \mu^-)}{\int_{L_3+L_2} d\omega(\mu^+ - \mu^- + \mu_0)}, \quad (2.24)$$

where  $n$  is the number of electrons in the valence state,  $\mu^+$  and  $\mu^-$  - absorption spectra for left and right circular polarized light respectively,  $\mu_0$  - absorption spectrum for X-rays linearly polarized along the magnetization direction,  $\omega$  - the X-ray frequency,  $T_z$  - a magnetic dipole term, which expresses the anisotropy of spin distribution within an atom and is less than 10% within the  $3d$  series of the  $S_z$  value. It can be assumed that  $T_z$  is zero, which is valid only for cubic systems, or this value should be known from experiments

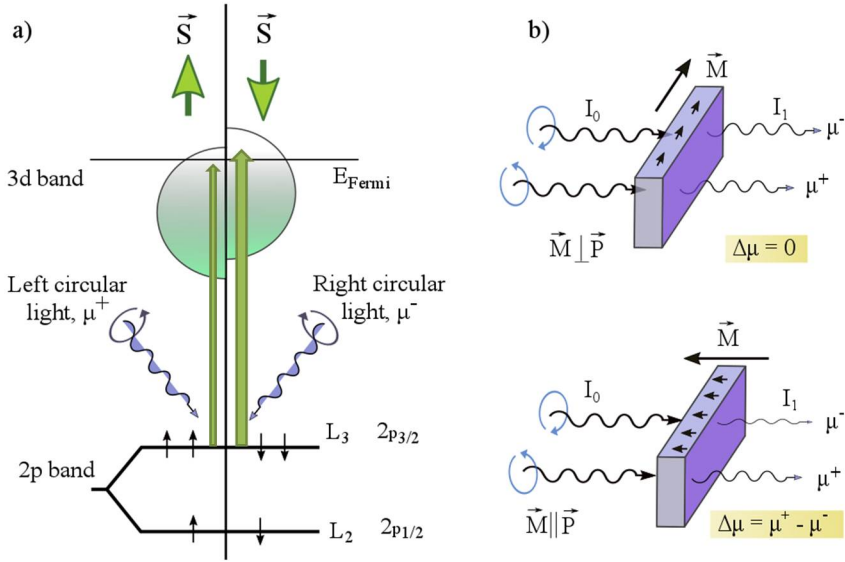


Figure 2.9: XMCD mechanism at  $2p_{3/2}$  initial state: a) the 3d band of magnetic material is probed with X-ray circularly polarized light having opposite polarities, since the band is split the light will see different density of states as a result producing different absorption contrast; b) magnetic materials with different magnetization directions,  $\vec{M}$ , parallel and perpendicular to vector of X-rays polarization,  $\vec{P}$ . The XMCD effect is the strongest for parallel (antiparallel) orientation of these vectors.

or theoretical approximation. Another important approximation is that  $L_3$  and  $L_2$  edges must be clearly separated; otherwise spin sum rule cannot be applied.

The orbital moment sum rule for  $L_{2,3}$  edges is given by:

$$L_z = 2(10 - n) \frac{\int_{L_3+L_2} d\omega(\mu^+ - \mu^-)}{\int_{L_3+L_2} d\omega(\mu^+ - \mu^- + \mu_0)}, \quad (2.25)$$

In practice XMCD effect reveals itself as an intensity difference of X-rays transmitted through magnetic materials with different magnetization directions, e.g magnetic domains. The magnetic dichroism in this case is a difference of absorption spectra with photon spins parallel  $\mu^+$  and antiparallel  $\mu^-$  :  $\Delta\mu_0 = \mu^+ - \mu^-$  (figure 2.9 b). The strength of dichroism depends on the orientation of the sample magnetization,  $\vec{M}$ , and

vector of X-rays polarization,  $\vec{P}$ :

$$\Delta\mu/\mu_0 \sim \vec{M} \cdot \vec{P} \cdot \cos\theta, \quad (2.26)$$

where  $\theta$  is the angle between  $\vec{M}$  and  $\vec{P}$ ,  $\mu_0$  - an average absorption value. In case of orthogonal orientation or non-magnetic absorption  $\mu_0$  is defined as:

$$\mu_0 = \frac{\mu^+ + \mu^-}{2} \quad (2.27)$$

Thereby through the change in the direction of the sample magnetization or polarization of X-rays the difference in absorption can be detected. If the material is magnetized in-plane and illumination is perpendicular to the magnetization direction, no magnetic contrast will appear. In order to get magnetic contrast the sample is tilted respective to the beam axis, normally, by  $30^\circ$ , which results in 50% of full XMCD contrast.

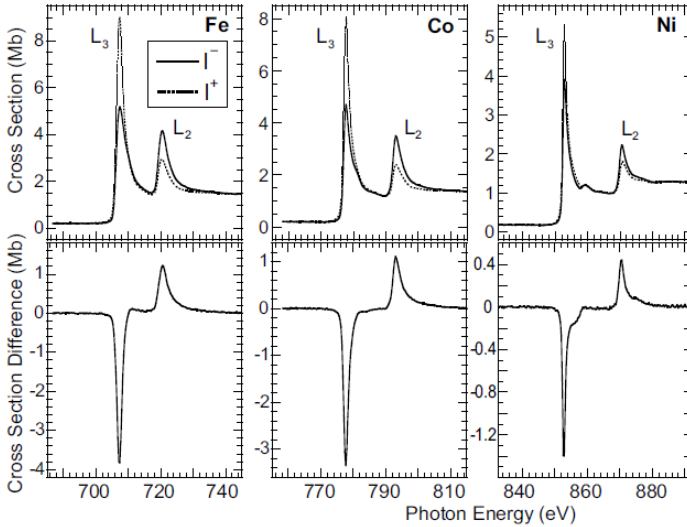


Figure 2.10: Absorption spectra for the Fe, Co and Ni at  $L_{2,3}$  edges using right and left polarized X-ray light,  $\mu^+$  and  $\mu^-$ , in the case when magnetization direction and vector of X-rays polarization are parallel to each other,  $\vec{M} \parallel \vec{P}$ . The difference of two spectra,  $\mu^+ - \mu^-$  gives a pure XMCD signal. Reproduced from [6].

Soft X-rays allow the access to absorption edges of transition metals (Fe, Co, Ni) at L-edges as it is shown in figure 2.10 and rare earth metals at M-edges, e.g. Gd, as the most important elements for magnetism. Here the absorption of X-rays is very intense at

resonance energy values. For example, attenuation length for X-rays in Fe at the  $L_3$  and  $L_2$  edges are 16.7 and 32 nm, while just below  $L_3$  edge this value equals to 591 nm [31]. In case of rare earth metals, Gd and Dy, the X-ray attenuation lengths are 6.2 nm and 12.1 nm, respectively [31]. It is seen from figure 2.10 that dichroic signal is very large - about 20% at  $L_{2,3}$  edges in Fe, Co and Ni.

## 2.3 Diffraction

Diffraction of X-ray light (or any electromagnetic waves) occurs when the wave passes an obstacle or a slit, which is comparable with the wavelength of light, by producing secondary spherical waves. The sum or interference of the secondary waves determines the resulting wavefront in the every point of the space. This phenomenon was described by the Huygens-Fresnel principle [32]. The diffraction of X-ray light provides a powerful instrument for studying the geometry and orientation of diffracting object by the analysis of the resulting diffraction pattern.

Analytical description of the principle can be presented as the resulting oscillation in an observation point on the detector plane coming from the wave surface of the object plane (figure 2.11):

$$\psi(x, y) = \frac{i}{\lambda} \iint q(X, Y) \frac{e^{ikr}}{r} dXdY, \quad (2.28)$$

where  $q(X, Y)$  is a transmission function at the planar object,  $dXdY$  - an infinite small surface element in the object plane producing secondary spherical wavelets,  $r$  - distance from the source of the secondary waves to the observation point,  $k$  - wave number [33]. The distance  $r$  is the length of the vector connecting the point in object  $(X, Y)$  and detector  $(x, y)$  planes:

$$r = \sqrt{[R^2 + (x - X)^2 + (y - Y)^2]} = \sqrt{(r_0^2 - 2xX - 2yY + X^2 + Y^2)} \quad (2.29)$$

Assuming  $\{R, r_0\} \gg \{x, X, y, Y\}$  we can rewrite equation 2.28 as following:

$$\psi(x, y) \cong \frac{ie^{ikr_0}}{\lambda r_0} \iint q(X, Y) \exp\left(ik \frac{xX + yY}{r_0}\right) \exp\left(ik \frac{X^2 + Y^2}{2r_0}\right) dXdY \quad (2.30)$$

The second exponential term in equation 2.30 introduces the curvature of the spherical wavefront, that becomes negligibly small in a far-field geometry.

Far-field and near-field regions of diffraction are defined according to diffraction behavior and guided respectively by Fraunhofer or Fresnel models, which are determined by the relation of distance from aperture to detector plane  $r$  and the square of the largest aperture dimension  $a$ . The Fresnel regime, or near-field diffraction, occurs when  $r \approx a^2/\lambda$ , and far-field Fraunhofer condition fulfills when  $r \gg a^2/\lambda$ .

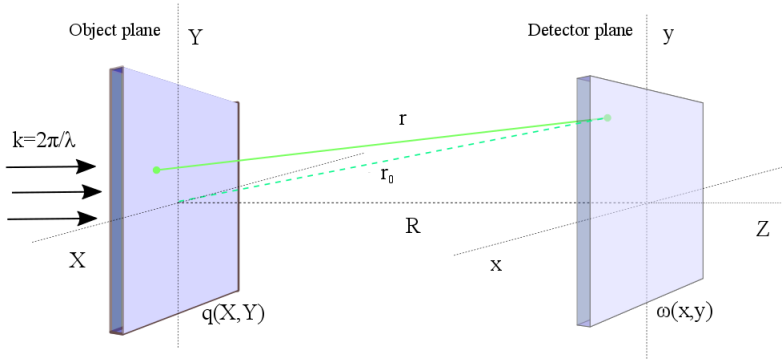


Figure 2.11: Propagation of a plane wave through a planar object with transmission function  $q(X, Y)$ .

In this work we are going to deal mostly with Fraunhofer regime in the far-field, when diffracted waves become planar. It is defined as being located at a distance which is significantly greater than  $a^2/\lambda$ , that means  $X^2, Y^2 \ll \lambda r$ . Observed intensities at Fraunhofer plane can be expressed as:

$$\phi(x, y) = -\frac{i \exp(ikr_0)}{\lambda r_0} \iint q(X, Y) \exp \frac{-ik(xX + yY)}{r_0} dXdY. \quad (2.31)$$

In the most of experimental cases so-called inverse problem has to be solved: the exit wave of the sample should be recovered from the obtained intensity distribution in far-field. It was proposed in 1982 [69] that the structure of isolated non-crystalline objects could be uniquely recovered basing on measured oversampled Fraunhofer speckles, where the missing phase information is obtained by iterative algorithms.

**Diffraction and coherence** In X-ray diffraction imaging fringes or diffraction patterns can be detected due to the interference on an ordered system. If the X-rays are highly coherent the scattering on disordered structures also produces speckled diffraction patterns similar to highly ordered crystal structures [35]. As it is depicted in the figure 2.12 a coherently illuminated sample produces diffraction pattern with multiple speckles which contain information about size and position of the objects relatively to each other. The angular width of these speckles depends on coherently illuminated area  $a$ :  $\Delta\theta \approx \lambda/a$ . While diffraction from incoherently illuminated sample can be characterized only by the distribution of maximum intensities of the concentric rings which depend on  $\lambda/d$ . Incoherent or partial coherent X-rays blur the speckled features of the pattern.

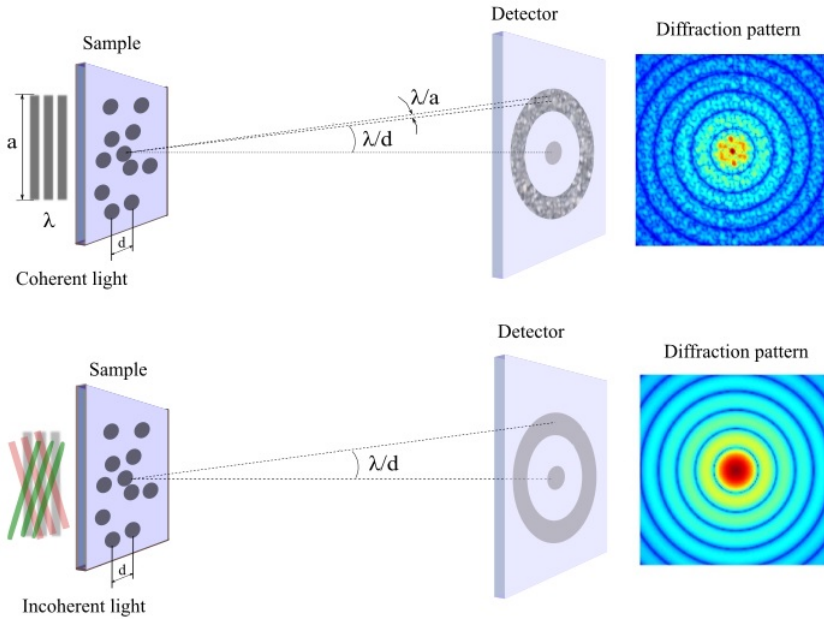


Figure 2.12: Schematic drawing illustrating a) coherent and b) incoherent illumination of the sample with particles placed in averaged distance  $d$  from each other. In the case of incoherent illumination, when spatial coherence is smaller than illuminated area, we see characteristic circular pattern which provides information about the period of studied structures. The coherent light gives even illumination of the exposed sample area. It produces interference from the minor sample details resulting in appearance of speckled pattern. Adapted from [35]

The intensity of soft X-rays scattered speckles is not significant but it can be enhanced by using the advantages of synchrotron radiation to tune the necessary resonance energy for specific materials [36]. Using coherent polarized light in magnetic material studies gives the strong dichroic effect and presence of magnetic speckles which allow static and dynamic studies of magnetic nanomaterials.

### 2.3.1 X-ray scattering

The interaction of the incident X-rays elastically scattered on an object can be expressed by a cross-section value similar to the absorption process. Since from the perspective of X-ray light an atom is nothing else but a cloud of electrons the scattering amplitude can be evaluated as a function of the electron charge density  $\rho(r)$ . It defines the probability of

an electron to be located at a defined position  $r$  in the atom. In this case the atomic form factor is a Fourier transform of the electron density  $\rho(r)$ , assuming that the scattering object has a spherical symmetry with radius  $r$ :

$$F(Q) = \int \rho(r) \exp(iQr) d^3r, \quad (2.32)$$

where  $Q$  is a difference between incident wave vector  $k$  and scattered one  $k'$ , and  $Qr$  is the phase shift between two neighboring scattering volumes.

$$\Delta\phi(r) = (k - k')r = Qr \quad (2.33)$$

For the forward scattering direction when the scattering angle  $\theta$  is close to 0 we can assume that atomic factor  $F(Q)$  is equal to the number of electrons in the atom  $Z$ ,  $F(Q = 0) = Z$ .

At the absorption edges electrons do not behave as an independent volume anymore, instead they start to show strong correlation with the atomic structure that reduces scattering length of atom. Due to anomalous dispersion near absorption edges the scattering form factor becomes a complex value which can be expressed as:

$$F(Q)_{res} = f_0 + \Delta f' + i\Delta f'', \quad (2.34)$$

where  $f_0$  is a non-resonant scattering function as it is presented in equation 2.32,  $\Delta f'$  and  $\Delta f''$  dispersion corrections which are energy depended functions. The first function  $\Delta f'$  is responsible for a phase shift, and  $\Delta f''$  - for a change of the magnitude in the resonant scattering events. Dispersion correction functions depend on the wavelength of the incident X-ray light and don't depend on scattering angle unlike the non-resonant scattering function. These values mostly determine macroscopic properties of material interacting with X-rays.

In the processes of X-rays scattering elastic (Rayleigh) and inelastic (Compton) processes normally occur and should be taken into account. In case if the interaction causes the change of the propagation direction of the photons without energy change we have elastic scattering, that mostly happens when electrons strongly bounded to the atom nucleus. Figure 2.6 illustrates that inelastic scattering in a range of soft X-rays has significantly smaller contribution in comparison with absorption and elastic scattering events. Inelastic scattering increases and becomes dominant in hard X-ray range and  $\gamma$ -radiation. Additionally assuming that in transmission geometry only small angle (elastic) scattering contributes to the registered diffraction patterns we can eliminate the presence of the Compton scattering in the diffraction imaging in transmission geometry.

**Index of Refraction** The atomic form factor is directly related to the complex refractive index. Refractive indices refer to the processes of scattering and absorption, and used for

macroscopic description of these interactions. In a forward scattering geometry the incident wave propagated through material exhibits an amplitude change and the phase shift. Since the atomic factor is a complex number the refraction index can be also expressed as a complex value:

$$n = 1 - \delta - i\beta \quad (2.35)$$

The real part  $\delta$  refers to the refraction strength of forward scattered initial waveplane with respect to vacuum resulting in phase shift. The imaginary part  $\beta$  is related to the absorption of X-rays in matter. We can express these values using form factor of atomic scattering:

$$\delta = \frac{r_e 2\pi N_a}{k^2} f', \quad (2.36)$$

$$\beta = \frac{r_e 2\pi}{k^2} \rho f'', \quad (2.37)$$

where  $r_e$  is an electron radius,  $N_a$  - Avogadro's constant,  $\rho$  - average electron density of the material. The electron density of a material can be found not only from the absorption value  $\beta$ , but from the phase shift information as well. The real part of atomic scattering factor can be expressed by the imaginary one using Kramers-Kronig relation:

$$f'(\omega) = Z^* - \frac{2}{\pi} P_c \int_0^\infty \frac{\omega' f''(\omega')}{\omega^2 - \omega'^2} d\omega', \quad (2.38)$$

where  $P_c$  is a Cauchy's function that allows to avoid singular points when  $\omega' = \omega$ .  $Z^*$  differs from atomic number  $Z$  by small relativistic correction:  $Z^* \approx Z - (Z/82.5)^{2.37}$ . It allows to calculate phase shifts occurring in the sample basing only on transmission measurements. In this case the relation between  $\delta$  and  $\rho$  can be derived:

$$\rho = \frac{2\pi}{r_e \lambda^2} \delta f' \quad (2.39)$$

That allows to find the electron densities of studying specimens having quantitative measurement of the phase shift of the incident light that successfully applied in phase contrast imaging techniques.

### 2.3.2 Resonant X-ray scattering for magnetic materials

For investigation of magnetic materials soft X-ray polarized light is used for magnetic scattering analysis. In classical X-ray diffraction theory the role of magnetic scattering was neglected since in the non-resonant state the interaction of X-rays with magnetic moments in ferromagnets is much weaker than the intensities coming from Thomson charge

interaction. The cross sections of the charge and magnetic scattering off the resonance are proportional to the following terms [37]:

$$\text{charge(Thomson)} \propto \left( \frac{e^2}{mc^2} \right)^2 N^2, \quad (2.40)$$

$$\text{magnetic} \propto \left( \frac{e^2}{mc^2} \right)^2 \left( \frac{\hbar\omega}{mc^2} \right)^2 N_m^2, \quad (2.41)$$

where  $N_m$  is the number of magnetic electrons which makes around 1/10 of number of all electrons,  $N$ . For instance, the ratio of magnetic and charge scattering at hard X-ray range is about  $10^{-6}$  [38]. However the use of resonant scattering close to absorption edges of chemical elements provides magnetic signal few orders of magnitude higher than off resonance signal.

The use of polarized X-rays makes real parts of the charge and magnetic scattering to interfere, that makes the magnetic scattering contribution few orders of magnitude higher [39]. Since the resulting speckles contain mixed information about charge and magnetic states it is important to be able to perform clean separation of two signals. The relevant elastic scattering amplitude in electric dipole on the near resonance condition can be expressed as following [40]:

$$f_n(\omega) = f_0(\epsilon_f^* \cdot \epsilon_i) - i f_1(\epsilon_f^* \times \epsilon_i) m_n + f_2(\epsilon_f^* \cdot m_n)(\epsilon_i \cdot m_n), \quad (2.42)$$

where  $m_n$  - local magnetic moment vector,  $\omega$  - selected photon energy,  $\epsilon$  presents either incoming or final polarizations, which are complex values for circular polarization. The values  $f_0, f_1$  and  $f_2$  are monopole, magnetic dipole and quadrupole parts of the scattering amplitudes, respectively. The third term is negligibly small here in comparison with  $f_0$  and  $f_1$ , so it can be skipped out in further considerations. The part  $f_0$  refers to the resonant charge scattering  $f'_c + i f''_c$ , which is larger near the absorption edge and is independent of the magnetic moment. The term  $f_1$  is the magnetization direction depended scattering  $f'_m + i f''_m$  that can be very pronounced on specific absorption edges and gives rise to XMCD effect. Figure 2.13 shows imaginary and real parts of charge and magnetic scattering. The peaks of phase dependent real parts are shifted to pre-edge relative to the resonant energy. The real part of magnetic component is twice smaller than imaginary one at  $L_3$  edge, indicating that the phase shift in magnetically contrasted samples is much weaker than absorption signal. The same as  $f'_c$  and  $f''_c$  the real and imaginary parts  $f'_m$  and  $f''_m$  are linked by the Kramers-Kronig relation. The  $f''_m$  values can be derived from the measurement of the XMCD amplitude as a function of energy.

The signal from magnetic scattering depends on the incoming X-ray beam polarization and relative orientation of magnetization direction in the sample. The scattering geometry is shown in figure 2.14. If the signal is observed with circular polarized light in transmission mode, then the scattering is registered in near-forward or  $z$  direction. The forward

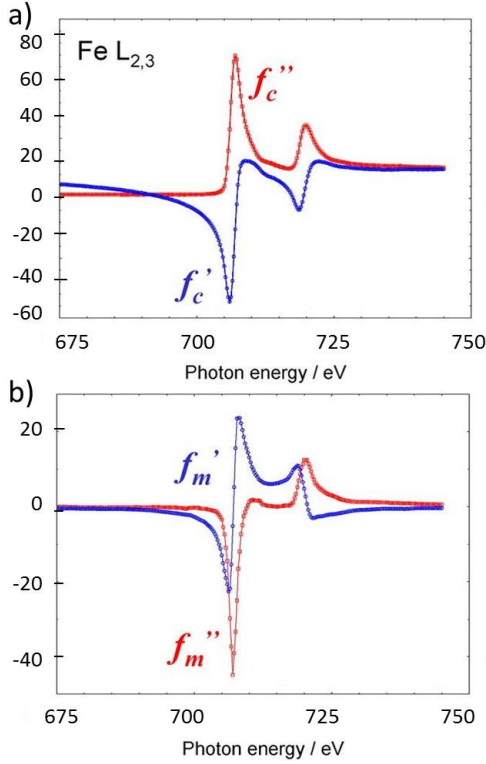


Figure 2.13: The real and imaginary parts of charge scattering  $f'_c$  and  $f''_c$  a) and magnetic scattering  $f'_m$  and  $f''_m$  b) at the Fe L<sub>3,2</sub> edges (values are in arbitrary units). Reproduced from [41].

scattering geometry is defined by the conservation of beam polarization  $\vec{e}_v = \vec{e}'_v$  and direction of the wave vector  $\vec{k} = \vec{k}'$ . In this case for *in-plane magnetization* of the sample the charge-magnetic interference and pure magnetic terms disappear and the cross-section only consists of pure charge scattering:

$$\frac{d\sigma}{d\Omega} \propto |\rho(Q)|^2 \quad (2.43)$$

That stays in agreement with absorption angle dependent XMCD effect presented in the previous chapters. For *out-of-plane magnetization*, when  $m(Q) \propto U_3$ , considering that  $\theta' \neq 0$  and using right circular polarized light, we can express the small angle scat-

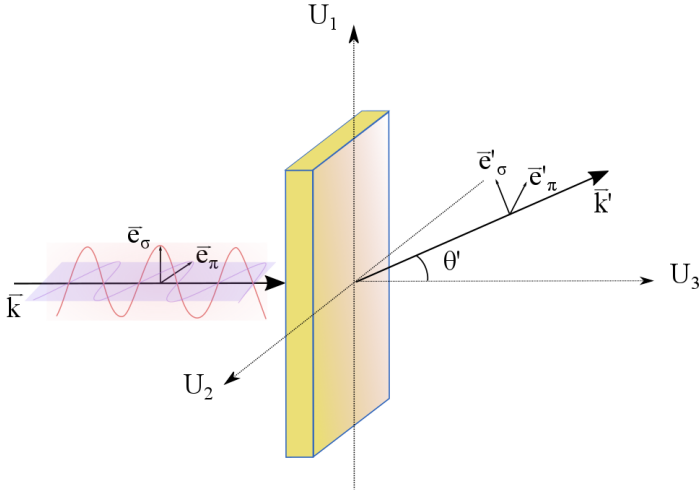


Figure 2.14: Scattering geometry in transmission mode. The incident angle  $\theta$  is  $90^\circ$  and the scattering angle  $\theta'$  is determined with respect to the surface normal. The forward scattering of circular polarized waves for absorptive processes is characterized by conservation of the direction of the wavevector  $\vec{k} = \vec{k}'$  and the state of polarization  $\vec{e}_\nu = \vec{e}'_\nu$ .

tering cross-section as:

$$\frac{d\sigma}{d\Omega} \propto \frac{1}{2}(1 + \cos^2(\theta')) \left[ |\rho(Q)|^2 |f_0|^2 + 4\pi^2 M^2(Q) |f_1|^2 - 4\pi\rho(Q)M(Q) (Re\{f_0\} Re\{f_1\} + Im\{f_0\} Im\{f_1\}) \right] \quad (2.44)$$

having  $\rho(Q)$  and  $M(Q)$  as charge density and magnetic moment structure factors.

The first two terms in equation 2.44 are pure charge and magnetic scattering which can be observed with linear polarized light as well [40]. The implementation of circular polarization additionally produces the interference term contributing to the final intensity which is proportional to  $\rho(Q)M(Q)$ . The more detailed description of the X-ray scattering of polarized light in magnetic materials is presented in works [38]-[41].

The atomic consideration of X-ray scattering, as it was described above, is applicable for the scattering description from larger structures in nm-scale. For example, soft X-ray light can be used for probing magnetic samples with magnetic domains with a period around 100 nm. The main advantage of polarized light application is a possibility to eliminate magnetic and charge scattering information as well as their interference part from the collected diffraction data [42]. As it is discussed the detected absorption intensities for

left and right circular light are not the same. In a sense of diffraction theory let assume the transmission profile having charge ( $t_c$ ) and magnetic ( $t_m$ ) contrast components for RCP and LCP light:

$$E_{t\pm}(x, y) = E_i(t_c(x, y) \pm t_m(x, y)) = c(x, y) \pm m(x, y). \quad (2.45)$$

In the far field the diffracted wave is expressed as a Fourier transform of 2.45:

$$E_{d\pm}(x, y) = F\{E_{t\pm}(x, y)\} = C(x, y) \pm M(x, y). \quad (2.46)$$

As a result the recorded intensities are:

$$I_{d+} = |C + M|^2 = |C|^2 + |M|^2 + 2|C||M|\cos\Delta\varphi \quad (2.47)$$

$$I_{d-} = |C - M|^2 = |C|^2 + |M|^2 - 2|C||M|\cos\Delta\varphi \quad (2.48)$$

where  $2|C||M|\cos\Delta\varphi$  is an interference between charge and magnetic components. Taking into account that linearly polarized light is nothing else but a superposition of two circularly polarized waves we can sum 2.47 and 2.48, which eliminates the interference term. It means that charge and magnetic waves in this case are orthogonal to each other. On the other hand the difference of the intensities with RCP and LCP light will cancel pure magnetic and charge components leaving only the interference part.

## 2.4 Relevant basics of magnetism

In the present work the study of magnetization in thin films produced from ferromagnetic materials will take a significant part. Elemental ferromagnetic metals, like Co, Ni, Fe, Gd, etc., have large positive susceptibility to an external magnetic field and are characterized by a net magnetic moment in the absence of an external magnetic field. These materials show the dependance curve of the flux density in the material  $B$  on the strength of applied magnetic field  $H$  in a shape of characteristic hysteresis loop (figure 2.15). With the field increase magnetization approaches a defined limit, or saturation  $M_s$ , and does not return to its original value when the field is set to zero showing residual magnetization. In order to demagnetize the ferromagnetic fully, so called, coercive force, that rearranges magnetic moments, must be applied. The soft and hard ferromagnetic are distinguished by the area of the hysteresis loops and, coordinately, by the coercive force, which should be applied for the full material demagnetization. The soft ferromagnetic have narrower hysteresis profile than hard ferromagnetic.

When the temperature of a ferromagnetic increases beyond a certain level, which is called the Curie temperature, the system can no longer maintain a spontaneous magnetization. In this state the magnetic susceptibility gets infinitely large and ferromagnetic starts to behave as paramagnetic.

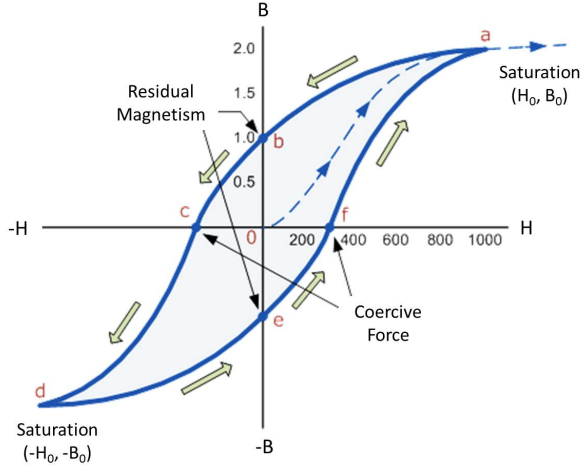


Figure 2.15: Typical hysteresis loop of ferromagnetic material as the relationship between flux density  $B$  and magnetic field strength  $H$ . Points  $a$  and  $d$  correspond to saturation states, when all magnetic moments aligned in the direction field; points  $b$  and  $e$  shows residual magnetism, when the applied field goes to 0 after saturation state; points  $c$  and  $f$  are coercive showing the magnetic field needed to bring sample magnetization to zero. Reproduced from [43]

### 2.4.1 Energy in ferromagnetic materials

In order to understand the magnetization processes we have to consider the minimum total energy of magnetic materials, which determines their magnetization behavior on different scales [44]. This energy is expressed as an integral of different energy densities over the volume of the specimen:

$$E = \int_V (\epsilon_{ex} + \epsilon_{an} + \epsilon_{demag} + \epsilon_{ext}) dV \quad (2.49)$$

The integrated sum of the energies includes:  $\epsilon_{ex}$  exchange,  $\epsilon_{an}$  anisotropy,  $\epsilon_{demag}$  magnetostatic,  $\epsilon_{ext}$  external field and  $\epsilon_{DMI}$  Dzyaloshinskii Moriya interaction (DMI) energies. In the following all energy components involved in equation 2.49 will be introduced in details.

- **Exchange energy  $\epsilon_{ex}$ .** On the quantum level exchange interaction is based on the Pauli principle that forbids electrons with the same spin to occupy the same orbit. The situation when electrons with the same spin orientation are located on the different orbitals is energetically more favorable. It explains the tendency of ferromagnetic materials to form extended regions with uniform magnetization, so called,

magnetic domains. The exchange energy is a short range interaction that includes only neighboring spins. In material with numbered spins it is expressed as:

$$\epsilon_{i,j} = - \sum_{i,j} J_{i,j} \vec{S}_i \vec{S}_j, \quad (2.50)$$

where  $J$  is an exchange constant that represents the energy difference between parallel and anti-parallel spin orientations. For example, for ferromagnetic materials  $J > 0$  and for antiferromagnetic  $J < 0$ .  $\vec{S}_i$  and  $\vec{S}_j$  are the associated spins. In the continuous magnetic material where spins are not perfectly collinear the exchange interaction can be expressed:

$$\epsilon_{ex} = A(\nabla \vec{m})^2 \quad (2.51)$$

$A$  is an exchange stiffness of the material and defined as:

$$A = \frac{JS^2n}{a}, \quad (2.52)$$

where  $n$  is the number of atoms per cell unit,  $S$  - the spin of the lattice,  $J$  - the exchange integral, and  $a$  - the lattice constant of the material. The exchange stiffness can be measured by the methods which probe the magnetic excitations, such as spin-wave resonance experiments, using temperature dependence of the spontaneous magnetization, Brillouin Light Scattering (BLS) or inelastic neutron scattering (NS). Exchange stiffness is difficult for reliable estimation since its value may locally vary depending on defects in the material. As it is seen from the equation 2.51 exchange energy depends on the angle between neighboring magnetic moments, but not on their relative orientation.

- *Anisotropy (magneto crystalline) energy  $\epsilon_{an}$ .* The main source of magnetocrystalline anisotropy is spin-orbit interaction. It results in existence of preferred magnetization directions with respect to the crystal lattice, i.e. easy axis, or vice versa unfavorable directions, hard axis, which require higher energy for magnetization. In case when only one axis direction is energetically degenerated the uniaxial anisotropy occurs. Therefore anisotropy energy can be expressed as a Tailor series with the first term:

$$\epsilon_{an} = K_1 \sin^2 \theta, \quad (2.53)$$

where  $K_1$  is the anisotropy constant of the first order and  $\theta$  is an angle between magnetization  $\vec{M}$  and direction of the easy axis. Often magnetic moments in material biased towards many particular directions which yield the existence of multiple easy axes. For example, Fe and Ni possess cubic crystal anisotropy that is given by first two orders of Tailor series:

$$\epsilon_{an} = K_1(\alpha_1^2 \alpha_2^2 + \alpha_2^2 \alpha_3^2 + \alpha_3^2 \alpha_1^2) + K_2 \alpha_1^2 \alpha_2^2 \alpha_3^2, \quad (2.54)$$

where  $\alpha_i$  is a direction cosines of magnetization vector in respect to crystallographic axes,  $K_1$  and  $K_2$  are anisotropy constants, which depend on temperature and specific for different materials. In case if second term can be neglected for  $K_1 > 0$  easy axes are located along the body edges (100) and  $K_1 < 0$  the easy axes exist along the diagonals (111). If  $K_2 \neq 0$  along with hard and easy axis intermediate magnetization axis can be distinguished. For example, Ni with anisotropy constants  $K_1 = -5.7 \cdot 10^3 \text{ J/m}^3$  and  $K_2 = -2.0 \cdot 10^3 \text{ J/m}^3$  [45] possesses easy axis along diagonal (111), intermediate and hard axis along (110) and (100), respectively.

Ferromagnetic thin films, single- and polycrystalline, as well as alloys, mostly have uniaxial anisotropy. Magnetocrystalline anisotropy can be modified by stress induced changes in crystal lattice of ferromagnetic material. The tensile or compressive strains change the distances between ions in crystal that modifies spin-orbit coupling in the material. Also anisotropy can be induced by symmetry breaking of the crystal structure at the interfaces and surfaces in multilayer structures.

- *Magnetostatic energy  $\epsilon_{demag}$ .* The magnetization of ferromagnetic material also can interact with magnetostatic field generated by the sample itself. This magnetic field  $H_d$  is demagnetizing or stray field and acts to reduce total magnetization. The energy density is given as:

$$\epsilon_{demag} = -\frac{1}{2}\mu_0 M_s H_d \cdot m, \quad (2.55)$$

where  $M_s$  is the saturation magnetization. The estimation of stray field  $H_d$  can be done using some fundamental relations based on Maxwell equations. In the absence of currents the magnetic scalar potential  $\phi$  can be introduced as:

$$H_d = -\nabla\phi \quad (2.56)$$

The magnetic potential  $\phi$  can be found as a solution of Poisson's equation that can be found in [46].

- *External field energy  $\epsilon_{ext}$ , or Zeeman energy.* This interaction refers to the energy occurring in the ferromagnetic material when it is placed in an external magnetic field. The external field energy correlates to the angle between the material magnetization  $M$  and applied field  $H_a$ :

$$\epsilon_{ext} = -\mu_0 H_a \cdot M, \quad (2.57)$$

where  $\mu_0$  is the vacuum permeability.

The basic magnetic parameters of Ni with face centered cubic (FCC) crystalline structure are listed in table 2.2.

Parameters	Ni
Saturation magnetization $M_s$	$4.9 \cdot 10^5$ A/m
Curie temperature $T_C$	627 K
Damping parameter $\alpha$	0.05
Exchange stiffness $A$	$9 \cdot 10^{-12}$ J/m
Anisotropic constant of the 1 <sup>st</sup> order $K_1$	$-5.7 \cdot 10^3$ J/m <sup>3</sup>
Exchange length $l_{exch}$	9.9 nm

Table 2.2: Magnetic parameters of Ni [47].

**Dzyaloshinskii Moriya interaction (DMI)** . DMI is an additional magnetic interaction which is observed in the systems with a lack of inversion symmetry. DMI is an antisymmetric exchange between two neighboring magnetic spins, which favors a spin canting of (anti)parallel aligned magnetic moments. If we look at the simplified case involving only two neighboring atomic spins  $\vec{S}_1$  and  $\vec{S}_2$  interfacial DMI is expressed as following:

$$\epsilon_{DM} = \vec{D}_{12} \cdot (\vec{S}_1 \times \vec{S}_2), \quad (2.58)$$

where  $\vec{D}_{12}$  is a Dzyaloshinskii vector, which sign determines left or right magnetization rotation. Initially starting from the ferromagnetic state vectors  $\vec{S}_1$  and  $\vec{S}_2$  are parallel, the DMI deflects the spins by rotation around  $\vec{D}_{12}$ . The interaction of two atomic spins with an atom having large spin orbit coupling (SOC) results in  $\vec{D}_{12}$  pointing outwards from the plane of the atoms (figure 2.16).

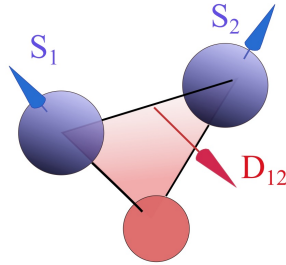


Figure 2.16: DMI interaction imaged at the atomic scales, where blue are ferromagnetic ions and red is an ion of SOC metal.  $\vec{S}_1$  and  $\vec{S}_2$  are two coupled spins and  $\vec{D}_{12}$  is a vector of Dzyaloshinskii Moriya interaction.  $\vec{D}_{12}$  is oriented perpendicular towards the triangle plane of involved ions.

The domain patterns of the samples contain information about DMI, since the domain width is determined by the balance between magnetostatic and wall energies. So mea-

surement of the spaces between domains allows to calculate the surface energy density,  $\sigma_{DW}$ :

$$\sigma_{DW} = 4\sqrt{AK_{eff}} - \pi |D|, \quad (2.59)$$

where  $D$  is the DMI constant,  $A$  is exchange stiffness, and  $K_{eff}$  is the effective uniaxial anisotropy constant that includes bulk and surface magnetic anisotropies.

**Shape anisotropy** The existence of preferred magnetization direction occurs not only due to crystal structure of the ferromagnetic material but also because of the shape of the structure itself. There are two main magnetization orientations in thin films: in-plane and out-of-plane as it is shown in figure 2.17 a. Out-of-plane orientation produces high surface charge ( $\vec{m} \cdot \vec{n}$ ) because all the magnetic moments aligned normally to the surface. Therefore this configuration is energetically less favorable since it requires to produce higher stray field than in-plane magnetization orientation.

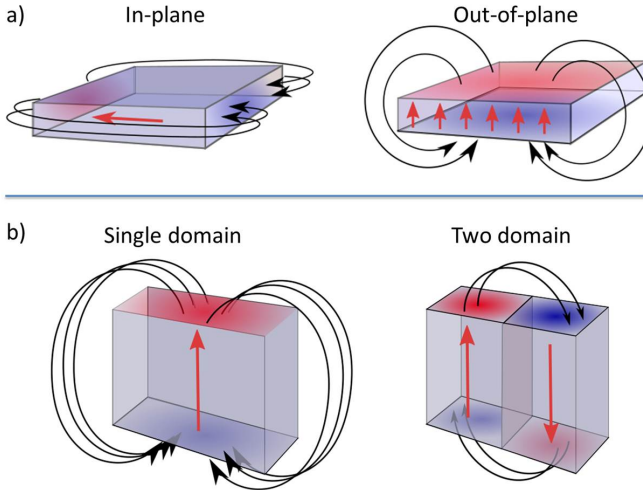


Figure 2.17: Magnetization configuration in materials with: a) shape anisotropy magnetization in-plane and out-of-plane configuration; b) in single domain and two-domain states of magnetization.

Magnetization of the ferromagnetic film can be in multi-domain state or single domain state as it is shown in figure 2.17 b. In multidomain state domains with different magnetization direction are separated by domain wall.

**Domain walls** The interface separating domains with differently oriented magnetization is a magnetic domain wall. Domain walls are formed in order to reduce the energy

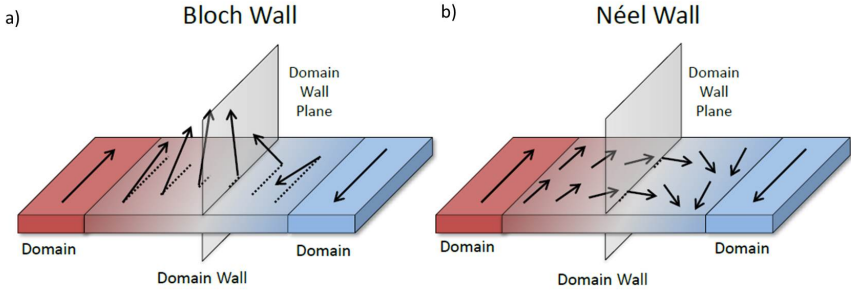


Figure 2.18: Two types of domain walls: a) Bloch wall and b) Néel wall. Reproduced from [47].

between magnetic domains. Magnetic moments in the walls gradually change their orientation forming Néel or Bloch walls as it is shown in figure 2.18. The Bloch wall has the magnetization direction laying in the plane of domain wall, while Néel wall has magnetization reorientation pointing perpendicular to it.

The width of domain walls depends on the equilibrium of exchange energy and the magnetic anisotropy. It can be estimated as following:

$$\Delta = \pi \sqrt{A/K_{eff}}, \quad (2.60)$$

where  $A$  is exchange stiffness, and  $K_{eff}$  is effective anisotropy. From the perspective of exchange energy domain walls are an energetically suboptimal state. The alignment of magnetic moments in the same direction make the magnetic walls wider. On the other hand, magnetic anisotropy energy increases when spins are not oriented in the direction of the easy axis and tends to reduce the width of the domain wall. Therefore the larger exchange interaction results in wider walls, when higher anisotropy yields thinner walls. Additionally, the multiple domains formation is beneficial since it significantly reduces stray field.

# Chapter 3

## X-ray Imaging

### 3.1 Background

Microscopy is a basic and essential technique with a very wide application in natural sciences and technology. The history of microscopy starts with invention of optical light microscope in the late 16th century. Modern advancement in optics allows to produce optical microscopes with resolution limited by the wavelength of visible light (400-700 nm) or even bypass diffraction limitations using laser stimulated emission depletion microscopy (STED) that provides resolution of 20 nm. Nowadays the most advanced microscopy instruments, transmission electron (TEM) or scanning tunneling microscopy (STM), have resolution in sub-nm scale allowing atomic level imaging [1, 2]. Despite all the advantages of high resolving power these methods have their own limitations. For example, TEM has small probing area, needs a fabrication of very thin specimens due to strong scattering of the electrons in the samples volume, also induces high radiation damage and requires sample cooling. STM and atomic force microscope (AFM) are applicable only for surface scanning and can't provide bulk information [48].

X-rays can be used for imaging, as a logical extension of optical microscopy, providing wavelength limited resolution in a range of few nm. The potential of the combination of spectroscopic method with high penetration depth of X-rays, chemical and magnetic sensitivity advantage it over other techniques. With the development of X-ray focusing optics, i.e. refractive lenses, Kirkpatrick-Baez mirrors and Fresnel Zone Plates, and new highly coherent and powerful X-ray sources provided by modern storage rings and XFELs, X-ray microscopy became a substantial tool covering a wide range of possible applications in materials science, biology, magnetism and time resolved imaging [49]. Moreover, new lensless diffractive imaging methods significantly improved the spatial resolution of X-ray microscopy to less than 10 nm [50] providing the possibility to retrieve phase contrast

information.

### 3.1.1 Types of X-ray Microscopy

#### Photoelectron Emission Microscopy (PEEM)

First generation PEEM microscopes were performed already in 1963 with a further development for synchrotron X-ray light application in the late 80s. A direct spectroscopic imaging is available in X-ray PEEM where monochromatic X-rays illuminate the sample. The number of emitted electrons from the illuminated area scales with the absorption cross section. PEEM does not require X-ray optics in the magnification process. Electron optics, electrostatic or magnetic lenses, are used for producing a magnified image of the emitted electrons on an electron sensitive camera. So far the resolution down to 30 nm can be achieved [51].

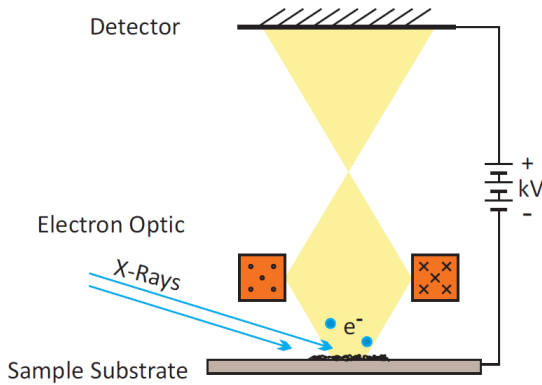


Figure 3.1: Schematic view of PEEM microscope [47]. Secondary electrons created in the X-ray absorption process in the sample are focused and magnified by electron optics. The sample potential accelerates electrons towards 2D detector.

The process is highly surface sensitive that is governed by photoelectron escape from the surface layer of 1-3 nm thick and does not require membrane deposition. The setup has a glancing incidence of the X-ray beam and sample surface that can be a geometrical limitation in investigation of magnetic out-of-plane components by XMCD. If the surface is 3-dimensional, or rough, that will reduce the spatial resolution of the image. Another limiting factor is the need to put the sample on a very high voltage potential in order to accelerate electrons towards the CCD. In order to ensure a free path for electrons, to avoid sample contamination and residual gas reactions UHV environment is required.

The sensitivity of electron trajectories to magnetic fields limits the method applicability for studying strongly magnetic samples and the use of bias fields.

### Full-field Transmission X-Ray Microscopy

Transmission X-ray Microscopy (TXM) is also referred to full-field microscopy and was pioneered by Schmahl, Rudolph and Niemann in 1976 [52]. The X-ray beam is focused at the sample plane with a condenser zone plate, the second smaller and high resolution zone plate is placed behind the sample. The small zone plate projects the illuminated area of the sample with certain magnification onto a CCD camera [53]. The resolution of the full-field microscope is limited by the resolution of the used FZP that is determined by the outer most zone width and requires partially incoherent light. High performance commercially produced FZPs have spatial resolution of about 20 nm. Since FZPs have strong chromatic aberrations, which are determined by the total number of zones, they can be used only with highly monochromatised X-rays. In order to avoid aberrations capillary condensers are used instead of FZPs [54].

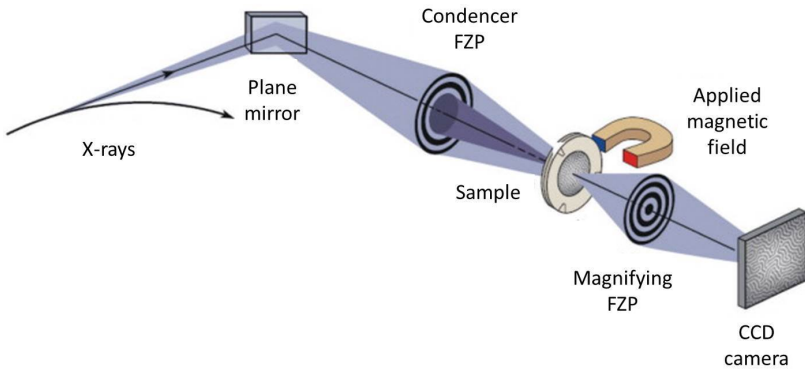


Figure 3.2: Schematic view of full-field transmission X-ray microscope. Adapted from [53].

The method is compatible with magnetic fields applied in any direction during the measurements. It allows microscopic studies of magnetization reversal processes. Due to direct imaging of the sample 3-D tomography can be performed by collecting multiple images while rotating the sample along the axis perpendicular to the X-ray beam.

### 3.1.2 Scanning Transmission X-ray Microscopy

Scanning X-ray microscopy was first applied in transmission mode (STXM) by the group of Janos Kirz in 1980 [55]. STXM is an imaging technique based on the raster sample

scanning by moving it step by step with high accuracy in vertical and horizontal direction perpendicular to the X-ray focused beam. The diameter of focal spot limits the image resolution. Depending on the parameters of the used focusing optics (FZP) it is normally about 20-50 nm. The beam, focused by the FZP, goes to the order sorting aperture (OSA) which removes unwanted diffraction orders, admitting only first order light (figure 3.3). Passing through the sample X-rays get partially absorbed, and the transmitted light can be registered by a point detector (photomultiplier tube, PMT, or avalanche photo diode, APD). The signal is collected from the every spot of the raster scan to built the whole image of the specimen point by point. To reach higher resolution and image quality the step size should be smaller than the focal spot size that helps to avoid aliasing caused by missing areas between the points. The scanning process itself can be done by moving the sample or the zone plate and requires highly precise positioning with moving motors in nanometers range and low level of vibrations.

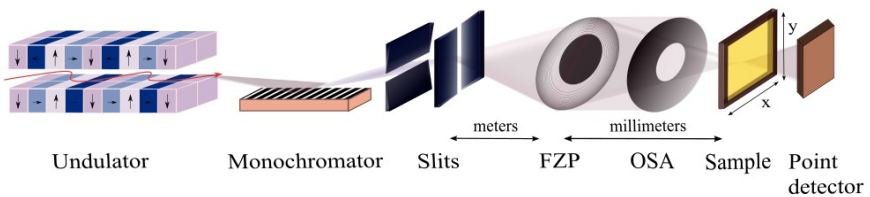


Figure 3.3: Schematic view of scanning transmission X-ray microscope. Monochromatic and coherent X-ray beam focused by FZP in the sample plane. Order sorting aperture is placed between FZP and sample to block 0th order light. The transmitted light is detected by point detector placed behind the sample.

STXM in the range of soft X-rays (up to 2 keV) is widely used in spectroscopic applications for light elements at K-edge, such as C, N and O in biological imaging, as well as for ferromagnetic materials at L-edge, e.g. Fe, Co and Ni [56], and M-edge (see table 2.1). In addition, STXM with high spatial resolving power is successfully used for dynamic imaging of magnetization behavior with temporal resolution limited by the length of synchrotron bunches  $< 100$  ps [49].

The preparation of the sample should be performed taking into account the total attenuation length of X-rays of the whole target. The thickness of samples with low density, like polymers or biological specimens, should be balanced for satisfactory absorption contrast [57]. For example, at carbon K-edge 300 eV the sample thickness is optimal in a range of 50 to 300 nm, for ferromagnetic samples the thickness of few nanometers is already

sufficient enough for reliable absorption contrast.

### Fresnel Zone Plate

One of the main components determining the resolution of STXM is the X-ray lens. A conventional binary absorption FZP consist of concentric alternating zones: fully opaque and transparent for the light. Coherent and monochromatic X-ray beam is diffracted on these rings. The light coming from the transparent region interfere, forming the focal spot. The opaque regions block the light which would interfere destructively. As a result several foci, which correspond to different diffraction orders, are formed as it is shown in figure 3.4. The *focal length* of the FZP depends on the X-ray wavelength  $\lambda$ , its diameter  $D$  and width of the outermost zone  $\Delta r$ . It is expressed as:

$$f = \frac{D\Delta r}{\lambda m} \tag{3.1}$$

where  $m$  is a number of diffraction order. The first order light with the strongest intensity is usually used for imaging. It contains only 10 % of initial X-ray light [14]. The higher diffraction orders have shorter focal lengths and much lower efficiency, that is proportional to  $1/m^2$ .

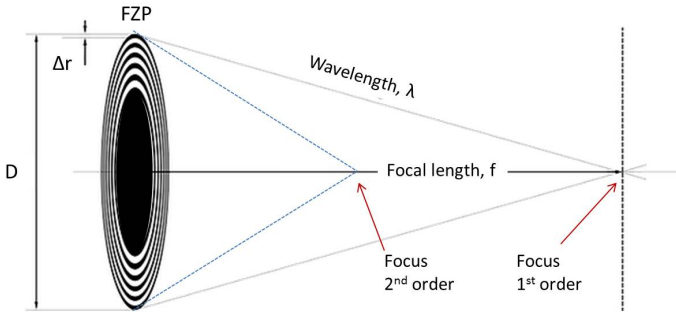


Figure 3.4: Illustration of X-rays diffraction on a FZP. The image shows diffraction orders of FZP, which have different focal length.

As it was mentioned above the STXM resolution is determined by the size of the illumination spot. When numerical aperture is relatively small the resolving power of the first diffraction order can be evaluated basing on Rayleigh criterion [14]:

$$\Delta r_{Rayl.} = 1.22\Delta r \tag{3.2}$$

The FZP resolution depends only on the width of the outermost zone. The difficulty to fabricate an extremely thin and at the same time opaque for X-rays outermost zone, for

example, by electron beam lithography (EBL), is one of the main limiting factors in FZP production. New nanofabrication techniques allow to produce FZP with 12 nm outer zone width [58]. However FZPs with so high resolution provide very low efficiency requiring elaborated fabrication process.

Another important characteristic of FZP related to the resolution is a *depth of focus* (DOF). It defines the distance which sample can be moved along the optical axis without loss of resolution:

$$\Delta z = \pm 2 \frac{(\Delta r)^2}{\lambda} \quad (3.3)$$

For example, FZP with  $\Delta r = 20$  nm at energy 700 eV has a  $DOF = \pm 0.235 \mu\text{m}$ . High value of DOF denotes that the samples with nonuniform surface topography can be imaged without correction of the sample distance, i.e. without refocusing. Also it assures the stability of the whole set up: small drifts of the sample around the focus will not change the size of the focal point.

## 3.2 Phase imaging and phase problem

In the imaging technique described above light is measured in terms of its intensity only. However the resulting wave consists of two parameters: absorption (related to resulting intensity) and phase shift. As it was discussed the wavefield, which is coming from the sample plane to the detector, is nothing else but the Fourier transformation of the samples transmission function (see equation 2.31). To get a complex value of the amplitude in the object plane the calculation of the inverse Fourier transform is necessary:

$$q(X, Y) = FT^{-1}(\phi(x, y)) \quad (3.4)$$

In the result the signal, measured by the detector, contains only intensity information, which is presented as a squared absolute value of the wave amplitude:

$$I(x, y) = |\phi(x, y)|^2 \quad (3.5)$$

The loss of the phase information is referred to the “phase problem”. The phase component allows restoring the complex diffracted amplitude from the reciprocal space that, in its turn, gives a unique determination of the density function of the object.

The progress in development of highly coherent X-ray sources was accompanied by the rapid increase of computational power and by the development of phase sensitive imaging techniques for soft and hard X-ray application [59, 60]. The coherent X-ray diffraction imaging, holography and ptychography became very prominent during the last years. They allow the phase reconstruction from the oversampled diffraction images using iterative algorithms.

### 3.2.1 Holography

X-ray holography is based on the utilizing highly coherent synchrotron light in order to reconstruct the hologram of the illuminated object. Holography with X-rays was initially performed in works [61, 62] in 1987 and 1992 year, respectively, in 2004 the method was revived for soft X-rays using XMCD effect [63] with spatial resolution of magnetic domains of 50 nm.

The main feature of this technique is the use of a golden mask having two holes: sample hole and smaller reference hole transparent for incoming beam as it is shown in figure 3.5. A CCD detector registers scattered X-rays in far-field to detect the characteristic diffraction pattern produced by the light interference between the known reference hole and the object. The hologram contains the sum of the scattering amplitudes associated with the object and the reference beams, their cross correlation and its conjugate [17]. The real space image is obtained by a Fourier transformation of the obtained holograms and followed by the iterative process for phase retrieval.

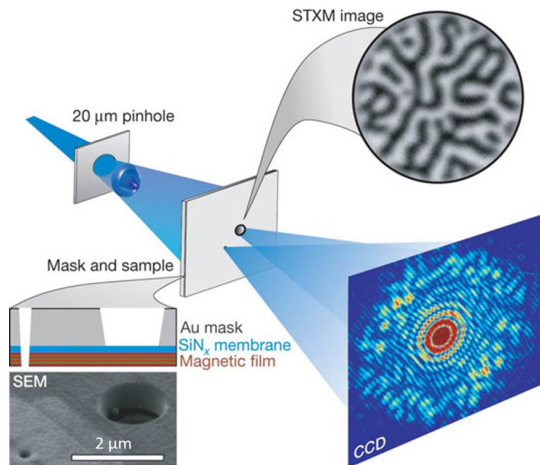


Figure 3.5: Principle of X-ray holography. The reference hole is placed next to the sample. The coherent X-ray beam create interference pattern between two objects, that is recorded by CCD camera in far-field. The top inset is a STXM image of the magnetic structure illuminated through the sample aperture with the field of view of  $1.5 \mu\text{m}$ . Reproduced from [63].

Therefore holography does not require high resolution focusing optics and provides phase shift information. However the spatial resolution of this method is limited by the size of the reference hole, which is the main confining factor for achieving wavelength limited resolution.

### 3.2.2 Coherent X-ray diffraction imaging

With the discovery of hard X-ray diffraction on crystals by Bragg in 1913 [64] crystallography has become a powerful instrument for reconstruction of three-dimensional images of regular crystal lattices and molecules with high spatial resolution. However, many objects with non-periodic structure, such as glasses, polymers, inorganic structures, or defects in crystals (dislocation, strains, deformation structures), cannot be visualized using the same approach. In 1980 Sayre proposed the idea of diffraction imaging with non-periodic objects [65] that resulted a creation of a new form of lensless highly resolving diffraction imaging.

The main principle of CXDI is getting a diffraction pattern downstream of the small isolated specimen using X-rays. While it is widely used with X-rays in the range of 0.5-4 keV due to high penetration capability, it can also be applied for electrons and optical light. The resulting diffraction pattern is detected by a CCD detector in far field regime. Using iterative algorithm the obtained pattern is converted into image of the object in real space. The use of coherent X-ray diffraction imaging (CXDI) has been growing rapidly, facilitating numerous discoveries in the field of material science, biology and nanocrystallography [66, 67].

**Iterative algorithm** The phase reconstructing algorithm for CXDI was firstly proposed by Gerchberg and Saxton in 1972 for electron microscopy [68]. The phase retrieval algorithm was greatly improved by Fienup by error reduction (ER) and then by hybrid input-output (HIO) methods in 1982 [69].

The basic idea of iterative algorithms is finding a solution for the missing phase information. It is done by refining the initial guess through back and forward Fourier transformations between the real and the reciprocal spaces (figure 3.6). First of all an initial guess defines the object in the real space,  $\phi_j(r)$ . Using Fourier transform we can get the complex value of the object in the reciprocal space. After replacing calculated intensities with measured ones the updated amplitude value is transformed back to the real space to get a refined object function  $\phi_{j+1}(r)$ . The procedure should be repeated a number of times till the convergence condition. To guarantee unique reconstruction and to speed up the convergence processes additional information has to be provided. This information is presented by constrains in real and reciprocal spaces. In this case measured intensities in Fourier space determines the Fourier constraint. The real space constraint in ER method is presented by so called “support” [70]. Support is an area with zero electron density which surrounds the sample and it has to be known *a priori*. The real object boundaries should be close enough to the estimated support to provide reliable reconstruction. ER algorithm searches for a minimum distance value between the real and the Fourier space constraints. However this method often stagnates getting trapped on the local minima without reaching the correct solution. A few modifications of the iterative algorithm were proposed to

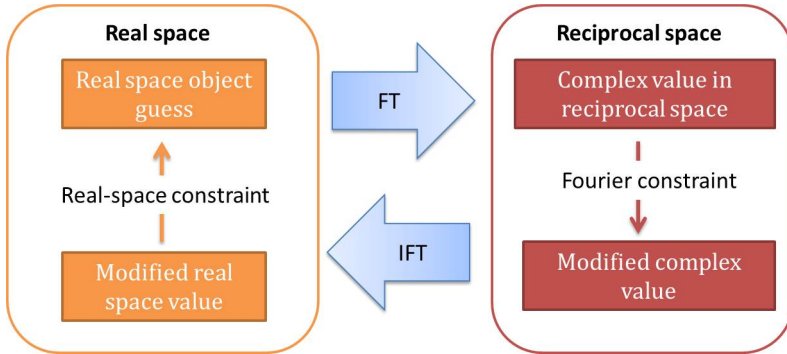


Figure 3.6: Scheme of iterative phase retrieval algorithm.

solve the problem, for example, HIO, difference map [71] and “shrink-wrap” algorithms [72].

**Advantages and disadvantages of CXDI** In comparison with conventional methods the resolution of CXDI is theoretically limited by the wavelength of X-rays, but not by the resolution of the used optics. Basically the objective lens is replaced with software, which converts an image from the reciprocal space diffraction pattern into the real space. That means absence of lens aberrations and no sample movement limitations induced by short focal lengths of the used optics. CXDI is a single shot technique not requiring raster scanning or any sample movements. In practice the main limiting factor is a  $q$ -space resolution given by the CCD detector size and distance between sample and detector. Also CXDI is dose limited since exposure time can be in a range of tens of seconds for low scattering specimens, e.g. biological samples. There are few further limitations that should be considered:

- The illuminated sample has to be isolated. The sample should be surrounded by “support” with known electron density which should be equal to 0.
- It requires the object to be smaller than an illumination spot of X-ray beam.
- High demands for X-ray coherence.

### 3.2.3 Ptychography

To overcome all the limitations of CXDI it was extended to ptychographic imaging method. Ptychography became a widely used diffraction imaging technique since its invention in the late 60s for electron microscopy in crystallography. The ptychography imaging is a

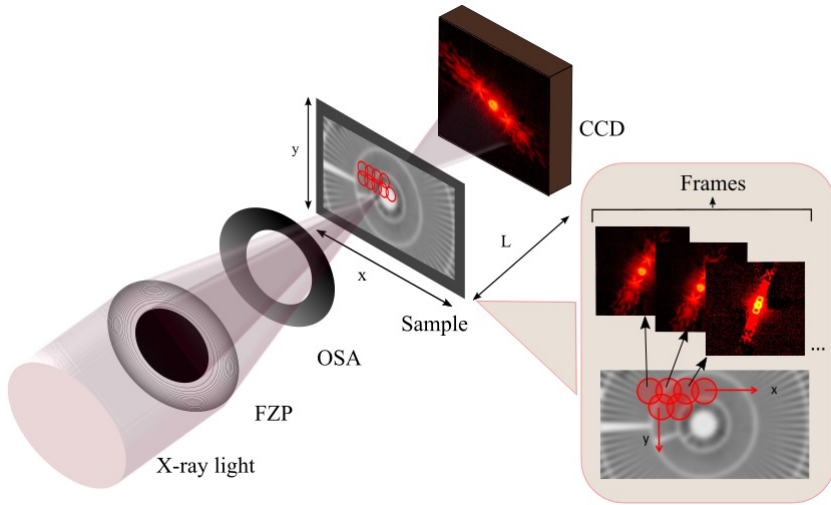


Figure 3.7: Experimental geometry of ptychographic imaging. The sample is raster scanned with focused beam and the sequence of diffraction patterns, frames, is recorded with CCD detector at the distance  $L$  for every scanning position.

combination of CXDI method with scanning microscopy. Similar to CXDI ptychography is a route to solve the phase problem. In 90s the ptychography imaging method was extended for non-periodic structures and completed with iterative phase retrieval methods by John Rodenburg [73]. Starting from the late 2000s it has been proven to be highly efficient in imaging with X-rays for material science [50], biology [74] and for characterization of X-ray optics [106]. Depending on experimental set up it can be done with simultaneous fluorescent data acquisition [148] or applied for 3D tomographic measurements [76].

In contrast to CXDI, which uses one diffraction pattern of a small object, ptychographic data set contains numerous diffraction patterns recorded at every scanning step. The basic feature of ptychography is that the sample scanning is done with significant overlapping of illuminating spots at the neighboring scanning positions (50 – 60%). The overlap in the object plane produces data redundancy in diffraction patterns that provides fast convergence of a reconstructing algorithm. Two diffraction patterns from the overlapped regions include the encoded phase information. This redundant data are applied as real-space constraints for ptychographic reconstruction.

Figure 3.7 depicts the schematic setup for ptychography imaging in transmission mode using FZP, which normally has medium resolution of 60-120 nm. The coherent X-ray

beam illuminates the specimen with the focused spot, called probe, with diameter down to hundreds nanometers. Conventionally the sample, or FZP, is moved in raster mode perpendicular to the confined beam. Non uniform scan grid patterns, concentric or spiral, can be used to reduce the mesh artifacts occurring in case of low overlapping degree [77]. The number of diffraction pictures, called frames, are registered in far-field region by CCD for every scanning position. Applying iterative phase retrieval algorithms it is possible to get an image reconstruction of the specimen with a resolution independent of the focusing optics.

The resolution of ptychographic set up is determined by a combination of several factors. Similar to CXDI the numerical aperture of the whole system is an important point since the highest diffraction orders of scattered X-rays in  $q$ -space contain the information about the smallest features. The performance of CCD camera is an important factor since scattering should be registered with high signal-to-noise ratio and dynamic range of few orders of magnitude at relatively short exposure time. Also the ptychography resolution strongly depends on the accuracy of the sample positioning during the scan that requires highly precise motor steppers.

The time of data acquisition for a ptychographic scan includes an exposure time and CCD camera read out time for all scanning positions. State-of-art CCD cameras with small pixel size and high read out rate open new opportunities for diffraction imaging. Also development of reconstruction algorithms for fly-scans ptychography, when the specimen continuously moves along the scan direction, can reduce data acquisition time by factor of 25 [78]. However this mode is applicable only for highly scattering samples in hard X-ray range, when the long data acquisition time is not required.

### Ptychographic Iterative Engine (PIE)

There are several mathematical algorithms dedicated to the ptychographic reconstruction. These algorithms use the overlap of diffraction patterns as a constrain to find a solution. Ptychographic Iterative Engine (PIE) for reconstruction of image from ptychographic data set was firstly proposed by Rodenburg in [79]. For reconstruction of the object function this algorithm requires accurate knowledge of the illumination probe function. In a real experiment it is quite challenging to find a known probe. That is why the PIE was modified to extended PIE (ePIE) [80], where both the probe and the object are updated through the reconstruction.

**Algorithm** Each image frame of the ptychographic scan can be describe by the Fourier transform of the resulting function, which is the product of the probe  $P(r)$ , illumination function, and the object transmission function  $O(r)$ , where  $r$  is the coordinate of the object plane. The recorded diffraction pattern is proportional to the absolute value of Fourier

transform of the wave function. It allows to introduce the resulting intensity as:

$$I_j(k) = |F(O_j(r)P_j(r - R_{n(j)}))|, \quad (3.6)$$

where  $k$  is a reciprocal coordinate of the real-space coordinate  $r$ ,  $R_{n(j)}$  is a distance of the probe position (or an object),  $j$  is a number of diffraction pattern and  $n(j)$  is their random sequence.

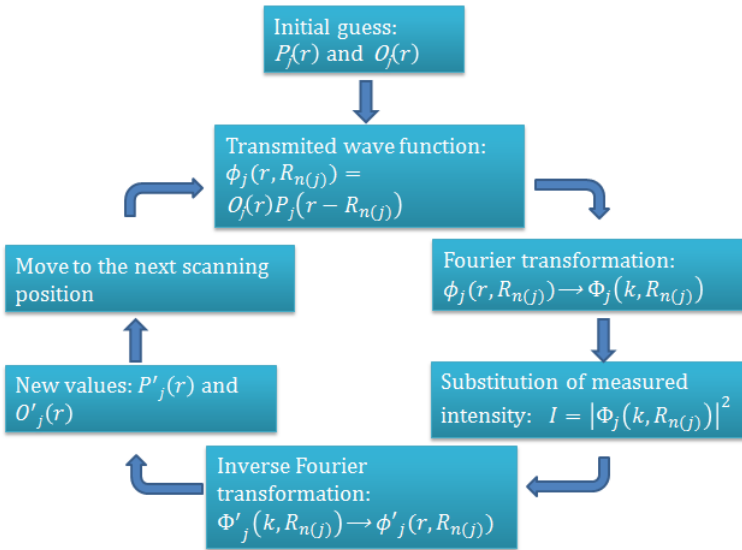


Figure 3.8: Extended ptychographic iterative engine (ePIE).

The algorithm for the reconstruction of the object function is introduced in figure 3.8 and consists of the sequence of the following operations:

1. The exit wave is initially determined by the current guess of the object function  $O(r)$  that is multiplied by the illumination function  $P(r - R_{n(j)})$  in the current position  $R_{n(j)}$ :

$$\phi_j(r, R_{n(j)}) = O_j(r)P_j(r - R_{n(j)}) \quad (3.7)$$

Normally, the first object guess is taken as an empty space and the illumination guess as a Gaussian function having zero phase shift.

2. The newly guessed exit wave is then Fourier transformed. Information about phase and amplitude in reciprocal space of this wave is preserved:

$$\Phi_j(k, R_{n(j)}) = FT[\phi_j(r, R_{n(j)})] = A_j(k, R_{n(j)})e^{i\alpha_j(k, R_{n(j)})} \quad (3.8)$$

Since the final exit wave in the reciprocal space is complex, it contains the amplitude  $A_j(k, R_{n(j)})$  and the phase components  $e^{i\alpha_j(k, R_{n(j)})}$ .

3. The reciprocal space function is refined using the measured amplitude of diffraction pattern obtained by CCD:

$$\Phi'_j(k, R_{n(j)}) = \sqrt{I_{n(j)}(k)}e^{i\alpha_j(k, R_{n(j)})} \quad (3.9)$$

4. Inversing transform of the updated guess we get a renewed and improved exit wave in the real space:

$$\phi'_j(r, R_{n(j)}) = FT^{-1} \Phi'_j(k, R_{n(j)}) \quad (3.10)$$

5. Now we can update the object function in the real space. The new object guess is expressed as a sum of the current object guess and the weighted correction of the wavefield:

$$O_{j+1}(\vec{r}) = O_j(r) + \alpha \frac{P_j^*(r - R_{n(j)})}{|P_j(r - R_{n(j)})|_{max}^2} (\phi'_j(r, R_{n(j)}) - \phi_j(r, R_{n(j)})), \quad (3.11)$$

where  $\phi'_j(r, R_{n(j)}) - \phi_j(r, R_{n(j)})$  is a difference between updated exit wave and its first estimation at the  $n$ th iteration. The term  $P_j^*(r - R_{n(j)})$  is a conjugate of the illumination function,  $|P_j(r - R_{n(j)})|_{max}^2$  is the maximum value of the illumination function and  $\alpha$  is a feedback parameter, which determines the amount of correction of the running estimate of the object function. It yields to the new guess of the object function. In similar way, we can get a new value for the illumination function:

$$P_{j+1}(r) = P_j(r) + \beta \frac{O_j^*(r - R_{n(j)})}{|O_j(r - R_{n(j)})|_{max}^2} (\phi'_j(r, R_{n(j)}) - \phi_j(r, R_{n(j)})), \quad (3.12)$$

where  $\beta$  is a constant for altering amount of corrections of the running estimate of the probe function updates.

6. The steps from 1 to 5 are repeated for the next scanning step. The process will continue till all diffraction patterns from the scan are used for object and probe guesses updates.

Basically the algorithm is fitting the set of unknown values to the known ones. Every proposed solution in comparison with recorded data at each iteration is associated with an error. To follow the progress of the reconstruction and to estimate convergence of the algorithm the error metric is used after each full iteration. That is presented as a normalized root mean square value:

$$E_{\Phi} = \frac{\sum_j \sum_k \left| \sqrt{I_j(k)} - |\Phi_j(k)| \right|^2}{\sum_j \sum_k I_j(k)} \quad (3.13)$$

To be able to find a unique solution for unknown values the diffraction patterns used for reconstruction have to fulfill additional requirements that they should be oversampled.

### 3.2.4 Sampling in diffraction imaging

Sampling in signal processing is the reduction of a continuous signal to a discrete one. The phase information about the studied sample is encoded in the corresponding far-field diffraction images. As a result we get discrete diffraction pattern measured by the CCD detector with  $N$  amount of pixels. The main requirement, which make the phase retrievable from the encoded information, is an oversampling of the diffraction pattern. The application of oversampling parameters helps to reduce noise, aliasing and improve resolution of recorded data.

There exist different approaches to estimate a proper oversampling rate allowing a reliable phase retrieval in coherent diffraction imaging (CDI). Firstly the phase problem solution by means of oversampling definition was proposed in crystallography by Sayre [81]. It was stated that an object should be sampled at least twice more than Nyquist frequency in each direction for multidimensional objects. If we suggest that the size of the crystal unit cell is  $a$ , thus Bragg peaks in reciprocal space occur at the frequency  $2\pi/a$ . In order to retrieve the phase the diffraction pattern must be probed at  $\pi/a$  spacing.

Due to experimental limitations diffraction speckles in reciprocal space are registered as discrete points in separate pixels of a CCD camera (figure 3.9). The clear separation of the speckles is a main sign that the diffraction pattern is well sampled. The CCD pixel size  $p$  and the distance between sample and detector  $L$  determine the separation between speckle points. In terms of pixel size of the CCD camera the sampling requirement is described by:

$$p \leq \frac{\lambda L}{2a}, \quad (3.14)$$

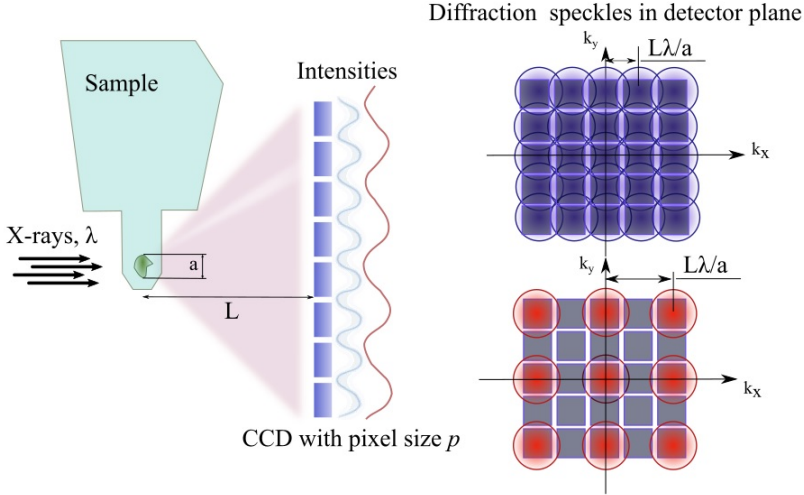


Figure 3.9: Intensity modulations of two different diffraction signals probed by the CCD with pixel size  $p$ . The distance between two neighboring intensity maxima is defined as  $L\lambda/a$ . The blue curve represents undersampled condition, the maxima peaks located to close that causes information loss. The red curve illustrates 2-fold oversampling condition.

where  $a$  is a size of the object,  $L$  - distance from the object and detector and  $\lambda$  - wavelength.

Consideration of oversampling as a mathematical problem was presented by Bates [82]. The auto-correlation function of any image has a double size of the image itself. Therefore, in every linear direction the phase information can be retrieved from the double oversampling for each direction. It means that for 2D image diffraction pattern should be 4 times and 3D diffraction pattern 8 times oversampled [83].

Another approach to estimate oversampling in coherent diffraction imaging (CDI) was defined by Miao et al [83]. Oversampling parameter is determined as  $\sigma$ :

$$\sigma = \frac{\text{total pixel number}}{\text{unknown-valued pixel number}}, \quad (3.15)$$

where *total pixel number* includes the surrounding pixels in a field of view, not containing the object as well. Here *unknown-valued pixels* have to be found. It states that having  $\sigma > 2$  allows to solve the phase problem. Multidimensional cases lead to the decreasing

of oversampling, i.e. the oversampling of the Fourier transform magnitude in 1D case must be  $> 2$ , 2D  $> 2^{1/2}$ , and 3D  $> 2^{1/3}$  in each direction.

In ptychography, due to redundant information coming from the probe overlap, the oversampling requirement is significantly relaxed. As it is shown by Edo et al. the lack of oversampling ratio  $\sigma$  can be covered by the size of the overlap of the neighboring probe positions [84]. The authors determine a new sampling parameter which is based on sampling in real ( $R$ ) and reciprocal ( $U$ ) spaces:

$$S_{x,y} = \frac{1}{UR} = \frac{\sigma}{1 - \varpi_{x,y}} \quad (3.16)$$

where

$$U = \frac{1}{d\sigma} \quad (3.17)$$

$$R = d(\varpi_{x,y} - 1) \quad (3.18)$$

In these formulas  $\varpi_{x,y} \in (0; 1)$  is an ptychographic overlap parameter,  $\sigma \in (0; 2)$  is the CDI oversampling ratio and  $d$  is a fringe size of the diffraction pattern. If  $S_{x,y} = 1$  the sampling requirement is fulfilled,  $S_{x,y} > 1$  it is oversampled and  $S_{x,y} < 1$  is undersampled. The experimental results showed that even if  $S_{x,y} < 1$  and accordingly  $\sigma < 2^{(1/2)}$  it is still possible to reconstruct a recognizable object image. This showed that conventional understanding of oversampling in CDI does not really fit for the ptychographic approach [85].

### 3.3 Magnetic microscopy

Imaging of magnetic nano structures are routinely performed by a number of techniques, most of which are extensions of the existing microscopic methods like TEM, STM and AFM [86].

*Lorentz microscopy*, as a variation of TEM, is one of the methods allowing high resolution magnetic imaging in nm range [87]. Electrons passing through the sample experience Lorentz force that deflects them from the initial pass depending on the local magnetization direction of the sample. Electron holography is another TEM technique which is commonly used to study electric and magnetic fields in thin films by measuring shift the phase of the interfering wave passing through the sample. This methods work only in transmission mode that requires very thin samples and it is not element selective. Additionally, the high energy electrons cause irradiation damage of the sample. Lorentz microscopy can not provide depth-selective information, but is suitable for time resolved measurements with less than 1 ps temporal resolution. Recently developed methods based on electron magnetic circular dichroism (EMCD) allow to obtain information on the magnetic properties of the atom using electron energy loss spectroscopy spectra taken in a magnetic fields with opposite helicities.

*Magnetic force microscopy (MFM)* is an extension of atomic force microscopy (AFM). The force between the magnetic specimen and a ferromagnetic scanning tip is detected locally and allows to reproduce the whole picture with resolution around 20 nm [88]. The method has some difficulties in image interpretation since it reproduces stray field between the tip and sample, not the sample magnetization. Another probe method is *spin polarized scanning tunneling microscopy (sp-STM)* which uses measurement of current tunneling through the vacuum gap between a tip and the sample that depends on spin polarized band structure of the studied specimen. The tip magnetization can be parallel or antiparallel to the sample magnetization and therefore result in different tunnel currents. The resolution of this method is extremely high, less than 1 nm, but it requires ultrahigh vacuum conditions. The described technique provides information only from the surface and upper atomic layers of the sample.

One of the widely used optical method for magnetic imaging utilizes *Magneto-optical Kerr effect (MOKE)* which enables scans with large field of view, hundreds of microns. The magnetization of the sample is detected by the change of polarization of light after reflection from the sample surface. The images can be taken in a full field regime or in scanning mode, when the final picture is built point by point by scanning a laser focus. Although this technique provides comparatively low resolution (300-500 nm) being fully optical it is suitable for application with high external magnetic fields, does not require vacuum condition and provides high time resolution (down to 20 fs). However the method does not give direct information about the electronic structure or magnetic moments and it is not element specific.

Recently, a technique that employs a single nitrogen-vacancy defect in diamond as a scanning atomic-size magnetometer to image magnetic surface structures by direct measurement of weak magnetic fields with a nanoscale resolution [89].

**Synchrotron X-ray light based techniques** Discovery of XMCD and XMLD effects and their application as a contrast mechanism became a breakthrough for magnetic X-ray imaging. XMCD results in different absorption level of domains with parallel and antiparallel magnetization direction to the X-rays helicity. The main strengths is elemental sensitivity and high penetration depth that allows to probe different elements or magnetic layers in the sample by changing the photon energy [90].

One of the method for magnetic imaging that uses XMCD and XMLD, is *X-ray photoelectron emission microscopy (X-PEEM)*. It is based on the detection of secondary electrons coming from the specimen irradiated with X-rays. The intensity of electrons is proportional to the X-ray absorption cross section and can be used for imaging of areas with different magnetization directions with lateral resolution of about 30 nm. The method profits from the large dichroic effect and gives quantitative estimation of magnetization in the specimen. Another XMCD technique is *magnetic transmission X-ray microscopy (MTXM)* [91], like STXM, it requires focusing optics and measures the intensity of trans-

mitted light to image the sample. In both techniques two images using opposite helicity are collected and subtracted in order to eliminate topographic contrast and get pure magnetic contrast.

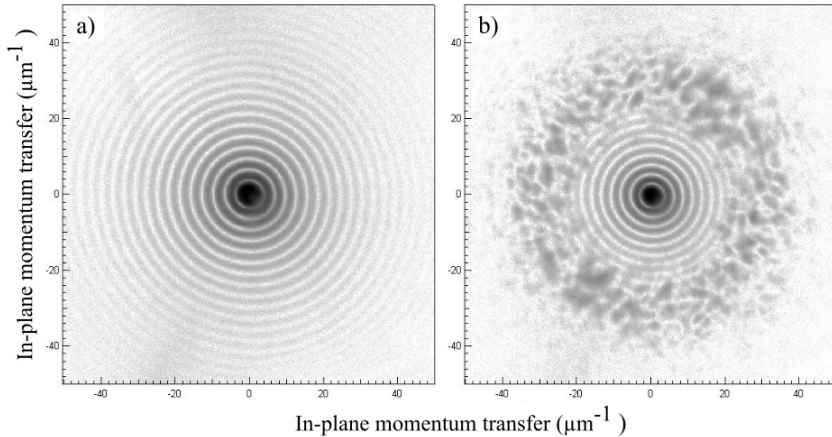


Figure 3.10: Diffraction patterns from a CoPt magnetic domain structure taken for X-ray holography using linearly polarized light: a) off the resonant energy of Co  $L_3$  edge (758 eV) and b) on the resonant absorption energy (778 eV). The Fraunhofer rings are coming from the diffraction on a pinhole. Speckled scattering at (b) originates from the scattering on the magnetic domains of the sample. Reproduced from [92].

Also diffraction techniques using highly coherent X-ray light have been shown to be efficient for the imaging of magnetic domains. One of them is *holography* that became a robust instrument for magnetic contrast imaging in a soft X-ray range [63]. A signal is obtained at the resonant energy, where magnetic scattering is the most significant, and presents interfered light from the sample and the reference hole as it is shown in figure 3.10. The use of circular polarized light provides additional scattering signal enhancement via interference between magnetic and charge scattering channels [42].

*CDI* single shot imaging was reported to be successfully implemented for Co based magnetic domain structures using linear polarized light with a spatial resolution of 75 nm [93]. Applying external magnetic fields a pure magnetic signal from the sample scattering was obtained as a difference of coercive and saturated coherent diffraction patterns. The saturated speckle pattern includes the total charge scattering and the specular component of magnetic scattering. The pattern measured at the coercive point additionally shows a diffuse scattering from the domain structure at higher  $q$  values.

It was shown by Shi et al [94] that magnetic and structural sample heterogeneities can

be imaged with *ptychography* with soft X-rays at Co  $L_3$  edge, with a resolution of the magnetic and charge scattered signals of 12 and 10 nm, respectively. FeGd multilayer was studied in a work of Donnelly et al [95] using ptychographic imaging with hard X-rays at the energies of Fe K edge and Gd  $L_3$  edge with the resolution of 45 nm.

## Chapter 4

# Ptychography at the MAXYMUS microscope

The important part of this work was the installation of a new in vacuum CCD camera for soft X-rays in collaboration with PNSensor GmbH (Munich, Germany) at the very early stage of the project. The back illuminated pnCCD camera with a detector chip provided by HHL (MPG Halbleiterlabor) was developed for imaging and spectroscopic purposes. The camera commissioning, calibration and implementation of ptychography were performed at MAXYMUS operated by department Schütz. The very first commissioning was conducted in February 2015 with the first ptychographic tests in July 2015. For ptychography in-house created FIB FZPs [96] and reconstruction software developed at the CXRO /Berkeley [97] have been used. The basics of ptychographic reconstruction software and computing power at MAXYMUS are present in Appendix A. The aim of this extensive upgrade was to improve the spatial resolution and contrast of conventional STXM imaging at MAXYMUS.

### 4.1 UE46 beamline at BESSY II

BESSY II (Berlin, Germany) is a 3<sup>rd</sup> generation synchrotron which was built in 1998 and now operates over 50 different experimental stations. The technical parameters of BESSY II storage ring are listed in the table 4.1. It features a Linac injector that allows top-up operation mode [98], when the charge of each individual bucket is continuously refilled so that the average current stays constant. Depending on the operation mode the length of the electron bunch inside of the bucket varies from few ps to 100 ps, that allows time resolved pump-probe experiments.

Parameter	Value
Beam current	300 mA
Electron energy	1.72 GeV
Circumference	240 m
Amount of electron buckets	400
Bucket frequency	500 MHz
Amount of bending magnets	32
Amount of undulators	11

Table 4.1: Parameters of the BESSY II storage ring.

MAXYMUS microscope was built in 2008 on the dedicated beamline UE46-PGM2. The X-rays are provided by the UE46 undulator, which is an elliptical polarizing insertion device of the APPLE-type, one of 6 helical undulators in operation at Bessy II. The undulator has 72 magnetic periods of 46.3 mm length each. It is specified to generate both linear and circular polarization light with energies starting from 150 eV up to 1900 eV at higher harmonics.

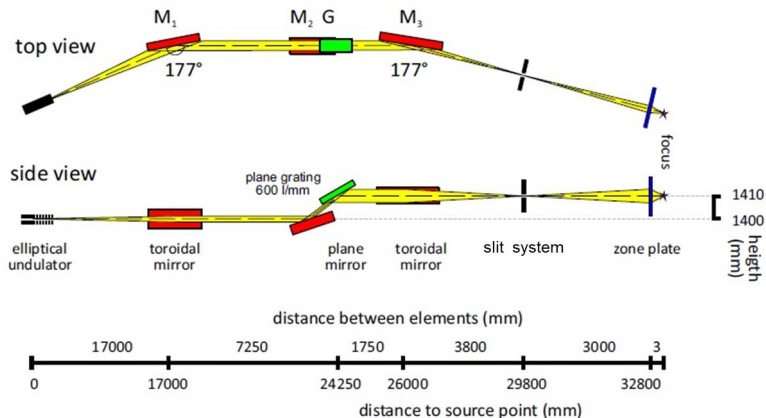


Figure 4.1: Layout of the beamline UE46-PGM2 at BESSY. The synchrotron radiation coming from an undulator source is focused by mirrors and plane grating monochromator (PGM), then passes through an exit slit system located 3 meters in front of the microscope position. Adapted from [12].

The UE46-PGM2 beamline, depicted in figure 4.1, was designed to provide partially coherent illumination of a zone plate enabling X-ray microscopic imaging under optimal conditions. Monochromatic X-rays are produced utilizing two focusing mirrors and a

plane grating monochromator (PGM), followed by vertical and horizontal slit systems. A single 600 lines per mm blazed grating is used as monochromator covering the wide energy range from 150 to 2000 eV with energy resolution  $E/\Delta E \geq 10\,000$ .

Two independent slit systems are placed on the distance 3 m from the microscope end station and used to filter X-rays with required parameters. The system can be adjusted vertically and horizontally to control the energy resolution, the level of coherence and photon flux of X-ray beam. It is possible to monitor beam position by detecting the photocurrent occurring due to incident radiation on the horizontal slit blades. This ensures much more flexible and fine control of the beam parameters and allows to reduce noise through the feedback loop [47]. The smaller beam size provides higher coherence and as a consequence higher spatial resolution, but at the same time lower photon flux.

To protect the microscope from external factors, such as temperature fluctuations and high frequency vibrations, which induce instabilities and noise, a hutch with high performance air conditioning system was built around the last beamline segment including the exit slit assembly in 2008 [47]. For the reduction of possible floor vibration the microscope is mounted on 1 ton stone block with rubber buffering on top. Five girder movers allow adjusting of the microscope position with 5 degrees of freedom in relation to the beam position.

### 4.1.1 MAXYMUS end station

MAXYMUS is a STXM based on a design originally developed at the ALS (Berkeley, USA) [99]. The microscope consists of five main components: exit slit, zone plate, OSA, sample and detector. Figure 4.2 shows sample environment at MAXYMUS. A zone plate for the soft X-ray range has a typical diameter in the range of 100 to 320  $\mu\text{m}$  and a focal length in the mm range. To allow a change in focal length, as well as to facilitate changing of the zone plate itself, Z translation of the zone plate is used.

*The OSA* is placed between zone plate and sample and moves only in X-Y plane. It has three circular apertures with different diameters and 500  $\mu\text{m}$  spacing between them to prevent light spillage through neighboring OSA apertures. The OSA size should be smaller than the center stop (*CS*) of the FZP in order to fully eliminate zero order light. For instance using high resolution FZP available at MAXYMUS with  $D = 320\ \mu\text{m}$ ,  $\Delta r = 18\ \text{nm}$  and  $CS = 155\ \mu\text{m}$  requires 120  $\mu\text{m}$  big OSA hole. The sample is placed behind the OSA at the distance  $A_0$  that depends on the focal length, the diameter of the used FZP and on the OSA aperture size.

All the components of microscope should be aligned along the optical axis that requires *multiple motor stages* for their accurate positioning. X- and Y-translations of the sample have to be performed in a big range of scales: in cm range to bring the sample region of interest into the optical axis, at the same time in nm range for raster scanning. It is fulfilled by stacking motor stage and fine piezo stages on top of each other. As an option

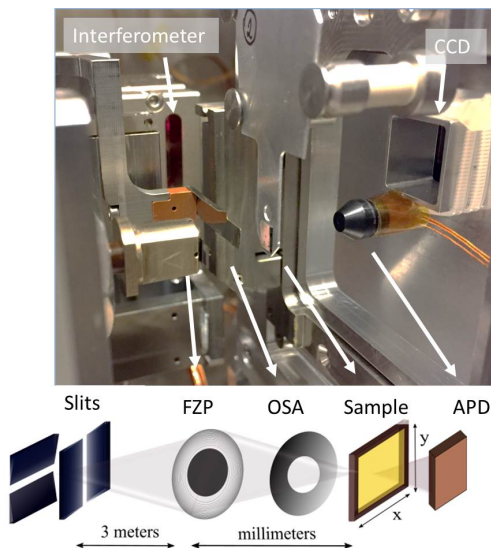


Figure 4.2: Image of sample environment in the MAXYMUS microscope showing the main components.

scanning can be performed by moving FZP in X- and Y-direction instead of the sample movement. The zone plate scanning is faster and more stable than the sample scanning due to smaller range and stiffer piezo stages. However it puts limitation on the size of the produced image, since moving FZP too much off the optical axis causes clipping of the light cone on the OSA.

*The detector* (APD, PMT or CCD) is placed behind the sample and can be moved in X and Y directions to center it on the optical axis, and in Z direction to vary the distance between sample and detector. All detector stages are mounted on a Z-axis sample motor stage that allows to move sample and detector together with the fixed distance between them.

STXM raster scanning, as well as ptychography scanning, requires high precision and repeatability of sample and FZP positions. To control movements of both sample stages and account for drifts and vibrations, the microscope is equipped with a differential *laser interferometer system* (figure 4.2, b). Laser mirrors are placed on the sample holder and the zone plate mount in vertical and horizontal orientation. Two interferometers for X and Y directions detect differential motions of the stages with the accuracy of 2.5 nm that allows to correct vibration and position drifts.

In order to generate an external magnetic field in the sample plane an assembly of four

*permanent magnets* can be installed [100], providing up to 250 mT magnetic field with selectable field strength and direction. Stepping motors allow independent movement of all four magnets producing homogeneous magnetic field in the center of the system for in-plane and out-of-plane sample orientation. Figure 4.4 shows a sketch of the magnet system with out-of-plane maximum field and the sample placed perpendicular to the X-ray beam.

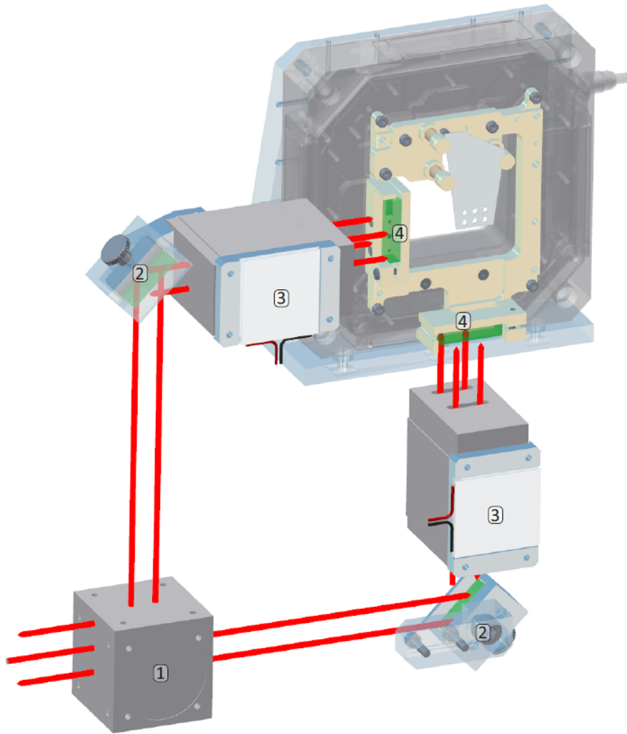


Figure 4.3: Overview over the interferometer system: 1 - 50% beam splitter to divide laser beam for X- and Y-axis, 2 - rotation deflection mirrors, 3 - the individual interferometer heads, 4 - end mirrors placed on the frame of the sample holder. The beam comes from the bottom left to the middle of the splitter, from the top and the bottom of the incoming beam returning beams are imaged. Reproduced from [47].

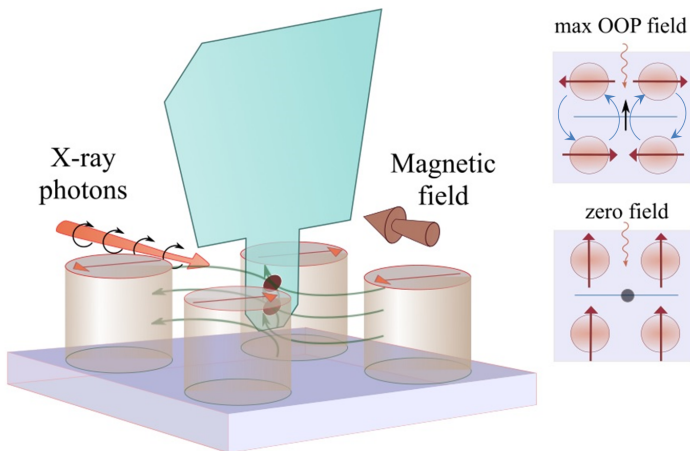


Figure 4.4: Magnet system with maximum out-of-plane (OOP) magnetic field at the sample position, which placed perpendicular to the incoming X-ray beam. On the right bottom the magnets configuration for zero field at the sample is shown.

## 4.1.2 Coherence at MAXYMUS

### Coherence after slits

Synchrotron light produced by undulator is only partially coherent. To increase the coherence most of the monochromator beamlines utilizes a set of slits or an aperture. As it was described in previous chapters UE46-PGM2 beamline is equipped with vertical and horizontal slits which allow optimal illumination of FZP located 3 meters downstream of the slits. Normally an FZP with a diameter in a range of hundreds of  $\mu\text{m}$  requires very small aperture size to be able to produce diffraction limited resolution. To estimate spatial coherence length of X-rays coming from the single slit we can use following expression [33]:

$$a_c = \frac{\lambda R}{d}, \quad (4.1)$$

where  $\lambda$  is wavelength of incident beam,  $R$  - distance between slit and observation point,  $d$  is the slit opening. The higher the energy of light the smaller the spatial coherence length. For example with the fixed slits opening of  $20 \mu\text{m}$  the light at energies of  $1000 \text{ eV}$  ( $\lambda = 1.24 \text{ nm}$ ) and  $600 \text{ eV}$  ( $\lambda = 2.07 \text{ nm}$ ) has spatial coherence lengths of  $185 \mu\text{m}$  and  $309 \mu\text{m}$ , respectively.

The complex degree of spatial coherence is used to characterize partially coherent extended light sources [33]. For the slit aperture it can be written as a normalized sinc

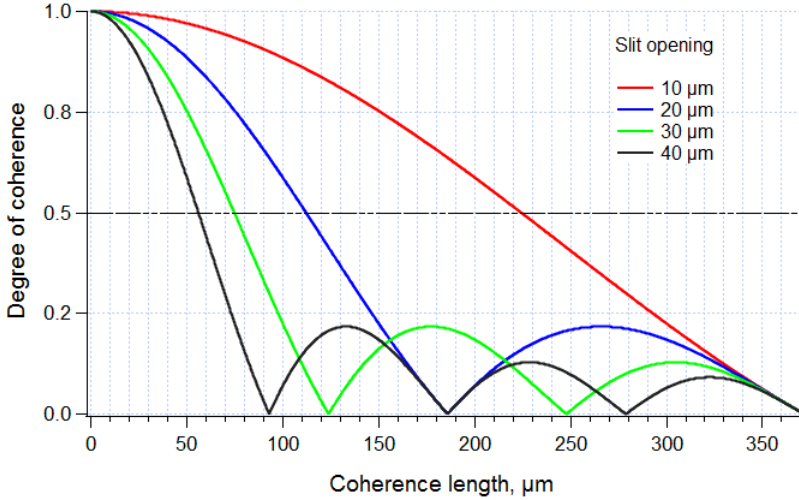


Figure 4.5: Degree of coherence of homogeneously illuminated slit apertures having different opening gaps at energy 1000 eV ( $\lambda = 1.24$  nm). The smaller slits produce a beam with higher spatial coherence length. The black horizontal line corresponds to half maximum of the peak.

function :

$$g(\Delta x) = \text{sinc} \left( \frac{\Delta x d}{\lambda R} \right), \quad (4.2)$$

where  $\Delta x$  is an observation area in the far field. The value  $|g(\Delta x)|$  lays in a range  $[0; 1]$  going from fully incoherent to absolutely coherent light. The degree of coherence for different slit sizes at energy of 1000 eV is plotted in figure 4.5. As it is seen the smaller slit gap produces a beam with higher coherence. To get constructively interfered signal from two separately standing features in the illumination plain the distance between them should be smaller then the full width at half maximum (FWHM) of this function. This value corresponds to spatial coherence length  $a_c$ .

At the UE46-PGM2 beamline two sets of slits 6 cm apart determine the vertical and horizontal spatial coherence of the beam. The simulated diffraction intensity distribution in the FZP plane is performed in figure 4.6, for simplicity we assume to have rectangular aperture illuminated by an uniform beam. The diffraction pattern forms typical spike-like shapes of intensities occurring perpendicular to the elongated sides of the aperture having maximum peak in the center and the first minima in the position determined by equation 4.1. In the real case intensity distribution at the FZP position is broadened due to the beam being not perfectly flat as a plane wave, but strongly focused in the slits plane.

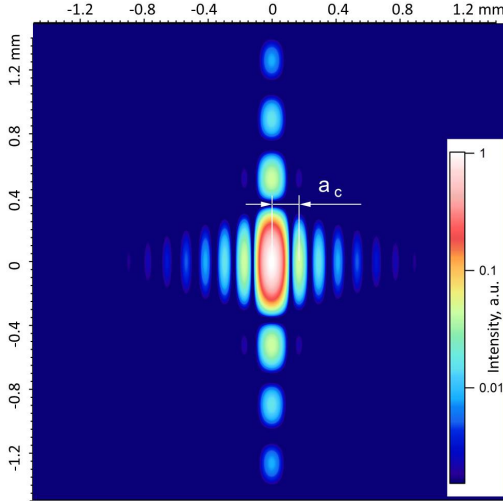


Figure 4.6: Simulated intensity distribution of the diffracted light at 3 m distance from the slits. The energy of the light is 1000 eV and the slits are opened for  $30 \mu\text{m}$  and  $10 \mu\text{m}$  in horizontal and vertical directions, respectively. For simplification we assume that slits are illuminated by a plane wave beam with uniform intensity.

As already mentioned smaller slits opening assures higher spatial coherence length, that is correlated with a drastic drop of the beam flux and reduced photon count rate. The observed effect happens when X-rays are diffracted on the small apertures, which produce wider illumination beam spot on the FZP spreading the light over bigger area. It requires a trade off between optimal exit slit settings for sufficient beam flux and degree of X-ray coherence.

The UE46-PGM2 beamline generates an X-ray beam with the focus size of  $15 \mu\text{m}$  in vertical direction and  $45 \mu\text{m}$  in horizontal direction at the position of the exit slits. The size of the focus spot is estimated as FWHM of Gaussian function assuming that the light within these dimensions is close to maximum monochromaticity and coherence. The Gauss shape explains the linear gain in intensity when opening the slits wider than the focus spot size, since only lower parts of the Gauss shaped curve get unblocked. However when the slits gap is smaller than focus spot size the photon flux behaves non linear and depends on diffraction processes happening on the slit system.

The temporal coherence of the X-ray beam doesn't depend on aperture parameters and can be estimated from the bandwidth of the undulator's center cone:

$$\frac{\Delta\lambda}{\lambda} = \frac{1}{iN}, \quad (4.3)$$

where  $N$  is the number of magnet periods, and  $i$  - undulator harmonics order. The AP-LE II undulator at UE46 beamline has 72 magnetic periods, that at 3rd harmonic results in bandwidth  $\Delta\lambda/\lambda = 1/216$ . The temporal coherence, according to equation 2.12, is about 223 nm at wavelength corresponding to 1000 eV, which is much smaller than spatial coherence. Further tuning of the energy resolution by the monochromator and the slit system provides  $\Delta\lambda/\lambda > 1/10000$  and improves the temporal coherence to the values higher than  $6 \mu\text{m}$  at the energy of 1000 eV.

### Coherence after focusing by a FZP

X-rays diffracted by focusing optics, like FZPs, change their coherence properties. Determination of the coherence degree in the focus spot is vital for the success of diffraction based imaging methods. We consider two different cases which are defined by the degree of coherence of the incident X-ray beam that illuminates an FZP: fully coherent and partially or low coherent illumination.

In order to reach the best FZP performance and to get diffraction limited focus spot size the spatial coherence length in illumination spot of X-ray beam coming from the slit system has to be bigger than FZP size. If we have fully coherently illuminated FZP we can estimate the spatial coherence length in the focus spot  $a_F$  using following expression [101]:

$$a_F = \Delta r_{Rayl.} \cdot \sqrt{1 + \frac{Z^2}{D^2}} \cdot \frac{a_c}{Z}, \quad (4.4)$$

where  $\Delta r_{Rayl.}$  - size of the first order focus spot,  $Z$  - size of the X-ray beam on the FZP, and  $D$  - FZP diameter. Strongly focusing FZPs, with small outermost zone width and big diameter, possess lower spatial coherence length in the focus spot.

Figure 4.7 represents the calculation of spatial coherence in the focus spot obtained from FZPs which are available at MAXYMUS microscope. We assume that FZPs are coherently illuminated with a beam coming from the vertical slits opened for  $20 \mu\text{m}$ . The FZPs have different parameters of  $D$  and  $\Delta r$  which, according to equation 4.4, mostly determine the degree of coherence in the focused X-ray beam. The graph shows that strongly focusing FZP with  $\Delta r = 18 \text{ nm}$  and  $D = 320 \mu\text{m}$  produces beam with smaller spatial coherence values. The FZPs with  $D = 100 \mu\text{m}$  and  $\Delta r = 70$  and  $120 \text{ nm}$  produce focus spot with higher spatial coherence length. In a range of soft X-rays, spatial coherence in the focused beam produced by coherently illuminated FZPs has values bigger than few hundred nm that exceeds in size the diameter of focused spot. Therefore in order to produce coherent light in the focus spot we just need to illuminate all the area of FZP with coherent X-ray beam.

Let's consider the case when an FZP is illuminated incoherently. In other words the FZP has a bigger size than coherence length of an incident beam. The focus spot will be broadened because of diffraction effect and final incoherence in the focus spot. As a result

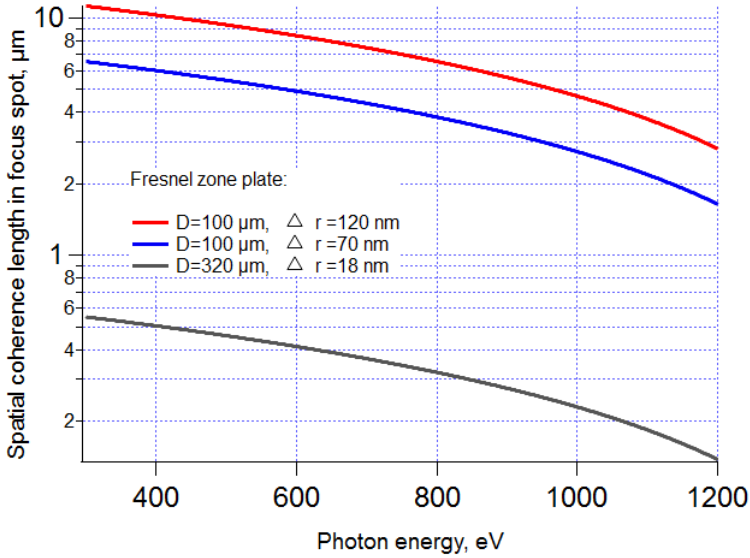


Figure 4.7: Spatial coherence length in the first order focus spot of coherently illuminated FZPs depending on photon energy with the slit width of  $20 \mu\text{m}$ . Strongly focusing FZP with small  $\Delta r=18 \text{ nm}$ , which is used for conventional STXM operation, produces a beam with smaller coherence length.

the FZP only modifies the radius of curvature of the X-ray beam illuminating it. The degree of spatial coherence in the FZP focus spot is evaluated as following [101] :

$$a_F = a_c \cdot M \quad (4.5)$$

$M$  is a magnification factor and presented as:

$$M = \left| \frac{f}{R - f} \right| \quad (4.6)$$

Here  $f$  is a focal length of FZP determined by equation 3.1,  $R$  is a distance between slits and focal plane. The difference between the coherence length in the FZP focus spot produced in the cases of fully coherent illumination and incoherent illumination varies strongly (table 4.2). In the second case coherence length can be smaller than size of the focus spot that should be taken into account. Ptychographic set up does not demand the use of highly resolved FZPs with big aperture, but comparatively small FZPs with big  $\Delta r$

and diameter, which do not require spatial coherence length of the X-ray beam bigger than  $200 \mu\text{m}$ .

Vertical slits opening, $\mu\text{m}$	Coherence length on FZP, $\mu\text{m}$	Spatial coherence in focus spot, nm
10	265.68	295.14
20	132.84	147.57
30	88.56	98.38
40	66.42	73.78
50	53.14	59.03

Table 4.2: Spatial coherence length for different vertical slits opening at 1400 eV, FZP diameter  $100 \mu\text{m}$  and outermost zone width 70 nm. Spatial coherence in focus spot is calculated for the case of incoherent illumination of FZP.

Table 4.2 shows the theoretical calculation of spatial coherence at the position of FZP and in the focused spot. The vertical slit width varied in a range from 10 to  $50 \mu\text{m}$  at X-ray energy of 1400 eV in order to obtain high and low degree of spatial coherence in illumination spot. For the calculation focusing FZP with diameter of  $100 \mu\text{m}$ , outermost zone width of 70 nm and size of focus spot of 85.4 nm was used. Spatial coherence of X-ray beam from the aperture opened to 10 and  $20 \mu\text{m}$  is larger than FZP diameter which ensures optimal illumination and results in highly coherent focus spot. With  $30 \mu\text{m}$  slits gap the FZP is illuminated partially incoherently but it is still sufficient enough to provide coherence in the focus higher than the size of the focus spot. The degree of coherence decreases rapidly at both positions if the vertical slit gap is increased.

## 4.2 Ptychographic imaging implementation in STXM

For implementation of ptychography a highly efficient and fast in-vacuum CCD camera was installed and commissioned. The camera is designed for registration of X-rays in soft energy range and capable of single photon counting operation. The detailed information about CCD parameters and operation is given in Chapter 4.2.1.

The detector stage was modified in order to place the CCD in the optical axis of the beam. Figure 4.8 shows the scheme of MAXYMUS microscope with CCD camera placed behind the sample. All the other components, i.e. FZP, OSA and sample, stay in the same configuration as for normal STXM operation. Due to space limitations and compact collocation of the stages it is not possible to move the CCD camera closer than 8 cm to the sample. The distance can be reduced to 4 cm by removing the sample piezo stages that provides two times higher scattering angle coverage by the CCD and improves the

resolution of the reconstructed image twice. In this case the raster scanning is performed by FZP movement instead of the sample movement.

In order to make initial alignment of all STXM components and easily navigate the sample position, an APD detector is attached to the top of the nozzle of the CCD metal cover, in the way that it is located 7 cm closer to the sample than CCD. Therefore the detectors can be easily switched just by changing Y-position of the detector stage without opening the chamber. The signal from the CCD camera is obtained using integrated digital/analog converter. It produces a voltage signal from the digitized read out for each CCD frame that is used by the STXM software as output signal of a point detector. This low resolution image is obtained simultaneously with ptychographic measurement and helps to determine the position of a running scan.

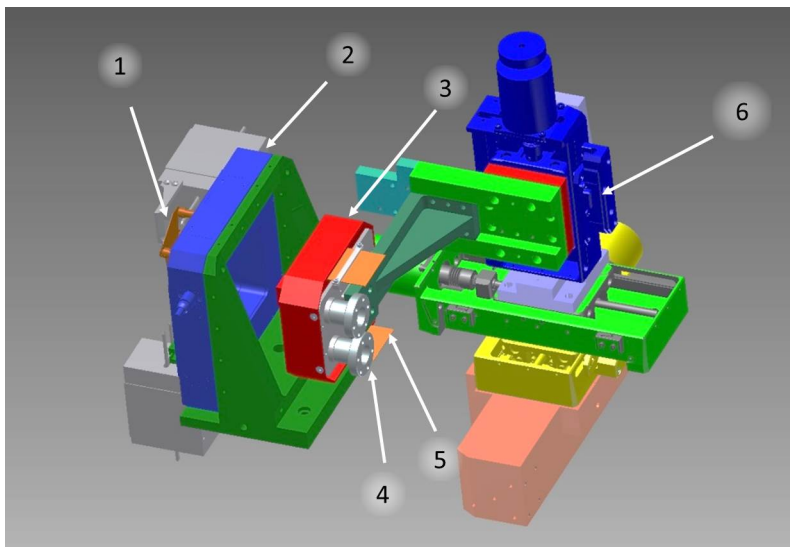


Figure 4.8: Scheme of MAXYMUS endstation with CCD camera setup: 1) sample, 2) sample piezo stage, 3) CCD camera, 4) flanges for cooling system, 5) connecting cables, 6) detector stage.

For ptychography a set of low resolving FZPs with  $\Delta r$  in a range of 75-120 nm and diameter of 100-120  $\mu\text{m}$  have been designed in order to produce relatively large focus spot to ensure reasonably fast scanning, at the same time, having high efficiency for bright illumination. The step size of the raster scan was chosen in agreement with the size of FZP focus spot providing at least 20 % overlap of FWHM of the neighboring regions. Single exposure time for each scanning point varied from 100 to 500 ms to assure sufficient photon count rate at the high diffraction angles in reciprocal space. The exposure time was changed depending on the scattering power of the used specimen. A dark field was

recorded before each ptychographic scan and subtracted from the diffraction patterns. The experimental calibration of the scanning parameters is presented in Chapter 4.4.

### 4.2.1 The CCD camera for X-ray detection

The first CCD camera was developed in 1969, Bell laboratory, USA. Due to the wide range of advantages over other types of detectors CCD cameras became a breakthrough in astronomy also for X-rays detection [102].

For efficient X-ray photon detection in diffraction imaging experiments the following characteristics of CCD are the most important:

- **High dynamic range** is an important feature since the central area of a diffraction pattern normally has few orders of magnitude more photon counts than distant areas with higher scattering angles. High dynamic range ensures that the diffraction image is not overexposed in the center and at the same time each photon on the weakly illuminated border areas of the CCD chip is detected.
- **Quantum efficiency (QE)** is the probability of a detector to respond to the photon signal and convert it to the measurable signal. To assure the best QE parameter the CCD camera has to be designed for specific energy range that is correlated with the thickness of the doped region.
- **Signal-to-noise ratio (SNR)** characterizes the ultimate performance of a detection system representing the ratio of the measured X-ray light signal to the noise which mostly consist of dark noise and read out noise. Dark noise is related to thermal current that is a result of spontaneous generation of electrons and holes not depending on whether the detector was exposed by X-rays or not. Read out noise is the result of converting CCD charge carriers into voltage signal and mostly comes from the on-chip preamplifiers.

#### Fast in vacuum CCD camera at MAXYMUS

**Features** PnCCD is a full frame fully depleted silicon detector for direct X-ray detection. This camera has image area  $12.7 \times 12.7 \text{ mm}^2$  and pixel size  $48 \mu\text{m}$  which can act as energy spectrometer or photon counter depending on operation mode. In comparison with other commercially available CCDs suitable for in-vacuum operation in soft X-ray range (Princeton Instruments, Andor, Hamamatsu, etc.) the current camera has comparatively big pixel size and small area. However taking into account sampling criteria and optical geometry of the set up it is sufficient for high numerical aperture and oversampling in the q-space. Implementation of frame store operation and column parallel readout, when all pixels in a row are processed in parallel, allows detector frame rate up to 930 Hz. The optimal operation frequency used for diffraction pattern capturing with sufficient statistics

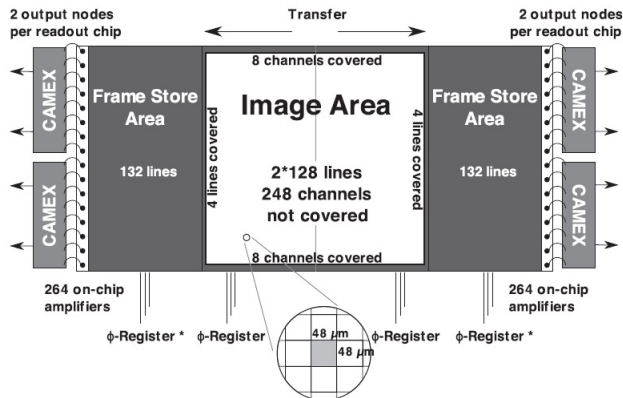


Figure 4.9: Illustration of the frame store operation for high speed read out [103]. Image area is split into two halves. Each channel ends with readout anode and JFET for first amplification, which are bonded to CAMEX chips for further amplification and filtering.

is about 440 Hz corresponding to 440 frames per second (fps). Normally, operation frequencies of the cameras with comparable size, read out noise and efficiency, are an order of magnitude smaller.

In order to provide high-speed operation it works in split frame transfer mode (figure 4.9). Each half image with 132 lines and 264 channels is transferred within  $50 \mu\text{s}$  to the corresponding storage region which is shielded from X-rays [103]. The high speed operation of the CCD dramatically reduces time for data acquisition during ptychographic measurements.

The main advantage of this CCD camera is a high dynamic range in combination with a high readout rate. Commonly double exposure technique is used to increase the dynamic range of detector. It combines long and short exposures in one diffraction frame for each scanning point [50]. However using this approach noticeably increases data acquisition and calculation time. The high performance of the CCD and application of the dynamic stacking of frames allow to use only single exposure diffraction data set. Due to this approach very fast read out rate do not reduce dynamic range of the registered patterns. The optimal settings for the experiment can be found as a combination of read out rate and gain to ensure noise level as low as possible and at the same time accurate registration of desired diffraction features.

The pnCCD has large detection volume with the thickness of  $450 \mu\text{m}$  that helps to achieve high quantum efficiency for soft X-rays. As it is shown in figure 4.10 the quantum efficiency is above 95% in the range from 3 to 10 keV. The CCD camera used at

MAXYMUS has 150 nm optical light stop layer made of Al that corresponds to red curve on the graph. For soft X-rays the most efficient part of 80 – 90% stays in the energy range of 700-2000 eV. The main characteristics of the pnCCD camera are summarized in the table 4.3 [103].

Parameter	Value
Number of pixels	$264 \times 264$
Pixel size	$48 \mu\text{m}$
Image area	$12.7 \times 12.7 \text{ mm}^2$
Frame rate	up to 1 kHz
Quantum efficiency	95 % at 3-10 keV
Read out speed	28 MPixel/s
Read out noise (RMS)	$<3 \text{ e}^-/\text{pixel}$
Full well capacitance	$10^5 \text{ e}^-$
Charge transfer efficiency	0.99995

Table 4.3: Specification of in-vacuum pnCCD detector

**Cooling** To reduce the dark current the CCD camera is operated under the optimized temperature  $-25^\circ \text{C}$ . At this low temperature and frame rate 440 Hz dark current noise contribution is less than  $1 \text{ e}^-/\text{pixel}$  RMS. Cooling is produced by thermoelectric modules with 31W cooling power each, which are connected to a copper heat exchanger cooled by water with a temperature of  $19^\circ \text{C}$ . The cooling water for the thermoelectric cooler comes from the external cooling circuit through two flexible vacuum hoses (figure 4.11).

The CCD camera should be fully cooled in order to switch on the voltages. The cooling can be started when vacuum chamber of STXM is under sufficiently low pressure, in a range  $10^{-5}$  mbar. It prevents condensation of residual gases from the chamber on the surface of the CCD chip. To vent the chamber for sample change all the procedure has to be done in reversed order.

**Data acquisition** To provide the voltages, which are necessary for pnCCD camera operation, a control unit with programmable power supplies is introduced and placed outside of the microscope vacuum chamber. The sequencer that works as a pattern generator produces pulses for charge transfer from one pixel to another, controlling clocks for CAMEX amplification and 4 analog-digital converters (ADC). In case of the power failure at BESSY the uninterruptible power supply (UPS) unit ensures back up to avoid camera damage. Transmission of data from ADC with approximate speed of 450 Mbit/s is made by two high-throughput fiber connection, which are stored in the Linux-based computer.

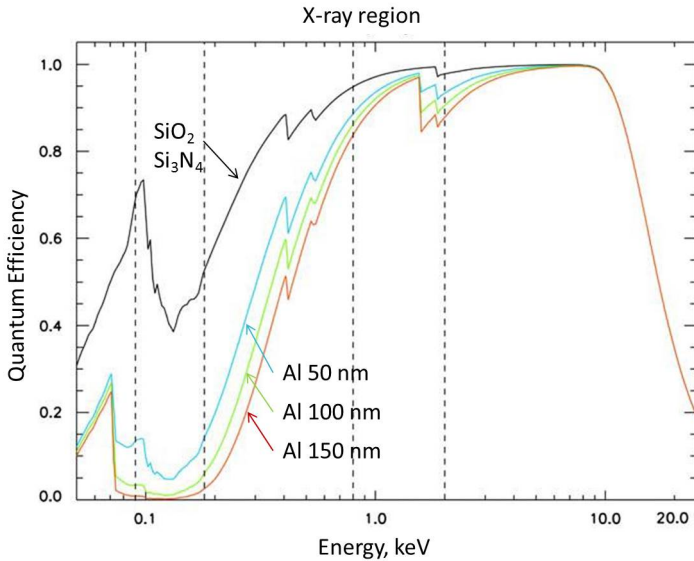


Figure 4.10: Quantum efficiency of the pnCCDs as a function of energy for a  $450 \mu\text{m}$  thick pnCCD detector with different light blocking filters. Red curve - Al coating of 150 nm, green curve - Al coating of 100 nm, blue curve - Al coating of 50 nm, black curve - a thin  $\text{SiO}_2$  and  $\text{Si}_3\text{N}_4$  passivation layer [104].

The fast data acquisition, filtering and transfer to the storage PC allows to perform data processing in real time.

**Dynamic stacking** For ptychography data acquisition the single diffraction pattern is created by stacking the multiple frames during the dwell time for each scanning point. Stacking the frames is a way to enhance the image contrast by reducing noise and increasing the dynamic range. Since the noise of the separate frames changes randomly from one to another, summing them together decreases the overall amount of background noise. At the same time the signal from the diffraction speckles is similar for all frames that results in enhancing of the real signal. The correct gain mode and slits opening gap are chosen in the way that the diffraction image is not overexposed at the region with high illumination and at the same time it is possible to distinguish dim speckles. Stacking helps to increase the number of possible digitized values linearly with the number of stacked images. In this case the dynamic range is improved by accumulating the signal from the dim regions which in case of one frame image would be drowned in the noise. The number of stacked

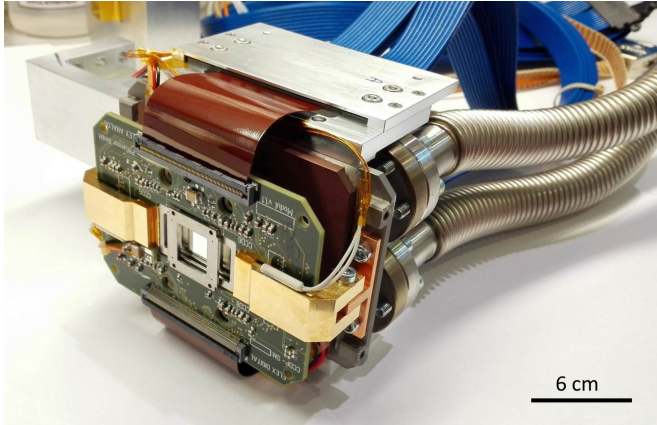


Figure 4.11: Photo of pnCCD camera without front cover. On the back side two flexible hoses for water cooling are attached.

frames is determined by the dwell time for each scanning position and frame rate of the CCD. The process is done automatically using CCD software.

Figure 4.12 shows radial profiles of the diffraction patterns obtained from the magnetic labyrinth domain sample (see Chapter 5.3) with dwell times 100 ms, 300 ms and 500 ms. The profiles demonstrate that the most of the photons concentrated in the first order diffraction of FZP that is equivalent to zero order light in regard to scattering. At the higher spatial frequencies we see drastic drop of the counts with variations in background signal depending on the dwell time. The shorter the dwell time the higher the noise, for instance, 100 ms dwell time has the noise about 2 times higher than signal at 500 ms. As a result using longer dwell time in diffraction imaging helps to improve contrast of the reconstructed image due to increase of SNR value.

### Diffraction pattern correction

The CCD camera doesn't have a global shutter, so it is still sensitive during the signal transfer towards the frame store areas. Therefore diffraction data need to be processed in order to reduce the artifacts produced by the signal from the highly illuminated first order of FZP, which is located in the center of the CCD chip. The noise creates long streaks propagating to the very edges of the diffraction image (figure 4.13). The CCD consist of two halves, and signal acquisition is done by transfer of the electrons as they are shifted from the center to both sides of the split CCD. The correction is done by subtraction of the median array obtained from the first and last 30 columns from the corresponding left and right halves of diffraction pattern. As a result it helps to avoid unwanted artifacts in

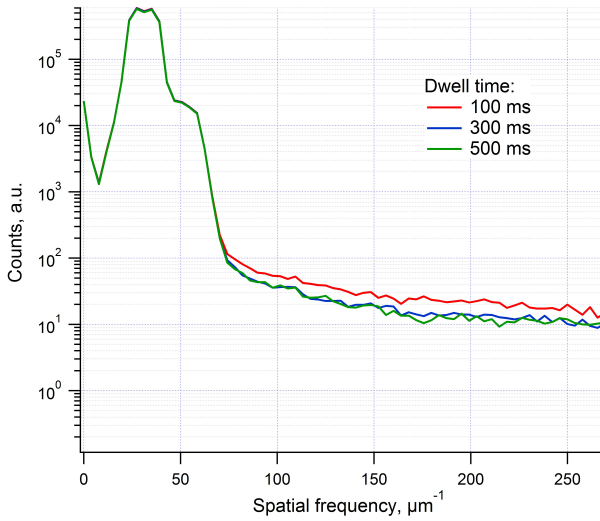


Figure 4.12: Radial profiles of diffraction images obtained from the low scattering sample using different dwell times: 100 ms, 300 ms and 500 ms.

reconstruction images, that normally would result in vertical periodic stripes and reduction of contrast.

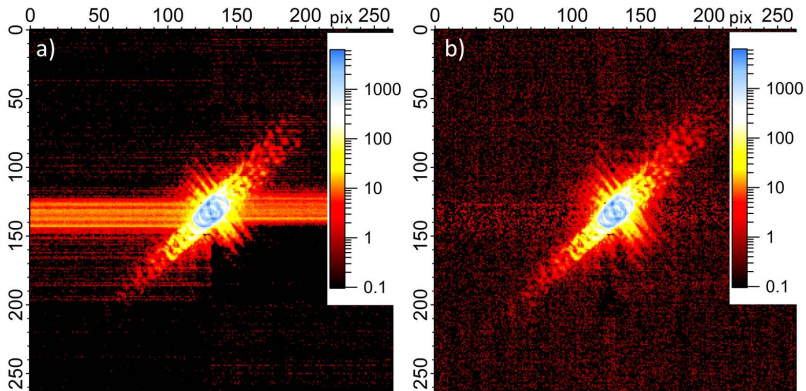


Figure 4.13: Correction of diffraction pattern: a) raw diffraction image and b) the same image with read out noise filter, both images are in logarithmic scale.

### 4.3 FZPs for ptychography

The FZPs used for ptychographic measurements at MAXYMUS microscope have been custom made by ion beam lithography (IBL) in department Schütz of the MPI-IS <sup>1</sup>. This technology showed a great potential for comparatively fast and robust fabrication of high resolution FZPs for soft X-ray application [96]. A set of FZPs listed in table 4.4 with different diameter, width of outermost zone, fabrication material (Au and Si) and beamstop method depositions have been produced.

**Au FZPs** For IBL FZP fabrication  $\text{Si}_3\text{N}_4$  X-ray transparent 100 nm thick membranes were coated with a gold layer by electron beam evaporation. Gold was chosen as a fabrication material due to high absorbency in soft X-ray energy range and appropriate performance for FIB micromachining. A  $\text{Ga}^+$  ion beam with 30 keV energy and 30 pA current was applied for patterning that resulted in a nominal beam size of 16 nm. The zones were milled starting from the outer part towards the center. A Pt center stop was made by successive electron and focused ion beam induced depositions on the not milled part in the center of FZP. The center stop is around 1  $\mu\text{m}$  thick and designed for efficient blocking of the not diffracting part of the incident beam. Since the center stop is deposited after milling the FZP zones, Pt is sputtered at the neighboring from the beamstop regions that reduces diffraction efficiency of FZP and its general performance.

**SiN FZPs** The FZPs made out of SiN were fabricated due to potentially higher efficiency in the soft X-ray range than ones made out of Au. The process of fabrication starts with Pt beamstop deposition using laser lithography. Unlike the previous technique it allows to produce thick beamstop not affecting adjacent diffracting area of FZP. Thicker beamstop reduces background light providing higher signal-to-noise ratio and higher contrast in scattering pattern.

The SEM image of IBL FZP with beamstop formed by laser lithography is shown in figure 4.14 a). The thickness of beamstop material is about 45  $\mu\text{m}$ . After the fabrication of beamstop the diffracting zones of FZP were written by IBL as it was described above.

**Diffraction efficiency** The efficiency of FZP is a main parameter which is defined by how much of the initial X-ray beam intensity ends up in the focus of particular diffraction order. In order to determine diffraction efficiency (DE) of the FZPs an aperture serving as a reference of incoming beam intensity was milled by FIB in the membrane. A pinhole placed in the sample position was scanned in focus of the first diffraction order to get the image of the focus spot and light spot coming from the aperture. The ratio of intensities

---

<sup>1</sup>The fabrication of ptychographic FZPs was performed by Umut Sanli, Margarita Baluktsian and Kahraman Keskinbora

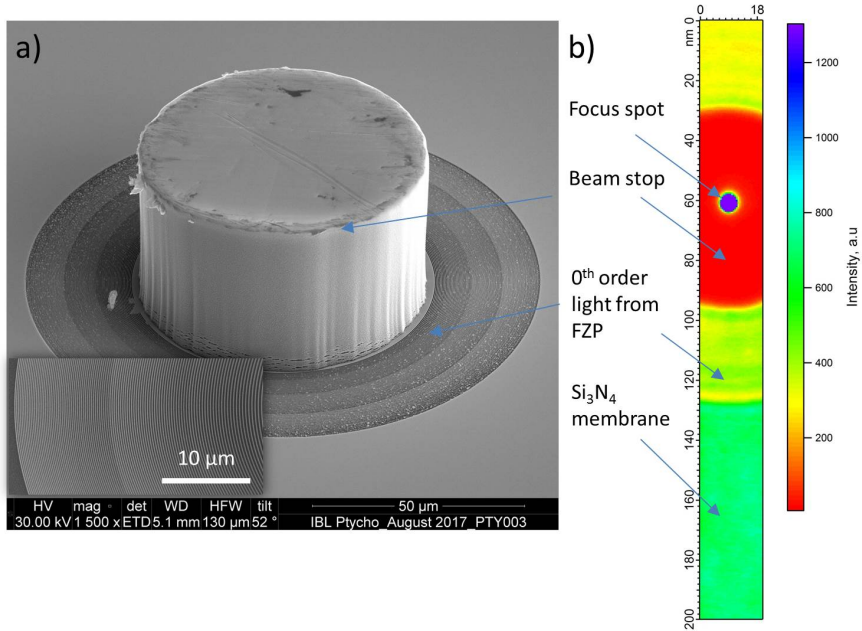


Figure 4.14: Performance of SiN FZP: a) SEM image of Au IBL FZP with  $45 \mu\text{m}$  thick beamstop produced by laser lithography. The inset shows zones of FZP fabricated out of SiN; b) scan of FZP focus spot and transparent window that were used for efficiency calculation.

in the focal spot to the amount of incident X-ray light on the active area of the FZP determines the value of DE. The incident light from the FZP active area  $I_{tot}$  was calculated as following:

$$I_{tot} = \frac{I_{ref} \cdot S_{FZP}}{S_p}, \quad (4.7)$$

where  $S_{FZP}$  is a diffracting area of FZP,  $S_p$  is the area of the scanned pinhole and  $I_{ref}$  is the light coming through the reference hole.

The distance between the aperture milled in FZP membrane and the FZP itself is around  $125 \mu\text{m}$ . A  $4.4 \mu\text{m}$  wide pinhole was made on a separate silicon nitride membrane covered with  $6.4 \mu\text{m}$  thick gold film for scanning the focus spot and the incident X-ray beam from the aperture. Measurements of efficiency of SiN FZP were done without reference hole since it doesn't have opaque Au layer around diffracting zones. The reference X-ray incident beam was obtained in the substrate area  $140 \mu\text{m}$  distant from the focus spot as it is shown in figure 4.14 b).

As seen in table 4.4 FZPs with a beamstop deposited by FIB has significantly lower

<b>FZP parameters</b>	<b>1</b>	<b>2</b>	<b>3</b>	<b>4</b>
Material thickness (nm)	Au	Au, 240	Au, 240	SiN
Diameter ( $\mu\text{m}$ )	50	120	100	120
Beam stop ( $\mu\text{m}$ )	30	60	50	60
Outermost zone width (nm)	125	100	75	100
Focus spot size (nm)	152.5	122	91.5	122
Diffraction efficiency 800 eV (%)	-	-	0.51	7.99
Diffraction efficiency 1200 eV(%)	-	0.64	1.45	4.98

Table 4.4: Parameters of ptychographic FZPs used at MAXYMUS

efficiency than FZPs with laser lithography beamstop. The energy range, where SiN FZP exhibits the highest efficiency of 7.99 %, is around 700-800 eV and goes down to 4.98 % with the increase of energy to 1200 eV. The efficiency of FZPs with FIB deposited center-stop have efficiency of around 0.51 % below 1000 eV with a maximum of 1.54 % at 1400 eV.

## 4.4 Ptychography resolution

### 4.4.1 Coherence and ptychography

To study the influence of X-ray coherence on the resolution of ptychographic reconstruction measurements of a strongly scattering test sample (FZP made out of Au with smallest structures of 30 nm) were performed. The FZP used as a focusing optics had diameter of 100  $\mu\text{m}$  and an outermost zone width of 70 nm, yielding a size of focus spot of 85.4 nm. Different degrees of coherence were created by tuning the gap of the vertical slits from 10 to 50  $\mu\text{m}$  at X-ray energy of 1400 eV, in accordance with calculation presented in the Chapter 4.1.2. Since the spatial coherence of the beam at the slits position in horizontal direction is around 45  $\mu\text{m}$  the opening of horizontal slits can be freely varied within this width in order to keep photon flux the same for different vertical gaps. Reconstructed phase images on figure 4.15 showed no loss in resolution for slits gaps 10, 20 and 30  $\mu\text{m}$ , since the spatial coherence is bigger than the focus spot. The images taken with vertical slits gap of 40  $\mu\text{m}$  significantly degraded, at 50  $\mu\text{m}$  - structures of the test target are not resolved. The observed degradation of the reconstructed images stay in a good agreement with estimated coherence values. However, even illumination spot with spatial coherence less than its size can provide usable ptychographic reconstruction as it was observed with the 40  $\mu\text{m}$  slits gap.

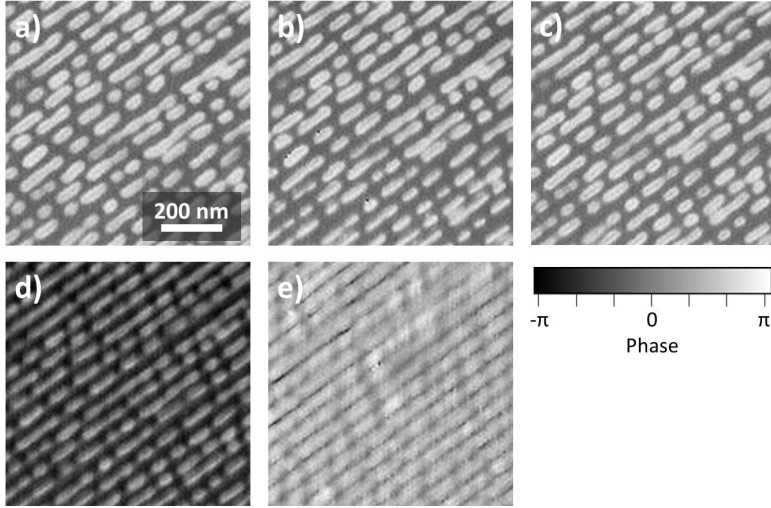


Figure 4.15: Phase reconstructions of resolution target (FZP) taken with different slit widths: a)  $10 \times 23 \mu\text{m}$  b)  $20 \times 16 \mu\text{m}$  c)  $30 \times 13 \mu\text{m}$  d)  $40 \times 12 \mu\text{m}$  e)  $50 \times 11 \mu\text{m}$ . The horizontal slit width varied in order to keep the total flux the same for different vertical slit opening.

#### 4.4.2 Numerical aperture

The resolution of diffraction imaging methods is determined in the first place by the highest scattering angle that can be measured by the CCD, that is expressed as a numerical aperture (NA) of the system. The property of the system to detect a diffraction pattern in accurate way relates to the sampling criteria. Since the diffraction pattern is recorded by the discrete pixels of CCD detector in reciprocal space we can estimate the sampling distance in the real space. Having feature size  $\Delta x$ , the CCD placed on distance  $L$  from the sample and wavelength  $\lambda$  we can calculate the speckle size in q-space as:

$$\Delta q = \frac{\lambda L}{\Delta x} \quad (4.8)$$

If pixel size of the CCD is  $p$  and amount of pixels in 1D direction is  $N$  the sampling size in the real space, or in other words, the pixel size of a reconstructed image is expressed as following:

$$\Delta x = \frac{\lambda L}{Np} \quad (4.9)$$

According to equation 4.9 a bigger the CCD chip area, higher energies or a shorter distance between sample and detector would result in a higher detection aperture and resolution.

Figure 4.16 shows the difference in numerical apertures with CCD placed at the distances  $L$  and  $2L$  from the sample. The closer placement of the CCD results in higher  $q$ -space coverage and, potentially, in higher ptychography resolution.

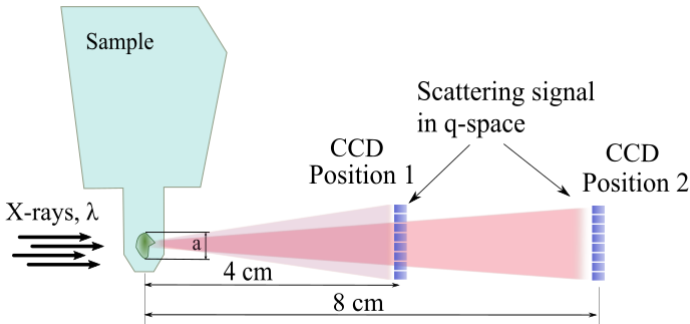


Figure 4.16: Sketch of the different numerical aperture provided by two positions of the CCD relative to the sample. In case of 8 cm distance at position 2 the CCD has twice smaller coverage of the reciprocal space in comparison with position 1.

At MAXYMUS microscope the conventional stages assembly allows minimal distance between detector and sample of 8 cm. In this case the CCD size of  $12.7 \times 12.7 \text{ mm}^2$  at energy 1200 eV give the resultant pixel size of 6.5 nm. Removal of the piezo sample stage allows to reduce distance to 4 cm that gives twice smaller sampling distance in real space. However this configuration is not possible if experimental set up involves a magnet system which is placed in front the CCD restricting its movement closer than 8 cm. Figure 4.17 shows the simulation of two ptychographic reconstructions taken by the systems with different numerical apertures. The a) diffraction pattern captures smaller scattering angles in  $q$ -space cutting off high diffraction orders. The diffraction pattern b) have twice bigger NA, that for example could correspond to twice smaller distance between detector and sample. As a result we have reconstructions with different pixel sizes, figure 4.17 c) has pixel size of 19.4 nm that is twice bigger than pixel size of 9.7 nm in figure 4.17 d), that directly reflects on the resolution and contrast.

### 4.4.3 Flux and scattering power

Sufficient flux and photon count rate at high scattering angles are another important factors for image resolution. In this case a high number of photons per area results in better spatial resolution of ptychographic reconstruction. In order to evaluate coherent intensity  $I_c$  at

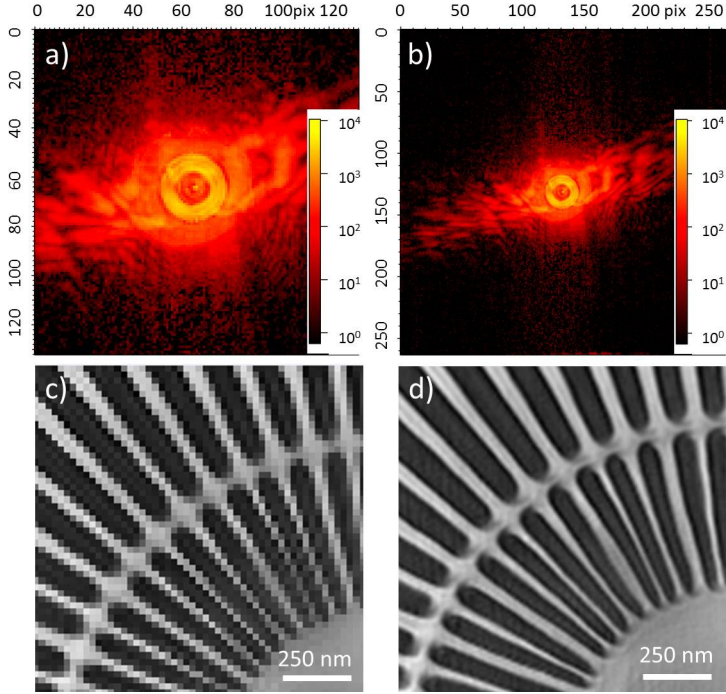


Figure 4.17: Comparison of two ptychographic reconstructions of Siemens Star obtained by systems with different NA: a) is a diffraction pattern with twice reduces NA obtained from diffraction pattern b) by cutting off  $q$  values at high diffraction orders. Images c) with pixel size of 19.4 nm and d) with pixel size of 9.7 nm are corresponding ptychographic reconstructions.

the focus spot the following equation can be used [105]:

$$I_c = \frac{F_c}{A_{eff}} \propto Br \times \frac{\Delta E}{E} \times NA^2 \times T, \quad (4.10)$$

where  $F_c$  - coherent flux obtained by the focusing optics,  $A_{eff}$  - the effective area of the diffraction limited focus  $A_{eff} \propto (\lambda/NA)^2$ ,  $Br$  - brilliance of X-ray source,  $\Delta E/E$  - the energy bandwidth,  $NA$  - numerical aperture of FZP, and  $T$  is the efficiency of FZP. Thus the highly efficient optics with big numerical aperture should be used for the larger fluence in diffraction signal. However ptychography needs comparatively big focus spot (around 100 nm) to ensure reasonably fast scanning that requires FZP with smaller NA.

In any case the intensity of a scattering signal strongly depends on the scattering power of a sample. For example, scattering from magnetic samples based on XMCD have signifi-

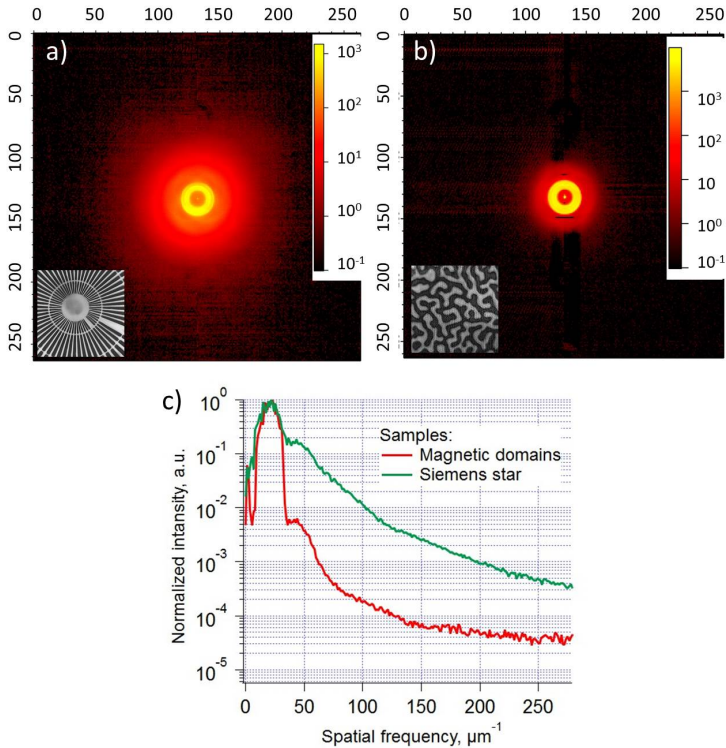


Figure 4.18: Averaged diffraction patterns from the ptychography scans of a) strongly scattering resolution target Siemens star made of Au at 800 eV, and b) weakly scattering magnetic domain structure at the Co-edge energy 780 eV. c) shows radial profiles of these diffraction patterns, where green curve corresponds to the resolution target, red curve - to the magnetic sample.

cantly lower intensities than from charge scattering samples. Figure 4.18 shows diffraction patterns averaged over two sets of ptychographic data, one of a resolution target (Siemens Star, Zeiss) made of Au about 150 nm thick at the energy of 800 eV, the other of a magnetic domain sample scanned at Co edge (780 eV) with total thickness in the multilayer of 15 nm. Since the sample materials and structures are not the same it gives only general understanding of the difference between charge and magnetic scattering systems. Scattering from the magnetic sample doesn't show strong pronounced speckles, but a faint halo around zero order at the low  $q$ -space frequencies. The diffraction pattern from the resolution target has higher level of scattering as shown in the radial profile graph in figure 4.18 c). At higher energies diffraction speckles from the resolution pattern can be clearly

visible at the very edges of the CCD detector providing NA limited resolution.

Since the radiation damage of the magnetic multilayer systems can be neglected the scattering statistics is improved by increasing dwell time for every scanning step. The basic issue in experiments with long exposure times is the specimen contamination with carbon that occurs due to the interaction of X-rays and residual gases in vacuum chamber. The carbon layer is built up on the surface of the scanned area that worsen the contrast of the resulting image. Also thermal drifts of the sample during long scans can be an issue causing resolution worsening.

## 4.5 Optimization of diffraction pattern acquisition

A Siemens star resolution sample was used to test the reliability of the ptychographic set up, scanning parameters and the result of phase retrieval algorithm. By reconstructing an object with high chemical scattering and known performance it is possible to identify system limitations, reliability of the reconstructing algorithm and possible artifacts. The further details about interpretation of phase images and relevant artifacts in phase reconstruction, as well as methods for resolution estimation used in this work, are presented in Appendices B and C.

### 4.5.1 Overlap ratio of scanning points

The overlap ratio of illumination probes of the neighboring scanning points determines the number of diffraction patterns for one image. In order to cover bigger area, minimizing the amount of frames and, as a result, time needed for one scan, the optimal value for overlapping ratio of scanning points should be determined.

In order to evaluate the effect of overlapping ratio on the quality of ptychographic reconstruction measurements with different step sizes have been performed. For the measurements FZP with outermost zone width  $\Delta r = 100$  nm and focus spot size 122 nm was used. The size of the illumination spot in focus plane is determined as the FWHM of sinc shaped profile of airy disk illumination spot. The scanning step was changed from 20 nm to 160 nm with 20 nm increment. In case of 20 nm step the overlapping ratio of the neighboring scanning spots is around 83 % as it is imaged in figure 4.19 a). Performing scanning steps equal or bigger than the focus spot, i.e. in a range of 120-160 nm, the overlap region decreases and includes low intensity parts of the illumination peak as it is shown in figure 4.19 b).

SEM image of inner part Siemens Star (Zeiss) with 30 nm wide structures is presented in figure 4.20. Figure 4.21 shows the resulting amplitude ptychographic reconstructions of the Siemens Star. The gradual increasing of step size till 120 nm did not show a noticeable change of the reconstruction quality. In figure 4.21 d) the scan with 120 nm step size is

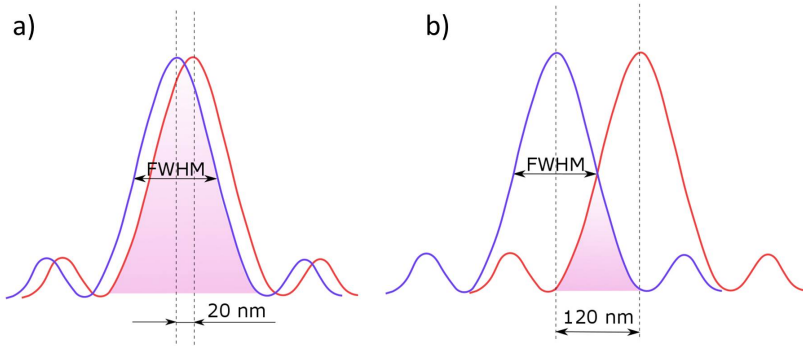


Figure 4.19: Overlap ratio of neighboring illumination spot profiles at the scans with step sizes a) 20 nm and b) 120 nm.

shown. This step size is out of FWHM of illumination profile, but reconstruction results in the same image resolution and contrast. Therefore step size as big as focus spot can be used for imaging of highly scattering samples without affecting the image quality and significantly reducing scanning time. The raster artifacts appear at the scans with the step size of 140 nm, the structures get partially unresolved in figure 4.21 f) when the step size is 160 nm.

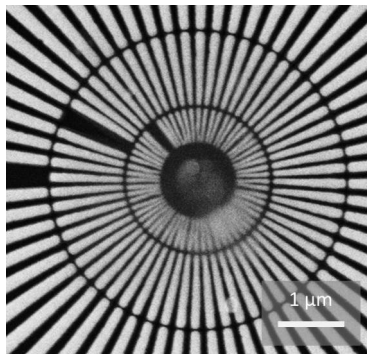


Figure 4.20: SEM image of the Siemens Star with smallest structures of 30 nm.

As it is shown a strongly reduced overlap of the neighboring spots in raster scanning leads to the grid artifacts in the image and resolution degradation. It is caused by inhomogeneous illumination at each scanning spot and, as a result, the lack of scattering signal in overlap region that negatively influences the retrieval process.

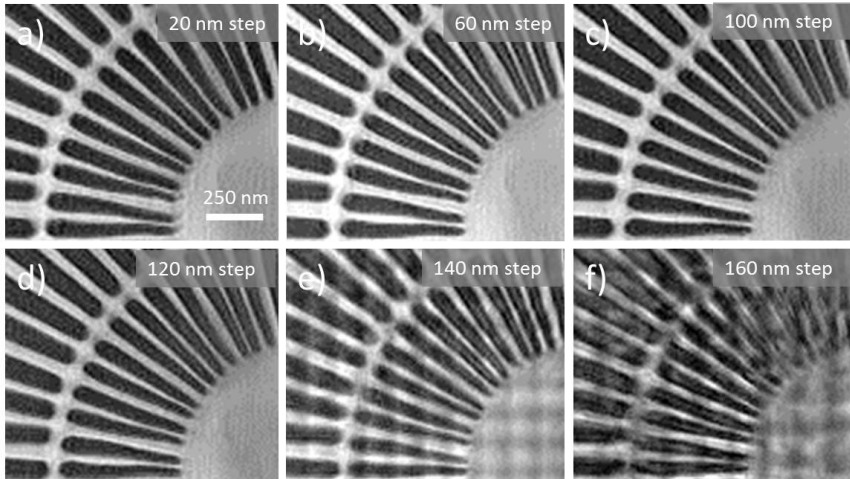


Figure 4.21: Ptychographic images obtained with different step sizes of the raster scan: a) 20 nm; b) 60 nm; c) 100 nm; d) 120 nm; e) 140 nm; f) 160 nm.

## 4.5.2 Defocus scanning

In order to cover bigger area during ptychographic raster scan not only overlap ratio can be changed but also the size of the illumination spot itself. It is done by shifting the sample out of focus as it is shown in figure 4.22 c). As it was reported in [106] resolution of ptychographic reconstruction isn't sensitive to the position of the sample relative to the FZP focus plane. Figure 4.22 b) is a simulated illumination profile in defocus position. It has a doughnut like shape, which comes from the divergent light cone of the first order light, and posses an order of magnitude less intensity than in the focus spot (figure 4.22 a), that has to be taken into account. The illumination spot size is estimated as  $S = \delta \frac{D}{f}$ , where  $\delta$  is defocus distance,  $D$  - diameter of FZP, and  $f$  - focal distance.

The experiment was done by gradually increasing distance from focus position with 5  $\mu\text{m}$  step moving sample backwards from FZP. Figure 4.23 a) shows image in focus with 120 nm scanning step size and corresponding focus spot size of 122 nm, determined as FWHM. Figure 4.23 b) shows beam profile in 25  $\mu\text{m}$  out-of-focus position with 140 nm scanning step size and illumination spot of around 387 nm. In real conditions the spot size might be smaller due to less defined boundaries and possible non-uniformity of the illumination in defocused position. As it was discussed in previous chapter, when the sample is in the focus position and scanned with the step of 140 nm, the reconstruction suffers from grid artifacts since the scanning step is significantly higher than FWHM of the focus spot (figure 4.23 a). In out-of-focus position the reconstruction doesn't posses

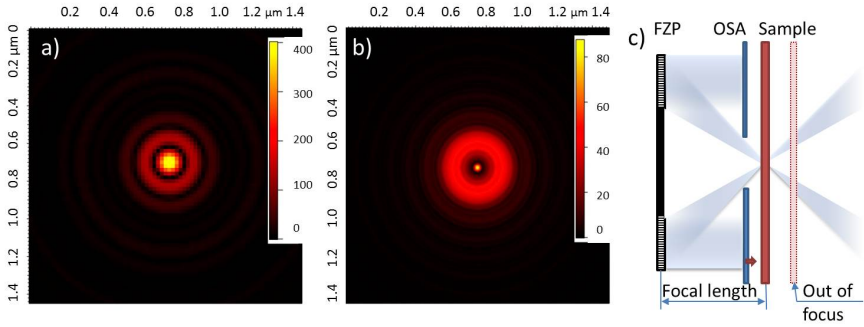


Figure 4.22: Simulated illumination profiles at sample position: a) in focus spot and b) 25 μm out of focus position; c) a schematic illustration of the scanning configuration with the sample in focus and out-of-focus positions.

artifacts at 140 nm scanning step and the 30 nm features are resolved as it is seen in figure 4.23 c).

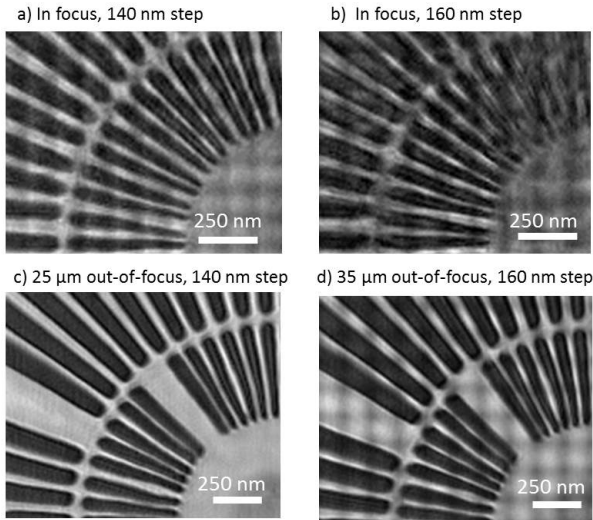


Figure 4.23: Ptychographic images obtained at 800 eV: a) in focus position with scanning step size of 140 nm and b) 160 nm; c) 25 μm out of focus with the step of 140 nm and d) 35 μm out of focus with the step of 160 nm.

Further increase of defocus distance haven't showed the same behavior. In figure 4.23 d) reconstruction with the defocus distance of  $35 \mu\text{m}$  and step size of  $160 \text{ nm}$  has the characteristic grid pattern. Although the  $30 \text{ nm}$  structures are resolved and the image has better quality in comparison with in focus configuration (figure 4.23 b). The presence of artifacts can be caused by inaccuracy of the initial guess of illumination function. The quality of reconstruction is also affected by a significant drop of the beam intensity in the unfocused illumination spot which reduces scattering statistics.

### 4.5.3 Resolving power and dwell time

For the estimation of ptychographic resolving power and its correlation with the numerical aperture (NA) of the setup  $15 \text{ nm}$  structure size Siemens Star (Applied Nanotools) was imaged. The scan was done at energy  $708.4 \text{ eV}$  and  $9 \text{ cm}$  detector distance that results in NA with  $12.5 \text{ nm}$  output pixel size. Therefore the smallest structures of the inner circle would result in around 1 pixel size in the reconstructed image. Figure 4.24 shows amplitude and phase reconstructions of clearly resolved Siemens star that proofs that we get NA limited resolution.

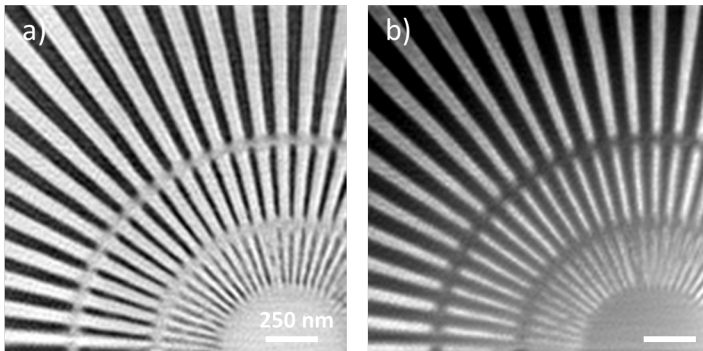


Figure 4.24: Siemens star with  $15 \text{ nm}$  wide inner circle structures imaged by ptychography: a) amplitude and b) phase reconstructions.

As it was discussed, in order to increase scattering statistics in diffraction the data dwell time per each scanning point should be increased. The main effect on the reconstructions is the increase of the contrast that improves the visibility of imaged features. In figure 4.25 the graph shows the dependance of ptychographic reconstruction contrast on the dwell time for a highly scattering sample, i.e. Siemens star, and low scattering magnetic domain structure multilayer  $\text{Ta}(5)/[\text{CoFeB}(1.5 \text{ nm})/\text{MgO}(2 \text{ nm})/\text{Ta}(3 \text{ nm})]_{15}$ . The

contrast of amplitude image was estimated as a Michelson contrast [107]:

$$Contrast = \frac{I_{max} - I_{min}}{I_{max} + I_{min}}, \quad (4.11)$$

where  $I_{max}$  and  $I_{min}$  represent the intensities of bright and dark regions, respectively. In the first case the change of the contrast doesn't not have a strong dependance on the dwell time, relative rise is within 2 % that is still in the range of standard deviation error. Therefore high scattering from the morphological edges of the Au features provides sufficient photon count statistics and signal to noise ratio even at 50 ms dwell time. At the same time, we see that magnetically scattering sample has 20 % contrast change between 100 and 500 ms dwell times. At the higher dwell time values the exponential curve gets into plateau evidencing that further increase will not improve image quality.

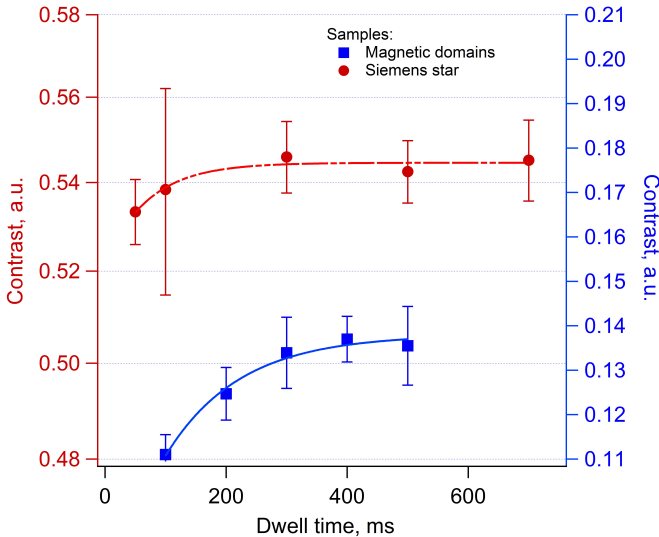


Figure 4.25: Contrast dependance of ptychographic amplitude images on scanning dwell time. The blue curve represents contrast change of magnetic domain sample obtained at Fe-edge 708 eV, the red curve - Siemens Star with 30 nm structures at energy 800 eV. The curves are fitted with exponential fits. The error bars are determined as standard deviation within 5 contrast measurements.

The observed behavior proves that quality of ptychographic reconstruction is mainly defined by the scattering properties of the sample itself and can't be endlessly improved by the change of signal accumulation time. As it was shown the increase of dwell time for charge scattering samples doesn't improve the reconstruction quality, extremely high

scanning time rather can cause the sample drift and carbon layer formation on the sample surface. For the further ptychographic measurements optimized dwell time values of 300-400 ms for pure magnetic contrast samples and 100-200 ms for charge scattering samples are used.

## 4.6 Conclusion

A fast in-vacuum CCD camera (PNSensor) with high readout speed and quantum efficiency has been installed and commissioned at MAXYMUS X-ray microscope at Bessy II in Berlin. With the use of CUDA based SHARP software running on a 8 GPUs computing cluster ptychographic imaging has been successfully implemented. The low read out noise, the high read out rate and, additionally, the dynamic stacking of the frames make this ptychographic set up very fast and sensitive for low scattering specimens. For higher ptychography performance a set of FIB FZPs were fabricated in cooperation with Micro/Nano Optics group (MPI IS) for ptychographic imaging at MAXYMUS. Laser lithography deposition allowed to produce  $45\ \mu\text{m}$  thick beamstop, additionally, the use of SiN instead of gold for FZP fabrication significantly improved their diffraction efficiency.

The coherence parameters of the beamline were estimated in dependance on the degree of the of the vertical and horizontal slits opening, focusing power of FZP and used energy. Low resolution FZPs with comparatively small diameter, which were used for ptychography, produce highly coherent focused spot in case if they are coherently illuminated. The resolution degradation of ptychographic images was observed when the spatial coherence length after focusing by FZP is less then illumination spot.

The calibration of scanning parameters was done using two Siemens star resolution targets with smallest structures of 30 nm and 15 nm. It was observed that the overlapping degree of FWHM of the neighboring scanning points for such highly scattering objects can be in a range of few percent for a reliable phase retrieval. The Siemens star with 15 nm structures was resolved with set-up configuration providing 12.5 nm out put pixel size, that close to be NA limited resolution. The possibility to move CCD detector to up to 4 cm distance from the sample using FZP scanning mode provides the reconstruction output pixel size of about 2-3 nm for X-ray energies higher than 1200 eV.

Out-of-focus ptychographic imaging potentially allows to reduce scanning time due to increase of the probe size. It was shown that providing comparatively big overlap, e.g. 60 %, of the neighboring illumination spots the ptychographic reconstruction gives artifact free image in defocused FZP position with the step size bigger then in-focus illumination spot. Further increase of the illumination spot by moving more out of focus did not show reliable results. Therefore defocused configuration could be applied only for highly scattering specimens that would guarantee high statistics even with low flux of the unfocused illumination spot. At the same time such measurements require a correction for the initial

guess of illumination function, which no longer has a Gauss but a doughnut shape.

Dwell time optimization showed no considerable improvement of the image contrast of a highly scattering resolution target in the range from 100 to 700 ms. At the other hand, low scattering domain magnetic sample gained 20 % of contrast with increase of dwell time from 100 to 300 ms and with no significant changes till 500 ms dwell time. It demonstrates that quality of the reconstructions can not be endlessly improved by increase of the dwell time values.

## Chapter 5

# Ptychographic chemical and magnetic contrast

### 5.1 Chemical contrast in $\text{LiFePO}_4$ battery nanoparticles

Today  $\text{LiFePO}_4$  particles are prominent materials for energy conversion and storage, that is efficiently realized in electrochemical systems, where a phase-separating battery electrode consists of numerous nanoparticles packed in dense (up to  $10^{15} \text{ cm}^{-3}$ ) ensembles [108]. These electrodes can be chemically inhomogeneous on nanoscale that causes uneven distribution of current load, as a result directly affecting their life cycle. Therefore it is crucial to understand the nature of Li migration and its insertion on nanoscale level by investigation of the corresponding particle morphology and processes occurring during (de)lithiation. As an actual system for energy storage the  $\text{LiFePO}_4$  battery nanoparticles have been investigated and spectroscopically imaged by soft X-ray ptychography.

The lithiation process, when  $\text{FePO}_4$  transforms to  $\text{LiFePO}_4$ , results in a change of the Fe oxidation state from  $\text{Fe}^{3+}$  to  $\text{Fe}^{2+}$ . A high spatially integrated reference spectra of the lithiated and delithiated batteries obtained at different energies across the Fe  $L_2$  and  $L_3$  absorption edges are shown in figure 5.1 a). As it is seen from the reference spectra these transformation causes a significant change, especially in the Fe  $L_3$  edge structure. The corresponding energy scans taken at the MAXYMUS STXM in figure 5.1 b) are of reduced quality due the instabilities in the energy scan accompanied with difficulties of the  $I_0$  monitoring. Nevertheless the images taken at 708.2 eV and 710.3 eV allows a clear separation of these two phases in correspondence with the particle structure, size and morphology.

The  $\text{LiFePO}_4$  nanoplates were produced and studied in collaboration with Department

of Materials Science and Engineering of Stanford University (USA). The extensive investigation of lithiation processes in these samples can be found in the following publications [109, 110, 111]. Till the recent time a significant limitation for studying these chemical reactions in the single-crystal particles was the narrow range of tools which provided sufficient spatial resolution and chemical sensitivity for the visualization at sub micrometer level. The first ptychography imaging of nano batteries have been performed at ALS (Berkeley, USA) and presented in papers [50, 110, 151].

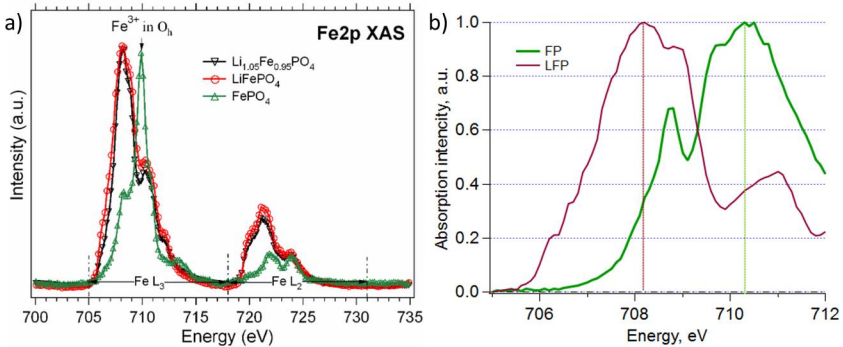


Figure 5.1: Absorption spectra of  $\text{LiFePO}_4$  nanoplates: a) absorption reference spectra of lithiated and delithiated areas of the battery. Adapted from [113]; b) the same spectra obtained at MAXYMUS on the  $\text{LiFePO}_4$  batteries over  $L_3$  absorption edge with peaks at 708.2 eV and 710.3 eV.

The STXM image of a typical nano platelet is shown in the figure 5.2 d)-f), it has around 1-2  $\mu\text{m}$  wide and 2-3  $\mu\text{m}$  long. The sample was scanned along Fe-edge for probing different oxidation states of Fe in charged and discharged phases. Ptychographic images, as well as STXM, show coexistence of two different oxidation phases  $\text{Fe}^{2+}$  and  $\text{Fe}^{3+}$  at the same time within one nanoplate. Optical density (OD) images a), b) and c) show that the lithiated area is located inside of the nanoplate and surrounded by the delithiated regions. The value of complex refractive index  $\beta$  of two phases differs for order of magnitude. For the same reason comparing images at different absorption edges we see that OD is much higher for the delithiated area. It provides significant contrast of the interface materials that makes this specimen a good test target for chemically sensitive high resolution ptychography.

The STXM images have obtained with FZP having  $\Delta r = 25$  nm with spatial resolution of about 30 nm, while ptychographic reconstructions have the real space pixel size of 11 nm at Fe absorption edge and 8 cm distance from sample to detector. Chemical contrast of the ptychographic images is estimated by the step width between two chemical phases which show sharp border at the neighboring regions. The width of the edge

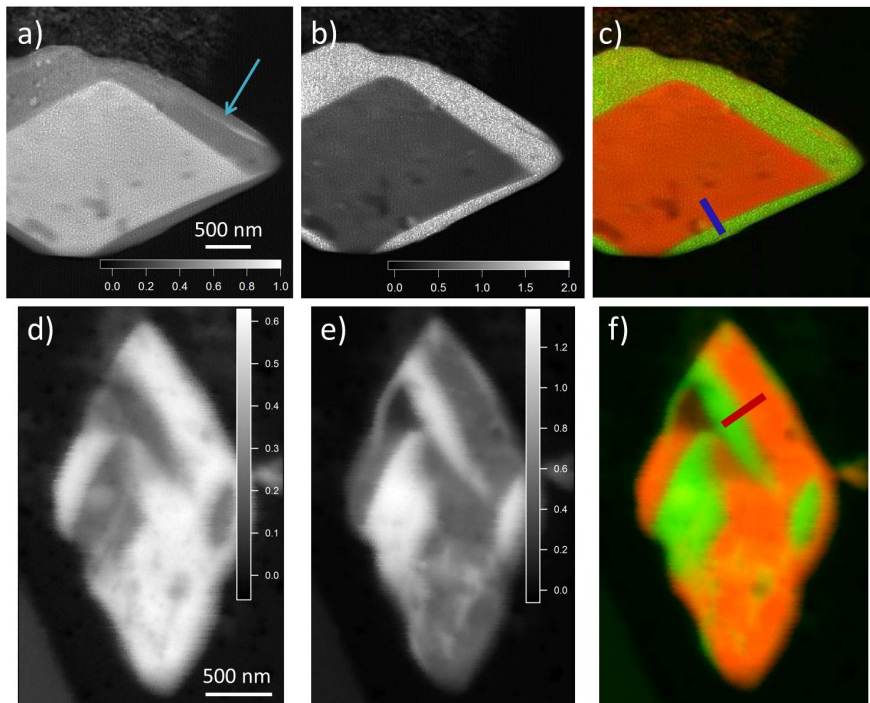


Figure 5.2: Comparison of STXM and ptychography imaging of chemical contrast in  $\text{LiFePO}_4$  nanoplates: a),b),c) OD images obtained by ptychography with a pixel size around 11.3 nm, d),e),f) OD STXM images obtained with 24 nm resolution focusing FZP with scanning step of 10 nm. Images a),d) and b),e) show  $\text{Fe}^{2+}$  and  $\text{Fe}^{3+}$  oxidation states, respectively, e) and h) correspond to overlap maps of two phases, where red is  $\text{Fe}^{2+}$  and green is  $\text{Fe}^{3+}$  phase.

is determined by the distance from 10% to 90% of intensity as it is seen in figure 5.3 b). The step width is 30.2 nm for ptychography and 59.7 nm for the STXM image that is about 2 times resolution improvement in the ptychographic image. The selected particles in the STXM and ptychography image sets are not the same and may have slightly different inclination relative to the beam direction. Therefore the measured profile values can not be used as an ultimate resolution evaluation giving just a general understanding of the resolution improvement.

The minor features, which would not be resolved at STXM images, are visible on the surface of the nanobatteries, e.g. cracks. It was shown in [50] that cracks occur along the longer side (c-axis) of the crystal due to lattice shrinkage along the shorter side (a-axis) during the transition of  $\text{LiFePO}_4$  to  $\text{FePO}_4$ . The thin crack marked with blue arrow

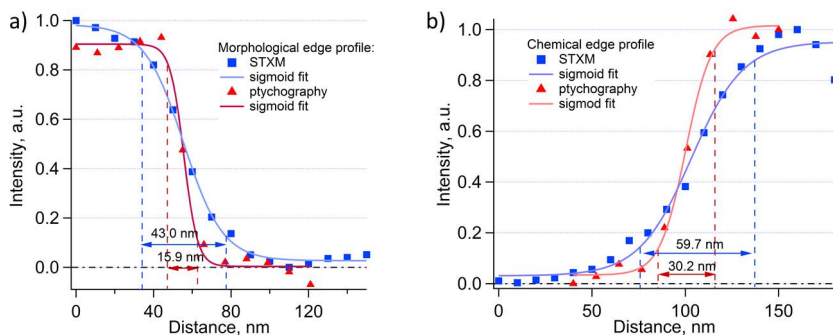


Figure 5.3: Line profiles of  $\text{LiFePO}_4$  nanoplates: a) line profile crossing the border of two different chemical phases, that showed 30.2 nm for ptychography and 59.7 nm for STXM image; b) line profile over morphological border with 15.9 nm and 43.0 nm step widths for ptychography and STXM, respectively. The step width was determined as a distance from 10% to 90% of intensity.

of about 23-50 nm in thickness is visible on the right edge of the nanoplate and reveals unreacted region below.

Resolution evaluation was done by measuring width of the step of the line profile going over the morphological edge of the particle from the substrate. Ptychography and STXM showed 15.9 nm and 43.0 nm step width, respectively, that corresponds to more than 2.7 times resolution improvement (figure 5.3 b). Therefore the half pitch resolution of ptychographic images is around 8 nm.

Pre-edge images were taken initially in order to get pure chemical contrast of the lithiated and delithiated regions by subtracting them from on-edge images. However pre-edge images were significantly blurred with some artifacts pronounced on the edges of the nanoplates. The observed artifacts are caused by the reduction of atomic scattering in the pre-edge region, where scattering factor  $f_2$  has value close to zero and  $f_1$  is negative. At the same time the presence of high scattering from morphological features, i.e. edges, produces disconformity of the scattering signal causing the problems in image reconstruction.

## 5.2 Rock varnish sample

Rock varnish is a black, in some cases red or brown layer with shiny surface that grows on slowly weathering rocks not depending on their lithology (figure 5.4 a, b). Similar rock varnishes have been observed in a wide variety of terrestrial environments and there have been quite a number of studies discussing the origin of these coatings. Both biological

and inorganic processes, as well as a combination of both, have been suggested.

The main chemical components of varnish are poorly crystallized Mn oxides, which are incorporated with layers of Fe oxides and clay minerals. Presumably the clay mineral fraction in varnish is formed by the atmospheric dust deposition. However the origin and precipitation of Mn are not yet fully understood. To conceive the genesis of varnish layer is of particular interest for specimens from arid deserts, because it would allow the study of climate changes on the timescale of the whole history of Earth. Therefore a specimen, labeled as CA14 JC-8, collected in Johnson Canyon of Death Valley (California, USA) was investigated using ptychographic imaging <sup>2</sup>.

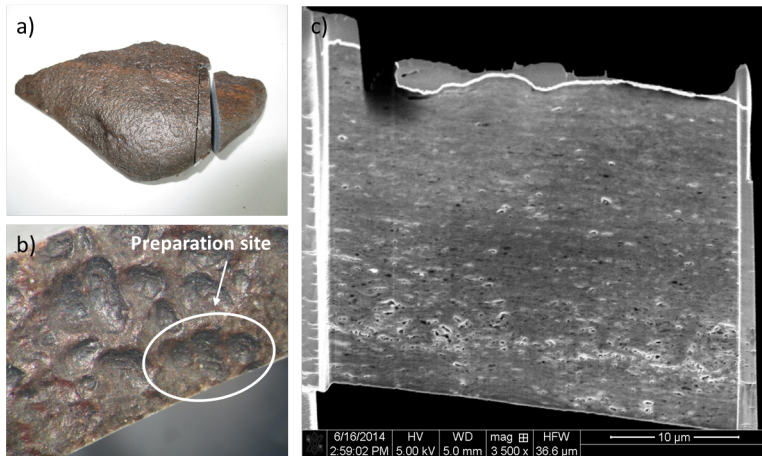


Figure 5.4: Preparation of the CA14 JC-8 rock varnish sample: a) cut of slice 0.5 cm thick made perpendicular to the varnish coating, b) example of a micro-basin chosen for FIB preparation, c) SEM image of FIB slice of the varnish sample.

Rock varnish has dense fine-grained layers and is formed on the atmosphere facing side. The side contacting with the soil was covered by an orange-red coating. Since the sample was taken from the ground a few to tens of centimeters of the sample consist of pebbles and small rocks which directly contacted with soil. In order to prepare thin slices for soft X-ray imaging and spectroscopy in transmission the sample was milled by FIB (Ga<sup>+</sup> ion beam) to sizes of about  $50 \times 30 \mu\text{m}$  and thicknesses of about 100-200 nm. The region containing thicker varnish, so called micro-basin that is a small depression on horizontal rock surfaces, was chosen for the cut and located by scanning electron microscopy (SEM) (figure 5.4 c). The main challenge in the sample slicing for

<sup>2</sup>The rock-varnish sample was provided by the Biogeochemistry Department, Max Planck Institute for Chemistry (Mainz, Germany).

STXM imaging was to cut the varnish strictly perpendicular to the direction of the layered structure. Even in case of insignificant inclination of the layers in respect to the X-ray beam direction the spectroscopic signal will not reveal the layers with different chemical compounds.

Previous study with conventional STXM presented in [114, 115] showed the presence of certain elements of interest, i.e. Fe, Mn, Ca, and C. The distribution of these elements in the sample has been recorded as images at discrete energies and combined in elemental maps. In this work we concentrate on the Mn and Fe content, because layers of these elements might reflect paleoclimate fluctuations. The main assumption is that Mn- layers represent wet climates and Fe rich layers dry climates [116].

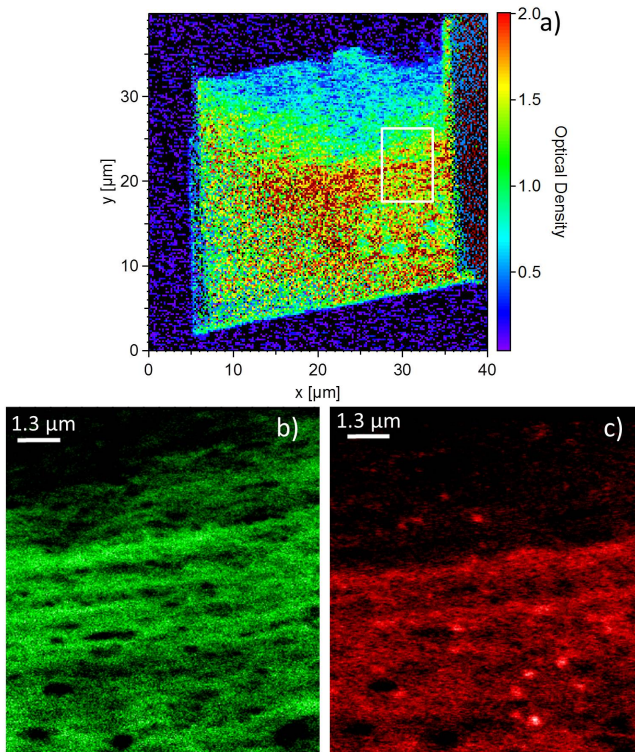


Figure 5.5: Element distribution maps obtained by scanning transmission X-ray microscopy: a) overview image of Mn map with white frame showing the region chosen for higher resolution imaging and presented on b) and c) ; b) Mn map; c) Fe map [114].

A femtosecond laser ablation-inductively coupled plasma-mass spectrometry (fs LA-

ICP-MS) with a spatial resolution of 10-40  $\mu\text{m}$  for the sample CA14 JC-8 is presented in paper [115] and provides determination of major, and in particular, trace element concentrations. Typically in the area close to the underlying rock Fe abundance is about 20% higher than Mn concentration. Closer to the varnish surface, the  $\text{Fe}_2\text{O}_3$  amount rises to 50% and the  $\text{MnO}_2$  concentration increases significantly to 25%. At the outer rim of the varnish,  $\text{MnO}_2$  and  $\text{Fe}_2\text{O}_3$  have approximately the same abundance, with high  $\text{Fe}_2\text{O}_3$  and  $\text{MnO}_2$  concentrations of up to 50%. The region in the middle of the varnish sample (around 12  $\mu\text{m}$  from the rim) displaying high amount of Mn (figure 5.5, a) was chosen for STXM element maps. The resolution of STXM images is 35 nm. Figure 5.5 b) and c) show alternating Mn- and Fe-rich layers, continuous and parallel to the host rock surface. From the Mn map we see that sample has 100-500 nm thick Mn-rich and Mn-poor layers. Fe map has a similar layered pattern but with additional more compact grains of few hundred nanometers in size. These grains refer to morphology of the varnish itself that showed the presence of cavities, which are homogeneously distributed inside the varnish. Fe-containing minerals were mapped in some of these cavities.

The presence of Mn can be explained by two mechanisms, abiotic and biotic, which both can be involved in Mn layer formation. The first suggestion is an abiotic mechanism, when Mn oxides are formed by chemical reduction and precipitation in rainwater with acidity  $\text{pH} \approx 5.7$  and reduction potential  $E_h \approx 0.8$  [117]. The second variant is a biotic mechanism when Mn reduction occurs due to biological realization by Mn reducing bacteria [118].

The presence of different oxides of Mn is a sign of the formation of different mineral phases or mineral compositions from the beginning of the varnish precipitation. Also they could appear as a result of redox reactions of thinner layers which had the same oxidation state in the beginning. In case of abiotic formation mechanism the presence of different phases can be explained by oxidation process from  $\text{Mn}^{2+}$  to  $\text{Mn}^{4+}$ . This process happens in two steps: initially Mn precipitates as an oxyhydroxide ( $\text{MnOOH}$ ) that secondly forms  $\text{Mn}^{4+}$  oxides, e.g.  $\text{MnO}_2$ . Pure  $\text{Mn}^{3+}$  minerals are unusual and mostly known as transition oxidation state.  $\text{Mn}^{3+}$  oxides can be present as oxyhydroxides which are formed also from oxidation of  $\text{Mn}^{2+}$  in the presence of abundant Fe oxyhydroxides, which are found in varnish.

### **Ptychography at rock varnish**

The main goal of a ptychographic study is to investigate different oxidation states in varnish samples that could potentially explain the formation mechanism of Mn layers. Naturally varnish has Mn of 2+, 3+, 4+ oxidation states. The X-ray absorption spectrum in figure 5.6 g) shows all three of them in the sample CA14 JC-8. Usually different oxides of Mn do not produce pure phases, instead they exist in a mix with other oxides in various ratios.

Ptychographic images were done with CCD camera placed downstream of the sample at the distance of 8 cm. The setup results in about 12.5 nm output pixel size at Mn absorption  $L_3$ -edges of different oxidation states 2+, 3+ and 4+ (642.6 eV, 643.4 eV, 645.8 eV), 11 nm at Fe  $L_3$ -edge (712.6 eV) and 5 nm at Al K-edge (1569 eV). Diffraction images at each scanning point were dynamically stacked for 100 ms. The strong scattering on the edges of layered structure provided high photon count rate at the high diffraction orders.

The chemical distributions of three oxides  $Mn^{4+}$ ,  $Mn^{3+}$  and  $Mn^{2+}$  are imaged in figure 5.6 a), b), c), and the image e) is an overlay of  $Mn^{2+}$  and  $Mn^{4+}$ . The ptychographic views on desert varnish sample showed that it has much finer structure that it was found in previous STXM studies. Few hundreds nm thick layers of Mn, which were observed on STXM images, exhibit thinner layers with thicknesses in a range of 18-20 nm, that is in agreement with a previously conducted energy filtered transmission electron microscopy (EFTEM) study which found layers of <20 nm [119].

Some layers possess much higher percentage of only one oxide, other areas have intermixed state without noticeable domination of one chemical phase over others. As it is seen on the  $Mn^{4+}$  and  $Mn^{3+}$  maps they have similar elemental distribution, that means these two oxides are incorporated in the same layers.  $Mn^{2+}$  map has significantly different pattern, that has less fine structures and distributed more homogenous over all the imaged area. It means that  $MnO_2$  minerals do not, or only in very small quantities, contain  $Mn^{2+}$ . The alternating layering of these oxides is the most visible close to the cavities. The alternating oxidation states of the individual Mn-rich layers contradict the idea of a simple leaching and re-precipitation process of layers along a sedimentary lamination, subsequent to a biogenic precipitation of concentric shells.

The ptychographic image in figure 5.6 f) shows overlay of  $Mn^{4+}$  and  $Fe^{3+}$  maps. Alike STXM images the  $Fe^{3+}$  map obtained with ptychography shows layered structure, which has wider layers in comparison with the  $Mn^{4+}$  map, and more compact inclusions evenly distributed in varnish. The layers of Fe belongs to the matrix which crystallized in-situ. The bigger visible spots of Fe on the images are Fe-rich dust grains, which were incorporated in the Mn- and Fe-rich layers from the precipitated mineral dust. Since Mn and Fe behave quite similar, they could be both included in the same mineral. Usually, Fe oxyhydroxides either incorporate Mn in the lattice structure by substitution, or they just absorb Mn from the sedimentary minerals.

Clay minerals, which comprise the bulk of the rock varnish (50-70%), are composed of Mg-Al-Si oxides and cemented by Fe-Mn layers. Therefore Al-rich silicate mineral is distributed fairly homogeneously in rock varnish. Aluminum absorption  $K_1$  edge has a peak at 1559.6 eV that results in 5 nm pixel size of the reconstructed ptychography image. Figure 5.7 shows the amplitude reconstruction with about 10 nm thin layering of Al. Such thin layering in varnish would not be resolved by normal STXM imaging. Aluminum fine layering confirms the sedimentary genesis of the rock varnish coatings.

Taking into account the general growth rate of rock varnish of 1-40  $\mu m$  per 1000 years

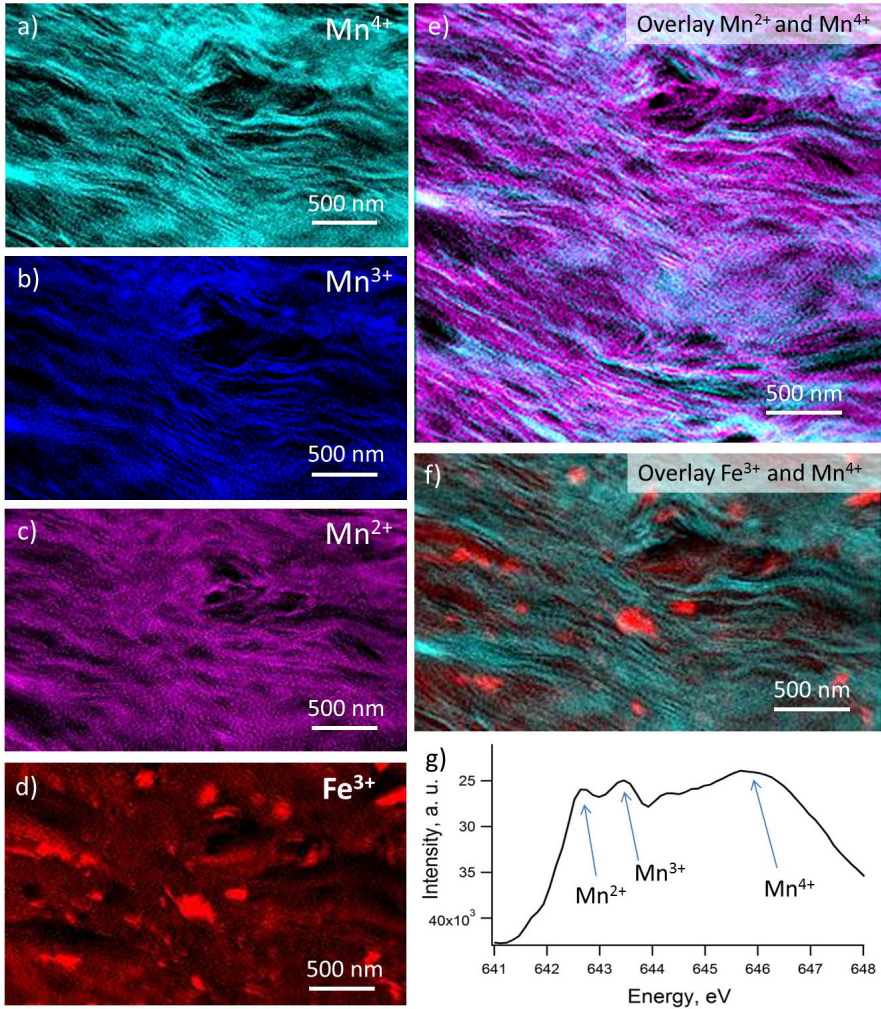


Figure 5.6: Element distribution in varnish sample CA14 JC-8 imaged by ptychography: a)  $Mn^{4+}$  map; b)  $Mn^{3+}$  map; c)  $Mn^{2+}$  map; d)  $Fe^{3+}$  map; e) overlay of oxide maps of  $Mn^{4+}$  and  $Mn^{2+}$ ; f) overlay of  $Mn^{4+}$  and  $Fe^{3+}$ ; g) absorption spectrum of Mn.

[120] with layers representing a continuous environmental record of surrounding area [121] time span of separate layers are assumed to be in a range of 0.5-18 years. This provides a paleoclimate record with a high temporal resolution which can be compared with

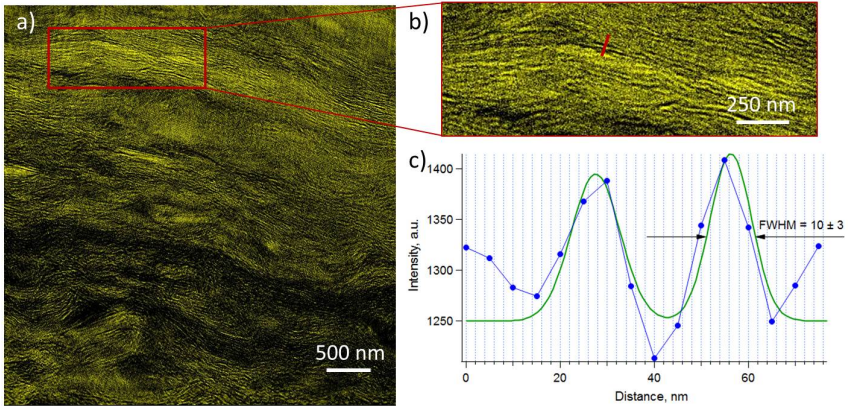


Figure 5.7: a) Al map of varnish sample obtained by ptychography with 5 nm pixel size; b) magnification of the area from the image a); c) profile along the red line in image b) fitted with double Gauss curve. FWHM of the peak on the line profile showed that layers have around 10.2 nm in thickness.

such paleoclimate records as speleothems, lake sediments, tree rings, or ice core records, which result in annual or even seasonal temporal resolution [122]. However the unique information for desert environment obtained from varnish by high resolution ptychographic studies can not be found in none of the above materials. Sub-10 nm ptychographic resolution is able to provide insight into the analysis of these samples to track paleoclimate changes with high temporal resolution.

### 5.3 Magnetic ptychography at domain labyrinth structure

Magnetic labyrinth domains were used as a test sample to evaluate ptychographic imaging of the specimens with pure magnetic contrast. The formation of magnetic labyrinth domains in films is caused by the interplay of exchange interaction (short-ranged), dipole-dipole interaction (long-ranged), perpendicular magnetic anisotropy (PMA) and DMI. If sufficiently large external magnetic field is applied it will overcome anisotropy energy and magnetization of all domains will be oriented in the direction of easy axis, which are turned in the direction of the applied field. Magnetic labyrinth structures have been used as a test sample for holography [63] as well as for ptychography [94] magnetic imaging, with the reported magnetic resolution up to 10 nm of the domain walls width of 10-15 nm.

A Ta(3)/Pd(3)/[Co(0.5)/Pd(0.8)]*n*/Pd(1.2) multilayer (see figure 5.8 c) was deposited

by magnetron sputtering with thicknesses marked in round brackets in nm, and the number of layer repetition  $n=30$ <sup>3</sup>. A 100 nm thick SiN window was used as a substrate for multilayer with additional Pd and Ta layers as buffer and protective layers. In STXM images the thin film sample showed strong out-of-plane magnetization with formation of magnetic labyrinth structure having about 100 nm wide domains at zero bias field.

Ptychography measurements were performed at the Co  $L_3$  resonant edge, 853 eV, with the use of circular polarized light. The CCD detector was placed 8 cm from the sample position yielding 9.8 nm pixel size in real space image. The magnetic domain sample with 15 nm total thickness of the Co layers and strong out-of-plane magnetization showed promising results even with the use of low dwell time of 50 ms per scanning frame. Magnetization of the domains is either parallel or antiparallel to the beam direction that corresponded to bright or dark contrast in the amplitude image shown in figure 5.8 a).

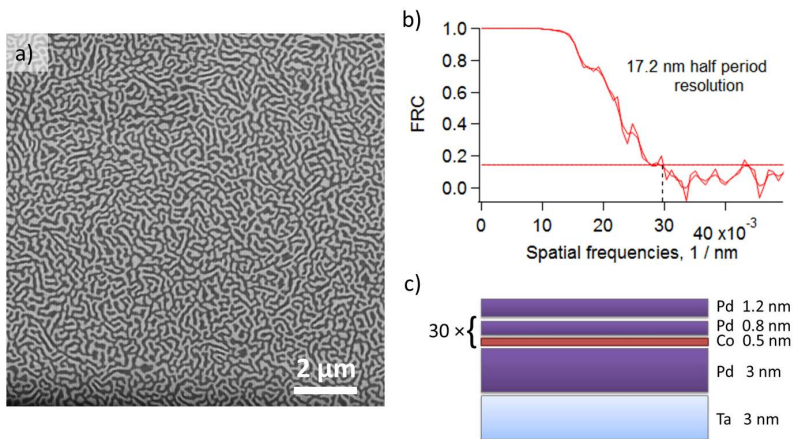


Figure 5.8: Ptychographic imaging of magnetic labyrinth domain structure: a) amplitude image of a  $10 \times 10 \mu\text{m}$  region; b) Fourier ring correlation (FRC) of two independent images of magnetic domains resulting in 17.2 nm half period resolution; c) multilayer structure of Ta/Pd/[Co/Pd] $n$ /Pd sample.

FRC was calculated for resolution estimation using two independent images of the same region, which were aligned with subpixel precision [123]. This approach helps to differentiate real features that are resolved in both individual images from noise and artifacts randomly appearing in the reconstructions. The FRC resolution of ptychography images is 17.2 nm half period using 1/7 threshold as it is shown in the figure 5.8 b), with domain wall width in a range of 30-40 nm estimated for multilayered Co/Pd samples

<sup>3</sup>The sample was provided by the group of Prof. S.Eisebitt TU Berlin

[124]. The step width of line profile over the edge of domain resulted in 28-30 nm.

Figure 5.9 shows phase and amplitude images depending on photon energy values with regard to  $L_3$  Co edge. The magnetic contrast at the amplitude images has a maximum directly on the peak of the  $L_3$  edge as expected. The phase contrast images however demonstrate higher magnetic contrast on the pre-edge with contrast reversal right after the resonance absorption peak. Figure 5.10 a) is a graph representation of phase and amplitude magnetic contrast obtained from the same domain in dependance on photon energy. The pre- and post-edge of absorption ptychographic reconstructions suffer from the contrast drop, artifacts and in some cases reconstruction failure due to lack of scattering signal. That is observed in the corresponding curve points, marked by brackets, which are quite deviate from the smooth curve propagation.

The obtained curves are proportional to the real and imaginary parts  $f'_m$  and  $f''_m$  of magnetization direction depended scattering factor and correspond to  $\beta_m$  and  $\delta_m$  of the optical constant for magnetically saturated Co. At the peak of the  $L_3$  edge the scattering contrast is highly absorptive, the real dispersive factor is close to zero. In this case the total magnetic scattering is mostly determined by the forward scattering cross section that corresponds to magnetic absorption. Non-resonant magnetic contrast from Co and absorption from SiN substrate, Ta and Pd layers contribute to the background attenuation.

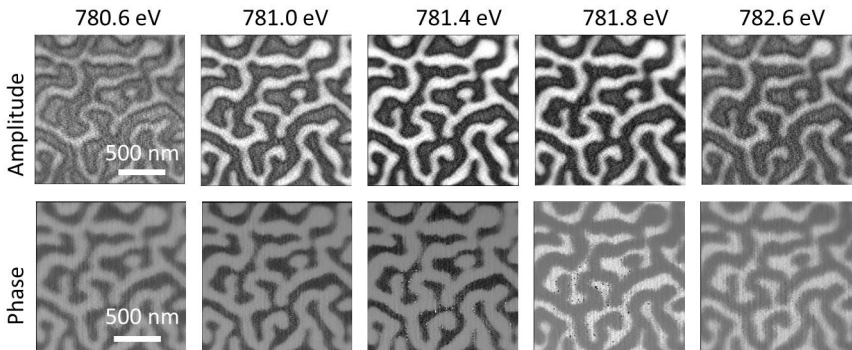


Figure 5.9: Phase and amplitude images of the reconstructed ptychographic images obtained using left circular polarized X-ray light as a function of energy across Co  $L_3$  edge (781.4 eV).

Figure 5.10 b) shows the curves of the ptychographic measurement of the phase signal (black line) and reference spectrum calculated from the amplitude ptychographic data using Kramers-Kronig relations (red line). Although both stay in agreement the measured phase is asymmetric around x-axis and shifted up in comparison with calculated one.

The possibility to measure both helicities allows to get pure magnetic contrast eliminating background contribution. XMCD contrast was calculated as a difference between

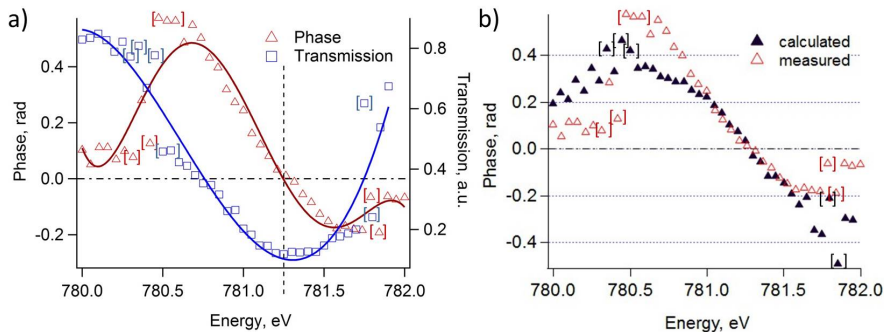


Figure 5.10: The data representation of ptychographic contrast measured at magnetic labyrinth sample in dependance on X-ray energy around Co absorption edge: a) amplitude and phase data obtained by ptychographic imaging for the same domain area; b) phase data measured with ptychography and calculated spectrum calculated with Kramers-Kronig relations.

images obtained with left- and right circular polarized light,  $I^-$  and  $I^+$ , normalized by their sum signal:

$$I_{XMCD} = \frac{I^- - I^+}{I^- + I^+}. \quad (5.1)$$

The resulting XMCD at the absorption peak at Co  $L_3$  edge is 0.51.

## 5.4 Conclusion

It has been shown that ptychographic images with high morphological and chemical diversity showed significant resolution improvement compared to STXM. The potential have been demonstrated on two target studies:

1. The phase distribution in the (de)lithiated nanoplates provides a contrast mechanism for different Fe oxidation states with much higher sensitivity that is not available in STXM. The resolution of ptychographic reconstructions of morphological features was 2.7 times and chemical 2 times higher than corresponding STXM image resolution. Ptychography images revealed structural details, like few tens of nm wide cracks, in the nanoplate crystal that could be a valuable information for understanding of material wearing during  $\text{LiFePO}_4 - \text{FePO}_4$  transition.
2. Chemical distribution of thin altering layers of Mn, Fe and Al in desert rock varnish sample was studied using ptychography. Mn with different oxidation states, which

are naturally occur in varnish, were found to form 18-20 nm thick layers. The different oxidation states of Mn have not been imaged before with sub-100 nm resolution. Due to capturing high spatial frequencies in reciprocal space ptychographic images provide higher tonal resolution of alternating varnish layers than STXM imaging. It makes ptychographic X-ray imaging a unique method for gathering oxidation state specific information at such small scales. The presence of 10 nm thick Al layers allows to assume that Mn forms layers with the same thickness or below. That leaves a room for further high resolution imaging studies of rock-varnish specimens.

First magnetic ptychography at MAXYMUS was done using multilayer structure exhibiting magnetic labyrinth pattern with 100 nm wide domains. Phase and amplitude images have been obtained in dependence on the energy value scanned around Co absorption edge and showed corresponding curves proportional to real and imaginary parts of magnetic scattering factor  $f'_m$  and  $f''_m$ . The flip of the domain color in the phase images corresponds to the change of sign of the real part of magnetic scattering factor. Even without sharp morphological or chemical edges in the deposited thin film the magnetic contrast is big enough to result in reliable and high quality image reconstruction with 9.8 nm pixel size. The obtained information allows direct estimation of scattering factors, charge and pure magnetic, that gives a throughput into fundamental studies of the investigated materials

## Chapter 6

# Ptychographic imaging of skyrmions

In this chapter high-resolved ptychographic imaging was performed on 2 types of typical room temperature skyrmions systems consisting of Ta/CoFeB(wedge)/MgO, Pt/CoFeB(0.6 nm)/MgO and Pd/CoFeB(0.6 nm)/MgO multilayers. Additionally careful magnetization characterization by SQUID have been performed on the same samples measured at the MAXYMUS. On the basis of the domain-spacing model DMI values have been deduced [125]. Furthermore an overview of the skyrmionic systems in terms of their applicability in real data storage devices have been performed.

### 6.1 Basics of skyrmions

Magnetic skyrmions are quasi-particles with “vortex-like” configuration which were theoretically predicted to exist by Tony Skyrme in 1962 [126]. Skyrmions can be defined as small vortex patterns of spins, which have the center spins oriented anti-parallel to the spins in the surrounding magnetization direction as it is shown in figure 6.1. Depending on the progression of the spin rotation two types of skyrmions are defined: Bloch (spiral) and Néel (hedgehog). Bloch skyrmions have spin orientation within DW and spins in Néel skyrmions point perpendicular to DW (figure 6.1).

Theoretically skyrmions are topologically protected structures that provides high physical stability, so the skyrmion state can be an energetically favored system condition. The stability of skyrmions is provided by the interaction of exchange energy, magneto-static energy and bulk or interfacial Dzyaloshinskii Moriya interaction (DMI) [128, 129]. The bulk DMI arises from the spin-orbit coupling occurring in the points of broken crystal in-

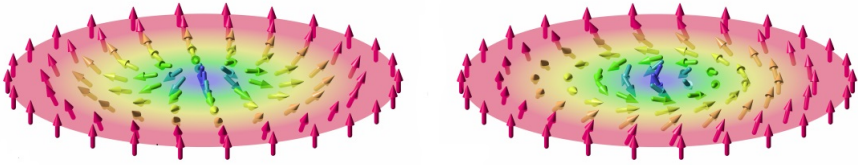


Figure 6.1: Two types of 2-dimensional skyrmions: Néel skyrmion (on the left) and Bloch skyrmion (on the right). Magnetization direction rotates by  $2\pi$  propagating from the edges to the center of the skyrmion. Reproduced from [127].

version symmetry. The first skyrmions have been experimentally observed in bulk samples such as MnSi [130] at low temperatures and FeGe close to RT [131].

The interfacial DMI effect is observed on the interfaces of multilayers [132, 133], when magnetic material is coupled with a nonmagnetic 4d or 5d heavy metal as shown in figure 6.2. In this case DMI is induced due to the influence of the strongly Z dependent spin-orbit interaction at the interface. In monoatomic layers, as Co or Fe (1 ML)/Ir(111), the combination of large DMI due to inversion symmetry breaking and strong spin orbit coupling leads to the formation of skyrmions of only few nanometer size at very low temperatures  $\approx 10$  K as described in [134].

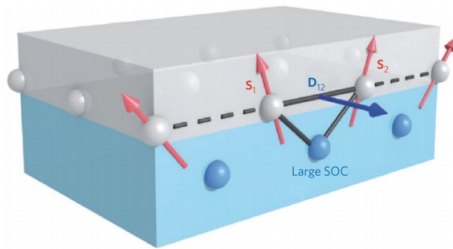


Figure 6.2: Principle of interfacial DMI effect: spins in the ferromagnetic (gray, upper) layer couple to each other through overlap of their wave functions with an atom with large spin-orbit coupling (blue, lower layer). Adapted from [135]

Room temperature skyrmions have been proven to exist in various multilayer structures [125, 133, 136]. A prerequisite for the appearance of skyrmions is the small thickness of magnetic layer, below 1.5 nm that corresponds to about 6 monolayers. The majority of the investigated specimens has a thickness of 0.6 to 1 nm. In these materials the magnetic domains are often formed worm-like structures with OOP magnetization at zero field. By increasing an external OOP field, magnetic skyrmions can be formed due to the

presence of DMI.

### 6.1.1 Methods to determine DMI

DMI values in multilayers are estimated experimentally using various methods based on domain wall studies. Here the basic experimental methods for DMI estimation are described.

- *Brillouin light scattering (BLS)* [138, 139]. The BLS method allows a direct estimation of DMI constant by measuring the frequency difference between counter-propagating Damon-Eshbach (DE) spin waves induced by DMI. The BLS geometry is shown in figure 6.3, where magnetic field is applied perpendicular to the incidence plane that allows spin waves propagation in in-plane direction. S-polarized laser light is incident on the sample and the p-polarized component of the back-scattered light is collected. The spin waves propagate in the plane of incidence with momentum  $|k| = 4\pi \sin\theta/\lambda$ , where  $\theta$  is an incident angle of laser beam and  $\lambda$  its wavelength. The Stokes  $f_S$  and anti-Stokes  $f_{AS}$  modes, which correspond to negative and positive frequency relative to that of the incident light, respectively, are then determined from the BLS spectra.

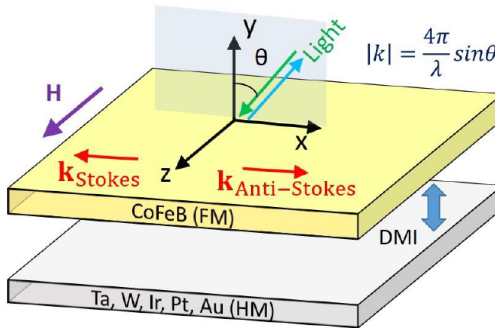


Figure 6.3: BLS in back-scattering geometry where the inelastically scattered light is collected in the direction of the incident p-polarized light. Adapted from [138].

In order to quantify the constant  $D$  the spectra over a set of various angles of the incident beam is measured and subtracted, that is resulted in a simplified formula:

$$\Delta f = f_S - f_{AS} = \frac{2\gamma}{\pi M_S} Dk, \quad (6.1)$$

where  $\gamma$  is the gyromagnetic ratio.

Another approach for DMI measurements based on DE spin waves was suggested in [140]. The spin waves have been excited by a microwave antenna in the shape of a coplanar waveguide with wave vector  $\vec{k}$  propagating on either side of the antenna. The dynamic of the spin wave propagation was imaged by time-resolved Kerr microscopy that allowed to detect wave numbers a factor of 3 smaller than the thermally activated spin waves studied by BLS [140].

The advantage of the method is that only the value of  $M_s$  and the gyromagnetic ratio  $\gamma$  have to be known.

- *Creep motion of domain walls.* In this method for DMI calculation the asymmetric domain wall creep velocity along the direction of an applied in-plane field is evaluated [141]. The in-plane field component breaks the rotational symmetry caused by the DMI effective field ( $H_{DMI}$ ) that facilitates the anisotropic domain expansion. The behavior of the domain movement, its direction and speed, allows to determine chirality of DWs and extract the  $H_{DMI}$  using the creep law fitting [141, 142]. The DMI constant  $D$  is extracted by using the following equation:

$$D = \mu_0 M_s H_{DMI} \Delta, \quad (6.2)$$

where  $\Delta$  is domain wall width.

- *Domain spacing model.* The dependence of domain widths with bright and dark contrast in multilayer film imaged by STXM or ptychography allows to calculate domain wall surface energy  $\sigma_{DW}$  using domain spacing model described in [125]. Knowing the thickness of the film,  $t$ , total period of domains with opposite magnetization orientation at low field,  $d$ , and saturation magnetization,  $M_s$ ,  $\sigma_{DW}$  is derived as following:

$$\frac{\sigma_{DW}}{\mu_0 M_s^2 t} = \frac{d^2}{t^2} \sum_{n=1_{odd}}^{\infty} \frac{1}{\pi n^3} \left[ 1 - \left( 1 + \frac{2\pi(2n-1)t}{d} \right) \exp\left( -\frac{2\pi(2n-1)t}{d} \right) \right], \quad (6.3)$$

where  $\mu_0$  is a vacuum permeability. Knowing the exchange stiffness,  $A$ , and the effective uniaxial anisotropy constant,  $K_{eff}$ , the DMI value is calculated using equation  $\sigma_{DW} = 4\sqrt{AK_{eff} - \pi|D|}$ .

The main drawback of the domain spacing model is a necessity of reliable estimation of  $M_s$ ,  $K_{eff}$  and especially  $A$  of the actual sample. In the corresponding publications these values are sometimes partially taken from the literature bulk values. As shown in the following chapters a careful magnetization measurement of magnetic properties is required for accurate DMI estimation. For the ultra thin magnetic layers, less than 1 nm,

any dead layer occurring at the interfaces reduces the effective thickness. Furthermore it has been proven that the Curie temperature  $T_C$  drops dramatically for magnetic layers below 1 nm [143, 144]. Therefore the exchange constant  $A$  may be significantly smaller than assumed bulk values of 10-20 pJ/m. On the other hand, due to the broken symmetry at the interface an increase of the surface magnetic moment can occur. All this mechanism are strongly dependent on the local morphology, which can vary dramatically due to instabilities and trapping of domain walls and skyrmions itself [145]. Therefore the understanding of a microscopic picture of nano magnetism in this systems can be rather complex task.

### 6.1.2 Skyrmion imaging

The imaging of skyrmions can be performed by a wide range of magnetic sensitive techniques. With the use of magnetic force microscopy or spin-polarized scanning tunneling microscopy these features can be imaged with a nearly atomic resolution. Electron based techniques, as Lorentz TEM and electron holography, provide about 10 nm resolution [146, 147]. Few nm big magnetic structures can be investigated by spin-resolved low-energy electron emission microscopy (SPLEEM) [148] and spin polarized STM [149, 150]. Larger skyrmions with several 100 nm of diameter are accessible by MOKE microscopy [151, 152, 153]. Soft X-ray imaging methods, like PEEM, TXM, STXM and X-ray holography, are successfully utilized providing magnetic contrast using XMCD effect providing spatial resolution of 20-30 nm [125, 133, 154, 155, 156]. X-ray ptychographic imaging, as reported in this chapter, was never utilized before for imaging of skyrmions with potential resolution below 20 nm. As a result the highly accurate visualization of sub-100 nm skyrmions in a wide field of view have been performed.

## 6.2 Ptychography on skyrmion systems

In this work the magnetization of skyrmionic structures in two typical multilayer systems have been studied. DMI constants have been estimated using the domain spacing model. For the accurate estimation of main magnetic parameters of multilayers ( $M_s$ ,  $K_{eff}$  and  $A$ ) SQUID studies have been performed on the same sample systems that have been used for X-ray ptychography. The details of magnetization parameters calculation are presented in Appendix D.

### 6.2.1 CoFeB based multilayers with different heavy metals: Pd and Pt

The thin films [Pd(5)/CoFeB(0.6)/MgO(2)]15 and [Pt(5)/CoFeB(0.6)/MgO(2)]15 (see figure 6.4) were deposited by magnetron sputtering on SiN substrate with thickness of single

CoFeB layer of 0.6 nm and 15 times stack repetition<sup>4</sup>. The multilayer was formed as a thin wire, or track, 2  $\mu\text{m}$  wide and 5  $\mu\text{m}$  long contacted by two gold striplines. The track was formed with electron beam lithography and lift-off process. The reason for nano structuring of the system was the intent to perform dynamic studies.

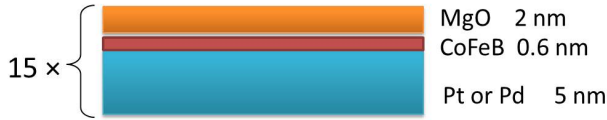


Figure 6.4: Multilayer structure of Pd/CoFeB/MgO and Pt/CoFeB/MgO samples.

### Magnetization measurements

Due to the geometrical constriction of multilayer race track the amount of magnetic material was rather low that complicated measurements of sample magnetization. An estimation of these values (table 6.1) was performed using the IP and OOP  $M(H)$  curves obtained by SQUID shown in figure 6.5. The hysteresis indicates a saturation magnetization for both ferromagnetic components about 0.5 MA/m, which amounts to  $\approx 1/3$  of the CoFeB bulk value. These strong reduction will be discussed in context of the next chapter. The  $K$  values have significant difference for two compositions: 0.026 MJ/m<sup>3</sup> for Pt and 0.015 MJ/m<sup>3</sup> for Pd based samples.

Parameters	Pd/CoFeB/MgO	Pt/CoFeB/MgO
Total film thickness, $t$	$15 \times 7.6$ nm	$15 \times 7.6$ nm
Total thickness of CoFeB, $t_m$	$15 \times 0.6$ nm	$15 \times 0.6$ nm
Total periodicity of domains, $d$	$300 \pm 50$ nm	$600 \pm 100$ nm
Saturation magnetization, $M_s$	0.53 MA/m	0.59 MA/m
Effective anisotropy, $K_{eff}$	0.015 MJ/m <sup>3</sup>	0.026 MJ/m <sup>3</sup>
Exchange stiffness, $A$	1.37 pJ/m	1.11 pJ/m
DMI constant, $ D $	0.01 mJ/m <sup>2</sup>	0.21 mJ/m <sup>2</sup>

Table 6.1: Magnetic parameters of skyrmion multilayer samples.

### Ptychographic imaging

The ptychographic imaging was done at Co  $L_3$  absorption edge with the distance between CCD and sample of 9 cm, that resulted in 11.3 nm pixel size in real space. STXM images

<sup>4</sup>The sample was provided by the group of Prof. Kläui, University of Mainz

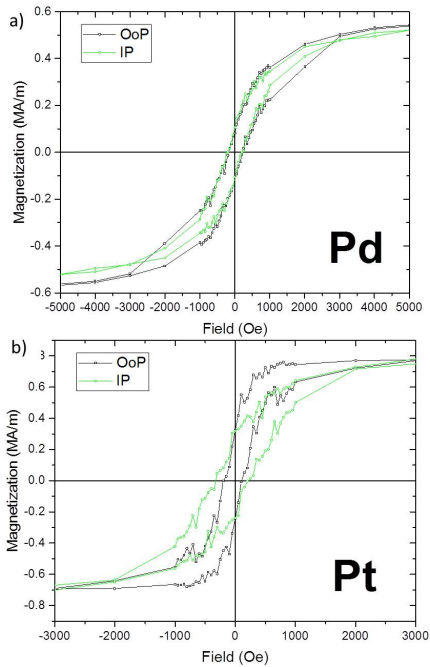


Figure 6.5: IP and OOP hysteresis loops for a) Pd/CoFeB/MgO and b) Pt/CoFeB/MgO multilayer structures.

also were performed using high resolution FZP with estimated resolution of 22 nm in order to get a reference data set. Before imaging samples were saturated at 240 mT OOP magnetic field, which was then reduced to 0 mT in order to get labyrinth magnetic domain state. Afterward the magnetic field was continuously decreasing till the condition when circular shaped small magnetic domains, or skyrmions, were observed. XMCD images (figure 6.6) were obtained by scanning the sample using polarized X-rays with left (-) and right (+) helicities.

Comparing images of two multilayers presented in figure 6.6 we see that Pt based sample has much wider domains packed less dense in comparison to the Pd sample. Resulting skyrmion sizes are in a range of  $193 \pm 7$  nm at the Pt sample and  $97 \pm 3$  nm at the Pd sample, a factor of two difference. The skyrmions do not form lattice and appear in isolated state. As it is seen the Pt based sample approaches much faster to the skyrmion state with a field sweep and possesses twice bigger diameters of magnetic structures. Com-

plete saturation state was observed at -50 mT external field. The Pd based sample showed higher stability during magnetic field swap with the first skyrmion formation at -60 mT. Going further with the field results in pure skyrmion state at -90 mT till the full saturation at about -100 mT.

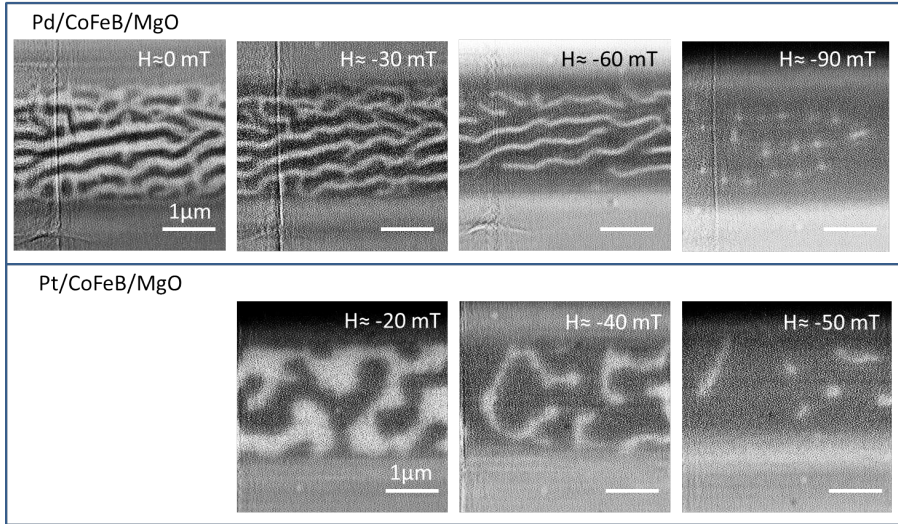


Figure 6.6: XMCD ptychographic images of domains evolution of Pd/CoFeB/MgO and Pt/CoFeB/MgO multilayers in applied external OOP magnetic field.

In order to calculate DMI values the domain spacing model is applied using the widths of the imaged domains at 0 bias field [157].

The Pt/CoFeB/MgO multilayer has higher values of DMI constant  $|D|$  and anisotropy constant  $K_{eff}$ , which correspond to the twice bigger domain width and low skyrmion density in comparison with the Pd/CoFeB/MgO multilayer. The lower value for  $K_{eff}$  of Pd/CoFeB/MgO multilayer is indeed corresponds to the higher density of the skyrmions. Skyrmions with lower  $K_{eff}$  are stable over a broader range of applied OOP fields as it is proved by experimental data. Pt/CoFeB/MgO sample has much higher DMI value twice bigger skyrmions and domains are observed, while Pd/CoFeB/MgO multilayer has narrower domains exhibiting lower value of DMI. It implies that isolated skyrmions are bigger in the systems with higher DMI values as it is discussed in [158].

## 6.2.2 Skyrmion samples with different thickness of ferromagnetic layer

In order to understand the influence of ferromagnetic layer on the properties of skyrmion formation in the HM/FM/MgO systems a set of multilayers with different CoFeB layer thickness have been produced and studied in collaboration with the group of Prof. Dr. Guoqiang Yu from Beijing National Laboratory for Condensed Matter Physics. The multilayer stacks Ta(5)/[CoFeB(0.8-1.4 nm wedge)/MgO(2)/Ta(3)]15 (numbers are thickness of layer in nm) was formed by magnetron sputtering on a thermally oxidized SiN substrate that had 5 cm in length. The film was annealed at 200°C for 30 minutes to enhance its PMA. The CoFeB layer was deposited as a wedge shape on the substrate, that gave a single interlayer thickness variation from 0.8 till 1.4 nm across the stack of 15 repetitions as it is seen in figure 6.7. Dividing this continuous film into 7 smaller pieces we got a set of magnetic samples with different thicknesses of ferromagnetic layer. Samples have been numerated from 1 to 7 for the corresponding total ferromagnetic wedge thickness from 11.7 to 21.7 nm, respectively.

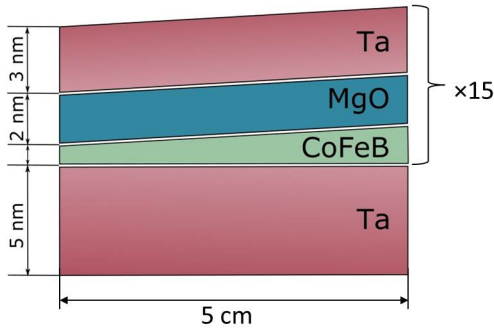


Figure 6.7: The sketch of sample stack of Ta/CoFeB/MgO/Ta with wedged CoFeB layer with thickness variation from 0.8 nm up to 1.4 nm.

### Magnetization measurements

The OOP saturation field values gradually go down with the decrease of ferromagnetic layer thickness from about  $\pm 150$  mT down to  $\pm 70$  mT as shown in figure 6.8 a). Samples 4 and 5 have the highest coercivity, while samples 1, 2, and 7 have almost zero value of coercive field. The corresponding IP hysteresis loops and calculated  $K_{eff}$  values for samples with different CoFeB thicknesses are shown in figure 6.8 b) and c), respectively.

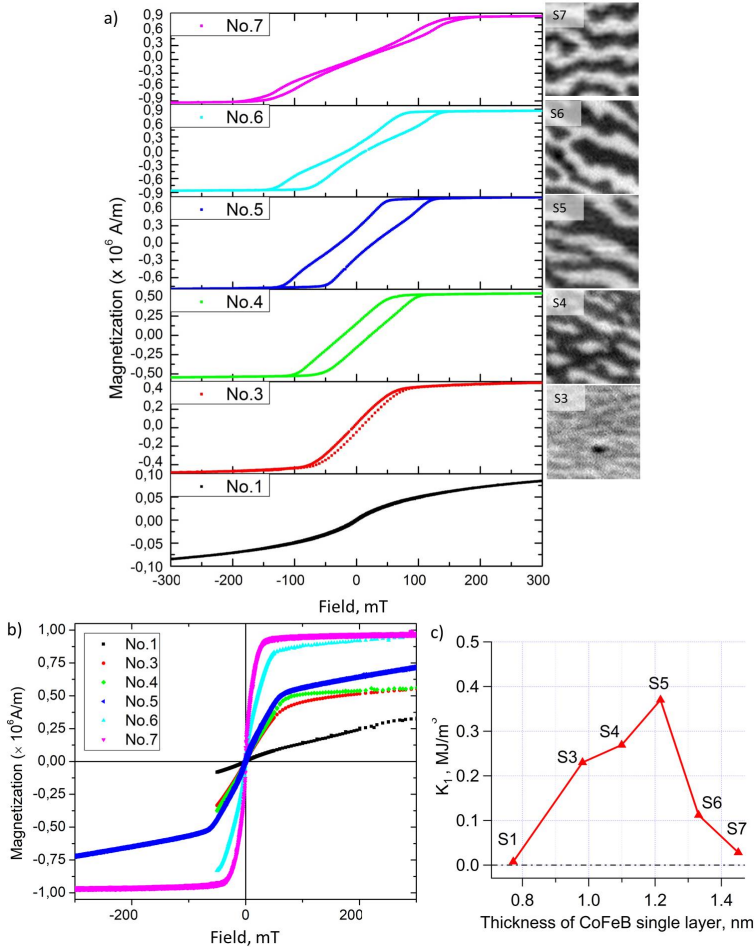


Figure 6.8: Magnetization of multilayer samples with different thicknesses of ferromagnetic layer numerated from 1 to 7 for the corresponding total ferromagnetic wedge thickness from 11.7 to 21.7 nm, respectively: a) hysteresis loops of out-of-plane with STXM images of the corresponding samples taken at zero magnetic field. The images of the thinnest sample 1 and 2 showed no contrast, samples starting from 3 to 7 have labyrinth domain pattern. The size of STXM images is  $1 \mu\text{m} \times 1 \mu\text{m}$ ; b) in-plane magnetization measured by SQUID; c) calculated  $K_1$  from IP and OOP hysteresis loops for samples with different CoFeB thicknesses.

### X-ray imaging

Pre-characterization was done with STXM using circular polarized X-ray light at Fe  $L_{3-}$  edge using FZP ( $\Delta r = 18$  nm) with estimated resolution of  $\approx 22$  nm. The absorption signal shows magnetic contrast at the samples 3-7, which correspond to 14.7 - 21.7 nm CoFeB total thickness (1.0-1.4 nm single layer thickness), and no contrast at thinner samples 1 and 2 with CoFeB 11.7 and 13.2 nm thick. The images have dark and light areas corresponding to up or down magnetization direction in respect to the film surface as it is shown in figure 6.8 a). The shape and the distribution of magnetic structures in the domain state are not the same for different samples. The thickest sample 7 possesses higher curvature of the domains 100-125 nm wide looking as a maze pattern. In comparison, the specimens 4, 5 and 6 have straighter structures with higher irregularity of the domains shape and more diverse width of magnetic domains. For example, sample 6 shows domains width variation from 95 nm up to 165 nm. The thinnest imaged sample 3 has significantly reduced contrast with densely packed 50-60 nm wide domains.

With the use of ptychographic imaging the samples were initially examined in the domain state in order to evaluate the amount of magnetic contrast depending on the thickness of the ferromagnetic layer (figure 6.9). The magnetic domains were clearly visible only at samples 5, 6 and 7 which correspond to 18.2 nm, 20.0 nm and 21.7 nm CoFeB thickness (with 1.2, 1.3 and 1.4 nm single layer thickness), respectively.

A directional tilt of magnetic domains observed on the images at zero OOP field possibly originates from the interfacial stress induced by multiple layer stacking over the initially large sample area of few cm. Beside the magnetic structure some inhomogeneities in the deposited multilayer are visible, which are possibly related to chemical inclusions and impurities.

Using ptychography images it is possible to estimate the width of domain walls by measuring line profiles perpendicular to domain propagation. The width of  $180^\circ$  DW can be calculated as  $\Delta = \pi \sqrt{A/K_{eff}}$ , where  $A$  is exchange stiffness, taken to be  $A=4.65$  pJ/m, and  $K_{eff}=0.028$  MJ/m<sup>3</sup>. The DW width then is about 40.3 nm wide. Comparison of the magnetic domain wall width imaged by STXM and ptychography is presented in figure 6.10. Ptychographic image resulted in DW width of  $40.6 \pm 4.8$  nm, while DW width imaged by STXM was in a range of  $63.3 \pm 6.6$  nm. The ptychographic DW width estimation is the same as a calculated one with value variation within 1 pixel. The reduced resolution of the edge profile at STXM image could happen due to broadening of focus spot because of the FZP chromatic aberrations or insufficient coherence of X-ray light.

### Size of the skyrmions

In order to get to the skyrmion state each sample was initially saturated at positive out-of-plane magnetic field (+240 mT). The change of the external magnetic field to smaller values results in increase of the domains with dark contrast, i.e. the area with the bright

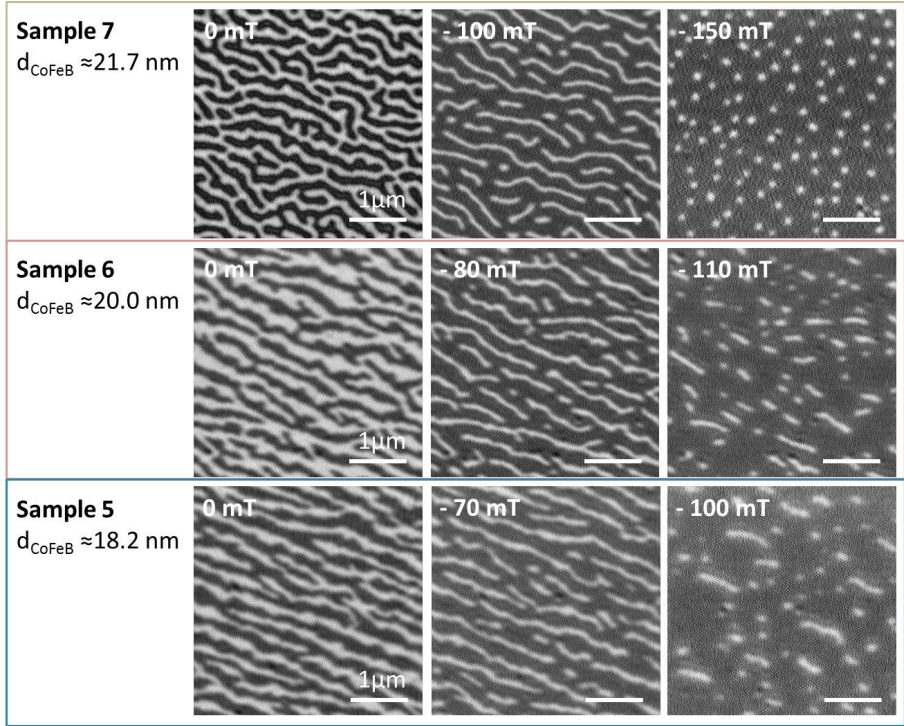


Figure 6.9: Ptychographic images of sample 7 with thickness of CoFeB  $d_{CoFeB} = 1.4 \times 15$  nm, sample 6 with  $d_{CoFeB} = 1.3 \times 15$  nm and sample 5  $d_{CoFeB} = 1.2 \times 15$  nm demonstrate the evolution of magnetic domains for different OOP magnetic field values.

contrast decreases. At some point of the field sweep skyrmions start to appear propagating from the mixed state, where skyrmions and extended magnetic domains are observed, to the pure skyrmion state (figure 6.9). With a further increase of field the skyrmions progressively disappear and fully vanish at saturation. Depending on the thickness of interlayer of the sample different levels of magnetic bias field are required to create a skyrmion state. The corresponding fields and skyrmion sizes obtained from the ptychographic data for samples 5, 6 and 7 are listed in table 6.2.

The sizes of skyrmions were compared for different samples in order to evaluate their change with reduction of ferromagnetic layer thickness using a FWHM of the Gaussian fit of their profiles measured through the center. The evaluation was done basing on the averaged value of 5 FWHM measurements of skyrmion profiles. It can be seen that the effective anisotropy increases with the decreases of CoFeB thickness for samples 5, 6 and 7.

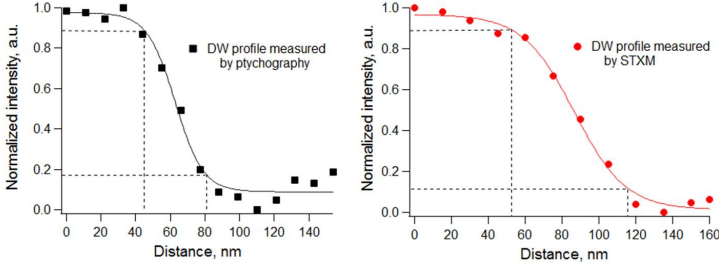


Figure 6.10: Comparison of domain wall width for the sample 7 at domain state using STXM (15 nm scanning step) and ptychography (11 nm real space pixel size). Ptychography shows DW of  $40.6 \pm 4.8$  nm, STXM -  $63.3 \pm 6.6$  nm. The profile data were fitted with sigmoid fit. The width of the edge is determined by the distance from 10% to 90% of intensity.

Sample number	5	6	7
Thickness of FeCoB (nm)	$1.2 \times 15$	$1.3 \times 15$	$1.4 \times 15$
Saturation magnetic field (mT)	-115	-140	-175
Magnetic field at skyrmion state (mT)	-105	-110	-130
Saturation magnetization, $M_s$ (MA/m)	0.88	0.97	1.18
Anisotropy constant, $K_{eff}$ (MJ/m <sup>3</sup> )	0.37	0.11	0.028
Exchange stiffness, $A$ (pJ/m)	2.54	3.54	4.65
DMI constant, $D$ (mJ/m <sup>2</sup> )	0.19	0.52	1.12
Average skyrmion size (nm)	$86.4 \pm 24.7$	$88.3 \pm 22.3$	$91.9 \pm 11.4$

Table 6.2: Parameters of multilayer skyrmion samples with different thickness of CoFeB.

Although the effective anisotropy is quite different, the skyrmion size in these three samples are essentially the same, in a minimal range of 85-90 nm right before disappearance, proving that anisotropy is not the main factors to decide skyrmion size.

The values of the exchange stiffness, obtained by temperature dependent SQUID measurements, are more than factor 3 smaller than volume literature values. The reduced  $A$  result in higher DMI values in comparison with expected values for comparable multilayer structures [153, 159]. DMI is the highest for sample 7 and gradually reduces at samples 6 and 5, that correlates with obtained data showing stable skyrmionic state only at sample 7.

Figure 6.11 a) shows that the skyrmion sizes decrease with the increasing of absolute value of applied OOP magnetic field. The size of the magnetic skyrmions progressively goes down and demonstrate sub-100 nm scales at magnetic fields close to saturation value. A line profile in figure 6.11 b) over a skyrmion at -165 mT bias field allows to conclude that skyrmions have compact shape without a plateau in the central area. Figure 6.12 a) and

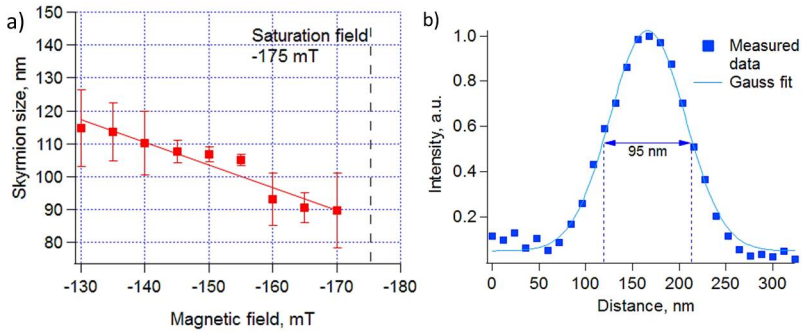


Figure 6.11: Skyrmion sizes a) as a function of OOP bias field for sample 7 imaged by ptychography. Error bars evaluated as a standard mean deviation of five independent measurements of skyrmion width; b) line profile of a skyrmion with the size of about 95 nm imaged by ptychography at -165 mT bias field.

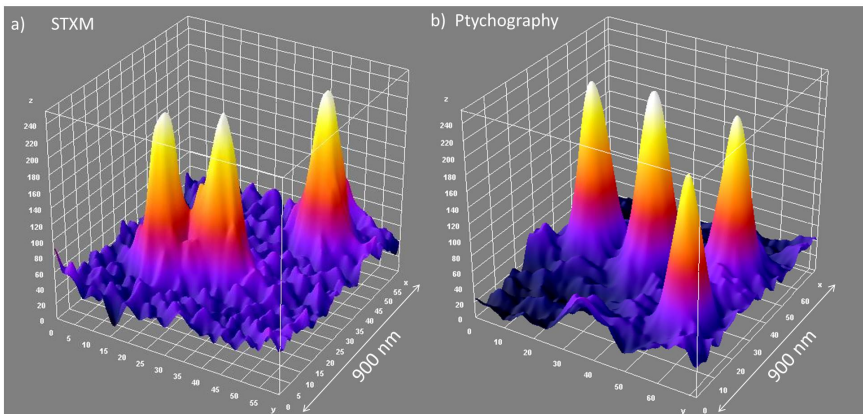


Figure 6.12: 3D profiles of the skyrmions under bias field of -165 mT imaged by a) STXM and b) ptychography.

b) show skyrmions imaged by STXM and ptychography in 3D surface plots. The contrast between magnetic features to background is more prominent for the ptychographic image showing smoother profiles of the observed skyrmions. The smallest skyrmions of sample 7 showed an average skyrmion width of  $87 \pm 3$  nm in the ptychographic images that is in the same size range derived from the STXM images.

The direct estimation of differences in skyrmion sizes measured by STXM and pty-

chography was not deduced due to impossibility to perform these measurements on the same skyrmions which are not repeatable in different cycles of bias field swap.

Due to possibility to cover bigger sample area using ptychography the statistical data of size distribution depending on applied magnetic field values were performed. The histogram of size distribution was obtained for 99 skyrmions at -145 mT field and 45 skyrmions at -165 mT from the same sample area. The size distribution in figure 6.13 shows that the maximum of the peak is shifted to the smaller values at higher magnetic field, from 118 nm to 113 nm.

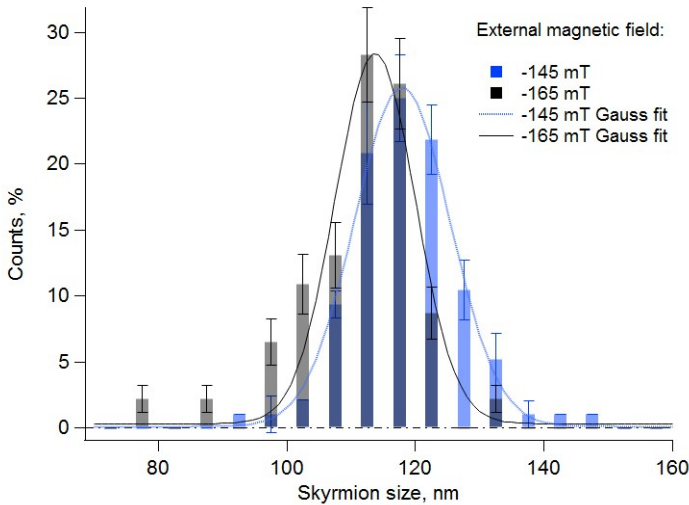


Figure 6.13: Histogram of skyrmion size distribution imaged by ptychography on sample 7. The lower magnetic field -165 mT shows the displacement of skyrmion sizes towards smaller values.

After nucleation most of the skyrmions stay visible with minor size deviations during further field change of 5-10 mT. Around 10% of observed skyrmions could survive more than 10 mT field change. In this case the stability of magnetic features can be explained by the pinning on the impurities of the multilayer [160], which potentially create different local DMI values. The initial assumption was that skyrmion reach critical smallest size before the collapse. However the results showed broad size distribution of the skyrmions before the disappearance with the average diameter of  $106 \pm 6.9$  nm. While the smallest skyrmions imaged by ptychography are in a range of 80-86 nm, that makes around 20-25 % of the size variation.

A pure skyrmion state wasn't reached at the samples 5 and 6 as it is visible from the figure 6.9. The skyrmions show higher variety of sizes and different saturation field

Magnetic field, mT	Amount of skyrmions	Density, skyrmions/ $\mu\text{m}^2$	Distance to the nearest neighbor, nm	Roundness
-130	89	5.94	$305 \pm 69$	0.76
-140	96	6.38	$305 \pm 50$	0.80
-150	97	6.38	$309 \pm 54$	0.82
-160	73	4.73	$345 \pm 51$	0.82

Table 6.3: Parameters of skyrmions imaged on sample 7 using ptychography with the image area of  $4 \times 4 \mu\text{m}$ .

strengths. Since the skyrmions do not have the same trend in the size change it complicates the estimation of mean value of skyrmion sizes in dependance on external magnetic field.

### Distribution and shape

Table 6.3 shows the parameters of skyrmion shape of sample 7 and their distribution which were analyzed using BioVoxel Toolbox in ImageJ image processing program [161]. The density of skyrmions shows their amount in one square  $\mu\text{m}$ . This evaluation ignores the differences in skyrmion shape and sizes. The distance to the nearest neighbor determines the statistical distribution of the magnetic features. Table 6.3 includes the shortest mean distance value measured for all skyrmions in a field of view of  $4 \times 4 \mu\text{m}$  with a standard deviation as an error. According to the data we have the biggest amount of skyrmions at the magnetic field values of -140 mT and -150 mT, 99 for the both cases. With the increase of the magnetic field the density gradually goes down and mean distance between skyrmions gets bigger.

Both ptychography and STXM images showed that skyrmions are shaped not perfectly round, most of the structures are slightly elongated and get more symmetric at higher values of magnetic field as it is seen in figure 6.14. The longer axis of skyrmion coincides with the long axis of former magnetic stripe domains. The roundness of the skyrmions presented in table 6.3 was calculated as:

$$Roundness = \frac{4 \cdot S}{\pi \cdot d_{max}^2} \approx \frac{b}{a}, \quad (6.4)$$

where  $S$  - area of a skyrmion, and  $d_{max}$  its the biggest diameter. The roundness corresponds to the inverse value aspect ratio of the long skyrmion axis,  $a$ , to the short one,  $b$ . The value of roundness varies from 0 to 1, where 1 corresponds to fully round structure. The shape mostly changes along the longer axis and present around 20% of size reduction starting from the moment of formation and ending at the point of disappearance, while along short axis the reduction has only 5%.

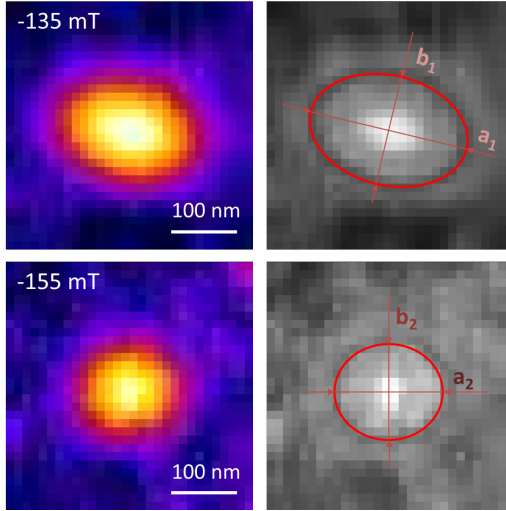


Figure 6.14: Skyrmions imaged by ptychography at -135 mT and -155 mT. The ratio of major and minor axis of elliptically shaped skyrmions gets smaller with propagation towards higher magnetic fields. Therefore the skyrmion has the ratio  $a_1/b_1 = 1.37$  at lower field, and  $a_2/b_2 = 1.17$  at higher field.

Elongated skyrmions shapes can occur because of so called elliptical instability as it was discussed in [162, 163]. As it is described in [162] the isolated skyrmions exist in metastable condition above a critical field. With the decrease of the field below this value the skyrmions transformed into lattice state or isolated skyrmions continue to exist with the observed uniaxial misshape. The same elliptic instabilities of magnetic bubbles have been described at a certain critical magnetic field [164]. The strip-out of the separate skyrmions starts at different fields and can be influenced by defects [162] or lattice strains in the surface layers [165]. Additionally thickness variations and structural disorders throughout the samples determine the pinning distribution, since these regions can have different values of DMI, saturation magnetization, interface anisotropy or exchange stiffness. These parameters have a direct influence on the skyrmion shape and stability [160].

### 6.3 Comparison of STXM and ptychography for skyrmion imaging

To compare two different imaging methods, STXM and ptychography, several aspects should be taken into account: resolution, speed and magnetic contrast sensitivity (table 6.4).

Power spectral densities have been calculated for STXM and ptychography images of sample 7 in the domain state (figure 6.15). The STXM image  $5 \times 5 \mu\text{m}$  big was obtained with line scan with 25 nm step size, and a ptychography amplitude image  $4 \times 4 \mu\text{m}$  big was done at Fe-edge with 11.5 nm pixel size. The thresholds of double noise level are plotted with dotted lines with corresponding real space resolutions. The main peak of frequency distribution is around 147-150 nm of half period real space values. At the same time PSD curve of the ptychographic image has smoother and wider peak corresponding to bigger frequency range in comparison the STXM PSD curve. It denotes that ptychography image provides more information about size variations of the imaged magnetic features than STXM.

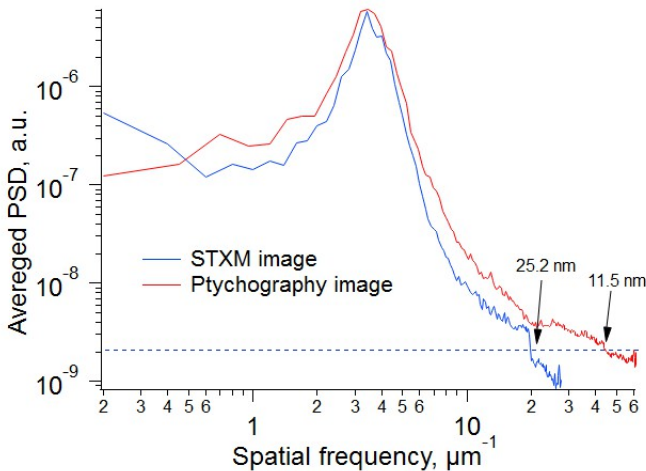


Figure 6.15: Power spectral density curves for STXM and ptychography images of sample 7 in domain state. Threshold values correspond to the real space pixel sizes of the images.

High resolution STXM images with 20 ms dwell time and 15 nm scanning step were compared with ptychographic images. The line profiles over the DWs imaged by ptychography and STXM in figure 6.10 also showed about 1.6 times resolution improvement in ptychographic image.

The Michelson contrast evaluation of STXM and ptychography images in dependence of external magnetic field were performed for sample 7 with 21.7 nm CoFeB total thickness. Analyzing the ptychographic images we see the large drop of contrast for the samples in skyrmion state. As it is shown in figure 6.16 the contrast for domain state is about 72 %, while skyrmion state showed around 23 % of contrast. Comparatively rapid change in contrast is observed when magnetic domains are narrow enough and separate skyrmions start to appear. The decrease of image contrast occurs due to reduced scattering from the small magnetic structures. As a result influence of background noise increases producing artifacts in reconstructed images, in some cases the resolution degradation and broadening of the edges of magnetic features. The contrast of STXM images obtained by fast line scan varies from 8.8 % to 4.1 % as it is seen in figure 6.16 the line fits have less significant contrast drop as ptychographic data. The contrast of ptychographic images is several times higher due to background retrieval that boosts the contrast of the useful features and suppresses background signal.

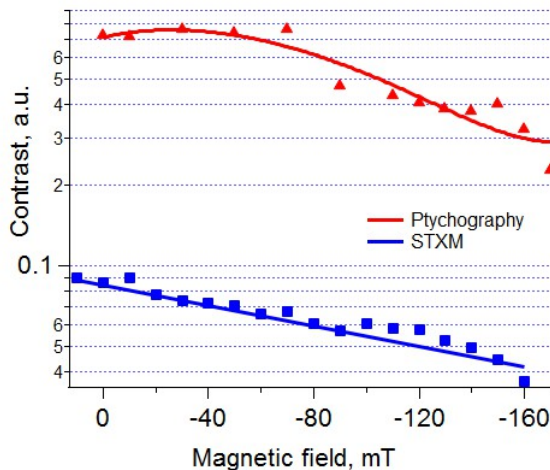


Figure 6.16: Contrast change of the images obtained by ptychography and STXM at sample 7 propagating from domain state to the skyrmion state by sweeping external magnetic field. The data fitted with line fit.

The comparable contrast change is observed at the samples with thinner ferromagnetic layer. The skyrmion multilayer samples 3 and 4 with total thickness of 16.1 nm and 16.5 nm CoFeB showed recognizable domain pattern at STXM images, however ptychographic scattering signal from the thinner specimens were not high enough for successful reconstructions.

To get more statistical data about skyrmion size variations ptychographic images have been used. Time for one STXM scan is determined by the step size of the scan, which should be smaller than focus spot to provide reliable photon count statistics. For the FZP with  $\Delta r=18$  nm and 20 ms dwell time for each step  $2 \times 2 \mu\text{m}$  big image is finished within 6 minutes. The total scanning time for one ptychographic image  $4 \times 4 \mu\text{m}$  size with 200 ms dwell time, 10 ms point delay and 100 nm step size takes about 5.6 minutes. The pixel size of ptychographic reconstruction on Fe-edge is 11 nm, that results in effective dwell time per reconstructed pixel around 3 ms. The iterative process consisted of 200 iterations, that is sufficient for finding stable solution, including illumination and background retrieval takes less than 1 minute. That assures 4 times bigger image for the approximately the same scanning time.

<b>Parameters</b>	<b>STXM</b>	<b>Ptychography</b>
<i>Exposure time</i>	Point by point scan with 20-30 ms per scanning step	Dwell time of 200 ms per scanning point results in 3 ms per reconstructed pixel
<i>Resolution</i>	Determined the $\Delta r$ of FZP: 22 nm full pitch resolution using optics with $\Delta r = 18\text{nm}$	Limited by the NA of the detector: 11 nm full pitch resolution at Fe-edge and 8 cm distance from sample to detector
<i>Sensitivity</i>	Highly sensitive for low contrast samples	Significant drop of the contrast at low scattering features
<i>Information</i>	Absorption	Amplitude and phase

Table 6.4: Comparison of STXM and ptychographic methods for magnetic imaging at Fe-edge.

## 6.4 Conclusion

Two different sets of skyrmion samples have been studied using magnetic sensitive ptychography: with different heavy metals and different thicknesses of ferromagnetic interlayer. The main advantage of ptychography for skyrmions studies is its suitability for imaging of extensive areas with the fixed output pixel size that as a result produces 4 times bigger field of view with the same scanning time as STXM technique. Background retrieval helps to get higher contrast of observed magnetic structures when it is in magnetic domain state. Ptychography resulted in higher resolution with about 1.5 smaller domain wall width than STXM. The size of the skyrmions for STXM and ptychography methods are in agreement.

The STXM imaging revealed magnetic structures on the samples with thinner Co-FeB layers and showed to be more sensitive for magnetic contrast than ptychography. Ptychographic imaging using three samples with the thickest CoFeB ferromagnetic layer have been done. The significant difference between the sizes of skyrmions in samples with different CoFeB thickness was not observed indicating that possible size variations are beyond the provided resolution, i.e. less than 11 nm of the pixel size. The smallest skyrmions imaged by ptychography is around 80-85 nm that is a confident result illustrating method applicability for sub-100 nm magnetic imaging of pure magnetic contrast samples.

High throughput ptychographic imaging revealed a great potential for its implementation for magnetic sensitive investigation of such systems, that can provide an insight in complex mechanism governing skyrmionic behavior. A main drawback of ptychography at MAXYMUS for skyrmionic studies is non suitability for dynamic imaging for visualization of driven motions of skyrmions.

Basing on the analysis of the ptychographic images the DMI values were determined with the domain spacing model. In order to use correct room temperature parameters of  $M_s$ ,  $K_{eff}$  and  $A$  for the actual samples the overall characterization of the system by numerous temperature dependent measurements of the hysteresis loops have been performed. It was established that the Curie temperature dramatically decreases, thus  $M_s$  and  $A$  decrease as well, with decreasing FeCoB layer thickness. This might explain the partly strong deviation of measured DMI values from the literature data.

The high variety of skyrmionic systems accompanied with tremendous amount of related research boosting during the last years give a vast overview on the state of art in this field. The literature observation allows to conclude that the properties of the skyrmions strongly depend on the composition, as well as the deposition routes and multilayer geometry performed in various ways in different works. As a result the big amount of skyrmionic systems with different structures and probably strong local variation of the magnetization landscape in and out-of plane are performed. Therefore to deduce reliable information on the DMI value correlations and the skyrmion phenomenon in general is not straightforward.

These might question the common statement that skyrmions can be used as a bit structure for future data processing technologies in small, fast and low-power devices. The room-temperature structures have sizes about 100 nm requiring a current line of about 300 nm that is significantly larger than structures in the present CMOS technologies. The current induced motion is rather slow not faster than 100 m/s = 100 nm/ns. Additionally multiple time-resolved measurement of current driven skyrmion motion showed that the typical currents necessary to move these feature with a speed of 100 m/s is above  $10^{11}$  A/m<sup>2</sup>. This has to be taken into account for race track memory application since such high current densities can cause the temperature rise and electromigration, which change nearly all magnetic parameters of the device and result in its fast damage. Moreover, a

controlled creation/annihilation and guiding of magnetic features can be obstructed by impurities and minor defects in multilayer film.

## Chapter 7

# 3D magnetization of Cu-Ni core shell nano particles

Hetero-nanostructures have been under active investigation since they can exhibit unique properties tailored by their size, shape and composition [166, 167]. Controllable fabrication of core shell nanoparticles allows to vary their mechanical, chemical, optical and magnetic properties. Also some magnetic properties of nanocrystals, such as magnetic saturation, blocking temperature or permanent magnetization, depend on surface anisotropy effects which are governed by the shape of the crystal [168].

Cu-based nano materials have attracted great interest because of the high cost efficiency in applications for conductive electrodes, plasmonics and catalytic processes [169]. In order to protect Cu nanoparticles they are covered by a coating metal, which is resistive for water, air and diluted acids, often by Ni [170] one of the elemental ferromagnetic. Cu-Ni nanoparticles are well studied in terms of morphology [171, 172] and thermo-magnetic properties [172]. Their finite size, complex geometry, breaking symmetry of the crystals and presence of surface strain can potentially result in nontrivial magnetization states in the thin magnetic film shell of such particles [173]. In most of the studies the magnetization of nanoparticles is investigated basing on the integrated data obtained from the big clusters of particles only [171, 172]. In this chapter high resolution magnetic sensitive ptychography is applied for investigation of magnetization of the separate core-shells.

## 7.1 Particle shape

### 7.1.1 Cu single crystal

The crystalline growth direction is determined by the surface free energy: it grows in the direction of higher surface energy in order to eliminate these planes and reduce surface energy of the whole crystal. Figure 7.1 a) shows that a single crystal of Cu has a cubooctahedral equilibrium shape. Different growth rates in the  $[111]$  and  $[100]$  directions, which are shown in figure 7.1 b) [174], change the shape of the particle from cubic to octahedral. If the growth in the  $[111]$  direction is higher than in  $[100]$  the crystal is shaped as a cube. If  $[100]$  direction growth rate increases and is comparable with  $[111]$  growth rate two different facets ( $100$ ) and  $(111)$  become visible. In figure 7.1 a) the octahedral shape corresponds to the condition when  $[100] \cong [111]$  that results in 6 facets in  $(100)$  and 8 facets in  $(111)$  directions. If the growth rate in  $[100]$  direction becomes dominant we get a truncated octahedral crystal that is followed by a fully octahedral shape. The crystal growth of single crystal nanoparticles can be controlled using different capping agents [175].

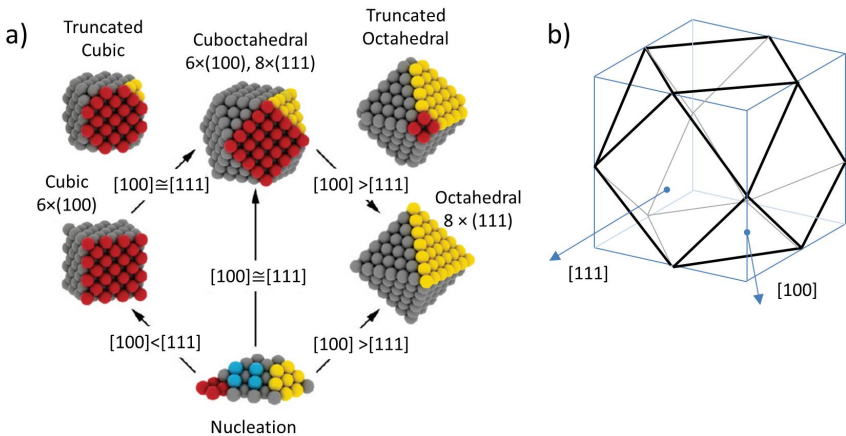


Figure 7.1: Single crystal shape of Cu: a) crystal shape evolution of Cu nanosized core [174]; b) cubooctahedral shaped Cu crystal with growth directions  $[111]$  and  $[100]$  corresponding to FCC lattice shape.

## 7.1.2 Twinned particles

The variation of the crystal shapes of a Cu core is observed when small counterparts form so called twinned or multiply twinned particles (MTPs). MTPs consist of regular tetrahedra which are stacked across  $[111]$  facets with the lowest energy and arranged around the fivefold symmetry axis. The most common MTP shapes for the fcc crystals are decahedral and icosahedral (figure 7.2). Decahedron is a bipyramid and contains 5 tetrahedra, which are stacked around single symmetry axis. Icosahedron has 20 tetrahedral subunits assembled around the 6 fivefold axes. The process of stacking occurs via the consecutive attachment of new subunits that results in the presence of intermediate state nanoparticles with the lower number of tetrahedra.

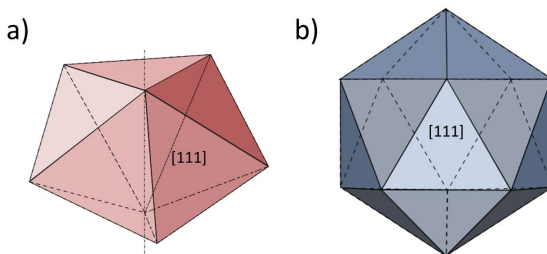


Figure 7.2: Typical morphologies observed in MTPs: a) decahedron, the bottom pyramid is hidden below the upper half, and b) icosahedron.

Along with the decahedra and icosahedra crystal shapes one-dimensional structure like nano-wires or nano-rods can be observed [176]. These structures are formed due to the anisotropic growth of the crystals along one axis that happens because of the angular misfit leading to lattice transformations or lattice defects. The presence of these defects introduces self-propagating ledges which work as active sites for crystal growth. Anisotropic growth can be controlled by the seed mediation, surfactant or by template [177]. In figure 7.3 a) MTPs with decahedral shape exhibit anisotropic growth along the symmetry axis in  $[110]$  direction that results in the prism structure capped with pentagonal pyramids from the ends. The growth of decahedra also appears in the directions of the edges of twin planes that stretches the nanoparticle shape into asymmetric flat plate as it is shown in 7.3 b). Icosahedral particles show less tendency for anisotropic growth since they are close to spherical shape and have minimal surface energy [176].

The appearance of the crystal nanoparticle in 2D projection in transmission imaging is strongly depends on its orientation on the substrate that challenges the identification of the particle shape. Therefore microscopy sensitive for the surface morphology, i.e. SEM or AFM, is required for the analysis of the particle shape.

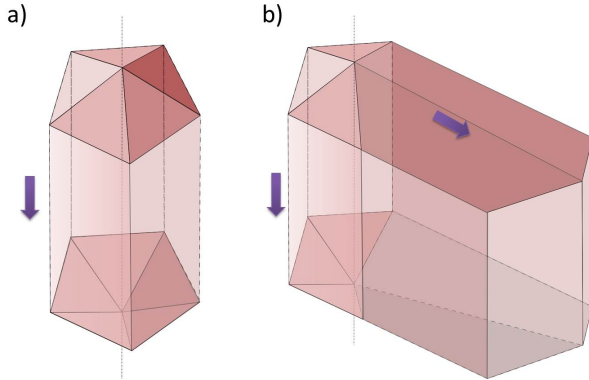


Figure 7.3: Schematic drawings of a) prism shaped nanorod grown from a decahedra along the symmetry axis and b) nanoplate obtained from the rod by the growth along the twin boundary.

### 7.1.3 Twin boundaries and strain

When different counterparts of the twinned crystals are placed together under certain angle the boundary region with two-dimensional defects is formed in the junction area. For example, in order to form pentagonal pyramid the assembly of five tetrahedral units need to fill the gap of  $7.4^\circ$  that comes from the mismatch of the angles. Types of junction boundaries depend on the tilting of the two crystal planes relative to each other and have different energy. Two examples of boundary types, twin boundary and tilt, are presented in figure 7.4.

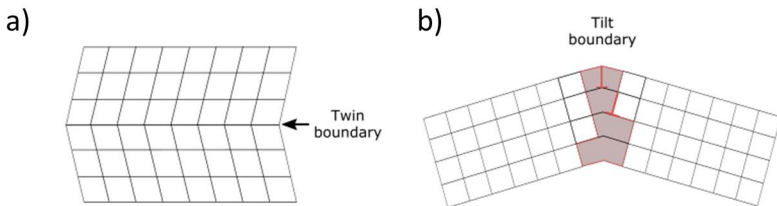


Figure 7.4: Schematic views of a) twin boundary and b) tilt boundary .

Comparatively small particles (up to 10 nm) with five fold symmetry made of metals with FCC symmetry have twin boundary between neighboring facets. In this case atomic arrangement on one side of the twin boundary is mirrored to the other side (figure 7.4 a). The energy of twin boundary is very low because of the perfect atomic fit between two

crystal planes. Also twin boundaries are observed on the relatively large structures with grains in the micrometer range and twin boundaries with up to a few tens of nanometers wide. A tilt boundary produces a tilt angle between neighboring lattice planes of the same type in adjacent faces as it is imaged in figure 7.4 b). It consists of a regular array of the dislocations at the plane edges and can have low (up to 10-15°) or high tilt angle. Dependence of the grain boundary energy on the angle orientation grows exponentially and comparatively higher than twin boundary energy.

## 7.2 Ni shell on Cu core grown by epitaxy

The Cu and Ni have both face-centered cubic (FCC) structure and similar lattice constants: 3.597 Å for Cu and 3.499 Å for Ni.

Small mismatch of the Ni and Cu lattices for 2.5% initiate pseudoamorphical growth of first monolayers (ML) of Ni that is observed up to 10 ML. Therefore the Ni film strain elastically in order to match the spacing between its atoms with the Cu substrate. With further growth of the film thickness strain accommodation is not possible and dislocation defects at the interface may form. The resulting film returns to its original lattice structure above the film/substrate interface. The strain from the interface of two metals decays as a logarithmic function with decrease of the distance from the core.

Nucleation of Ni atoms during epitaxy can take place on mono-atomic steps, on defects, or directly on the surface. Besides the performing dislocation defects with strain relief the thin film can repeat the crystal defects of the substrate material. High energy regions of the substrate, like boundaries, cause islands formation instead of homogenous layer by layer epitaxial growth that might affect thin film properties.

### 7.2.1 Ni shell magnetic properties

Shape anisotropy usually dominates over magneto-crystalline anisotropy in thin films fabricated out of soft magnetic materials, especially, with cubic symmetry. However previous studies of ultra thin Ni grown on top of the Cu substrate showed that magnetization properties of Ni films have a dependence on the thickness and the symmetry of the substrate surface. It was shown in [178, 179, 180, 181] that Ni in the initial stage of growth on Cu(100), Cu(110) and Cu(111) has in-plane magnetization. A Ni thickness up to 7-8 ML on Cu(100) [178] and Cu(111) [179], also 8-9 ML thick Ni on Cu(110) [180] result in domination of an out-of-plane magnetization component. It was established that the perpendicular magnetic anisotropy in Ni/Cu(001) systems is caused by strain in Ni films with the thicknesses between 10 and 75 MLs [181]. Above this critical thickness level films become relaxed in order to reduce the strain and show bulk magnetic properties with in-plane magnetization [182].

In general, defects determine magnetic properties of thin films since they act as local the minima of energy producing stable conditions for domain allocation that causes the pinning of magnetic domain walls [183].

3D curved shape of a substrate under a magnetic thin film also can be a source of anisotropic and chiral effects [184]. The curvature of the surface induces an additional energy contribution to the magnetic exchange energy. Theoretically, the existence of a curvature-induced effective anisotropy and Dzyaloshinskii-Moriya-like interaction were predicted that opens a new range of magnetic properties in the curved magnetic materials. The effect of topologically induced magnetization have been studied for various shapes, like cylinders or hollow tubes, cones, spheres and hemispherical caps [184].

### 7.3 Sample preparation

Cu-Ni core-shell particles were fabricated in the Central Scientific Facility (CSF) (MPI IS, Stuttgart) by the group of Dr. Gunther Richter. The particles have been grown under ultra-high vacuum conditions by molecular beam epitaxy (MBE) on a 100 nm thick  $Si_3N_4$  membrane. MBE provides deposition of a mono-crystalline film produced of highly pure elements with precise control of surface morphology.

The deposition process is shown in figure 7.5. The membrane was initially covered with 30 nm amorphous carbon layer by magnetron sputtering for better Cu diffusion, core crystal nucleation and growth. The Cu element was heated at the separate effusion cell and deposited on the substrate with the rate of 0.05 nm/s. 100 nm thick Cu was formed on the rotating substrate which was heated to 710° C. The rotation of the sample ensures even growth of the depositing material over its surface. The temperatures of the Cu effusion cell are used to control the flux of an atomic beam. For the homogenous heating of this cell two elements on top and bottom with corresponding temperatures of 1220° C and 1148° C were used. After the deposition process of Cu that took 50 minutes the sample was cooled down till 20° C. Afterward a Ni layer 10 or 15 nm thick was deposited at room temperature at the rate of 0.01 nm/s with the same sample rotation.

The deposition process was optimized for the formation of crystal Cu nano particles with highly defined facets. Initially the Cu layer was deposited on  $Si_3N_4$  substrate without additional carbon inter-layer. The low diffusion of Cu adatoms on the uncovered  $Si_3N_4$  resulted in undefined particle crystal shapes with rounded edges. Figure 7.6 a) shows Cu-Ni particles with the size of 200-300 nm deposited on  $Si_3N_4$  substrate without carbon layer with thicknesses of Cu of 45 nm and Ni 15 nm.

Figure 7.6 b) shows a SEM scan of the core-shell sample obtained by MBE with 30 nm C layer. As it is observed from the image particles vary in size range of 400-1000 nm and possess different shapes: extended in one direction rods or wires, flat platelets or 3D crystals with multiple facets (figure 7.7).

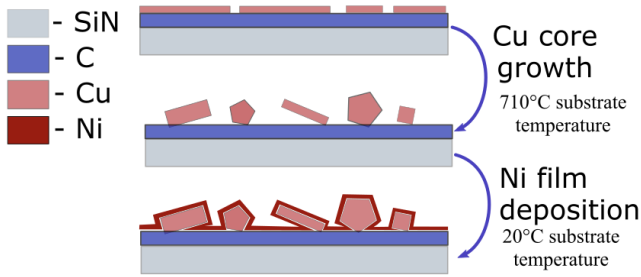


Figure 7.5: Deposition process of Cu-Ni core-shell particles: SiN substrate covered with 30 nm C layer is heated to 710° C for Cu diffusion and crystal core formation. 10 or 15 nm thick Ni film is deposited on top of the whole membrane area when it is cooled down to 20° C.

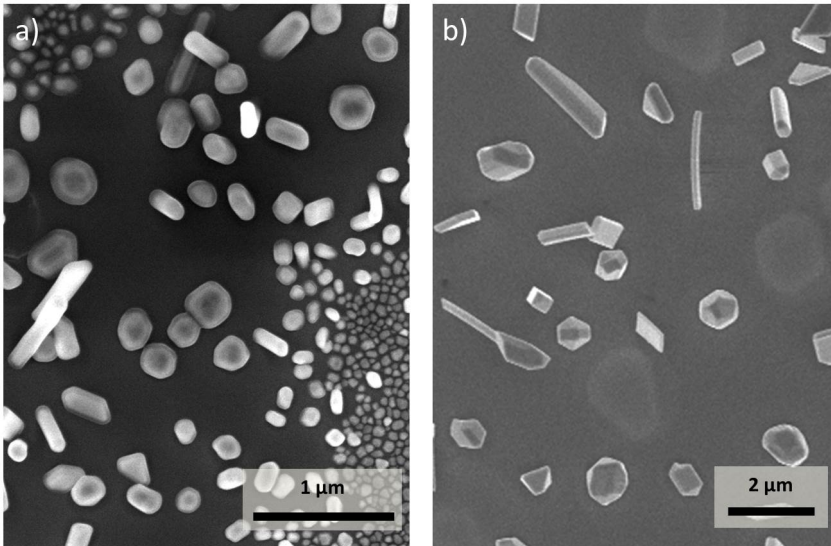


Figure 7.6: SEM image of Cu-Ni core-shell particles deposited by MBE: a) without C layer on the substrate with Cu thickness of 45 nm and Ni 15 nm; b) with 30 nm C layer on the substrate with Cu thickness of 100 nm and Ni 15 nm.

The heating of the substrate at the deposition process of Cu is a key component for crystal grain growth. It helps to obtain a high mobility of the adatoms on its surface due to low interaction with the amorphous C layer that provides a continuous formation and

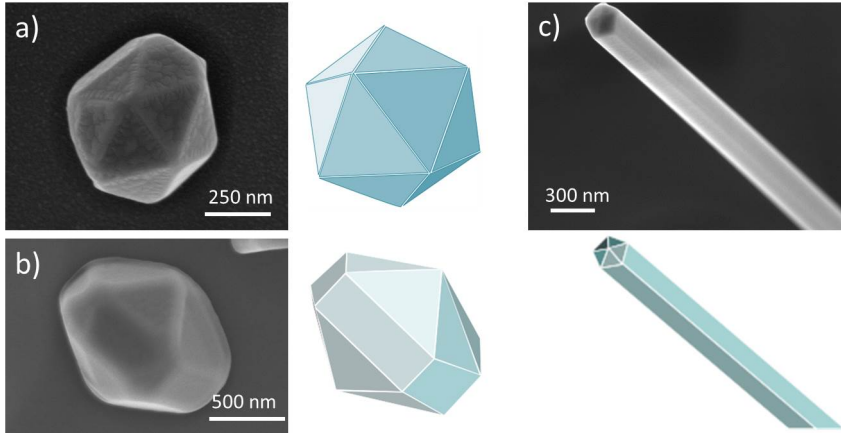


Figure 7.7: SEM image of Cu-Ni core-shell particles with a) icosahedral shape, b) decahedron extended along  $[100]$  crystallographic axes, and c) pentagonal nanorod.

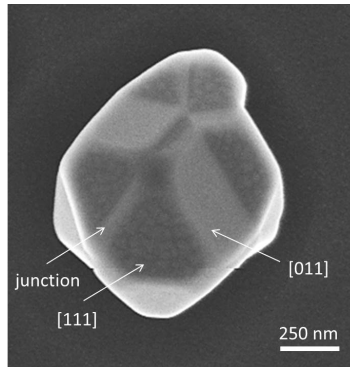


Figure 7.8: SEM image of five-fold symmetry Cu-Ni core-shell particle overgrown along  $[110]$  crystal direction exhibiting heterogeneous surface morphology.

growth of the Cu core particles. The room temperature of the substrate at Ni deposition promotes formation of small and closely packed islands because the adatom mobility is comparatively small. For a strained Ni epilayer with small interface energy, initial growth occurs layer-by-layer, but thicker 10-15 nm layers obtain higher strain energy and start to form isolated islands in order to relax this strain. Therefore we observe Stranski-Krastanow (SK) growth mode [185].

As it is seen in figure 7.7 a) the surface of the particular core-shells and the substrate

around mostly form grainy structure with the grains having rounded shapes. The regions on the junction parts of the facets have much denser grain packing that makes edges look smoother and prominent over the flat surface of the adjoined facets. However the morphology of Ni layer is not the same on the surface of the particles. Figure 7.8 shows particle with the pentagonal upper part which has been grown in the [100] direction and exhibit heterogeneous morphology on the different crystallographic facets. The low energy (111) facets have grainy surface with 40-45 nm grain size, when the regions in between and on the junction areas have smooth surface. The substrate surface next to the particle is not uniform as well, but has smaller grain sizes. The inhomogeneous growth of Ni on the different crystal planes of the Cu core could be referred to the dissimilar growth mechanisms in the different crystallographic directions.

## 7.4 Magnetic properties

Hysteresis loops were obtained by SQUID at room temperature with magnetic field parallel and perpendicular to the sample deposited on the SiN membrane (figure 7.9).

Ni was deposited on the whole surface of the  $5 \times 5$  mm big substrate, excluding minor areas where it was fixed for deposition that isn't taken into further considerations. Knowing the film thickness of Ni the volume magnetization per  $\text{cm}^3$  and the density flux value were evaluated.

The core-shells with different thickness of Ni layer of 10 and 15 nm have been studied and both showed anisotropic behavior as it seen in figure 7.9 a) and b). The samples have in-plane easy axis orientation and weak ferromagnetic properties. The samples get into saturation around the same values:  $\pm 850$  Oe in-plane (IP) and  $\pm 6000$  Oe out-of-plane (OOP) sample orientations. The coercivity values for the sample with 15 nm Ni were estimated to be 12.9 Oe, while for the sample with 10 nm Ni - 7.3 Oe. In comparison, bulk Ni has smaller coercivity of about 0.7 Oe and higher density of flux of 646 mT [186], versus 370 mT OOP and 509 mT IP flux density for 15 nm Ni shell.

The hysteresis loop with applied magnetic field perpendicular to the film plane in figure 7.9 b) indicates that different parts of the film change the magnetization in different ways. The perpendicular magnetization curve approaches slower to the saturation state and shows a less pronounced hysteresis. This behavior relates to the presence of 3D shaped magnetic particles on the membrane (see figure 7.6) with inhomogeneous magnetization of their facets. Obviously, the particles change OOP magnetization direction at different values of applied external field.

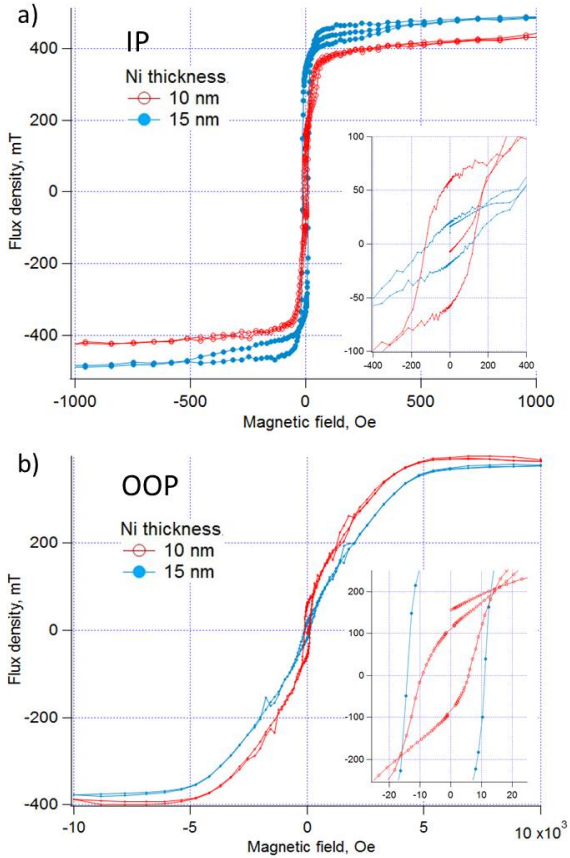


Figure 7.9: Hysteresis obtained a) in in-plane and b) out-of-plane configurations for core-shell samples with 10 and 15 nm Ni thicknesses. Inset: low-field enlargement.

## 7.5 STXM spectroscopy and magnetic contrast of core-shell structures

The particles with 100 nm Cu and 15 nm thick Ni shell were studied at MAXYMUS microscope. STXM imaging has shown the presence of Cu only in the core shell particles itself and bigger round shaped islands homogeneously distributed on the surface of the membrane as it can be seen from SEM image in figure 7.6. The islands, which remain from non-crystallized Cu covered with Ni, look like a uniform film and have much lower

optical density than crystallized particles. The elemental maps of a separate core-shell particle are presented in figure 7.10. Cu is observed in the center of the particle with Ni homogeneously covering the core. The image profile in figure 7.10 d) were made across the particle and shows Cu core of about 1  $\mu\text{m}$  with total particle size of 1.1  $\mu\text{m}$ . Since the edges of the particle are not perpendicular to the surface of the membrane, but tilted under a certain angle determined by the particle geometry, Ni shell thickness seems to be higher than expected.

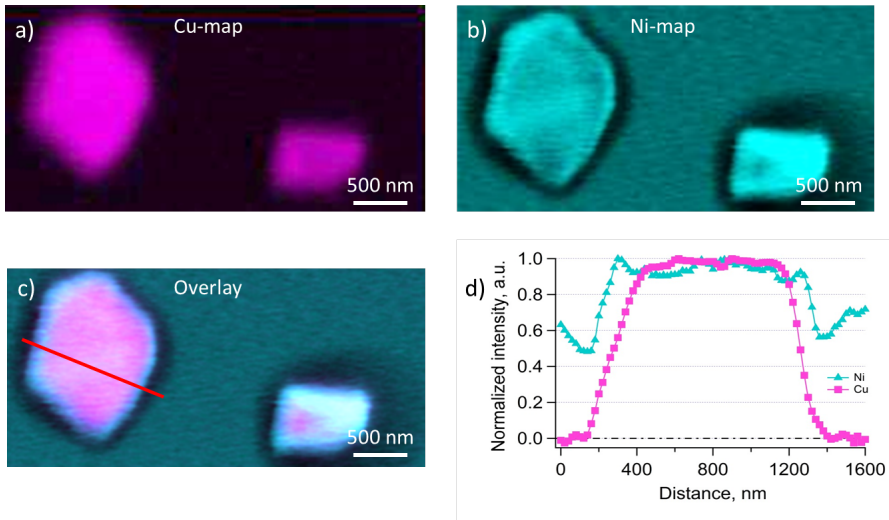


Figure 7.10: STXM resonant absorption images of core shell particles: a) Cu-map ; b) Ni-map; c) overlay of Ni and Cu maps; d) line profile over the particle marked as red line on the image c).

Magnetic absorption spectra were obtained using polarized light with positive and negative circularity over  $L_3$  Ni edge on the membrane and on the core-shell particles (figure 7.11). Most of the particles showed pronounced XMCD effect of around 15% that corresponds to 12-13 nm Ni thickness. The reduced thickness value is referred to the fact that upper Ni layers get oxidized and coordinately do not contribute to the XMCD signal. The spectra obtained on the membrane do not show the contrast difference between left and right polarized light absorption as expected for in-plane magnetization orientation.

Figure 7.12 shows  $8 \times 8 \mu\text{m}$  STXM XMCD overview image including few particles of different shapes, substrate and non crystallized round structures covered with Ni. Without an applied bias field the substrate doesn't show any magnetic domains that proves that film deposited on the substrate has in-plane magnetization. The round flat structures with the diameter of 2.5  $\mu\text{m}$  have out-of-plane magnetization that is revealed in comparatively

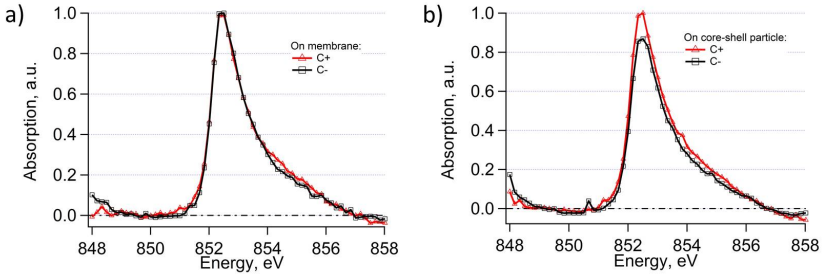


Figure 7.11: STXM absorption spectra of core-shell sample made with different X-ray light polarization a) on the membrane and b) on the particle.

big magnetic domains as it is marked with a blue circle in figure 7.12 with 0 mT OOP field. The particles exhibit single domain magnetization in case if it has 2D geometry (red circle in figure 7.12), the ones with a 3D facet orientation (white circle in figure 7.12) show different magnetic contrast within one particle.

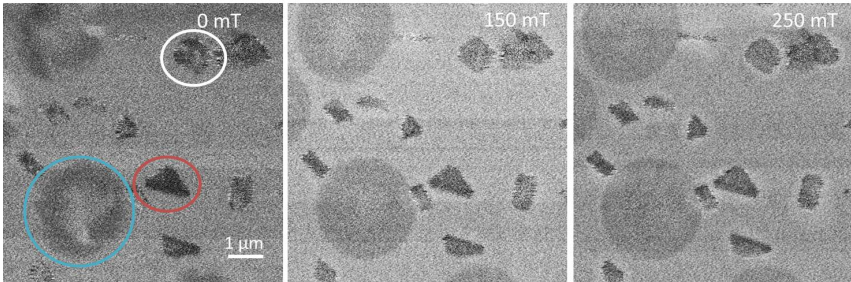


Figure 7.12: Overview STXM XMCD images of a core-shell sample obtained at different OOP magnetic fields. Blue circle denotes non-crystallized Cu, red circle - a flat particle, white circle - a 3D shaped particle with facets oriented under different angles relative to substrate plane.

Increasing OOP external magnetic field the change of magnetization orientation is observed, that is nicely visible at the non crystallized round structures. Two domains with bright and dark contrast get to the uniformly magnetized single domain state. As much as it is seen from the overview scan, magnetization of the particles becomes oriented in the direction of the applied bias field and have more homogeneous magnetic contrast.

The STXM overview image does not resolve separate facets due to resolution limitations. That is why it is hard to conclude weather the XMCD effect comes from the out-of-plane magnetization of Ni grown on the Cu crystal or it is a result of the various

tilts of in-plane magnetized facets of the 3D shaped particle.

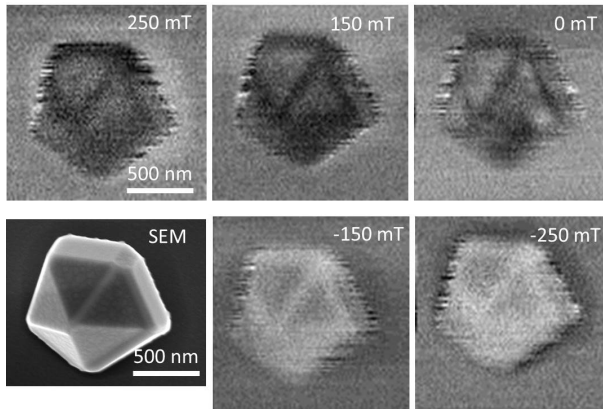


Figure 7.13: SEM and STXM XMCD images of a core-shell having pentagonal pyramid shape obtained at different OOP magnetic fields.

Close up of the particle with pentagonal pyramid shape was performed using point by point scanning mode with 20 ms dwell time and 15 nm scanning step size as shown in figure 7.13. The triangular facets have different magnetic contrast due to unequal angle orientations towards the direction of X-ray beam. The junction region between two upper facets is more magnetically absorbing which indicates that magnetization oriented out of plane. The increase of OOP bias field changes magnetization of the particle facets in different manner: some areas get magnetized in the direction of external field faster than the others, which are partially not fully magnetized in the direction of the bias field of 250 mT. Simulations of icosahedral and decahedral particles with the field are presented in Appendix E, showing that 250 mT bias field results in partial IP magnetization of the facets oriented perpendicular, or close to perpendicular, to the direction of the magnetic field, that is in agreement with the STXM data.

## 7.6 Simulation of 3D magnetization

Micro-magnetic simulations of nanoparticle magnetic shell magnetization were performed using open source MicroMagnum software [187]. It runs on CPUs as well as on GPUs and utilizes CUDA platform. MicroMagnum is a Python module that can be extended for the simulation of magnetic 3D shell with defined geometrical shape.

In order to determine the discretization of the simulated object and its size a grid is defined in accordance with the cell size in X, Y and Z-directions. The algorithm allows

to predefine the magnetic parameters of the used material. For example, for Ni shell the values of  $M_s$ ,  $\alpha$ ,  $A$  and  $K_1$  have been set according to the data in table 2.2. The initialization of the structures requires a geometrical pattern to resemble the core shell particles. The shape class extension code <sup>5</sup> allows to define the outer shell and inner particle, i.e. core, and to fill the magnetization in between those two structures.

The solve method computes the evolution of a magnetic system in time and stops if the relaxed state, which is determined by a termination condition, is reached. The solve method is based on Landau-Lifshitz-Gilbert equation (LLGE) with possibility to include following effective fields: demagnetization field, exchange field, uniaxial and cubic anisotropy field, also external bias field. The simulated data are saved as .omf file with every 0.5 ns of simulation time. For visualization of simulated 3D particle magnetization Wolfram Mathematica package has been used [188].

The simulations of magnetization of 15 nm thick Ni shells of different sizes, 300, 500 and 700 nm, with and without cubic anisotropy and applied bias field are presented in Appendix E. The simulation of 700 nm big particles of icosahedral and decahedral shapes without anisotropy are discussed in the following chapters.

### 7.6.1 Magnetization simulation of icosahedral shape

Figure 7.15 shows the images of 700 nm big particle with magnetization vectors observed from the different sides of its 3D shape which are marked in figure 7.14. The magnetization is mostly governed by the geometry of the facets and has similar behavior for the opposite sides. The views from above or below (figure 7.15 a, d) show two facets magnetized homogeneously in the same direction, which don't form separate magnetic domains. The front and back images (figure 7.15 b, e) show that neighboring facets have opposite magnetization direction. On the junction area the flip of the magnetization is observed over the whole length of the edge in a counterclockwise direction with magnetic vectors whirling into vortex like configuration in the center of the edge from the both sides. As it is seen in figures 7.15 c) and f) magnetization vectors change their orientation along the narrow region at the facet edge when the adjusting regions have opposite magnetization direction without forming a magnetic whirl in the center as well. Figure 7.14 demonstrates the general vector magnetization orientation on the one half of the icosahedron. It shows that magnetic vectors are wrapped around the particle without formation of multiple domains within separate faces.

In practice magnetic contrast, observed with X-rays in transmission geometry, is only the projection of magnetization vector on the plane oriented perpendicular to the beam and depends on the orientation angle between beam direction and vector magnetization of the material. For the better understanding how magnetic contrast would look like in STXM image the magnetization vectors have been projected on the different planes assuming the

<sup>5</sup>the extension code was developed by Kai Litzius

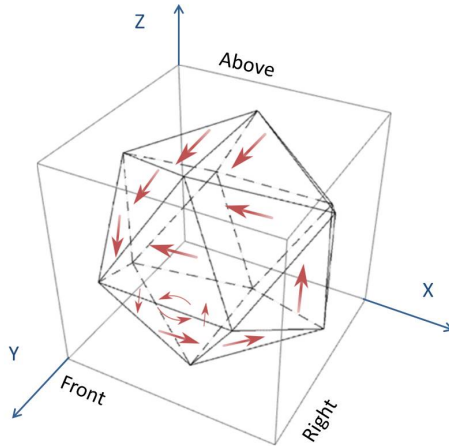


Figure 7.14: Icosahedral particle in XYZ coordinates with corresponding view from above, right and front.

X-ray beam passing through the particle in X, Y and Z directions. As it is shown in figure 7.15 g),h) and i) the normals of vectors on all three planes XY, XZ and XZ are found from the corresponding observation points: from right, front and above. The colors of the faces show the normalized size of the magnetization vector on the projection planes and varies from 0 black to 1 white, corresponding to IP and OOP magnetization, respectively. The arrows on the projection images correspond to the main directions of magnetization vectors. Since the angles between neighboring faces are comparatively large, dihedral angle is  $\approx 138^\circ$ , the faces in the center of the projection are oriented only with  $21^\circ$  tilt from the perpendicular position relative to the beam direction. It gives good overview of the magnetization vector orientation with respect to the facet surface.

It can be seen in figure 7.15 g), h) and i) that magnetization vectors are mostly oriented in-plane of the faces that corresponds to white color on the projections. The surrounding faces which are observed under certain angle have a tilt out of projection plane and have darker color. The areas between faces with opposite direction of magnetization have also IP rotation of vectors over the edge that is seen on the images of YZ and XZ plane projections. The vortex like object is projected as a localized dark round domain at the projection on the XZ plane.

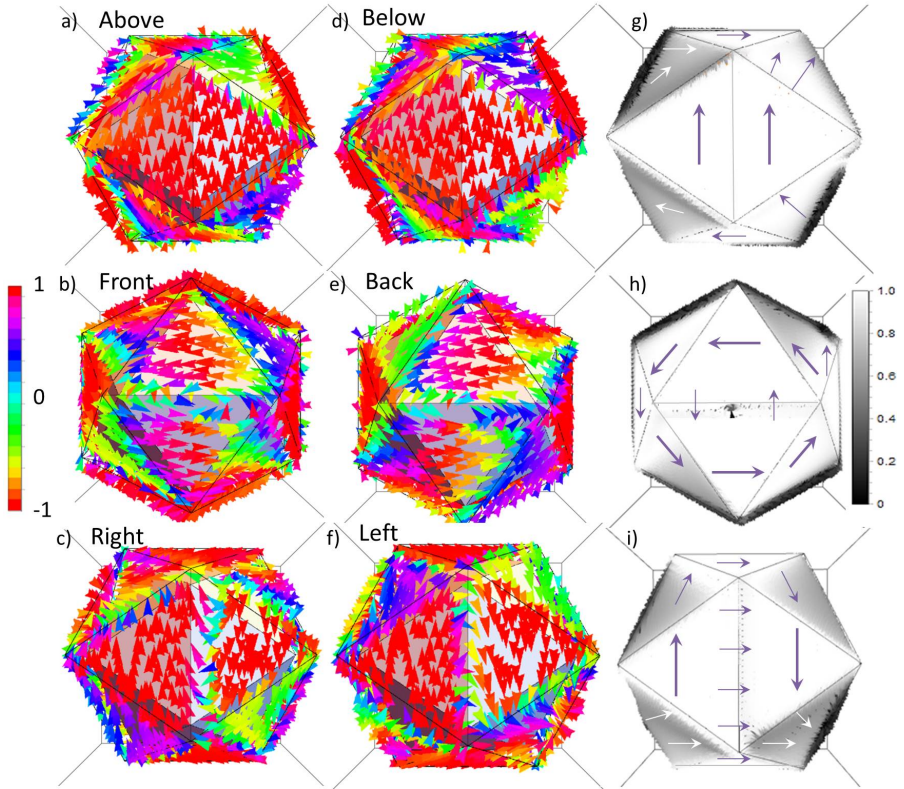


Figure 7.15: The magnetization of 700 nm big icosahedral particle shown from the different observation points as it is depicted in figure 7.14: a) above , b) front, c) right, d) below, e) back and f) left. The color refers to the orientation of magnetization relative to Z direction, with -1 anti-parallel and 1 parallel orientations; projections of magnetization vectors from the below, back and left observation points on the g) XY plane, h) XZ plane and i) YZ plane, respectively.

## 7.6.2 Magnetization simulation of pentagonal dipyramid shape

The simulation of magnetization of the pentagonal dipyramid shell was performed for 700 nm size as it is shown in figure 7.16. The above view shows that three faces magnetization bend around the pyramid surface in clockwise direction around the pyramid top, while 2 others have opposite vector direction (figure 7.17 a). The bottom view has 4 faces magnetized in clockwise direction while only 1 face has opposite magnetization direction (figure 7.17 d). For all configurations the vectors seem to be oriented in the face planes along the

base edge of the pyramid. The edges, where the faces with opposite magnetization start up or meet, have out-of-plane component and don't coincide for top and bottom pyramids. Front and back views show that the faces of upper and bottom pyramids magnetized in opposite direction (figure 7.17 b,e). Unlike in case with icosahedral particle we do not observe any specific magnetization turn on the junction due to much sharper angle between them.

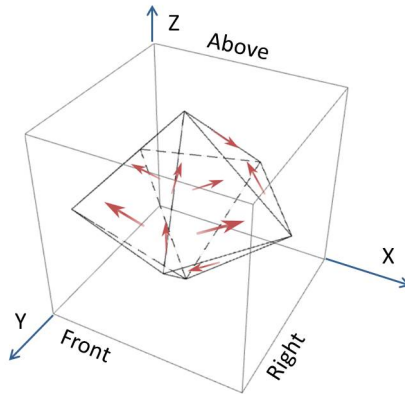


Figure 7.16: Pentagonal dipyrmaid shape of the particle in XYZ coordinates with marked views from above, right and front.

Figure 7.17 g), h) and i) shows the projections of magnetization vectors on the planes YZ, XZ and XY in a way as they would look in transmission images with beam as a normal of the according plane. The orientation of the particle in 3D space is given in figure 7.16 with corresponding views, from above, right and front. The magnetization on the two side edges mentioned before on XY projection has comparatively low out-of-plane component and is shown in light gray color. It can be explained with a small angle of about  $37.5^\circ$  between a side edge and base plane of the single pyramid. In general faces look uniformly magnetized in-plane, with magnetic contrast arising mostly from the different orientation angles of faces relative to the beam direction.

## 7.7 Magnetic ptychography on core-shells

For ptychographic imaging core-shell structures with the most defined shape of twinned particles have been selected by high-resolution SEM images, which allow to observe the particles from the upper side. The icosahedral particles have been more frequently observed than pentagonal dipyrramids. At 850 eV absorption Ni-edge and 5.3 cm sample to

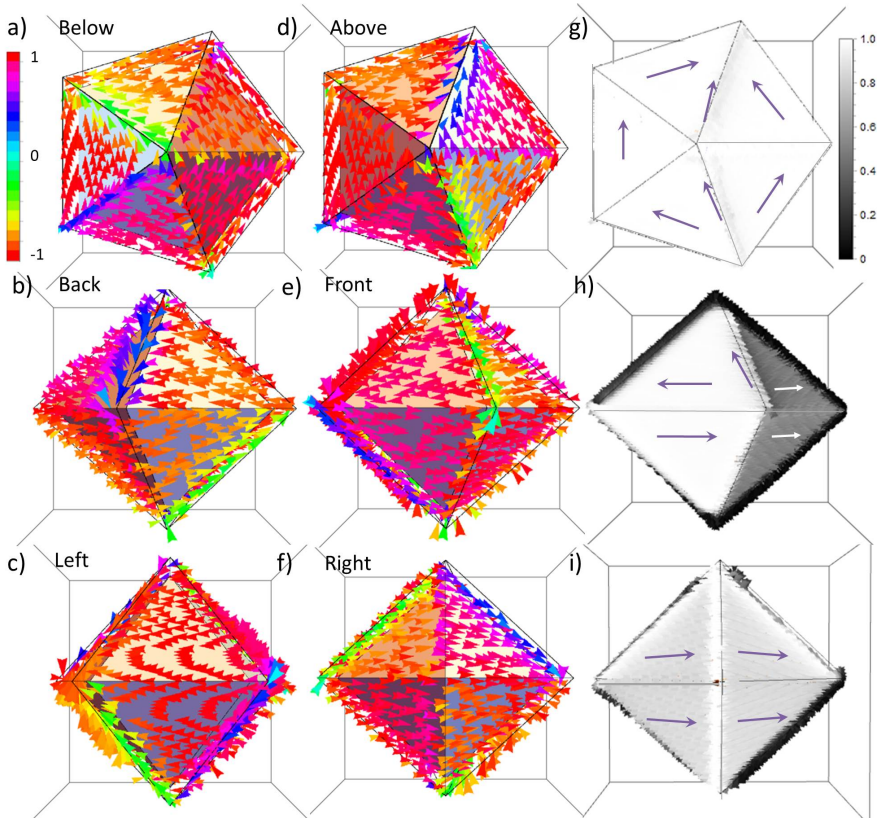


Figure 7.17: The magneization of 700 nm big pentagonal dipyrmaid particle shown from the different observation points as it is depicted in figure 7.16: a) below , b) back, c) left, d) above, e) front and f) right. The color refers to the orientation of magnetization relative to Z direction, with -1 anti-parallel and 1 parallel orientations; projections of magnetization vectors of above, front and right view on the g) XY plane, h) YZ plane and i) XZ plane, respectively.

detector distance pixel size of ptychography scan is 6.1 nm, at Cu-edge energy of 930 eV the pixel size is 5.6 nm. In order to perform measurements with applied external magnetic field the detector was moved away form the sample to the distance of 8.3 cm that corresponds to pixel sizes of 9.5 nm at Ni edge and 8.8 nm at Cu edge.

SEM image of 3D shaped particles with 500-700 nm sizes is presented in figure 7.18 a). The corresponding amplitude ptychography and STXM scans of the same particles are presented in 7.18 b) and c), respectively. The ptychography image exhibits more structural

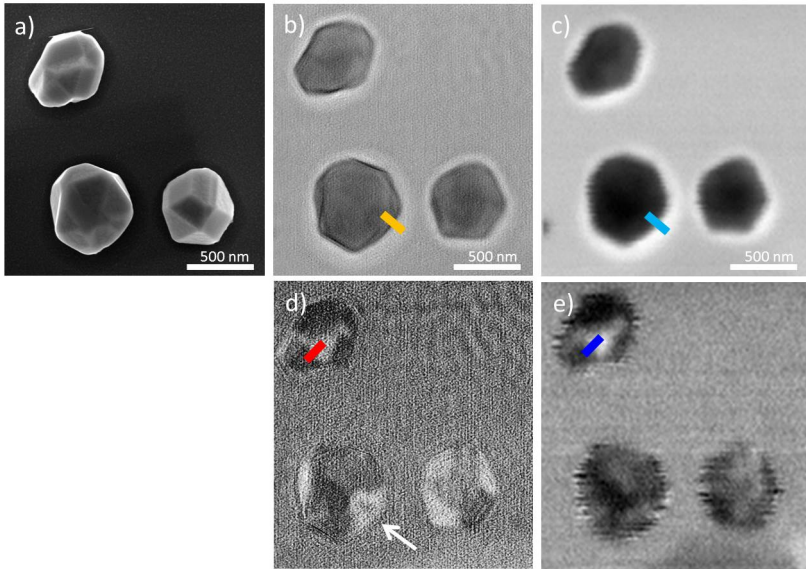


Figure 7.18: Images of core shell particles with 15 nm Ni thickness obtained with a) SEM, b) ptychography and c) STXM. XMCD images of the same particles were calculated from d) ptychography and e) STXM scans with left and right X-ray light polarization.

details on the edges of the particles.

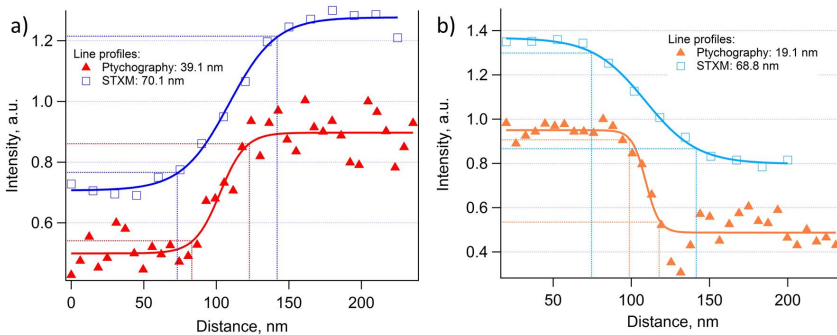


Figure 7.19: Line profiles over the a) magnetic and b) morphological edges of core shell particles shown in the figure 7.18.

The line profiles, marked by lines in figure 7.18, crossing the edge of a region with

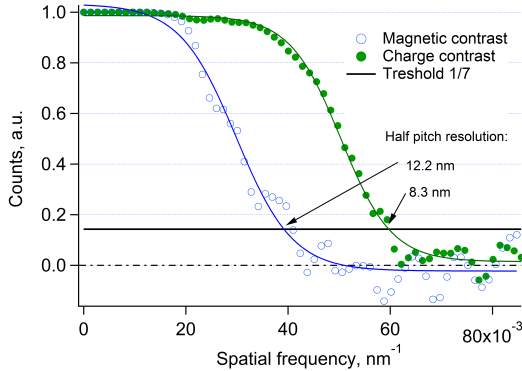


Figure 7.20: FRC graph of core shell ptychography image with charge and magnetic contrast with 1/7 threshold line. Output pixel size of the reconstructed image is 5.7 nm with half pitch image resolution of 8.3 nm for charge and 12.2 nm for magnetic contrast images.

different magnetization and the morphological edge were obtained from the same particles and presented in figure 7.19. The step width over the border of two magnetic domains resulted in 39.1 nm in ptychographic image versus 70.1 nm in STXM image, and respectively 19.1 nm and 68.8 nm over the morphological edge of the particle. STXM image suffers from the edge jitter because of the incorrect pixel distribution that is enhanced in XMCD image due to misalignment.

XMCD images showed that magnetic domains on the Ni shell are mostly governed by the facet shape providing a single domain phase on the flat crystal surfaces. Some smaller details in magnetization are revealed in the ptychographic image, for example, small line on one of the faces marked by arrow in figure 7.18 d).

FRC for resolution evaluation in figure 7.20 was obtained from the same diffraction data set divided into two subsets and reconstructed into two individual images. The output pixel size of the images was 6.1 nm. The FRC with 1/7 threshold level resulted in 8.3 nm half period resolution for charge and 12.2 nm for magnetic contrast.

In figure 7.21 three particles, which give an observation of icosahedral 3D shape from the different sides, are imaged with SEM and ptychography with the use of XMCD contrast. Since the average icosahedral angle is about  $138^\circ$  in case of normal beam orientation to one of the faces other ones would make around  $48^\circ$  relative to the beam direction. Even if all the faces in-plane magnetized we should see strong magnetic contrast provided by the orientations of face planes. In ptychographic XMCD images beside the uniformly magnetized faces the smaller magnetic features, like dots in images 7.21 a) and c) or a line along the face junction in image 7.21 b) marked with white arrows are observed.

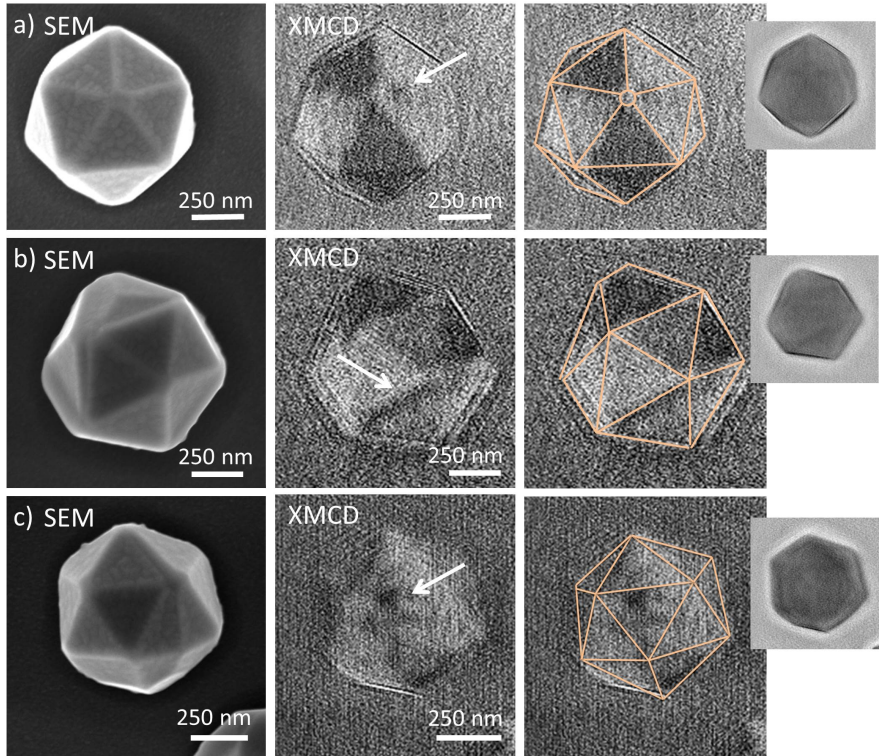


Figure 7.21: The particles a), b) and c), which have icosahedral shape, are imaged by SEM and ptychography using XMCD contrast. The last row images present XMCD ptychographic images with crystal edges marked by lines with smaller insets corresponding to amplitude ptychographic reconstructions.

The SEM images do not show any unexpected morphological features on the surface of these regions. Therefore the observed magnetic structures might be a result of geometrical whirling of vectors or structural impurities of Ni film. The size of the observed small domain in image 7.21 a) is around 40 nm, while in image 7.21 c) it is around 72 nm.

Some of the investigated particles showed undefined magnetization even exhibiting almost perfect pentagonal symmetry in their shapes. For example a particle in figure 7.21 c) has some unexpected minor magnetic domains in the central facet.

In figure 7.22 SEM and ptychographic XMCD images of core-shells with various and less defined shapes are shown. In image 7.22 a) a particle with big facet area of about  $460 \times 650$  nm elongated along one axis exhibits out-of-plane magnetization with multiple

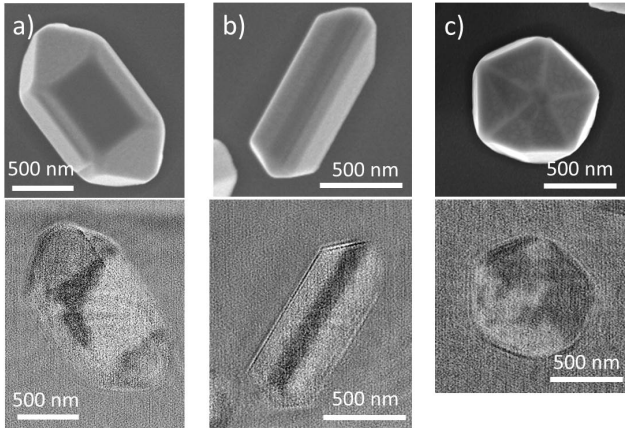


Figure 7.22: Core-shell particles with various shapes imaged by SEM and ptychography using XMCD contrast: a)  $1.5 \mu\text{m}$  big particle with a large facet area; b) extended along one symmetry axis; c) pentagonal pyramid with a flat profile.

domains in Ni shell within one face. Core-shells, extended along one symmetry axis and having narrow faces as it is shown in image 7.22 b), mostly have faces uniformly magnetized through all particle length. A particle in image 7.22 c) shaped as a pentagonal pyramid has small height to edge length ratio, that makes its profile flat. In this case the orientation angle between neighboring faces is too large and we observe magnetic domains going over the facet edges. The magnetization pattern on such particle surface is no longer defined by the particle geometry.

### Experimental data and simulations

The most of the core-shell particles have deviations from the ideal geometry of the simulated shapes. Additionally, they are oriented under different angles relative to the surface and only one side of the particle can be observed. Therefore in order to find a correct correspondence with simulated magnetization the estimation of particle position and shape is required. It has also to be considered that in some cases a particle is inhomogeneously covered with Ni that depends on its orientation and placing on the membrane. It might happen that the bottom part can be hardly reachable and get less Ni during the deposition. This fact can also affect the magnetization configuration, since simulation assumes homogeneous particle coverage with Ni.

The particle in figure 7.23 a) is turned with a pentagonal cap towards the beam with a slight tilt upwards, so that we can see side face on the bottom of the particle. X, Y and Z components of vector magnetization should be considered if we would look at the

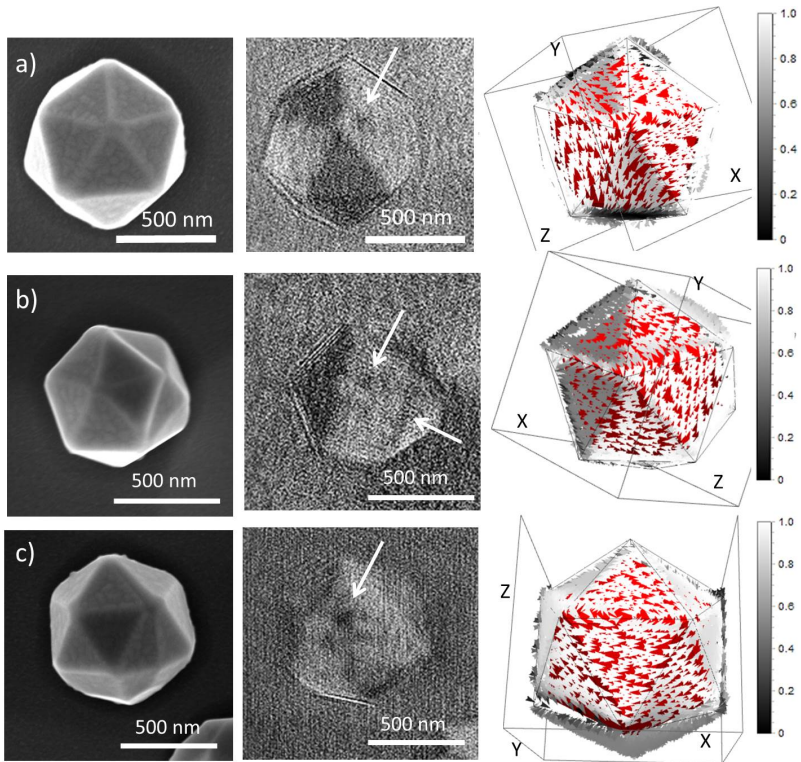


Figure 7.23: Icosahedral particles: imaged by SEM, the same particles in XMCD image obtained from ptychography measurements and simulated magnetization vectors. Red background here and after is used for better vectors visibility.

particle from right above with a small tilt from X axis. In this case we assume that our projection plane YZ is tilted for about  $30^\circ$  that corresponds to the peak of the side cap. Therefore the vector coordinates were corrected using Euler rotation matrix around Y axis, additional small tilt in X direction was not taken into account. Figure 7.23 a) shows simulated particle magnetization oriented in a way that it corresponds to the ptychographic image. On the both images we see only two faces having magnetization vectors pointing out of projection plane. These faces seem to be separate with some in-plane magnetized region on the top point of the pentagonal structure, that is observed in the measured data as well. A dark spot is seen on the edge of two faces with opposite magnetization which create a narrow region where vectors change their orientation for  $180^\circ$ . Since the precise angles of particle orientation relative to the beam direction are unknown only qualitative

estimation of measured and simulated magnetization can be done.

The same correction of vector coordinates has been done for particles in figure 7.23 b) and c) in order to get accurate vector projection from the certain rotation angles. The core shell in image 7.23 b) corresponds to  $60^\circ$  vector rotation around Z axis. In the simulated image we see two neighboring faces having dark magnetic contrast, while three others have magnetization almost parallel to the projection plane. It is similar to the measured data, although we see that the core-shell is partially distorted on its right side. This shape difference produces a morphological edge with a step that visible on SEM image and might be a source of a dark thin edge line on the XMCD image. Also a small magnetic domain of about 60 nm is observed near to one of the edge.

The core-shell in image 7.23 c) have round shaped 72 nm big magnetic domain right in the middle of the morphological edge, that has been observed in simulated data. If the vectors of the simulation have a turn for about  $30^\circ$  around X axis XZ projection would give similar particle orientation as it is imaged by ptychography. The magnetization on the side faces indeed looks inhomogeneous having relatively small magnetic contrast. The center of the whirl of the simulated magnetization vectors is located at the same position and potentially exhibit out-of-plane magnetization.

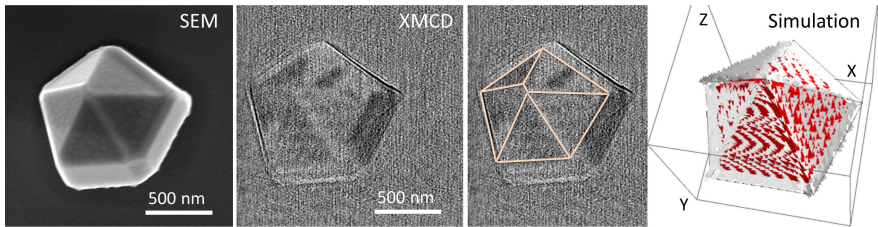


Figure 7.24: SEM, ptychographic XMCD and corresponding simulated magnetization images of core-shell particle shaped as pentagonal pyramid.

In figure 7.24 a pentagonal pyramid, only half of simulated dipyrmaid, is shown and oriented with its base slightly tilted out the substrate plane. For the magnetization vector correction the tilt in all three directions has been taken into account. The simulation of pentagonal shape showed that all faces have in-plane magnetization directed along the base edges of the pyramid. Therefore magnetic contrast of the facets mostly a result of its complex tilt. Additionally in the XMCD image the brighter magnetic contrast on the front edge is observed. This region corresponds to magnetization vectors oriented along the side edge. Some minor magnetic domains are present on the faces which are not shown in simulation and presumably caused by Ni film features.

## 7.8 Conclusion

The magnetization of separate 500-800 nm big core-shell particles with twinned symmetry crystal, i.e. icosahedral and pentagonal dipyramid shapes, have been studied with the use of X-ray ptychography. The half period of charge scattering resolution of obtained ptychographic images estimated with FRC is 8.3 nm for charge and 12.2 nm for magnetic contrast and showed significant improve in comparison with STXM images. It is possible that magnetic contrast in ptychographic images have been additionally enhanced due to strong scattering from the morphological edges of the facets.

Core-shell nano structures with Cu crystal core and epitaxially grown Ni film have been investigated and presented large diversity of particle shapes and sizes. Micromagnetic simulations of magnetization in Ni shell of twinned particles with complex geometries showed dependance of magnetization configuration on the 3D shape of the structure. It denotes the possibility to tailor the magnetic properties by changing the crystal geometries of the core. According to the simulation icosahedral shape has magnetization vectors wrapping around the particle and forming vortex like structures from the opposite sides of the shell. It happens due to comparatively big angles between neighboring facets in icosahedron, so it is close to the spherical shape. Pentagonal dipyramid simulation resulted in magnetization of two pyramids be quite independent from each other and have vectors laying in plane of the facets along the base edges. Unusual magnetization configurations occur on the junction areas right along the edges where facets with opposite magnetization meet. The cubic anisotropy simulations resulted in insignificant vectors turn more in the facet plane that corresponds to their reorientation along easy crystallography axis of magnetization. However the general magnetization configuration is determined by the shape anisotropy of Ni shell.

Ptychographic imaging showed more structural and magnetic details on the core-shell surfaces than STXM images that allowed to determine the complex multidomain state of the magnetic shell. Due to geometrical deviations of the real core-shell structures from the simulated ones the various magnetization configuration have been observed. Particles with comparatively big faces exhibit magnetic state with multiple domains, as the facet areas are big enough that single domain state is already energetically unfavorable. The small magnetic dot like domains of 40-70 nm diameter size have been observed on the face edges. The origin of these magnetic domains is geometrical or caused by magnetic domains pinning on the Ni film impurities caused by dislocations in the junction areas. The point like magnetic domains on the edges and line domains along the facet edges showed a good agreement with simulated data. The observed correspondence reveals that magnetization is governed by the particle shape and can be predicted and controllable modified by varying the angles between the facets. At the same time the reproducibility and homogeneity of the particle shapes have been found to be of a great importance for the magnetization studies.

# Chapter 8

## Summary and outlook

**Ptychography at MAXYMUS microscope** A new ptychographic imaging technique was implemented at the MAXYMUS beamline at BESSY II in Berlin as a part of this thesis. For this purpose a highly efficient, low read out noise and fast CCD camera, optimized for the soft X-ray range, was installed and commissioned. In order to produce ptychographic reconstructions a SHARP code developed at ALS (USA) was implemented on a computing cluster with 8 GPU processing units. In collaboration with Micro/Nano Optics group of department Schütz special Fresnel Zone Plates (FZPs) optimized for ptychographic imaging were designed and produced by ion beam lithography. They had an outermost zone width from 75 nm to 125 nm to speed up the data acquisition. The FZPs have been tested for diffraction efficiency at different X-ray energies to ensure a high photon flux in illumination spot in order to provide high scattering statistics in diffraction images of ptychographic scans. SiN FZPs with extra thick beamstop produced by laser lithography deposition exhibit highest efficiency of 8.0 % for the energies of 700-800 eV versus 0.51 % for conventionally produced Au FZP.

To optimize resolution and contrast of ptychographic reconstructions different scanning parameters, like overlap ratio of neighboring scanning points, defocused position, different numerical apertures, dwell time and degree of coherence, were tested using a strongly scattering Au Siemens Star pattern. The optimized overlap degree showed successful reconstruction results even with step size as big as focus spot. The larger step size reduces scanning time significantly, while the further increase of scanning step produces a grid artifact pattern. In defocused configuration the sample was moved back from the FZP that resulted in artifact free reconstructions with the step size 15 % bigger than illumination spot in the focused position. It proved independence of the method from the sample position relative to the focus of the used optics. The reduced photon flux in defocused position is a main limitation for this configuration application for low scattering specimens.

The tests with the real data set of the Siemens star sample showed the direct dependence from the pixel size of the reconstruction on the amount of diffraction orders captured by CCD. The imaging of 15 nm innermost feature size Siemens star with 12.5 nm output pixel size was performed in order to illustrate numerical aperture limited resolution of the used setup. Therefore for highly scattering samples the resolution is mostly determined by the pixel size of the reconstructed image.

Since the photon statistics in diffraction pattern is crucial for reconstruction quality the dependence of the image contrast on dwell time for highly scattering Siemens star and low scattering magnetic domain sample have been studied and showed different behaviour. The increase of dwell time for the charge scattering samples doesn't improve the reconstruction quality significantly. However for the magnetic sample the contrast improvement of 20 % with a plateau value around 300-400 ms is observed. The further increase of the dwell time did not show any changes in image quality. The degree of coherence of the beamline after aperture slit at FZP position and after FZP in the focus spot was evaluated for the set of different FZPs available at MAXYMUS. A confident agreement with experimental data for different degree of coherence obtained by the change of vertical slits opening have been observed at 1400 eV. If the coherent length is smaller than the focus spot the features of resolution target were not resolved. In general if FZP is illuminated coherently the coherence length in focus spot is always adequate for artifact free ptychographic reconstruction.

A set of research related samples, made from specific materials with high scattering, have been chosen for ptychographic imaging in order to test its perspectives for experimental use and to compare it with conventional STXM imaging. LiFePO<sub>4</sub> nano batteries with lithiated and delithiated phases showed profound resolution improvement on morphological edges as well as on the borders of the regions with different chemical states. Ptychography reveals structural details with sizes in order of few tens of the nanometer which can be hardly resolved with STXM. Desert varnish specimen consisting of ultra thin altering layers of Mn, Fe, Si and Al are found as a crust growing on the rocks in desert environments. Ptychographic images at Al-edge revealed 10 nm thick layering of the material that was never imaged or investigated before.

As a result the MAXYMUS microscope was successfully upgraded for high resolution ptychographic imaging of wide range of samples. The system allows ptychography with applied external magnetic fields, a possibility to rotate sample for 30° and use of a cooling device for low temperature measurements. The combination of the sensitive CCD camera with high read-out rate, the high efficiency FZPs and the powerful computing system allows realization of fast and reliable imaging of scientifically relevant samples. The resolution scales achieved using highly scattering samples resulted in a confident improvement in comparison with STXM allowing qualitatively new level in investigation of research related materials.

**Ptychographic magnetic imaging of skyrmions** Investigation of the skyrmionic state of multilayer samples using ptychographic imaging was a further subject of this thesis. Skyrmions are claimed to be promising candidates for spintronic applications. This would require an effective control over their sizes, which can be as small as few nanometers. Therefore high resolution imaging of small sub-100 nm skyrmions at room temperature would allow to investigate such specimens giving an insight in understanding of the role of various magnetic interactions occurring in various multilayer systems.

Different sets of multilayer samples [Pd and Ta/CoFeB(0.6nm)/MgO] $\times$ 15 and [Ta/CoFeB (wedge 0.78 - 1.45 nm) /MgO] $\times$ 15 with OOP easy axes have been imaged using ptychographic reconstructions with XMCD contrast. The existence of skyrmions is indicated to be in isolated state with sizes strongly varying in dependence on the used heavy metal. The sizes of domains and skyrmions were changed by applied external magnetic field perpendicular to the film surface. The temperature dependent SQUID characterization on the same samples has been performed to determine the accurate values of  $M_s$ ,  $K_{eff}$ , and  $A$ . The sample with lower  $K_{eff}$  showed much denser and smaller domain packing. DMI values were calculated using domain spacing model. The strong variation of the results and the deviation from various literature values proved a complexity of force interplay in multilayer systems that determines the skyrmion formation. Therefore, the size and stability of magnetic skyrmions are obviously correlated not only to the DMI, but also to the exchange interaction, anisotropy and dipolar interaction as well as the magnetization. All these values are found to be sensitively dependent on the layer composition, sample quality and defect structure.

A special focus was given on the comparison of STXM and ptychography in terms of magnetic sensitivity for imaging of skyrmions and domains. The contrast of two sets of images showed different behaviour depending on the size of observed magnetic features. In skyrmion state ptychography has a strong contrast drop due to reduced scattering that reflects on the background retrieval of the reconstruction process. In general, STXM showed to be more sensitive for the magnetic contrast at the samples with thinner ferromagnetic layer, which did not show any contrast at ptychography. At the domain state ptychography resulted in comparatively higher resolution for domain wall width with the image contrast and visibility much higher than at the STXM images. At the same time the method was used for collecting high amount of statistical data about shape and size of skyrmions. Due to large field of view and faster scanning it was possible to depict around 100 skyrmions within one image in the same time as 4 times smaller STXM image. The thorough investigation of shape change of the separate skyrmions depending on the applied magnetic field has been done and showed some uniaxial misshape.

Ptychography showed certain advantages as a research instrument due to suitability for extended area imaging and fast scanning. Additionally it provides phase information that allows direct estimation of the magnetic scattering factors of studied materials.

**Core-shell magnetization** Magnetization of complex 3D geometrical shapes has been studied with ptychography on core-shell Cu-Ni nanoparticles. The thin magnetic film deposited on a curved or bended substrate possesses complex multi domain state that is determined by the shape of the substrate and influences their magnetic response. Characteristic length scales of magnetic features induced by magnetochiral effects and topology due to a DMI-like interaction have been studied in the tens of nanometer regime by ptychography. Ni grown by epitaxy on top of variously shaped polycrystalline Cu structures showed shape anisotropy with in-plane easy axis. 3D shaped magnetic particles on the membrane result in additional magnetic component causing saturation of OOP magnetization at different values of applied external field. STXM images with bias magnetic field showed that speed of re-magnetization of the particle facets along applied field is determined by their orientation to the membrane surface.

The fabricated particles exhibited various shapes, sizes and ratio of their spatial lengths and were pre-characterized with SEM. The XMCD ptychography revealed smaller magnetic structures, in a range of 40-50 nm, which were not observed with STXM. Magnetic ptychographic contrast was additionally enhanced by strong scattering from morphological edges, which in some cases coincided with the borders of magnetic domains.

In order to understand the magnetization behaviour of separate particles micromagnetic simulations were performed for different geometrical shapes. The python code for simulation of shape dependent magnetization has been developed for the Micro Magnum simulation environment. The results showed correspondence with experimental ptychography data and predict the magnetization configurations on different particle faces. The magnetization vectors are “wrapped” around the particle with interaction of neighbouring faces dependent on their mutual orientation angle. In particular edge effects and small dot domains, supposedly vortex like magnetization, have been imaged. Simulation with applied OOP external magnetic film stayed in agreement with the experiment showing in-plane magnetization component for the separate faces laying almost perpendicular to the beam direction. Due to high resolution of ptychography it was observed that at the facets of the real core shell particle in contrast to the expected singles domain state a multi-domain structure can be favoured.

This preliminary study indicates that ptychography has a big potential for imaging of such complex structures. In combination with strong chemical and morphological scattering components from particle edges it provides magnetically sensitive imaging with resolution higher than STXM imaging.

**Outlook** This study has shown promising results for magnetic sensitive X-ray ptychography that in some particular applications revealed details which are not resolved by conventional STXM imaging or other methods. The further steps for the method development at MAXYMUS beamline would be the implementation of ptychographic time-resolved imaging of magnetic structures, as well as 3D tomography for imaging of the bulk sam-

ples or samples with 3D shape as used in this thesis. In order to perform measurements in 3D mode the rotating sample holder with goniometric system must be implemented, that is technically possible in the existing set up. The late ptychography studies [189, 190] showed a potential for high resolution 3D ptychographic tomography even for magnetic material application [191]. Some approaches for time-resolved ptychography have been proposed earlier in [192] and use single-shot ptychography approach for reconstruction of multiple frames from a single camera snapshot with 150 ps temporal resolution. For the time resolved imaging of magnetic structure pump-and-probe synchronized system for ptychographic application has to be realized.

For the higher sensitivity of pure magnetic contrast in ptychographic images the reconstruction algorithm has to be tuned by enforcing background retrieval to enhance the weak contrast of imaged structures.

# Appendix A

## Ptychographic reconstruction engine at MAXYMUS

### A.1 Reconstruction software

A few software packages [193, 194] have been developed for reliable performance in experimental application.

Ptychographic reconstruction at MAXYMUS microscope was performed with CUDA based SHARP software (Scalable Heterogeneous Adaptive Real-time Ptychography) initially developed for the ptychographic setup at the Advanced Light Source [195, 196]. The thorough description of the SHARP software based on the iterative phase retrieval algorithm (see the Chapter 3) is presented in [97]. Here the basic sequence of algorithm is presented. A typical reconstruction includes following steps:

- Input data are provided in CXI file format and include set of diffraction patterns  $I(q)$  and translation matrix  $x$  that contains coordinates of the sample subregions.
- If initially not provided, an illumination  $w^{(0)}$  is generated as a Fourier transform of the square root of the average frame. If initial image  $\varphi^{(0)}$  is not included in input CXI file it is built by producing the image with randomly distributed values in the range of  $[0,1)$ .
- Generation of the illumination operator  $Q$ , which scales the extracted frame point-wise by the illumination function  $w$ . Additionally  $Q^*$ ,  $(Q^*Q)^{(-1)}$  and frames  $z^{(0)} = Qw^{(0)}$  are determined.

- Each frame  $z$  is updated according to [197] projector operators  $P_Q$  and  $P_a$ :

$$z^{(l)} := [2\beta P_Q P_a + (1 - 2\beta)P_a + \beta(P_Q - I)]z^{(l-1)}, \quad (\text{A.1})$$

where  $I$  is the identity operator,  $\beta \in (0.5, 1]$  is a scalar value of Relaxed Averaged Alternating Reflection (RAAR) algorithm,  $P_a$  is a projection function, which ensures that the frame  $z$  matches the experiment, and  $P_Q$  is a projection function, which checks that overlapping frames are consistent with each other.

- The image  $\varphi^{(l)}$  is updated using the expression:

$$\varphi \leftarrow \frac{Q^* z}{Q^* Q} \quad (\text{A.2})$$

- The new illumination function  $w$  is calculated from the object function  $\varphi$  and updated frame  $z$ . The illumination Fourier mask and the illumination Fourier intensities constraints are applied in order to improve the contrast of high frequencies signal. The center of mass of illumination is computed and shifted for the fixed translation of the object.
- Background retrieval can be performed by the estimation of static background and its removal in the iteration as described in [198].
- To monitor the progress of the reconstruction metrics Fourier error  $\epsilon_a(z)$  and overlap error  $\epsilon_Q(z)$  are used. When one of the metrics drops below the limit, defined by a user, the iterative process will be stopped. The metrics are defined as the normalized mean square root error of the corresponding projection  $z$ :

$$\epsilon_a(z) = \frac{\|(P_a - I)z\|}{\|a\|} \quad (\text{A.3})$$

$$\epsilon_Q(z) = \frac{\|(P_Q - I)z\|}{\|a\|} \quad (\text{A.4})$$

At the end of the iterative process reconstructions real and imaginary parts of illumination function  $w$  and object function  $\varphi$  are returned.

- Images of the phase,  $\phi$ , and amplitude,  $A$ , are calculated from real and imaginary parts of the reconstruction as following:

$$\phi = \arctan \frac{\text{Imag}}{\text{Real}}, \quad (\text{A.5})$$

$$A = \sqrt{\text{Real}^2 + \text{Imag}^2}. \quad (\text{A.6})$$

## A.2 Computing power

The code is implemented in CUDA, running in NVIDIA GPU environment. The parameters of reconstructing computer, which was installed at MAXYMUS microscope for ptychographic data processing, are listed in the table A.1.

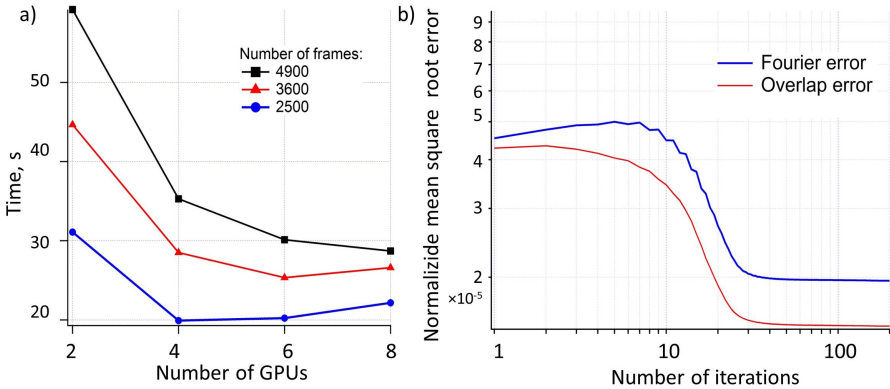


Figure A.1: Performance of the reconstruction process: a) time for the reconstruction of images with different amount of frames: 4900, 3600, 2500. The images were reconstructed with 200 iterations including time for calculation of initial illumination profile and initial object image; b) Fourier and overlap errors of Siemens Star reconstruction of size  $20 \times 20$  frames made with 200 iterations.

The computing cluster has 8 GPUs that allows processing the images up to  $170 \times 170$  frames. The number of GPUs to be used can be selected by the user before reconstruction process. To provide the optimal timing of reconstruction the amount of frames per GPU shouldn't be lower then 600 frames, otherwise frames division and afterward summing over the multiple GPUs result in increase of the total reconstruction time. As it is shown in figure A.1 a) big amount of GPUs for the reconstruction of comparatively small images,  $50 \times 50$  or  $60 \times 60$  frames, leads to increase of the time that is caused by inefficient frames distribution. The calculation of the error metrics obtained for the reconstruction of Siemens Star resolution target run with 200 iterations is presented in figure A.1 b). It shows that ptychographic reconstruction reaches a stable solution after about 60 iterations. Further increase of the number of iterations ( $>400$ ) doesn't improve the output image and in some cases causes the rise of reconstruction errors.

The figures A.2 a) and b) show the characteristic reconstruction of phase and amplitude of the illumination function obtained from the simulated data. The line profile through the middle of the amplitude in figure A.2 c) shows the expected illumination intensity profile in the FZP focal plane.

Parameter	Value
Number of GPUs	8
Cuda cores	24576
GPU memory	96 GB
RAM CPU	128 GB
Performance	up to 56 TFlops single precision floating point (peak); up to 1.6 TFlops double precision floating point (peak)
Data storage	36 TB storage, 1 TB SSD working volume

Table A.1: Parameters of ptychography reconstructing computer at MAXYMUS.

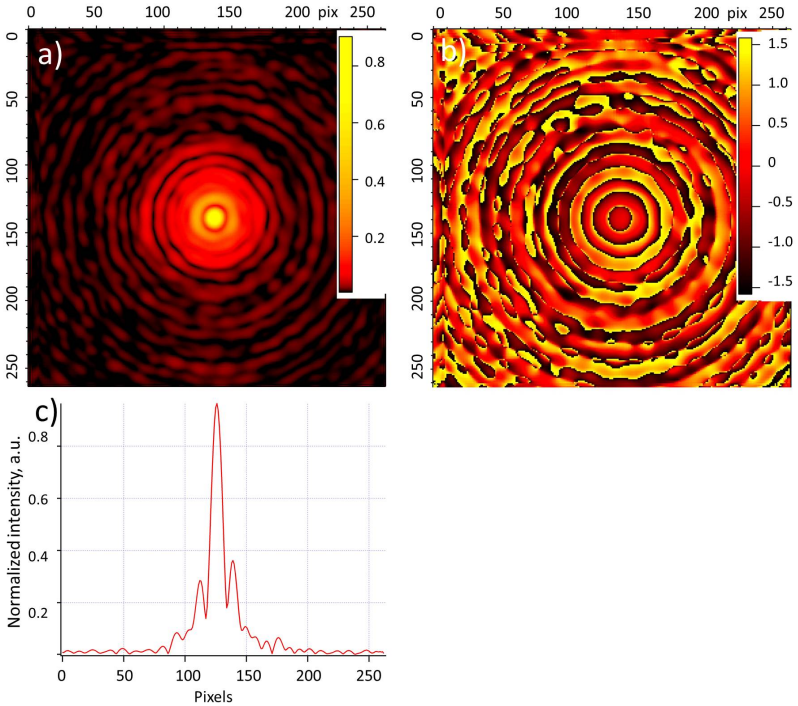


Figure A.2: a) Amplitude and b) phase reconstruction in radians of illumination function of a simulated data set; c) profile of the center of illumination amplitude.

# Appendix B

## Phase imaging and phase information

### B.1 Interpretation of phase information

The retrieval of phase information is one of the main advantages of ptychographic imaging. Reconstructed phase image gives an enhanced contrast of weakly absorbing objects. The phase information can be used to calculate electron density and mass density of an investigated specimen. The phase image contrast is proportional to  $2\pi\delta t/\lambda$ , while the natural log of the amplitude image gives  $2\pi\beta t/\lambda$ . In order to evaluate the correctness of the reconstructed phase image the thickness of resolution target Siemens Star with height of structures of  $150\text{ nm} \pm 10\%$  is calculated. The refraction index component  $\delta = 0.0028543$  for Au at 800 eV X-ray energy.

The phase reconstruction was corrected by background image subtraction (figure B.1 a) in order to minimize effect of carbon contamination in the center of Siemens Star. The background image was generated from the phase image using Subtract background tool in ImageJ package. According to the calculated image in figure B.1 b) the height of the structures in the inner circle is  $127 \pm 25\text{ nm}$ , the second row with bigger structures has  $135 \pm 25\text{ nm}$  in height. A slight deviation from the expected values might be explained by the real discrepancy of the height of 30 nm structures to the specification data. That might occur due to difficulty to produce structures with the same height to thickness aspect ratio for all resolution features during fabrication process. The tendency of the structure height growth towards outer circles with bigger structures allows to conclude so. Another possible source of inaccuracy is the background correction that has the most significant impact in the area with the smallest structures.

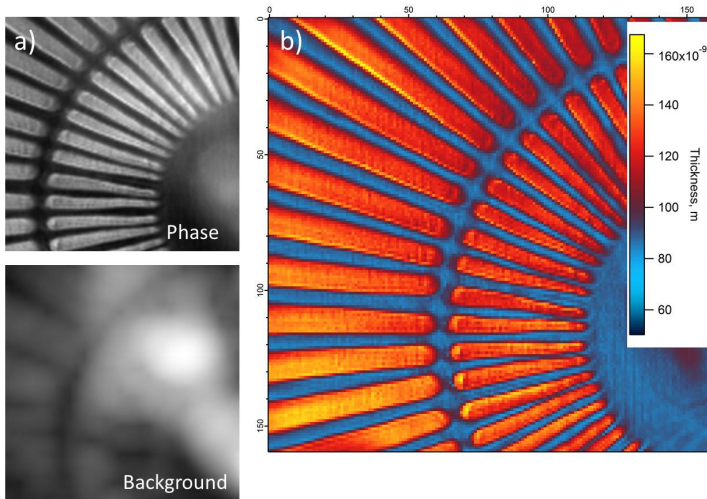


Figure B.1: Estimation of the height of the Siemens Star 30 nm big structures using phase contrast: a) phase reconstruction of Siemens star and background correction image; b) calculated thickness of the Siemens Star from the phase image.

## B.2 Artifacts

it occurs very often that ptychographic phase reconstructions suffer from the different types of imaging artifacts. One of them is phase halo that is known from optical phase sensitive microscopy and Zernike X-ray microscopy [199]. This effect is pronounced whenever there is a significant difference in the indices of refraction between the neighboring sample regions. Figure B.2 a) shows the ptychographic phase reconstruction of  $\text{LiFePO}_4$  nanoplate imaged on Fe absorption edge (see Chapter 5.1). The areas with different oxidation states show different contrast of halo occurring at the edge of the particle. Whether it is bright or dark contrast is determined by the ratio of the phase shift in the particle itself and in the background media. So the center part of the nanoplate produces dark halo on the border with background that has lower phase shift as it is seen from the graph in figure B.2 b). The dark regions of nanoplate have bright halo because the phase shift is smaller than in background media (figure B.2 c). The bright halo near the sample edge is a result of refracted X-rays on the interface which is summed up with the direct beam outside the sample area [200]. This effect is a limiting factor for studying process occurring at the edges of a specimen since it is hard to distinguish the real features contrast and contrast coming from the halo artifacts. However it is observed only at the samples exhibiting sharp morphological edges.

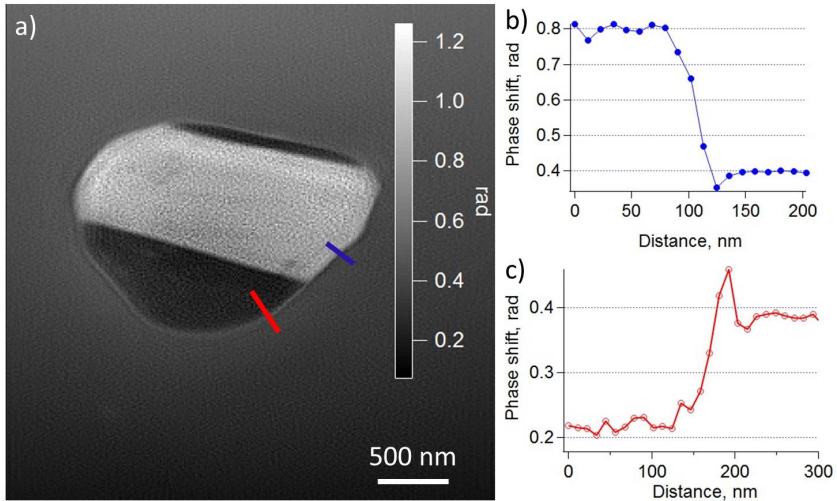


Figure B.2: Edge artifacts: a) phase image of LiFePO<sub>4</sub> nanoplate obtained by ptychography showing halo artifact; b) line profile corresponding to the blue line and c) line profile corresponding to the red line in the image a).

Another possible artifact leading to incorrect phase image projection is a missing or incorrect unwrapping of the phase. The phase difference bigger than  $\pi$  results in incorrect phase unwrapping. The phase wrapping is shown in figure B.3 a) that is projected as a black area with big negative values in the region supposedly having positive phase shift. The figure B.3 b) is a corrected phase image obtained by changing the values which have jumps greater than  $\pi$  to their  $2\pi$  complement. This process is called phase unwrapping that is free from  $2\pi$  jumps and returns the wrapped phase to a continuous phase signal. The image was corrected using Python programming language.

Another source of error is differential phase clipping which occurs when the phase changes within one pixel. Mainly it happens at the edges of highly scattering objects, when the change of the phase from background to the particle is comparatively high.

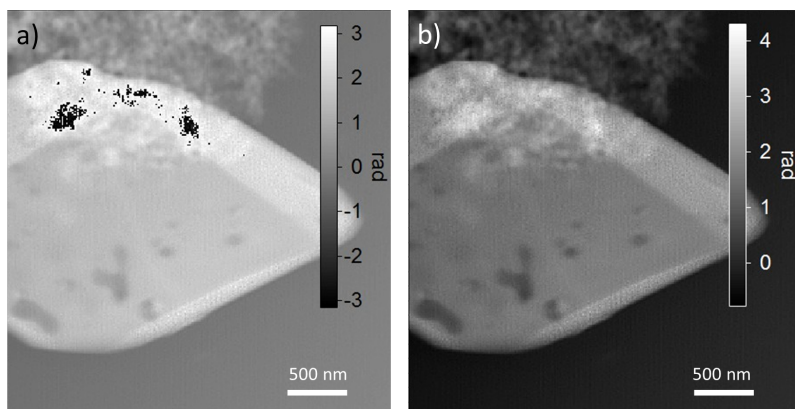


Figure B.3: Phase images of LiFePO<sub>4</sub> nanoplate: a) shows the wrapping of the phase to negative values that cause incorrect color projection, b) corrected phase image.

# Appendix C

## Methods for resolution evaluation

Spatial resolution is a fundamental parameter of any imaging technique. As it was discussed in the previous chapters resolution of a reconstructed ptychographic image depends on many experimental factors: scattering power of sample, coherence, numerical aperture of detector, as well as external noises and sample deformations. Therefore resolving power of ptychography must be analyzed using the reconstructed image itself. Beside the conventional methods of resolution evaluation, e.g. imaging of test targets or measurement of step profile of the regions with different contrast, there are methods which examine image resolution in the Fourier space, described in literature [201, 202, 203, 204]. In the current work power spectral density (PSD) and Fourier ring correlation (FRC) are used.

**Power spectral density (PSD)** shows the strength of the signal in reciprocal space as a function of frequency. In this case resolution of the image is estimated as a signal power depending on the spatial frequency in Fourier space. It derived as following:

$$PSD = FT[\rho(r)], \tag{C.1}$$

where  $\rho(r) = x(r) \cdot x(-r)$  is an auto-correlation function of the signal  $x(r)$ . The 2D PSD function is presented as a 1D radial profile spectrum over all  $\varphi$  in reciprocal space. The spatial frequency analysis indicates the achievable reconstruction resolution that is determined as a double level of statistical noise. The flat profile at the highest frequencies end of PSD curve can be regarded as the noise level.

**Fourier ring correlation (FRC)** is a method that initially was used for the evaluation of resolution in electron microscopy [202]. However it became commonly used for diffraction imaging techniques. FRC estimates the similarity of two independent ptychographic reconstructions of the same sample in the reciprocal space. It determines the resolution threshold at which both reconstructions are consistent. To calculate the correlation a diffraction data set of one image has to be split into two sets and reconstructed

into two independent images, which then are Fourier transformed and multiplied. The normalized average correlation is computed for  $N_r$  concentric rings of increasing radius, which correspond to increasing spatial frequencies in the Fourier space, and expressed as following:

$$FRC(R) = \frac{\sum_{i \in R} I_1(r_i) I_2(r_i)^*}{\sqrt{(\sum_{i \in R} |I_1(r_i)|^2) \cdot (\sum_{i \in R} |I_2(r_i)|^2)}}, \quad (C.2)$$

where  $R$  - ring number,  $r_i$  - the individual pixel at radius  $R$ ,  $I_1$  and  $I_2$  Fourier transforms of two ptychography images. The number of rings determines the binning of the FRC curve. Determination of resolution in FRC is still controversial issue [205]. Currently three basic threshold methods are used:

- The  $1/2$  - *bit* threshold is a method when the intersection of the threshold line with the FRC curve defines the point where information per pixel is equal to  $1/2$  bit.
- The fixed threshold of 0.143 [206] that is an estimated value representing the average signal-to-noise ratio in a reciprocal space resolution ring and the error in the structure factors.
- The threshold of  $\sigma$ -factor aims to determine the high-frequency limit, where the signal stays significantly above the random-noise level. So the intersection of the FRC curve with this threshold line corresponds to the value where the FRC begins primarily represent high frequency noise.

The described methods are used for resolution evaluation in this thesis.

## Appendix D

# Magnetic properties of skyrmion multilayer with different thickness of ferromagnetic layer

Multilayer films Ta(5)/[CoFeB(1.1 nm wedge)/MgO(2)/Ta(3)]15 (numbers are thickness of layer in nm) with total CoFeB layer thicknesses between 11.55 and 21.75 nm have been magnetically investigated by SQUID magnetometry at different temperatures from 5 to 350 K. The samples were numbered from 1 to 7 in accordance with the FeCoB single layer thickness as following: No.1=0.8 nm, No.2=0.9 nm, No.3=1.0 nm, No.4=1.1 nm, No.5=1.2 nm, No.6=1.3 nm, No.7=1.4 nm.

The intrinsic magnetic material parameters were determined: saturation polarization  $J_s$  (or saturation magnetization  $M_s = J_s/\mu_0$ ), exchange constant  $A$  and magnetocrystalline anisotropy constant  $K_1$  as it is shown in figures D.1 and D.2.

The saturation polarization  $J_s$  is directly obtained with the approach to saturation of the magnetic polarization in the OOP hysteresis loops shown in figures D.3, D.4, D.5. The samples with higher CoFeB layer thicknesses have larger  $J_s$  values for a given temperature as it is seen from figure D.1 a). The exchange constant  $A$  relates to the strength of interaction between neighboring magnetic moments due to exchange interaction and cannot be determined directly. It is evaluated as a function of temperature from the temperature dependence of the saturation polarization, that is given as following:

$$A(T) = \frac{J_s(T)D_{sp}}{2g\mu_0\mu_B} = \frac{J_s(T)k_B T_C}{2g\mu_0\mu_B} \left( \frac{0.117\mu_0\mu_B}{J_s(0)} \right)^{2/3}, \quad (\text{D.1})$$

where the parameter  $g$  is the Landé g-factor,  $D_{sp}$  is the spin wave stiffness constant,  $\mu_B =$

$9.274 \times 10^{-24}$  A/m is the Bohr magneton,  $J_s(0)$  describes the spontaneous magnetic polarization at  $T = 0$  K,  $T_C$  is the Curie temperature and  $k_B$  is the Boltzmann constant. The parameters  $J_s(0)$  and  $T_C$  can be determined by plotting  $J_s(T)$  versus  $(T/T_0)^{3/2}$  and extrapolating it to the axes. The exchange constant continuously increases with increasing of CoFeB thickness as it is seen from figure D.1 b).

The anisotropy describes the energy required to rotate the magnetization vector from easy to hard direction in ferromagnetic. The temperature dependent magnetocrystalline anisotropy constant  $K_1(T)$  for skyrmion samples have been determined by using following expression:

$$K_1(T) = K_1(0) \left( \frac{J_s(T)}{J_s(0)} \right)^3 \quad (\text{D.2})$$

Initially the  $K_1(0)$  values have been obtained by inserting the experimentally derived  $K_1(RT)$  and  $J_s(RT)$  values into equation D.2. Opposite to the behavior observed for the saturation polarization  $J_s$  and exchange constant  $A$  the magneto-crystalline anisotropy constant decreases with the increase of CoFeB thickness as it is shown in figure D.2.

Curie temperature  $T_c$  can strongly depend on the thickness of ferromagnetic layer. It is found to drop significantly for the Ta systems as it is shown in figure D.6.

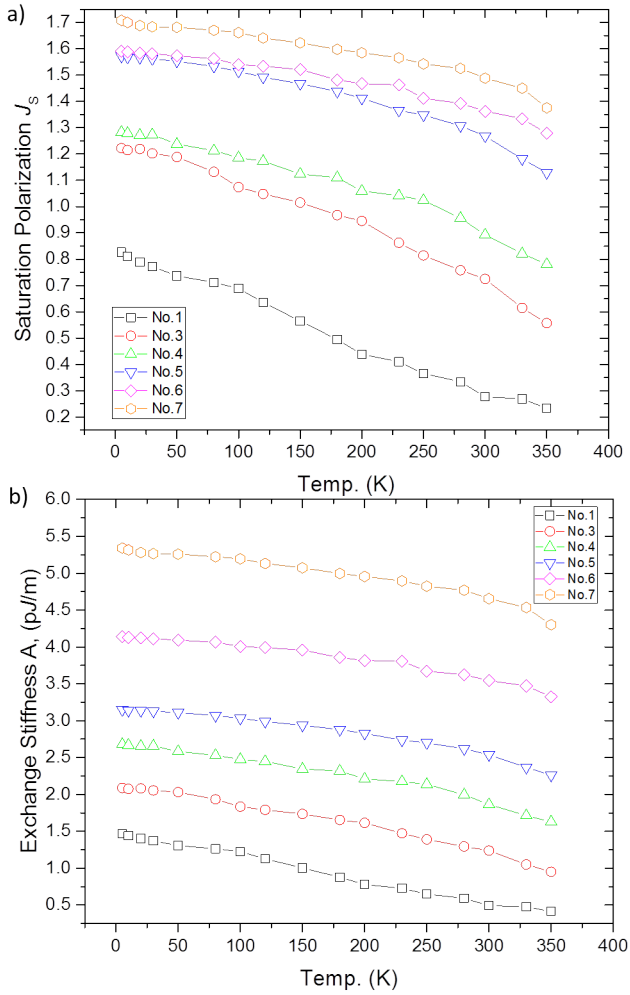


Figure D.1: Temperature dependent magnetic properties of Ta/CoFeB/MgO/Ta skyrmion samples with different thickness of ferromagnetic layer: a) polarization saturation  $J_s$  and b) exchange stiffness  $A_e$ .

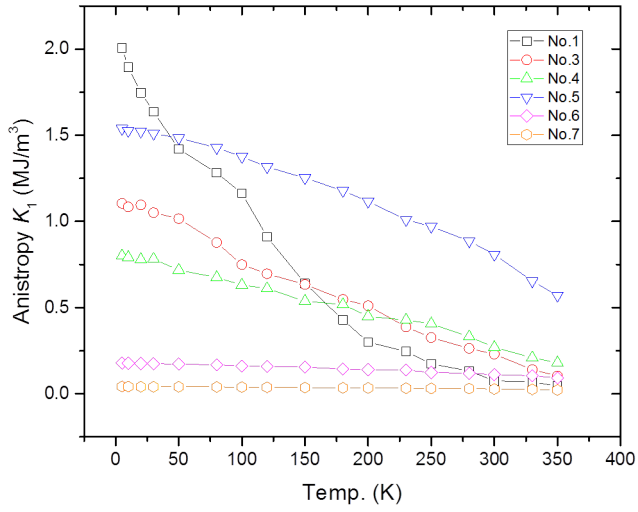


Figure D.2: Temperature dependent anisotropy constant  $K_1$  of Ta/CoFeB/MgO/Ta skyrmion samples with different thickness of ferromagnetic layer.

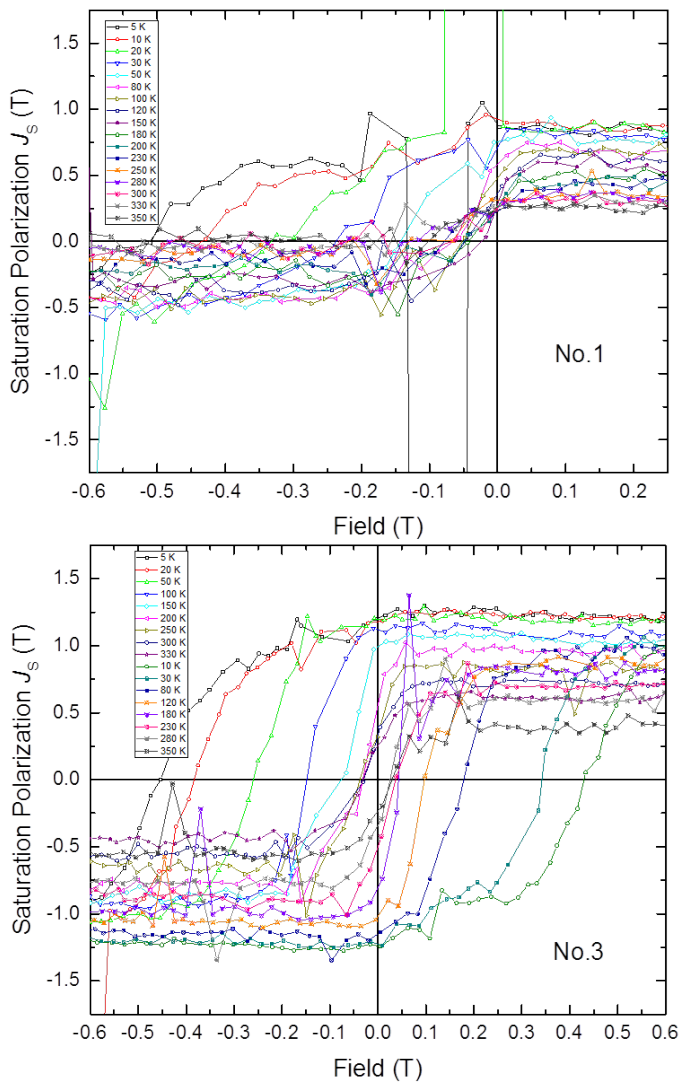


Figure D.3: Temperature dependent hysteresis loops for skyrmion samples No. 1 and 3.

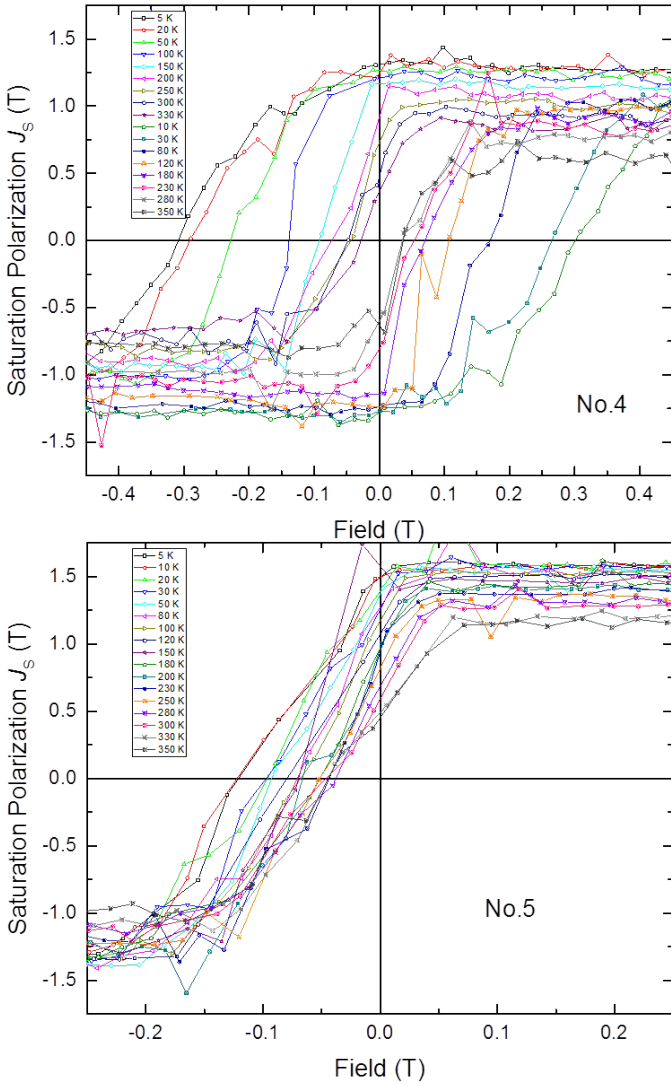


Figure D.4: Temperature dependent hysteresis loops for skyrmion samples No. 4 and 5.

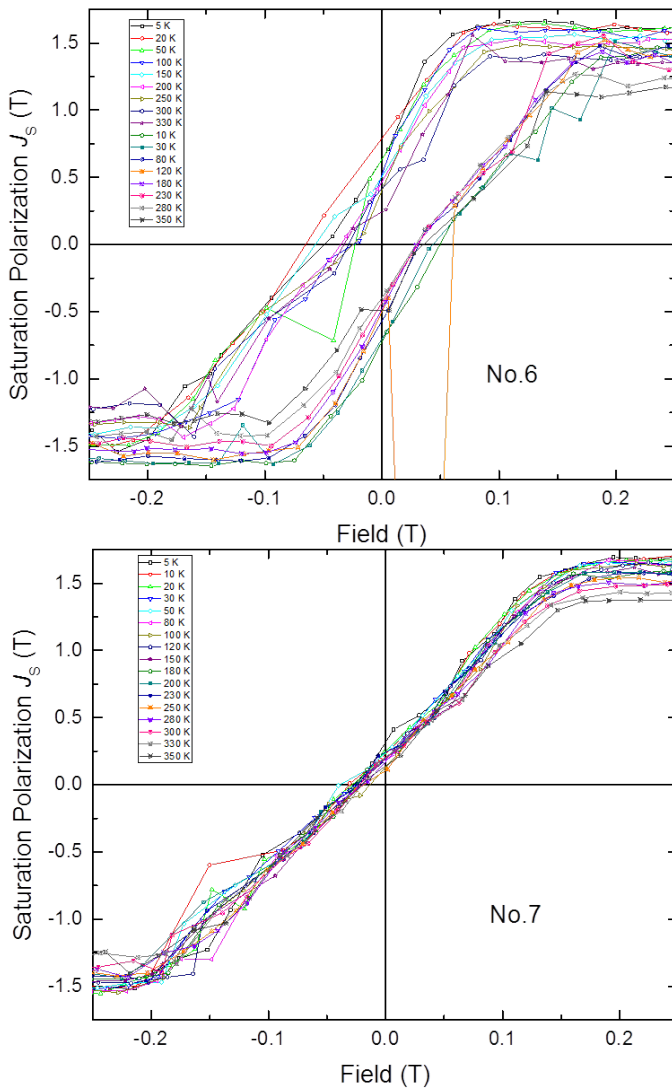


Figure D.5: Temperature dependent hysteresis loops for skyrmion samples No. 6 and 7.

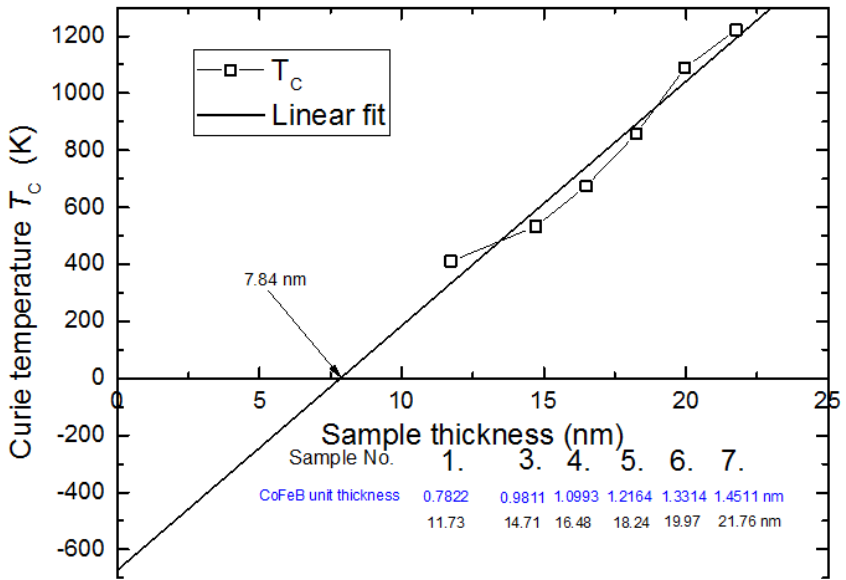


Figure D.6: Dependence of Curie temperature on the thickness of CoFeB layer in skyrmion multi-layer.

# Appendix E

## Magnetisation simulation of nanoparticle Ni shell

### E.1 Cell size of the simulations

The cell size requirement for the simulation is defined by the exchange length of Ni, which is 9.9 nm. Since the thickness of Ni core is 15 nm the cell size of 5 nm was chosen that assures the complete coverage of the surface of simulated volume with square subunits. The size of the cell determines the processing time of simulations, since the total amount of calculated points is scaled with a cube of the cell size. Amount of simulated cells is also limited by computational power of the GPUs: the maximum total particle size is  $255 \times 255 \times 255$  for 1 GPU.

The simulated shell volume was calculated as a difference of the total volume of the particle and the core volume. In order to estimate the simulated shell volume let's consider icosahedron shape. The volume of icosahedron shell is determined as:

$$V = \frac{5(3 + \sqrt{5})}{12} (a_{part}^3 - a_{core}^3), \quad (E.1)$$

where  $a_{part}$  and  $a_{core}$  are the edge lengths of the whole particle and the core, respectively. If particle size is 700 nm and  $a_{part}=368$  nm the simulated volume is  $1.27 \cdot 10^7 \text{ nm}^3$ . Using 5 nm cell size it results in  $1.02 \cdot 10^5$  simulated cells in total. All the values related to the core of the particle are set to zero.

## E.2 Icosahedral particle

The following simulations have been performed for the different sizes of the core-shell particles: 300 nm, 500 nm and 700 nm. The basic parameters of particle sizes are present in the table E.1.

Total size ( <i>nm</i> )	Edge length ( <i>nm</i> )	Face area ( $\mu m^2$ )
300	157	0.01
500	263	0.03
700	368	0.06

Table E.1: Parameters of the simulated icosahedral shapes.

The thickness of Ni shell of 15 nm have been simulated with and without cubic anisotropy. Figure E.1 shows all 6 configurations for different core shell sizes and anisotropy considerations. The color of the magnetization vectors presents their orientation relative to Z direction and gives general view on the magnetization on the particle surface. As it is seen from the 3D views of the simulations there are insignificant changes in magnetization whether the cubic anisotropy is taken into account or not. The minor differences in the facet planes are observed in the bigger 700 nm particles that might be caused by the larger facet area. Cubic anisotropy changes the magnetization vectors relative to Z direction, for example the light green face gets yellow coloring in the case when cubic anisotropy is present. It means that magnetization tends to orient in the direction of its easy crystallographic axis, in Ni FCC it is [111] direction. If Ni film is grown on (111) icosahedral face it gives higher in-plane component for magnetization vectors, that we observe in the simulation. Since the particles of 500 nm and 700 nm in size have larger facets the magnetization looks more regular, the edge effects are scaled down and look more localized.

## E.3 Pentagonal dipyramid particle

The magnetization simulations of Ni pentagonal dipyramid shells of different sizes, 300, 500 and 700 nm, as well as with and without cubic anisotropy are shown in figure E.2.

We assume that each pyramid consist of 5 tetrahedrons with a right angle and equal edges on the front side of the pyramid. The basic parameters of the simulated particles are listed in the table E.2. The areas of the faces are almost twice bigger than face areas in icosahedral particles with the corresponding total sizes. The angle between faces of two pyramids is about  $75^\circ$ , which is steeper than the angle between faces of the separate pentagonal pyramid,  $108^\circ$ . The color scale of the faces reflects magnetization vector

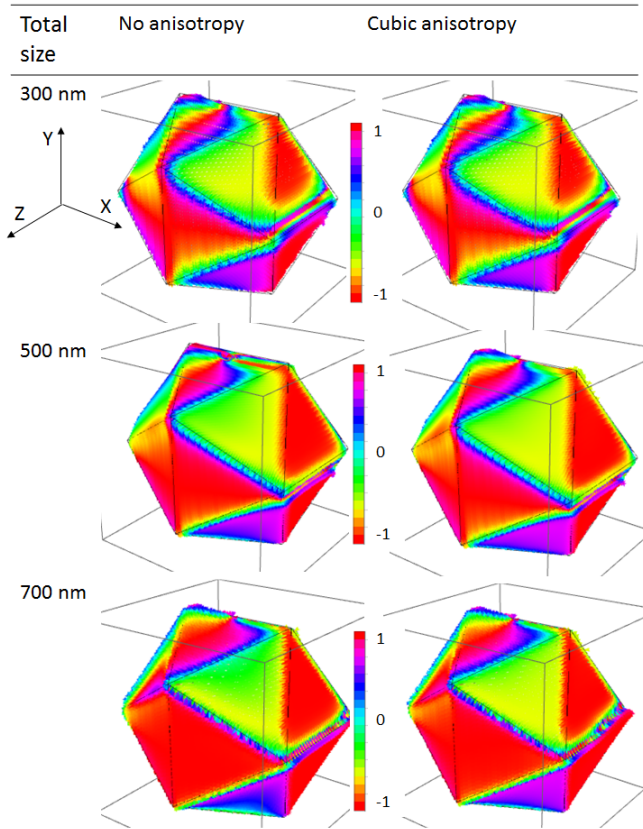


Figure E.1: Simulation of magnetization of 15 nm thick Ni shell on the surface of icosahedral particle which have 300 nm , 500, nm and 700 nm in size. The magnetization is simulated with and without cubic anisotropy. The color of the magnetization vectors presents their orientation relative to Z direction.

Total size (nm)	Edge length (nm)	Face area ( $\mu m^2$ )
300	193	0.023
500	321	0.063
700	450	0.12

Table E.2: Parameters of the simulated pentagonal dipyramid shape.

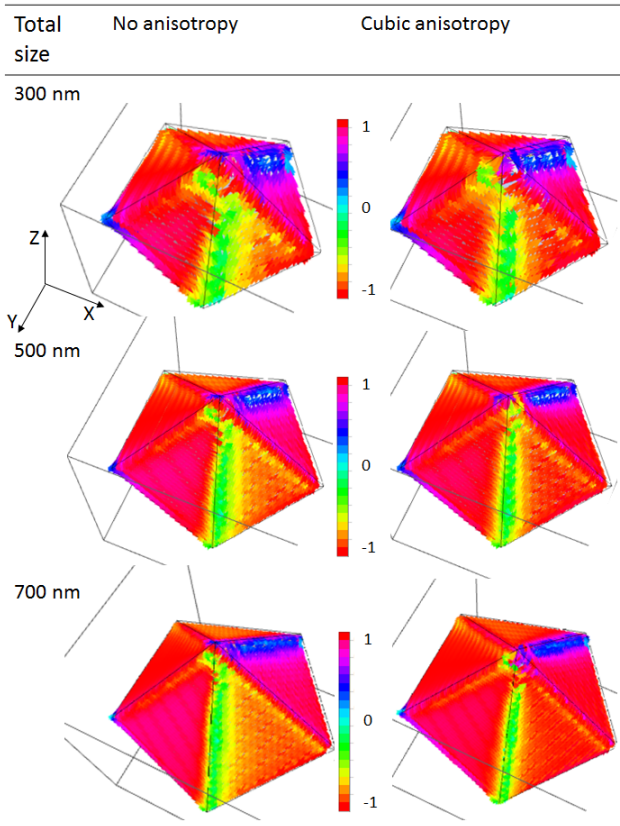


Figure E.2: Simulation of magnetization of 15 nm thick Ni shell on the surface of pentagonal dipyrmaid particles which have 300 nm, 500 nm and 700 nm in size. The magnetization is simulated with and without cubic anisotropy. The color of the magnetization vectors presents their orientation relative to Z direction.

orientation relative to Z direction. Again a minor vector orientation change is more noticeable for 500 nm and 700 nm big particle in case if the cubic anisotropy is considered in the simulation. The change of the color, for example, observed on the two front faces which have orange and magenta shades without cubic anisotropy and turn red with magnetic anisotropy. In the second case magnetization get turned more in the face plane, almost parallel to the base edge, that again might correlate to the vectors reorientation along the easy crystallographic axis. In all configurations the most noticeable change of direction is

observed in two junction regions which have vectors turned along the side edges pointing up and down relative to Z axis. In the images these areas have green and blue vector colors as it is seen in figure 7.17 from above and bottom views. On the bigger particle this effects look much more localized.

## E.4 Simulation with external magnetic field

The simulated external magnetic field of 250 mT was applied along X axis of the icosahedral and pentagonal dipyramid particles as it is shown in figure E.3 a) and b), respectively.

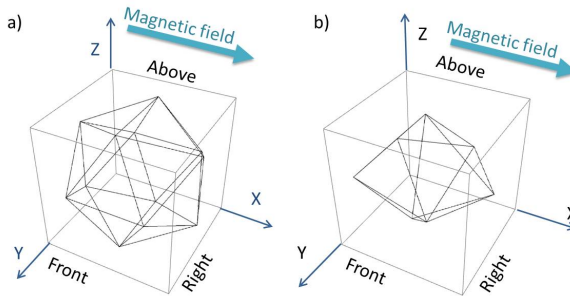


Figure E.3: Simulated particles in external magnetic field: a) icosahedral shape in 3D space with field applied along X axis; b) pentagonal dipyramid shape in 3D space with field applied along X axis.

To simplify the calculations the cubic anisotropy of Ni was not taken into account. YZ and XZ projections of icosahedral particle magnetization have vectors laying in projection plane for most of the observed faces (figure E.4). The orange background is used here and after to improve the visibility of the vectors. In case if all vectors are turned along the magnetic field the YZ projection should look totally dark, although we see that magnetization vectors still have big in-plane component and just partially turned along the applied field. Indeed, according to the OOP hysteresis loop measurements the full saturation of the 15 nm thick Ni film happens around 600 mT.

The same behavior is observed for pentagonal dipyramidal shape of the particle in figure E.5. The faces oriented perpendicular or under small angle towards the magnetic field direction still have magnetization component partially laying in plane. The YZ projection imaged from the left above observation point shows that two side faces are totally black corresponding to vectors completely turned along the applied field. However the faces which point to the front in the YZ projection are still dark gray.

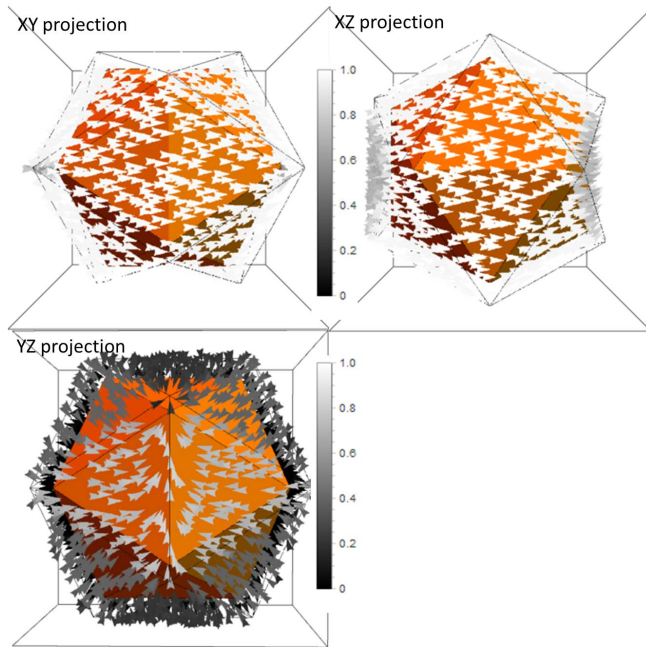


Figure E.4: Projections of magnetization vectors of icosahedral particle placed into magnetic field with direction along X axis on the YZ, XZ and XY planes .

The simulated data with external magnetic field are in agreement with the observed magnetization behavior studied with STXM (figure 7.13). The magnetization flip on the faces, turned almost perpendicular to the membrane surface, was much slower than on other faces. Due to limitation of the magnet system to 250 mT field the complete out-of-plane magnetization of the Ni shell couldn't be reached.

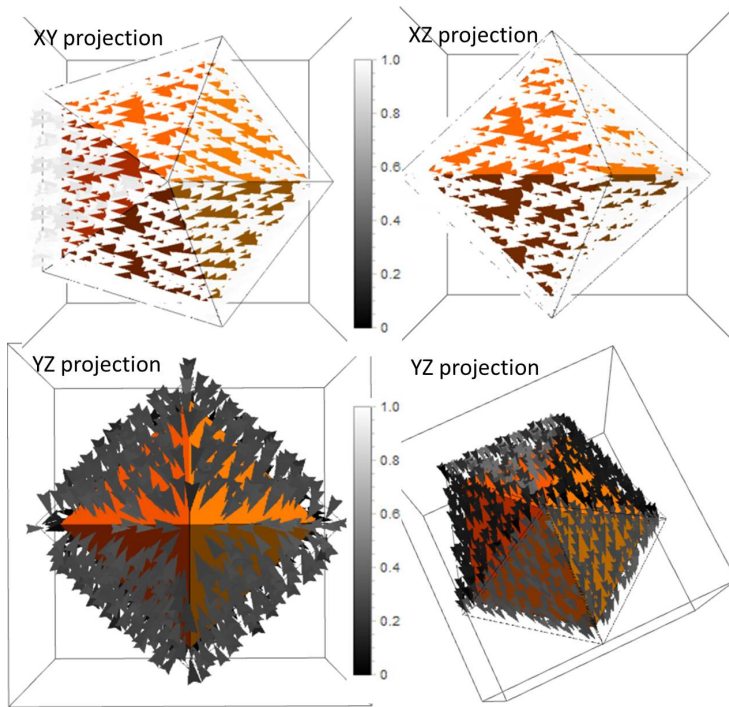


Figure E.5: Projections of magnetization vectors of the particle placed into magnetic field with direction along X axis on the YZ, XZ and XY planes. The projection on YZ plane has additional view from above to demonstrate faces not visible from the right observation point.

# Bibliography

- [1] P. J. Goodhew, J. Humphreys, R. Beanland. Electron Microscopy and Analysis, Third Edition. *CRC Press, 2000.*
- [2] C. Bai. Scanning Tunneling Microscopy and Its Application. *Springer Science & Business Media, 2000.*
- [3] J. Kirz and C. Jacobsen. The history and future of X-ray microscopy. *J. Phys.: Conf. Ser. 186, 2009.*
- [4] W. Chao, B. D. Harteneck, J. A. Liddle, E. H. Anderson and D. T. Attwood. Soft X-ray microscopy at a spatial resolution better than 15 nm. *Nature 435, 2005.*
- [5] P. Thibault, M. Dierolf, A. Menzel, O. Bunk, C. David, F. Pfeiffer. High-resolution scanning X-ray diffraction microscopy. *Science 321(5887), 2008.*
- [6] J. Stoehr and H.C. Siegmann. Magnetism from fundamentals to nanoscale dynamics. *Springer-Verlag Berlin Heidelberg, 2006.*
- [7] B. T. Thole, P. Carra, F. Sette, G. van der Laan: X-ray circular dichroism as a probe of orbital magnetization. *Phys. Rev. Lett. 68, 1943, 1992.*
- [8] F. R. Elder, A. M. Gurewitsch, R. V. Langmuir, and H. C. Pollock. Radiation from Electrons in a Synchrotron. *Phys. Rev., 71:829-830, Jun 1947.*
- [9] J. J. Skrzypek, A. W. Ganczarski, F. Rustichelli, H. Egner. Advanced Materials and Structures for Extreme Operating Conditions. *Springer, 2008.*
- [10] DESY synchrotron homepage. <http://www.desy.de/>, last visited: 30.04.2017.
- [11] P. Willmott. An Introduction to Synchrotron Radiation: Techniques and Applications. *Wiley, July 2011.*
- [12] BESSY II in Berlin. Helmholtz-Zentrum (Berlin) homepage. <https://www.helmholtz-berlin.de/zentrum/>, last visited: 10.05.2017.

- 
- [13] M. Abo-Bakr. Bunch length measurement at BESSY. In *Proceedings of the 2003 Particle Accelerator Conference, 2003*.
- [14] D. Attwood. Soft X-Rays and Extreme Ultraviolet Radiation. *Cambridge University Press, 1999*.
- [15] A. Thompson, I. Lindau, D. Attwood, P. Pianetta, E. Gullikson, A. Robinson, M. Howells, J. Scffeld, K.-J. Kim, J. Underwood, J. Kirz, D. Vaughan, J. Kortright, G. Williams, and H. Winick. X-ray data booklet. *Center for X-Ray Optics and Advanced Light Source, 2001*.
- [16] P. Schmueser, M. Dohlus, J. Rossbach, C. Behrens. Free-Electron Lasers in the Ultraviolet and x-ray Regime Physical Principles, Experimental Results, Technical Realization. *Springer, 2014*.
- [17] J. Als-Nielsen. Elements of Modern X-Ray Physics. *John Wiley & Sons, Copenhagen, 2002*.
- [18] J. Goodman. Statistical Optics. *Wiley Classics Library Edition Published, 2000*.
- [19] G. Margaritondo, Y. Hwu, G. Tromba. Synchrotron light: From basics to coherence and coherence-related applications. *Synchrotron Radiation: Fundamentals, Methodologies and Applications, eds. Mobila and Vlaic, p.25-53, 2003*.
- [20] J. H. Hubbell, H. A. Gimm. Pair, Triplet, and Total Atomic Cross Sections (and Mass Attenuation Coefficients) for 1 MeV-100 GeV Photons in Elements Z=1 to 100. *J. Phys. Chem. Ref. Data 9, 1023, 1980*.
- [21] The Center for X-ray Optics. X-Ray Interactions With Matter. [http : //henke.lbl.gov/optical\\_constants](http://henke.lbl.gov/optical_constants), last visited: 10.12.2016.
- [22] T. Mayer-Kuckuk. Atomphysik. *Teubner Studienbücher, 1997*.
- [23] E. Merzbacher. Quantum Mechanics. 3rd ed. *JOHN WILEY & SONS, INC, 1998*.
- [24] O. Šípr, J. Vackář and J. Minár. Finite lifetime broadening of calculated X-ray absorption spectra: possible artefacts close to the edge. *J. Synchrotron Rad. 25, 523-52, 2018*.
- [25] S. Voss, M. Fonin, and U. Ruediger. Electronic structure of Mn<sub>12</sub> derivatives on the clean and functionalized Au surface. *Physical review B 75, 2007*.
- [26] B.K. Agarwal and L.P. Verma. A rule for chemical shifts of X-ray absorption edges. *Journal of Physics C: Solid State Physics 3, 1970*.

- [27] D. Nolle, E. Goering, T. Tietze, G. Schütz, A. Figuerola and L. Manna. Structural and magnetic deconvolution of FePt/FeOx-nanoparticles using X-ray magnetic circular dichroism. *New Journal of Physics* 11, 2009.
- [28] J. L. Erskine and E. A. Stern. Calculation of the M23 magneto-optical absorption spectrum of ferromagnetic nickel. *Phys. Rev. B*, 12:5016-5024, Dec 1975.
- [29] G. Schütz, W. Wagner, W. Wilhelm, P. Kienle, R. Zeller, R. Frahm, and G. Materlik. Absorption of circularly polarized x-rays in iron. *Physical Review Letters*, 58(7), 1987.
- [30] J. Stöhr, Y. Wu. X-ray magnetic circular dichroism: Basic concepts and theory for 3d transition metals, in *New Directions in Research with Third-Generation Soft X-Ray Synchrotron Radiation Sources*. A. S. Schlachter, F. J. Wuilleumier (Eds.). *NATO ASI Series E 254, Kluwer Academic, Dordrecht, 1994*.
- [31] G. van der Laan. Applications of soft X-ray magnetic dichroism. *Journal of Physics: Conference Series* 430, 012127, 2013.
- [32] C. Huygens. *Treatise on Light. Translated by Silvanus P. Thompson. London: Macmillan, 1912.*
- [33] M. Born, E. Wolf. *Principles of Optics: Electromagnetic Theory of Propagation, Interference and Diffraction of Light*. 7th ed. *Cambridge University Press, Dec 1999*.
- [34] J. R. Fienup . Phase retrieval algorithms: a comparison. *Appl. Opt.* 21, 2758-2769, 1982.
- [35] F. van der Veen and F. Pfeiffer. Coherent X-ray scattering. *Journal of Physics: Condensed Matter*, 16(28), 5003, 2004.
- [36] E. Beaurepaire, F. Scheurer, G. Krill, J.-P. Kappler. *Magnetism and Synchrotron Radiation. Springer, Berlin, Heidelberg, 2001.*
- [37] A. Furrer. *Complementarity Between Neutron and Synchrotron X-Ray Scattering. World scientific publisher, 1998.*
- [38] M. Blume. Magnetic scattering of X-rays. *J. Appl. Phys.* 57, 3615, 1985.
- [39] D. Haskel, E. Kravtsov, Y. Choi, J.C. Lang, Z. Islam, G. Srajer, J.S. Jiang, S.D. Bader, and P.C. Canfield. Charge-magnetic interference resonant scattering studies of ferromagnetic crystals and thin films. *Eur. Phys. J. Special Topics* 208, 141, 2012
- [40] S. Lovesey, S. Collins. *X-Ray Scattering and Absorption by Magnetic Materials. Oxford series on synchrotron radiation, Oxford University Press Inc., New York, 1996.*

- [41] G. van der Laan. Soft X-ray resonant magnetic scattering of magnetic nanostructures. *C.R. Physique* 9, 570, 2008.
- [42] S. Eisebitt, M. Loergen, W. Eberhardt. Polarization effects in coherent scattering from magnetic specimen: Implications for x-ray holography, lensless imaging, and correlation spectroscopy. *Physical Review B* 68, 104419, 2003.
- [43] Electronics tutorials. <https://www.electronics-tutorials.ws/>, last visited: 30.05.2018.
- [44] J. M. D. Coey. Magnetism and Magnetic Materials. *Cambridge University Press*, 2009. ISBN-13 978-0-521-81614-4.
- [45] B. D. Cullity, C. D. Graham. Introduction to Magnetic Materials. *John Wiley & Sons*, 2005. ISBN 0-201-01218-9.
- [46] W. Nolting. Grundkurs Theoretische Physik 3. *Springer-Verlag Berlin Heidelberg*, 2004.
- [47] M. Weigand. Realization of a new magnetic scanning X-ray microscope and investigation of Landau structures under pulsed field excitation. *PhD thesis, University of Stuttgart*, 2014.
- [48] M.T. Bray, S. H. Cohen, M. L. Lightbody. Atomic Force Microscopy/Scanning Tunneling Microscopy. *Springer Science and Business Media*, 1994.
- [49] J. Guo. X-Rays in Nanoscience: Spectroscopy, Spectromicroscopy, and Scattering Techniques. *John Wiley & Sons*, 2011.
- [50] D. A. Shapiro, Y.-S. Yu, T. Tyliczszak, J. Cabana, R. Celestre, W. Chao, K. Kaznatcheev, A. L. D. Kilcoyne, F. Maia, S. Marchesini, Y. S. Meng, T. Warwick, L. Lisheng Yang and H. A. Padmore. Chemical composition mapping with nanometre resolution by soft X-ray microscopy. *Nature Photonics* 8, 765, 2014.
- [51] X. M. Cheng and D. J. Keavney. Studies of nanomagnetism using synchrotron-based x-ray photoemission electron microscopy (X-PEEM). *Rep. Prog. Phys.* 75, 026501, 2012.
- [52] B. Niemann, D. Rudolph, and G. Schmahl. X-ray microscopy with synchrotron radiation. *Applied Optics* 15(8), 1976.
- [53] P. Fischer, D.-H. Kim, W. Chao, J. A. Liddle, E. H. Anderson, D. T. Attwood. Soft X-ray microscopy of nanomagnetism. *Materials Today* 9(1-2), 26-33, 2006.
- [54] G. Schneider, P. Guttman, S. Heim, S. Rehbein, D. Eichert, and B. Niemann. X-ray microscopy at BESSY: From nano-tomography to fs-imaging. *AIP Conference Proceedings* 879, 1291, 2007.

## BIBLIOGRAPHY

---

- [55] J. Kirz and Sayre D. Soft X-ray microscopy of biological specimens Synchrotron Radiation Research. *New York: Plenum, 1980.*
- [56] H. Ade and H. Stoll. Near-edge X-ray absorption fine-structure microscopy of organic and magnetic materials. *Nature Materials* 8, 281, 2009.
- [57] J. C. Andrews, F. Meirer, Y. Liu, Z. Mester, and P. Pianetta. Transmission X-ray microscopy for full-field nano-imaging of biomaterials. *Microsc Res Tech.*, 74(7), 671, 2011.
- [58] W. Chao, J. Kim, S. Rekawa, P. Fischer, and E. H. Anderson. Demonstration of 12 nm Resolution Fresnel Zone Plate Lens based Soft X-ray Microscopy. *Optics Express* 17(20), 17669, 2009.
- [59] A. Momose. Recent Advances in X-ray Phase Imaging. *Jpn. J. Appl. Phys, Volume 44, Part 1, Number 9A, 2005.*
- [60] B. Kaulich, P. Thibault, A. Gianoncelli and M. Kiskinova. Transmission and emission x-ray microscopy: operation modes, contrast mechanisms and applications. *J. Phys.: Condens. Matter* 23, 2011.
- [61] M. Howells, C. Jacobsen, J. Kirz, R. Feder, K. Mcquaid, and S. Rothman. X-Ray Holograms at Improved Resolution - A Study of Zymogen Granules. *Science*, 238(4826), 514-517, 1987.
- [62] I. McNulty, J. Kirz, C. Jacobsen, E.H. Anderson, M. R. Howells, and D. P. Kern. High-resolution Imaging By Fourier-transform X-ray Holography. *Science*, 256(5059), 1009-1012, 1992.
- [63] S. Eisebitt, J. Luenig, W. F. Schlotter, M. Loergen, O. Hellwig, W. Eberhardt and J. Stoehr. Lensless imaging of magnetic nanostructures by X-ray spectro-holography. *Nature* 432, 885, 2004.
- [64] W. Bragg. The Diffraction of Short Electromagnetic Waves by a Crystal. *Proceedings of the Cambridge Philosophical Society*. 17, 43, 1913.
- [65] D. Sayre. Imaging Processes and Coherence in Physics. Volume 112 of the series Lecture Notes in Physics. *Springer, 1980.*
- [66] J. Miao, R. L. Sandberg, and C. Song. Coherent X-ray Diffraction Imaging. *IEEE Journal of selected topics in quantum electronics*, 2011.
- [67] H. N. Chapman and K. A. Nugent. Coherent lensless X-ray imaging. *Nature photonics* 4, 2010.

- [68] R. W. Gerchberg and W. O. Saxton. A Practical Algorithm for the Determination of Phase from Image and Diffraction Plane Pictures. *Optik* 35(2), 1972.
- [69] J. R. Fienup. Phase retrieval algorithms: a comparison. *Applied optic, Vol. 21, No. 15*, 1982.
- [70] J. R. Fienup. Reconstruction of a complex-valued object from the modulus of its Fourier transform using a support constraint. *Opt. Soc. Am. A* 4(1), 1987.
- [71] V. Elser. Phase retrieval by iterated projections. *J. Opt. Soc. Am. A/Vol. 20, No. 1*, 2003.
- [72] S. Marchesini, H. He, H. N. Chapman, S. P. Hau-Riege, A. Noy, M. R. Howells, U. Weierstall, and J. C. H. Spence. X-ray image reconstruction from a diffraction pattern alone. *Phys. Rev. B* 68, 2003.
- [73] J. M. Rodenburg and R. H. T. Bates. The theory of super-resolution electron microscopy via wigner-distribution deconvolution. *Phil. Trans. R. Soc. Lond. A*, 339:521, 1992.
- [74] K. Giewekemeyer, P. Thibault, S. Kalbfleisch, A. Beerlink, C. M. Kewish, M. Dierolf, F. Pfeiffer, and T. Salditt. Quantitative biological imaging by ptychographic x-ray diffraction microscopy. *PNAS* 107(2), 529, 2010.
- [75] S. Chen, J. Deng, D. J. Vine, Y. S. G. Nashed, Q. Jin, T. Peterka, C. Jacobsen, S. Vogt. Simultaneous X-ray Nano-Ptychographic and Fluorescence Microscopy at the Bionanoprobe. *X-Ray Nanoimaging: Instruments and Methods II*, edited by Barry Lai, *Proc. of SPIE, Vol. 9592*, 2015.
- [76] M. Holler, A. Diaz, M. Guizar-Sicairos, P. Karvinen, E. Färm, E. Härkönen, M. Ritala, A. Menzel, J. Raabe and O. Bunk. X-ray ptychographic computed tomography at 16 nm isotropic 3D resolution. *Scientific Reports* 4, Article number: 3857, 2014.
- [77] X. Huang, H. Yan, R. Harder, Y. Hwu, I. K. Robinson, and Y. S. Chu. Optimization of overlap uniformness for ptychography. *Optics Express, Vol. 22, No. 10*, 2014.
- [78] J. Deng, Y. S. G. Nashed, S. Chen, N. W. Phillips, T. Peterka, R. Ross, S. Vogt, C. Jacobsen, and D. J. Vine. Continuous motion scan ptychography: characterization for increased speed in coherent x-ray imaging. *Optics Express, Vol. 23, No. 5*, 2014.
- [79] J.M. Rodenburg, H.M.L. Faulkner. A phase retrieval algorithm for shifting illumination. *Appl. Phys. Lett.*, 85 (20), 4795, 2004.
- [80] A. M. Maiden, and J. M. Rodenburg. An improved ptychographical phase retrieval algorithm for diffractive imaging. *Ultramicroscopy* 109, 1256, 2009.

- [81] D. Sayre. Direct Methods of Solving Crystal Structures. *Edited by H. Schenk. NATO ASI Ser. Ser. B (Physics), Vol. 274, 353, 1991.*
- [82] R. H. T. Bates. Uniqueness of solution to two-dimensional Fourier phase problems of localized and positive images. *Comput. Vis. Graph. Image Process.* 25, 205, 1984.
- [83] J. Miao, D. Sayre, and H. N. Chapman. Phase retrieval from the magnitude of the Fourier transforms of nonperiodic objects. *J. Opt. Soc. Am. A, Vol. 15, No. 6, 1998.*
- [84] T. B. Edo, D. J. Batey, A. M. Maiden, C. Rau, U. Wagner, Z. D. Pešić, T. A. Waigh, and J. M. Rodenburg. Sampling in x-ray ptychography. *Phys. Rev. A, 87:053850, 2013.*
- [85] D. J. Batey, T. B. Edo, C. Rau, U. Wagner, Z. D. Pesic, T. A. Waigh, and J. M. Rodenburg. Reciprocal-space up-sampling from real-space oversampling in x-ray ptychography. *Physical Review A* 89, 043812, 2014.
- [86] W. Kuch. Magnetic Imaging. *Lect. Notes Phys.* 697, 275, 2006.
- [87] M. S. Cohen. Magnetic measurements with Lorentz microscopy. *IEEE Trans. Magn., 1(3):156, 1965.*
- [88] M. R. Koblischka, U. Hartmann, T. Sulzbach. Improvements of the lateral resolution of the MFM technique. *Proceedings of Symposium J on Growth and Evolution of Ultrathin Films: Surface and Interface Geometric and Electronic Structure, of the E-MRS Spring Conference.* 428(1-2), 93, 2003.
- [89] A. Laraoui, F. Dolde, C. Burk, F. Reinhard, J. Wrachtrup and C. A. Meriles. High-resolution correlation spectroscopy of  $^{13}\text{C}$  spins near a nitrogen-vacancy centre in diamond. *Nature Communications volume 4, 1651, 2013.*
- [90] W. Kuch, L.I. Chelaru, F. Offi, M. Kotsugi, X. Gao, K. Fukumoto and J. Kirschner. Layer-resolved Magnetic Domain Imaging Using X-ray Photoelectron Emission Microscopy. *Synchrotron Radiation News, Vol. 15, No. 6, 2002.*
- [91] T. Eimuller, P. Fischer, G. Schutz, P. Guttman, G. Schmahl, K. Pruegl, G. Bayreuther. Magnetic transmission X-ray microscopy: imaging magnetic domains via the X-ray magnetic circular dichroism. *Journal of Alloys and Compounds* 286, 20, 1999.
- [92] M. Loergen. Coherent Soft X-Ray Magnetic Scattering and Lensless Imaging. *PhD thesis, Technical University Berlin, 2004.*

- [93] J. J. Turner, X. Huang, O. Krupin, K. A. Seu, D. Parks, S. Kevan, E. Lima, K. Kisslinger, I. McNulty, R. Gambino, S. Mangin, S. Roy, and P. Fischer. X-Ray Diffraction Microscopy of Magnetic Structures. *Physical Review Letters* 107, 2011.
- [94] X. Shi, P. Fischer, V. Neu, D. Elefant, J. C. T. Lee, D. A. Shapiro, M. Farmand, T. Tyliczszak, H.-W. Shiu, S. Marchesini, S. Roy, S. D. Kevan. Soft x-ray ptychography studies of nanoscale magnetic and structural correlations in thin SmCo<sub>5</sub> films. *Appl. Phys. Lett.* 108, 094103, 2016.
- [95] C. Donnelly, V. Scagnoli, M. Guizar-Sicairos, M. Holler, F. Wilhelm, F. Guillou, A. Rogalev, C. Detlefs, A. Menzel, J. Raabe, and L. J. Heyderman. High Resolution Hard X-ray Magnetic Imaging with Dichroic Ptychography. *Phys. Rev. B* 94, 064421, 2016.
- [96] K. Keskinbora, C. Grévent, U. Eigenthaler, M. Weigand, and G. Schuetz. Rapid Prototyping of Fresnel Zone Plates via Direct Ga<sup>+</sup> Ion Beam Lithography for High-Resolution X-ray Imaging. *ACS Nano* 7 (11), p. 9788, 2013.
- [97] S. Marchesini, H. Krishnan, B. J. Daurer, D. A. Shapiro, T. Perciano, J. A. Sethiana and F. R. N. C. Maiab. SHARP: a distributed GPU-based ptychographic solver. *Journal of applied crystallography*, 49(4), 1245-1252, 2016.
- [98] T. Atkinson, W. Anders, H. Glass, P. Goslawski, A. Jankowiak, F. Kramer, P. Kuske, D. Malyutin, A. Matveenko, A. Neumann, M. Ries, M. Ruprecht, A. Schällicke, T. Schneegans, D. Schüler, P. Volz, G. Wüstefeld. Status and prospects of the BESSY II injector system. *Proceedings of IPAC2016, Busan, Korea, 2016*.
- [99] A. L. D. Kilcoyne, T. Tyliczszak, W. F. Steele, S. Fakra, P. Hitchcock, K. Franck, E. Anderson, B. Harteneck, E.G. Rightor, G.E. Mitchell, A.P. Hitchcock, L. Yang, T. Warwick, and H. Ade. Interferometer controlled scanning transmission X-ray microscopes at the Advanced Light Source. *Journal of Synchrotron Radiation*, 10 (2), 125-136, 2003.
- [100] D. Nolle, M. Weigand, P. Audehm, E. Goering, U. Wiesemann, C. Wolter, E. Nolle, and G. Schuetz. Note: Unique characterization possibilities in the ultra high vacuum scanning transmission x-ray microscope (UHV-STXM) MAXYMUS using a rotatable permanent magnetic field up to 0.22 T. *Review of scientific instruments* 83, 046112, 2012.
- [101] A. Singera and I. Vartanyants. Coherence properties of focused X-ray beams at high brilliance synchrotron sources. *J Synchrotron Radiat.*, 21 (1), 5-15, 2014.

- [102] D. H. Lumb, G. D. Berthiaume, D. N. Burrows, G. P. Garmire and J. A. Nousek. Charge Coupled Devices (CCDs) in X-ray Astronomy. *Experimental Astronomy* 2, 179-201, 1991.
- [103] I. Ordavo, S. Ihle, V. Arkadiev, O. Scharf, H. Soltau, A. Bjeoumikhov, S. Bjeoumikhova, G. Buzanich, R. Gubzhokov, A. Guenther, R. Hartmann, P. Holl, N. Kimmel, M. Kuehbacher, M. Lang, N. Langhoff, A. Liebel, M. Radtke, U. Reinholz, H. Riesemeier, G. Schaller, F. Schopper, L. Strueder, C. Thamma, R. Wedell. A new pnCCD-based color X-ray camera for fast spatial and energy-resolved measurements. *Nuclear Instruments and Methods in Physics Research A*, 654(1), 250-257, 2011.
- [104] L. Strueder, S. Epp, D. Rolles, R. Hartmann, P. Holl, G. Lutz, H. Soltau, R. Eckart, C. Reich, K. Heinzinger, C. Thamm, A. Rudenko, F. Krasniq, K. Kuehnel, C. Bauer, C. Schroeter, R. Moshhammer, S. Techert, D. Miessner, M. Porro, O. Haelker, N. Meidinger, N. Kimmel, R. Andritschke, F. Schopper, G. Weidenspointner, A. Ziegler, D. Pietschner, S. Herrmann, U. Pietsch, A. Walenta, W. Leitenberger, C. Bostedt, T. Moeller, D. Rupp, M. Adolph, H. Graafsma, H. Hirsemann, K. Gaertner, R. Richter, L. Foucar, R. L. Shoeman, I. Schlichting, J. Ullrich. Large-format high-speed X-ray pnCCDs combined with electron and ion imaging spectrometers in a multipurpose chamber for experiments at 4th generation light sources. *Nuclear Instruments and Methods in Physics Research A* 614, 483-496, 2010.
- [105] A. Schropp, R. Hoppe, J. Patommel, D. Samberg, F. Seiboth, S. Stephan, G. Wellenreuther, G. Falkenberg, and C. G. Schroer. Hard X-ray scanning microscopy with coherent radiation: Beyond the resolution of conventional X-ray microscopes. *Appl. Phys. Lett.* 100, 253112, 2012.
- [106] J. Vila-Comamala, A. Diaz, M. Guizar-Sicairos, A. Mantion, C. M. Kewish, A. Menzel, O. Bunk, and C. David. Characterization of high-resolution diffractive X-ray optics by ptychographic coherent diffractive imaging. *Optics Express* 19 (22), 2011.
- [107] A. A. Michelson. *Studies in Optics*. University Press, 1927.
- [108] M. S. Whittingham. Lithium Batteries and Cathode Materials. *Chem. Rev.* 104 (10), 2004.
- [109] Y. Li, F. E. Gabaly, T. R. Ferguson, R. B. Smith, N. C. Bartelt, J. D. Sugar, K. R. Fenton, D. A. Cogswell, A.L.D. Kilcoyne, T. Tyliczszak, M.Z. Bazant, and W.C. Chueh. Current-induced transition from particle-by-particle to concurrent intercalation in phase-separating battery electrodes. *Nature Materials* 13, 1149, 2014.
- [110] Y. Li, S. Meyer, J. Lim, S. Chul Lee, W. E. Gent, S. Marchesini, H. Krishnan, T. Tyliczszak, D. Shapiro, A. L. David Kilcoyne, and W. C. Chueh. Effects of Particle

- Size, Electronic Connectivity, and Incoherent Nanoscale Domains on the Sequence of Lithiation in  $\text{LiFePO}_4$  Porous Electrodes. *Adv. Mater.* 27, 2015.
- [111] J. Lim, Y. Li, D. Hein Alsem, H. So, S. Chul Lee, P. Bai, D. A. Cogswell, X. Liu, N. Jin, Y. Yu, N. J. Salmon, D. A. Shapiro, M. Z. Bazant, T. Tylliszczak, W. C. Chueh. Origin and hysteresis of lithium compositional spatiodynamics within battery primary particles. *Science* 353 (6299), 2016.
- [112] Y.-S. Yu, M. Farmand, C. Kim, Y. Liu, C.P. Grey, F.C. Strobridge, T. Tylliszczak, R. Celestre, P. Denes, J. Joseph, H. Krishnan, F.R.N.C. Maia, A.L.D. Kilcoyne, S. Marchesini, T. Perciano Costa Leite, T. Warwick, H. Padmore, J. Cabana and D. A. Shapiro. Three-dimensional localization of nanoscale battery reactions using soft X-ray tomography. *Nature Communications* volume 9, 921, 2018.
- [113] G.V. Zhuang, J.L. Allen, P.N. Ross, J.-H. Guo, T.R. Jow. Electronic Properties of  $\text{LiFePO}_4$  and Li doped  $\text{LiFePO}_4$ . *Lawrence Berkeley National Laboratory*, 2008.
- [114] D.S. Macholdt, K.P. Jochum, C. Poehlker, B. Stoll, U. Weis, B. Weber, M. Mueller, M. Kappl, S. Buhre, A.L.D. Kilcoyne, M. Weigand, D. Scholz, A.M. Al-Amri, M.O. Andreae. Microanalytical methods for in-situ high-resolution analysis of rock varnish at the micrometer to nanometer scale. *Chemical Geology*, 411, p.57, 2015.
- [115] D. S. Macholdt, K. P. Jochum, C. Poehlker, A. Arangio, J.-D. Foerster, B. Stoll, U. Weis, B. Weber, M. Müller, M. Kappl, M. Shiraiwa, A.L.D. Kilcoyne, M. Weigand, D. Scholz, G.H. Haug, A. Al-Amri, M.O. Andreae. Characterization and differentiation of rock varnish types from different environments by microanalytical techniques. *Chemical Geology* 459, p. 91, 2017.
- [116] W. S. Broecker and T. Liu. Rock Varnish: Recorder of Desert Wetness? *AGU Fall Meeting Abstracts*, 2001.
- [117] C. G. Engel, R.P. Sharp. Chemical data on desert varnish. *Geological Society of America Bulletin* 69, 487-518, 1958.
- [118] R. I. Dorn, T. M. Oberlander. Microbial origin of desert varnish. *Science* 213, 1245-124, 1981.
- [119] L. A. J. Garvie, D. M. Burt, P. R. Buseck. Nanometer-scale complexity, growth, and diagenesis in desert varnish. *Geology*, 36 (3), 2008.
- [120] T. H. Liu, W.S. Broecker. How fast does rock varnish grow? *Geology*, 28 (2): 183-186, 2000.
- [121] R. I. Dorn. Rock varnish as an indicator of aeolian environmental change. *Aeolian geomorphology*: 291-307, 1986.

- [122] R. S. Bradley. Paleoclimatology: reconstructing climates of the Quaternary. *Academic Press* 68, 1999.
- [123] M. Guizar-Sicairos, S. T. Thurman, and J. R. Fienup. Efficient subpixel image registration algorithms. *Opt. Lett.* 33, 156-158, 2008.
- [124] V. Kamberský, P. de Haan, J. Šimšová, S. Porthun, R. Gemperle, J.C. Lodder. Domain wall theory and exchange stiffness in Co/Pd multilayers. *Journal of Magnetism and Magnetic Materials* 157/158, 1996.
- [125] S. Woo, K. Litzius, B. Krueger, M. Im, L. Caretta, K. Richter, M. Mann, A. Krone, R. Reeve, M. Weigand, P. Agrawal, P. Fischer, M. Klauui, G. S. D. Beach. Observation of room temperature magnetic skyrmions and their currentdriven dynamics in ultrathin Co films. *Nature Materials* 15, 501-506, 2016.
- [126] T.H.R. Skyrme. A unified field theory of mesons and baryons. *Nucl. Phys.* 31, 556-569, 1962.
- [127] Article about magnetic skyrmions. [https://en.wikipedia.org/wiki/Magnetic\\_skyrmion](https://en.wikipedia.org/wiki/Magnetic_skyrmion), last visited: 22.06.2018.
- [128] I. Dzyaloshinsky. A thermodynamic theory of 'weak' ferromagnetism of antiferromagnetics. *J. Phys. Chem. Solids* 4, 241-255, 1958.
- [129] T. Moriya. Anisotropic superexchange interaction and weak ferromagnetism. *Phys. Rev.* 120, 91-98, 1960.
- [130] S. Muehlbauer, B. Binz, F. Jonietz, C. Pfleiderer, A. Rosch, A. Neubauer, R. Georgii, P. Boeni. Skyrmion Lattice in a Chiral Magnet *Science*. 323, 915-919, 2009.
- [131] S. L. Zhang, I. Stasinopoulos, T. Lancaster, F. Xiao, A. Bauer, F. Rucker, A. A. Baker, A. I. Figueroa, Z. Salman, F. L. Pratt, S. J. Blundell, T. Prokscha, A. Suter, J. Waizner, M. Garst, D. Grundler, G. van der Laan, C. Pfleiderer and T. Hesjedal. Room-temperature helimagnetism in FeGe thin films. *Scientific Reports* 7(123), 2017.
- [132] G. Chen, T. Ma, A.T. N'Diaye, H. Kwon, C. Won, Y. Wu, A.K. Schmid. Tailoring the chirality of magnetic domain walls by interface engineering. *Nature Commun.* 4, 2013.
- [133] C. Moreau-Luchaire, C. Moutafis, N. Reyren, J. Sampaio, C. A. F. Vaz, N. Van Horne, K. Bouzehouane, K. Garcia, C. Deranlot, P. Warnicke, P. Wohlhueter, J.-M. George, M. Weigand, J. Raabe, V. Cros, A. Fert. Additive interfacial chiral interaction in multilayers for stabilization of small individual skyrmions at room temperature. *Nature Nanotech.* 11, 444448, 2016.

- [134] S. Heinze, K. von Bergmann, M. Menzel, J. Brede, A. Kubetzka, R. Wiesendanger, G. Bihlmayer, S. Blügel, Spontaneous atomic-scale magnetic skyrmion lattice in two dimensions. *Nature Phys.* 7, 2011.
- [135] A. Fert, V. Cros and João Sampaio. Skyrmions on the track. *Nature Nanotechnology volume 8, pages 152156, 2013.*
- [136] A. Soumyanarayanan, M. Raju, A. L. G. Oyarce, A. K. C. Tan, M. Im, A. P. Petrovic, P. Ho, K. H. Khoo, M. Tran, C. K. Gan, F. Ernult, and C. Panagopoulos. Tunable room temperature magnetic skyrmions in Ir/Fe/Co/Pt multilayers. *Nature Materials* 16, 898-904, 2017.
- [137] M. Ezawa. Giant skyrmions stabilized by dipole-dipole interactions in thin ferromagnetic films. *Physical review letters* 105 (19), 2010.
- [138] X. Ma, G. Yu, C. Tang, X. Li, C. He, J. Shi, K. L. Wang, and X. Li. Scaling of Dzyaloshinskii-Moriya interaction at heavy metal and ferromagnetic metal interfaces. *Phys. Rev. Lett.* 120, 2018.
- [139] A. Hrabec, M. Belmeguenai, A. Stashkevich, S. M. Chérif, S. Rohart, Y. Roussigné, and A. Thiaville. Making the Dzyaloshinskii-Moriya interaction visible. *Appl. Phys. Lett.* 110, 242402, 2017.
- [140] H. S. Korner, J. Stigloher, H. G. Bauer, H. Hata, T. Taniguchi, T. Moriyama, T. Ono, and C. H. Back. Interfacial Dzyaloshinskii-Moriya interaction studied by time-resolved scanning Kerr microscopy *Phys. Rev. Lett. B* 92, 220413(R), 2015.
- [141] A. Hrabec, N.A. Porter, A. Wells, M. J. Benitez, G. Burnell, S. McVitie, D. McGrouther, T. A. Moore, and C. H. Marrows. Measuring and tailoring the Dzyaloshinskii-Moriya interaction in perpendicularly magnetized thin films. *Phys. Rev. B* 90, 020402(R), 2014.
- [142] S.-G. Je, D.-H. Kim, S.-C. Yoo, B.-C. Min, K.-J. Lee, and Sug-Bong Choe. Asymmetric magnetic domain-wall motion by the Dzyaloshinskii-Moriya interaction. *Phys. Rev. B* 88, 214401, 2013.
- [143] P. Srivastava, F. Wilhelm, A. Ney, M. Farle, H. Wende, N. Haack, G. Ceballos, and K. Baberschke. Magnetic moments and Curie temperatures of Ni and Co thin films and coupled trilayers. *Phys. Rev. B* 58, 5701, 1998.
- [144] C. M. Schneider, P. Bressler, P. Schuster, J. Kirschner, J. J. de Miguel, and R. Miranda. Curie temperature of ultrathin films of fcc-cobalt epitaxially grown on atomically flat Cu(100) surfaces. *Phys. Rev. Lett.* 64, 1059, 1990.

- [145] D. Stosic, T.B. Ludermir, and M. V. Milošević. Pinning of magnetic skyrmions in a monolayer Co film on Pt(111): Theoretical characterization and exemplified utilization. *Phys. Rev. B* 96, 214403, 2017.
- [146] S. McVitie, S. Hughes, K. Fallon, S. McFadzean, D. McGruther, M. Krajenak, W. Legrand, D. Maccariello, S. Collin, K. Garcia, N. Reyren, V. Cros, A. Fert, K. Zeissler, C. H. Marrows. A transmission electron microscope study of Néel skyrmion magnetic textures in multilayer thin film systems with large interfacial chiral interaction. *Scientific Reports* 8, 5703, 2018.
- [147] S.D. Pollard. Observation of stable Néel skyrmions in cobalt/palladium multilayers with Lorentz transmission electron microscopy. *Nature Communications* 8, 14761, 2017.
- [148] G. Chen, A. Mascaraque, A.T. N’Diaye, and A. K. Schmid. Room temperature skyrmion ground state stabilized through interlayer exchange coupling. *Appl. Phys. Lett.* 106, 242404, 2015.
- [149] N. Romming, C. Hanneken, M. Menzel, J.E. Bickel, B. Wolter, K. von Bergmann, A. Kubetzka, R. Wiesendanger. Writing and deleting single magnetic skyrmions. *Science* 341, Issue 6146, 636-639, 2013.
- [150] P.-J. Hsu, L. Rózsa, A. Finco, L. Schmidt, K. Palotás, E. Vedmedenko, L. Udvardi, L. Szunyogh, A. Kubetzka, K. von Bergmann and R. Wiesendanger. Inducing skyrmions in ultrathin Fe films by hydrogen exposure. *Nature Communications* volume 9, 2018.
- [151] Yu, G., A. Jenkins, X. Ma, S. A. Razavi, C. He, G. Yin, Q. Shao, Q. He, H. Wu, W. Li, W. Jiang, X. Han, X. Li, A. C. Bleszynski Jayich, P. K. Amiri, and Kang L. Wang. Room-temperature skyrmions in an antiferromagnet-based heterostructure. *Nano Letters* 18, 980-986, 2018.
- [152] W. Jiang, P. Upadhyaya, W. Zhang, G. Yu, M.B. Jungfleisch, F.Y. Fradin, J.E. Pearson, Y. Tserkovnyak, K. L. Wang, O. Heinonen, S.G.E. te Velthuis, A. Hoffmann. Blowing magnetic skyrmion bubbles. *Science* 349, 283, 2015.
- [153] W. Jiang, X. Zhang, G Yu, W. Zhang, X. Wang, M. B. Jungfleisch, J. E. Pearson, X. Cheng, O. Heinonen, K. L. Wang, Y. Zhou, A. Hoffmann and S. G. E. te Velthuis. Direct observation of the skyrmion Hall effect. *Nature Physics* volume 13, 2017.
- [154] K. Litzius, I. Lemesh, B. Krüger, P. Bassirian, L. Caretta, K. Richter, F. Büttner, K. Sato, O. A. Tretiakov, J. Förster, R. M. Reeve, M. Weigand, I. Bykova, H. Stoll, G. Schütz, G. S. D. Beach and M. Kläui. Skyrmion Hall effect revealed by direct time-resolved X-ray microscopy. *Nature Physics* 13, 170, 2016.

- [155] O. Boulle, J. Vogel, H. Yang, S. Pizzini, D. de Souza Chaves, A. Locatelli, T. O. Montes, A. Sala, L. D. Buda-Prejbeanu, O. Klein, M. Belmeguenai, Y. Roussigné, A. Stashkevich, S. Mourad Chérif, L. Aballe, M. Foerster, M. Chshiev, S. Auffret, I. Mihai Miron and G. Gaudin. Nature Nanotec Room-temperature chiral magnetic skyrmions in ultrathin magnetic nano-structures. *Nature Nanotechnology* 11, 449, 2016.
- [156] F. Büttner, C. Moutafis, M. Schneider, B. Krüger, C. M. Günther, J. Geilhufe, C. v. Korff Schmising, J. Mohanty, B. Pfau, S. Schaffert, A. Bisig, M. Foerster, T. Schulz, C. A. F. Vaz, J. H. Franken, H. J. M. Swagten, M. Kläui S. Eisebitt Dynamics and inertia of skyrmionic spin structures. *Nature Physics* 11, 225, 2015.
- [157] Kai Litzius. Personal communication.
- [158] A. Siemens, Y. Zhang, J. Hagemester, E. Y. Vedmedenko and R. Wiesendanger. Minimal radius of magnetic skyrmions: statics and dynamics. *New Journal of Physics* 18, 2016.
- [159] Zázvorka, J., et al.: Thermal skyrmion diffusion applied in probabilistic computing. *ArXiv*, 2018.
- [160] K. Zeissler, M. Mruczkiewicz, S. Finizio, J. Raabe, P. M. Shepley, A. V. Sadovnikov, S. A. Nikitov, K. Fallon, S. McFadzean, S. McVitie, T. A. Moore, G. Burnell and C. H. Marrows. Pinning and hysteresis in the field dependent diameter evolution of skyrmions in Pt/Co/Ir superlattice stacks. *Scientific reports* 7, 15125, 2017.
- [161] BioVoxel Toolbox for ImageJ: [https://imagej.net/BioVoxel\\_Toolbox](https://imagej.net/BioVoxel_Toolbox). Last visited: 29.01.2018.
- [162] A. O. Leonov, T. L. Monchesky, N. Romming, A. Kubetzka, A. N. Bogdanov and R. Wiesendanger. The properties of isolated chiral skyrmions in thin magnetic films. *New Journal of Physics* 18, 2016.
- [163] A. Bogdanov and A. Huber. The properties of isolated magnetic vortices. *Phys. Stat. Sol. (b)* 186, 527, 1994
- [164] A. A. Thiele. Theory of the static stability of cylindrical domains in uniaxial platelets. *Journal of Applied Physics* 41, 1139, 1970.
- [165] P.-J. Hsu, A. Finco, L. Schmidt, A. Kubetzka, K. von Bergmann, and R. Wiesendanger. Guiding spin spirals by local uniaxial strain relief. *Physical review letters* 116, 017201, 2016.

- [166] M.B. Gawande, A. Goswami, T. Asefa, H. Guo, A. V. Biradar, D.-L. Peng, R. Zboril and R. S. Varma. Core-shell nanoparticles: synthesis and applications in catalysis and electrocatalysis. *Chem Soc Rev*, 44, 7540-7590, 2015.
- [167] C. Burda, X. Chen, R. Narayanan, and M.A. El-Sayed. Chemistry and Properties of Nanocrystals of Different Shapes. *Chem. Rev.* 105, 2005.
- [168] A. G. Kolhatkar, A. C. Jamison, D. Litvinov, R. C. Willson, and T. R. Lee. Tuning the Magnetic Properties of Nanoparticles. *Int J Mol Sci.*, 14(8), 15977-16009, 2013.
- [169] M. B. Gawande, A. Goswami, F.-X. Felpin, T. Asefa, X. Huang, R. Silva, X. Zou, R. Zboril, and R. S. Varma. Cu and Cu-Based Nanoparticles: Synthesis and Applications in Catalysis. *Chem. Rev.*, 116, 3722-3811, 2016.
- [170] T. G. Kim, H. J. Park, K. Woo, S. Jeong, Y. Choi, and S. Y. Lee. Enhanced Oxidation-Resistant Cu@Ni Core-Shell Nanoparticles for Printed Flexible Electrodes. *ACS Appl. Mater. Interfaces*, 10, 1059-1066, 2018.
- [171] T. Yamauchi, Y. Tsukahara, K. Yamada, T. Sakata, and Y. Wada. Nucleation and Growth of Magnetic Ni-Co (Core-Shell) Nanoparticles in a One-Pot Reaction under Microwave Irradiation. *Chem. Mater.*, 23 (1), pp 75-84, 2011.
- [172] H. Guo, J. Jin, Y. Chen, X. Liu, D. Zeng, L. Wang and D.-L. Peng. Controllable synthesis of Cu-Ni coreshell nanoparticles and nanowires with tunable magnetic properties. *Chem. Commun.*, 52, 6918, 2016.
- [173] B. Issa, I. M. Obaidat, B. A. Albiss, and Y. Haik. Magnetic nanoparticles: surface effects and properties related to biomedicine Applications. *Int J Mol Sci.*, 14(11), 21266-21305, 2013.
- [174] A. Radi, D. Pradhan, Y. Sohn, and K. T. Leung. Nanoscale shape and size control of cubic, cuboctahedral, and octahedral Cu-Cu<sub>2</sub>O core-shell nanoparticles on Si(100) by one-step, templateless, capping-agent-free electrodeposition. *ACS Nano* 4(3), 1553-1560, 2010.
- [175] A. Abedini, A. A. A. Bakar, F. Larki, P. S. Menon, Md. S. Islam, and S. Shaari. Recent Advances in Shape-Controlled Synthesis of Noble Metal Nanoparticles by Radiolysis Route. *Nanoscale Res Lett.*, 11, 287, 2016.
- [176] H. Hofmeister. Shape variations and anisotropic growth of multiply twinned nanoparticles. *Zeitschrift für Kristallographie - Crystalline Materials*, 224 (11), 528-538, 2009.
- [177] P. R. Sajanlal, T. S. Sreeprasad, A. K. Samal, and T. Pradeep. Anisotropic nanomaterials: structure, growth, assembly, and functions. *Nano Reviews*, 2 (1), 2011.

- [178] X. Liu, A. Berger, M. Wuttig. Stability of the perpendicular magnetic anisotropy of ultrathin Ni films on Cu(100) upon multiple magnetization reversals. *Physical review B*, 63, 144407, 2001.
- [179] F. Matthes, A. Rzhetskii, L.-N. Tong, D. Venus, and C. M. Schneider. Growth and magnetic properties of epitaxial ultrathin Ni films on Cu(111) using Sb as a surfactant. *Journal of Applied Physics* 93, 8740, 2003
- [180] R. Denk, M. Hohage, and P. Zeppenfeld. Extremely sharp spin reorientation transition in ultrathin Ni films grown on Cu(110)-(2×1)O. *Physical review B*, 79, 073407, 2009.
- [181] J. C. Jiménez-Sáez, J. Domínguez-Vázquez, A. MCPérez-Martín and J. J. Jiménez-Rodríguez. Molecular dynamics study of a Ni/Cu(001) interface. *Nanotechnology* 14, 701708, 2003.
- [182] J.B. Yi, Y.Z. Zhou, J. Ding, G.M. Chow, Z.L. Dong, T. White, Xing Yu Gao, A.T.S. Wee, X.J. Yu. An investigation of structure, magnetic properties and magnetoresistance of Ni films prepared by sputtering. *Journal of Magnetism and Magnetic Materials* 284, 303-311, 2004.
- [183] T. Komine, Y. Mitsui, and K. Shiiki. Micromagnetics of soft magnetic thin films in presence of defects. *Journal of Applied Physics* 78, 7220, 1995.
- [184] R. Streubel, P. Fischer, F. Kronast, V. P. Kravchuk, D. D. Sheka, Y. Gaididei, O. G. Schmidt and D. Makarov. Magnetism in curved geometries. *J. Phys. D: Appl. Phys.* 49, 363001, 2016.
- [185] V.A. Shchukin, N.N. Ledentsov, D. Bimberg. Epitaxy of nanostructures. *Springer-Verlag Berlin Heidelberg New York*, 2004.
- [186] P.K. Choudhury, S. Banerjee, S. Ramaprabhu, K.P. Ramesh, R. Menon. Variations in magnetic properties of nanostructured nickel. *J. Nanosci. Nanotechnol.* 13(12), 2013.
- [187] Fast Micromagnetic Simulator for Computations on CPU and Graphics Processing Unit : <http://micromagnum.informatik.uni-hamburg.de/>. Last visited: 20.02.2018.
- [188] Wolfram Mathematica: <http://www.wolfram.com/>. Last visited: 22.02.2018.
- [189] M. Dierolf, A. Menzel, P. Thibault, P. Schneider, C. M. Kewish, R. Wepf, O. Bunk and F. Pfeiffer. Ptychographic X-ray computed tomography at the nanoscale. *Nature* 467, 436439, 2010.
- [190] P. Li and A. Maiden. Multi-slice ptychographic tomography. *Scientific Reports* 8, 2018.

## BIBLIOGRAPHY

---

- [191] C. Donnelly, M. Guizar-Sicairos, V. Scagnoli, S. Gliga, M. Holler, J. Raabe and L. J. Heyderman. Three-dimensional magnetization structures revealed with X-ray vector nanotomography. *Nature* 547, 328331, 2017.
- [192] P. Sidorenko, O. Lahav, and O. Cohen. Ptychographic ultrahigh-speed imaging. *Optics Express* 25(10), 2017.
- [193] Y.S. G. Nashed, D. J. Vine, T. Peterka, J. Deng, R. Ross, and C. Jacobsen. Parallel ptychographic reconstruction. *Opt Express*, 22(26), 32082-32097, 2014.
- [194] Ptychography for Python, <http://ptycho.github.io/ptypy/>. Last visited: 30.07.2017.
- [195] Ptychography Software: SHARP-CAMERA. <http://www.camera.lbl.gov/>. Last visited: 01.08.2017.
- [196] D. A. Shapiro, R. Celestre, P. Denes, M. Farmand, J. Joseph, A.L.D. Kilcoyne, S. Marchesini, H. Padmore, S. V. Venkatakrishnan, T. Warwick and Y.-S. Yu. Ptychographic imaging of nano-materials at the advanced light source with the nanosurveyor instrument. *J. Phys.: Conf. Ser.* 849, 2017.
- [197] D R. Luke Relaxed averaged alternating reflections for diffraction imaging. *Inverse Problems* 21, 37-50, 2005.
- [198] S. Marchesini<sup>1</sup>, A. Schirotzek, C. Yang, H. Wu and F. Maia. Augmented projections for ptychographic imaging. *Inverse problems* 29 (11), 2013
- [199] I. Vartiainen, R. Mokso, M. Stampanoni, and C. David. Halo suppression in full-field x-ray Zernike phase contrast microscopy. *Optics Letters* 39(6), p. 1601, 2014.
- [200] Tutorial for shade-off and halo phase contrast artifacts, <https://www.microscopyu.com>. Last visited: 08.12.2017.
- [201] H. N. Chapman, A. Barty, S. Marchesini, A. Noy, S. P. Hau-Riege, C. Cui, M. R. Howells, R. Rosen, H. He, J. C. H. Spence, U. Weierstall, T. Beetz, C. Jacobsen, and D. Shapiro. High-resolution ab initio three-dimensional x-ray diffraction microscopy. *J. Opt. Soc. Am. A*, 23(5), 1179-1200, May 2006.
- [202] N. Banterle, K. H. Bui, E. A. Lemke, M. Beck. Fourier ring correlation as a resolution criterion for super-resolution microscopy. *Journal of Structural Biology* 183, 363-367, 2013.
- [203] R. N. Wilke, M. Vassholza and T. Salditta. Semi-transparent central stop in high-resolution X-ray ptychography using Kirkpatrick-Baez focusing. *Acta Crystallographica Section A Foundation and Advance*, 69 (5), 490-497, 2013.

- [204] R. Mizutani, R. Saiga, S. Takekoshi, C. Inomoto, N. Nakamura, M. Itokawa, M. Arai, K. Oshima, A. Takeuchi, K. Uesugi, Y. Terada, and Y. Suzuki. A method for estimating spatial resolution of real image in the Fourier domain. *Journal of Microscopy*, 261 (1), 57-66, 2016.
- [205] M. van Heel, M. Schatz. Fourier shell correlation threshold criteria. *Journal of Structural Biology*, 151(3), 250-262, 2005.
- [206] P.B. Rosenthal, R. Henderson. Optimal determination of particle orientation, absolute hand, and contrast loss in single-particle electron cryomicroscopy. *J Mol Biol.* 333, 721-745, 2003.

# List of Figures

2.1	The characteristic emission of an electron in the average electron speed and in the laboratory frames. . . . .	8
2.2	Radiation cones and energy spectra for bending magnet and undulator. . .	9
2.3	Schematic drawing of an APPLE II undulator at different settings. . . . .	10
2.4	Temporal and spatial coherence lengths . . . . .	13
2.5	Typical beamline components based on layout of UE46 beamline at BESSY II . . . . .	14
2.6	Total photon cross section in carbon as a function of energy. . . . .	15
2.7	Absorption edges of ferromagnetic materials Gd, Co, Ni. . . . .	17
2.8	XAS spectra obtained from Mn over $L_2$ and $L_3$ edges. . . . .	19
2.9	XMCD mechanism at $2p_{3/2}$ initial state. . . . .	21
2.10	X-ray polarization dependent absorption spectra for the Fe, Co and Ni. . .	22
2.11	Propagation of a plane wave through a planar object with transmission function $q(X, Y)$ . . . . .	24
2.12	Schematic drawing illustrating diffraction patterns obtained from coherent and incoherent illuminated sample. . . . .	25
2.13	Magnetic and charge scattering factors of Fe at $L_{3,2}$ edges in dependance on X-ray energy. . . . .	29
2.14	Scattering geometry in transmission mode. . . . .	30
2.15	Typical hysteresis loop of ferromagnetic material. . . . .	32
2.16	DMI interaction imaged at the atomic scales. . . . .	35
2.17	Magnetization configuration in materials with shape anisotropy and in single and two-domain states. . . . .	36
2.18	Two types of domain walls. . . . .	37
3.1	Schematic view of PEEM microscope. . . . .	39
3.2	Schematic view of full-field transmission X-ray microscope. . . . .	40
3.3	Schematic view of scanning transmission X-ray microscope. . . . .	41

---

3.4	Illustration of X-rays diffraction on a FZP. The image shows diffraction orders of FZP, which have different focal length. . . . .	42
3.5	Principle of X-ray holography. . . . .	44
3.6	Scheme of iterative phase retrieval algorithm. . . . .	46
3.7	Experimental geometry of ptychographic imaging. . . . .	47
3.8	Extended ptychographic iterative engine (ePIE). . . . .	49
3.9	Schematic view of diffraction pattern probed by CCD detector in under-sampling and oversampling conditions. . . . .	52
3.10	Diffraction patterns from a CoPt magnetic domain structure taken for X-ray holography using linearly polarized light. . . . .	55
4.1	Layout of the Beamline UE46-PGM2 at BESSY. . . . .	58
4.2	Image of sample environment in the MAXYMUS microscope. . . . .	60
4.3	Overview over the laser interferometer system for detection of stage motions. . . . .	61
4.4	Schematic view of magnet system with four rotatable magnets. . . . .	62
4.5	Graph of degree of coherence of homogeneously illuminated slit apertures having different opening gaps at energy 1000 eV. . . . .	63
4.6	Simulated intensity distribution of the diffracted light at 3 m distance from the vertical and horizontal slits. . . . .	64
4.7	Graph of spatial coherence length in the first order focus spot of coherently illuminated FZPs depending on photon energy with the vertical slit width of 20 $\mu\text{m}$ . . . . .	66
4.8	Scheme of MAXYMUS endstation with CCD camera setup. . . . .	68
4.9	Illustration of the frame store operation for CCD high speed read out. . . . .	70
4.10	Quantum efficiency of the pnCCDs as a function of energy. . . . .	72
4.11	Photo of pnCCD camera without front cover. . . . .	73
4.12	Radial profiles of diffraction images obtained from the low scattering sample using different dwell times: 100 ms, 300 ms and 500 ms. . . . .	74
4.13	Correction of diffraction pattern before ptychographic reconstruction. . . . .	74
4.14	Performance of FZP fabricated out of SiN with beamstop produced by laser lithography. . . . .	76
4.15	Phase reconstructions of resolution target (FZP) taken with different degrees of X-ray coherence. . . . .	78
4.16	Sketch of the different numerical aperture provided by two positions of the CCD relative to the sample. . . . .	79
4.17	Comparison of two ptychographic reconstructions of Siemens Star obtained by systems with different NA. . . . .	80
4.18	Averaged diffraction pattern from the ptychography scans of strongly scattering resolution target and weakly scattering magnetic domain structure. . . . .	81

## LIST OF FIGURES

---

4.19	Overlap ratio of neighboring illumination spot profiles at the ptychographic scans with different step sizes. . . . .	83
4.20	SEM image of the Siemens Star. . . . .	83
4.21	Ptychographic images obtained with different step sizes of the raster scan. . . . .	84
4.22	Simulated illumination profiles at sample position in focused and defocused states. . . . .	85
4.23	Ptychographic images obtained at 800 eV with different defocus distances. . . . .	85
4.24	Siemens star with 15 nm wide inner circle structures imaged by ptychography. . . . .	86
4.25	Contrast dependance of ptychographic amplitude images on scanning dwell time. . . . .	87
5.1	Reference absorption spectra of lithiated and delithiated battery areas and line profile over two different phases. . . . .	91
5.2	Comparison of STXM and ptychography imaging of chemical contrast in LiFePO <sub>4</sub> nanoplates. . . . .	92
5.3	Line profiles of STXM and ptychographic images of LiFePO <sub>4</sub> nanoplates. . . . .	93
5.4	Preparation of the CA14 JC-8 rock varnish sample . . . . .	94
5.5	STXM imaging of element distribution in varnish sample. . . . .	95
5.6	Element distribution in varnish sample CA14 JC-8 imaged by ptychography. . . . .	98
5.7	Al map of varnish sample obtained by ptychography with 5 nm pixel size. . . . .	99
5.8	Ptychographic imaging of magnetic labyrinth domain structure. . . . .	100
5.9	Phase and amplitude images of the reconstructed ptychographic images obtained using left circular polarized X-ray light as a function of energy across Co L <sub>3</sub> edge (781.4 eV). . . . .	101
5.10	The graph of ptychographic phase and amplitude image contrast measured at magnetic labyrinth sample in dependance on X-ray energy around Co absorption edge. . . . .	102
6.1	Schematic view of Néel and Bloch skyrmion types. . . . .	105
6.2	Principle of interfacial DMI effect. . . . .	105
6.3	BLS in back-scattering geometry where the inelastically scattered light is collected in the direction of the incident p-polarized light. Adapted from [138]. . . . .	106
6.4	Multilayer structure of Pd/CoFeB/MgO and Pt/CoFeB/MgO samples. . . . .	109
6.5	IP and OOP hysteresis loops for a) Pd/CoFeB/MgO and b) Pt/CoFeB/MgO multilayer structures. . . . .	110
6.6	XMCD ptychographic images of domains evolution of Pd/CoFeB/MgO and Pt/CoFeB/MgO multilayers in applied external OOP magnetic field. . . . .	111
6.7	Performance of skyrmion Ta/CoFeB/MgO/Ta wedge multilayer sample. . . . .	112

---

6.8	Magnetization of multilayer samples with different thicknesses of ferromagnetic layer numerated from 1 to 7 for the corresponding total ferromagnetic wedge thickness from 11.7 to 21.7 nm, respectively. . . . .	113
6.9	Ptychographic images of samples 7,6 and 5 showing evolution of magnetic domains for different OOP magnetic field values. . . . .	115
6.10	Comparison of domain wall width for the sample 7 at domain state using STXM (15 nm scanning step) and ptychography (11 nm real space pixel size). . . . .	116
6.11	Skyrmion sizes depending on OOP bias field for sample 7 imaged by ptychography. . . . .	117
6.12	3D profiles of the skyrmions under bias field of -165 mT imaged by a) STXM and b) ptychography. . . . .	117
6.13	Histogram of skyrmion size distribution imaged by ptychography on sample 7 for different OOP field values. . . . .	118
6.14	Skyrmion shape change in dependance on applied OOP field imaged by STXM and ptychography. . . . .	120
6.15	Power spectral density curves for STXM and ptychography images of sample 7 in domain state. . . . .	121
6.16	Contrast change of the images obtained by ptychography and STXM at sample 7 propagating from domain state to the skyrmion state by sweeping external magnetic field. . . . .	122
7.1	Single crystal shape of Cu. . . . .	127
7.2	Crystal shapes of multiply twinned particles. . . . .	128
7.3	Schematic drawings of MTPs grown along different axis. . . . .	129
7.4	Schematic views of twin boundary and tilt boundary. . . . .	129
7.5	Deposition process of Cu-Ni core-shell particles. . . . .	132
7.6	SEM image of Cu-Ni core-shell particles deposited by MBE. . . . .	132
7.7	SEM image of Cu-Ni core-shell particles with different shapes. . . . .	133
7.8	SEM image of five-fold symmetry Cu-Ni core-shell particle overgrown along [110] crystal direction exhibiting heterogeneous surface morphology. . . . .	133
7.9	Hysteresis obtained by SQUID in in-plane and out-of-plane configurations for core-shell samples with 10 and 15 nm Ni thicknesses. . . . .	135
7.10	STXM resonant absorption images of core shell particles at Cu and Ni edges. . . . .	136
7.11	STXM absorption spectra of core-shell sample made with different X-ray light polarization on the membrane and on the particle. . . . .	137
7.12	Overview STXM XMCD images of a core-shell sample obtained at different OOP magnetic fields. . . . .	137

## LIST OF FIGURES

---

7.13	SEM and STXM XMCD images of a core-shell having pentagonal pyramid shape obtained at different OOP magnetic fields. . . . .	138
7.14	Icosahedral particle in XYZ coordinates with corresponding view from above, right and front. . . . .	140
7.15	The magnetization of 700 nm big icosahedral particle shown from the different observation points. . . . .	141
7.16	Pentagonal dipyrmaid shape of the particle in XYZ coordinates with marked views from above, right and front. . . . .	142
7.17	The magneization of 700 nm big pentagonal dipyrmaid particle. . . . .	143
7.18	Images of core shell particles with 15 nm Ni thickness obtained with SEM, ptychography and STXM with XMCD contrast. . . . .	144
7.19	Line profiles over the magnetic and morphological edges of core shell particles imaged by STXM and ptychography. . . . .	144
7.20	FRC of core shell ptychographic image with 1/7 threshold line. . . . .	145
7.21	SEM and XMCD images of icosahedral particles obtained from ptychographic reconstructions. . . . .	146
7.22	Core-shell particles with various shapes imaged by SEM and ptychography using XMCD contrast. . . . .	147
7.23	Icosahedral particles: simulated magnetization vectors, XMCD image obtained from ptychography measurements and the same particles imaged by SEM. . . . .	148
7.24	SEM, ptychographic XMCD and corresponding simulated magnetization images of core-shell particle shaped as pentagonal pyramid. . . . .	149
A.1	Performance of the ptychographic reconstruction process. . . . .	158
A.2	Ptychographic reconstruction of illumination function of a simulated data set. . . . .	159
B.1	Estimation of the height of the Siemens Star 30 nm big structures using phase contrast. . . . .	161
B.2	Edge artifacts in phase images . . . . .	162
B.3	Phase reconstructions displaying artifacts with wrapped pixels. . . . .	163
D.1	Temperature dependent magnetic properties of skyrmion Ta/CoFeB/MgO/Ta samples with different thickness of ferromagnetic layer. . . . .	168
D.2	Temperature dependent anisotropy constant $K_1$ of Ta/CoFeB/MgO/Ta skyrmion samples with different thickness of ferromagnetic layer. . . . .	169
D.3	Temperature dependent hysteresis loops for skyrmion samples No. 1 and 3. . . . .	170
D.4	Temperature dependent hysteresis loops for skyrmion samples No. 4 and 5. . . . .	171
D.5	Temperature dependent hysteresis loops for skyrmion samples No. 6 and 7. . . . .	172

---

D.6	Dependance of Curie temperature on the thickness of CoFeB layer in skyrmion multilayer. . . . .	173
E.1	Simulation of magnetization of 15 nm thick Ni shell on the surface of icosahedral particle which have 300 nm , 500, nm and 700 nm in size. . .	176
E.2	Simulation of magnetization of 15 nm thick Ni shell on the surface of pentagonal dipyramid particles which have 300 nm, 500 nm and 700 nm in size. . . . .	177
E.3	Simulated particles in external magnetic field applied along X axis. . . . .	178
E.4	Projections of magnetization vectors of icosahedral particle placed into magnetic field with direction along X axis on the YZ, XZ and XY planes .	179
E.5	Projections of magnetization vectors of the particle placed into magnetic field with direction along X axis on the YZ, XZ and XY planes. . . . .	180

# List of Tables

2.1	Absorption edges of basic elements in soft X-ray range (up to 2000 eV). . .	16
2.2	Magnetic parameters of Ni. . . . .	35
4.1	Parameters of the BESSY II storage ring. . . . .	58
4.2	Spatial coherence length on FZP and in focus spot for FZP with diameter 100 $\mu\text{m}$ and outermost zone width 70 nm and different vertical slits opening at 1400 eV. . . . .	67
4.3	Specification of in-vacuum pnCCD detector . . . . .	71
4.4	Parameters of ptychographic FZPs used at MAXYMUS . . . . .	77
6.1	Magnetic parameters of skyrmion multilayer samples. . . . .	109
6.2	Parameters of multilayer skyrmion samples with different thickness of Co-FeB. . . . .	116
6.3	Parameters of skyrmions imaged on sample 7 using ptychography with the image area of $4 \times 4 \mu\text{m}$ . . . . .	119
6.4	Comparison of STXM and ptychographic methods for magnetic imaging at Fe-edge. . . . .	123
A.1	Parameters of ptychography reconstructing computer at MAXYMUS. . .	159
E.1	Parameters of the simulated icosahedral shapes. . . . .	175
E.2	Parameters of the simulated pentagonal dipyrmaid shape. . . . .	176

# List of publications

## Journal Articles:

- K. Litzius, I. Lemesh, B. Krüger, P. Bassirian, L. Caretta, K. Richter, F. Büttner, K. Sato, O. A. Tretiakov, J. Förster, R. M. Reeve, M. Weigand, **I. Bykova**, H. Stoll, G. Schütz, G. S. D. Beach, M. Kläui. Skyrmion Hall effect revealed by direct time-resolved X-ray microscopy. *Nature Physics* 13 (2), pp. 170 - 175, 2017.
- K. Yamamoto, A. Klossek, R. Flesch, F. Rancan, M. Weigand, **I. Bykova**, M. Bechtel, S. Ahlberg, A. Vogt, U.U. Blume-Peytavi, P. Schrade, S. Bachmann, S. Hedtrich, M. Schäfer-Korting, E. Rühl. Influence of the skin barrier on the penetration of topically-applied dexamethasone probed by soft X-ray spectromicroscopy. *European Journal of Pharmaceutics and Biopharmaceutics* 118, pp. 30 - 37, 2017.
- U. T. Sanli, C. Jiao, M. Baluktsian, C. Grévent, K. Hahn, Y. Wang, V. Srot, G. Richter, **I. Bykova**, M. Weigand, G. Schütz, and K. Keskinbora. 3D nanofabrication of high-resolution multilayer Fresnel Zone Plates. *Advanced Science*, 1800346, 2018.
- S. Chung, Q. Tuan Le, M. Ahlberg, M. Weigand, **I. Bykova**, A.A. Awad, H. Mazraati, A. Houshang, S. Jiang, T. N. A. Nguyen, E. Goering, G. Schütz, J. Gräfe, J. Åkerman. Direct observation of magnetic droplet solitons in all-perpendicular spin torque nano-oscillators. *Phys. Rev. Lett.* 120, 217204, 2018.

## Working Papers:

- G. Dieterle, J. Förster, H. Stoll, A. S. Semisalova, S. Finizio, A. Gangwar, M. Weigand, M. Noske, M. Fähnle, **I. Bykova**, D. A. Bozhko, H. Yu. Musiienko-Shmarova, V. Tiberkevich, A. N. Slavin, C. H. Back, J. Raabe, G. Schütz, S. Wintz. Coherent excitation of heterosymmetric spin waves with ultrashort wavelengths. (2017)

- F. Lisiecki, J. Rychły, P. Kuświk, H. Głowiński, J. W. Klos, F. Gross, **I. Bykova**, M. Weigand, M. Zelent, G. Schütz, M. Krawczyk, F. Stobiecki, J. Dubowik and J. Gräfe. Propagating spin waves and mini-band gaps in one-dimensional thin film magnonic quasiperiodic structures. (2018)
- K. Keskinbora, U. T. Sanli, H. Ceylan, **I. Bykova**, M. Weigand, M. Sitti, G. Schütz. 3D Nano-printed Plastic X-ray Optics.(2018)
- D. S. Macholdt, **I. Bykova**, C. Pöhlker, J.-D. Förster, M. Müller, B. Weber, M. Kappl, A. L. D. Kilcoyne, M. Weigand, M. O. Andreae. Rock varnish: cutting-edge data using X-ray microscopic and ptychographic analyses. (2018)
- W. Li and **I. Bykova** (authors with equal contribution), Y. Guang, G. Yu, C. He, Q. Shao, H. Wu, M. Weigand, Joachim Gräfe, Z. Zeng, P. Khalili Amiri, K. L. Wang, G. Schütz, G. Finocchio and X. Han. Tailoring Skyrmion Bubbles size in Ta/MgO/CoFeB structures at room temperature.(2018)
- Y. Guang, **I. Bykova**, Y. Liu, G. Yu, E. Goering, M. Weigand, J. Gräfe, J. Zhang, H. Zhang, W. Li, C. Wan, X. Wang, C. Guo, J. Feng, H. Wei, Y. Peng, X. Han and G. Schütz. Creating a sub-100 nm zero-field skyrmion in exchange-biased multilayers through X-ray illumination. (2018)

**Conference Proceedings:**

- **I. Bykova**, K. Keskinbora, U. Sanli, J. Gräfe, M. Bechtel, G. Yu, E. Goering, H. Stoll, G. Schütz, M. Weigand. Soft X-ray Ptychography for Imaging of Magnetic Domains and Skyrmions in Sub-100 nm Scales. International X-Ray Microscopy Conference. (2018)
- U. Sanli, H. Ceylan, C. Jiao, M. Baluktsian, C. Grevent, K. Hahn, Y. Wang, V. Srot, G. Richter, **I. Bykova**, M. Weigand, M. Sitti, G. Schütz, K. Keskinbora. New Concepts for 3D Optics in X-ray Microscopy. International X-Ray Microscopy Conference. (2018)

# Acknowledgments

This work would not be done without help of some people which I want to sincerely thank for their work, advisory comments and assistance:

- Prof. Dr. Gisela Schütz for the chance to be a part of the Modern Magnetic Material department at the first place, for scientific supervision and support during all my PhD study, optimism and confidence in the success of this work.
- Prof. Dr. Jörg Wrachtrup for being a second referee of this thesis.
- Dr. Markus Weigand for extensive help at the beamline during experiments, scientific supervision and thesis correction.
- Michael Bechtel for providing a great moral and technical support during my work at BESSY, for helping me to start a new life in Berlin.
- Members of the Micro-Nano Optics Working Group (MPI IS) for development and fabrication of ptychographic Fresnel zone plates used in this thesis: Dr. Kahraman Keskinbora, Umut Sanli (Direct-write IBL-FZPs in Au layers) and Margarita Balutskan (Ion beam implantation process for  $\text{Si}_3\text{N}_4$  FZPs). Mr. Sanli and Mrs. Baluktisian developed the process of making a beamstop out of organo-mineral resists with the experimental help from Robert Sittig. Additional thanks to Dr. Keskinbora and Mr. Sanli for support during beamtimes, performing SEM imaging and fruitful discussions; also to Dr. Keskinbora for fabrication of the Au test sample for ptychography and help with Matlab calculations of wave-field propagation.
- Members of the group of Prof. Dr. Kläui (Johannes Gutenberg University Mainz). In particular, Kai Litzius for providing Pd/Co FeB/MgO and Pt/CoFeB/MgO skyrmion multilayer samples and DMI calculations, also for providing extension code for micromagnetic simulations of magnetic core-shell particles and data visualization. Samridh Jaiswal and Dr. Jakub Zazvorka for measurements of magnetic saturation and anisotropy of the skyrmion samples,

additionally Samridh Jaiswal for the sample development and Alex Kronenberg for sample fabrication.

- Dr. Joachim Gräfe for the finding useful working contacts, providing samples for the experiments and help during beamtimes.
- Dr. Kwanghyo Son for performing SQUID measurements and main magnetic parameter calculations for the various skyrmion samples used in this thesis.
- Dr. Gunther Richter for providing Cu-Ni core-shell nanoparticles and helpful discussion about crystal growth and epitaxy.
- Dr. Wenting Huang for Cu-Ni core-shell samples development, their fabrication and SEM imaging. Additionally Hilda David for SEM imaging and Ilsemarie Lake-meyer for further sample preparations.
- Prof. Dr. Stephan Eisebitt for providing Ta/Pd/[Co/Pd]30/Pd magnetic labyrinth sample for the first magnetic ptychography tests.
- Dr. Dorothea Macholdt and Jan-David Förster for the possibility to perform measurements on rock varnish samples and topic discussions.
- Prof. Dr. Guoqiang Yu for fabrication and pre-characterization of Ta/[CoFeB/MgO/Ta]15 skyrmion samples.
- Dr. Stephen Ruoss for assistance during multiple SQUID measurements.
- Felix Gross for MOKE measurements.
- Monika Kotz for taking care of all non scientific organizational issues during my work in the department.
- All Schütz department for good atmosphere during my stay in Stuttgart.
- Dr. Alexander Schavkan for thesis corrections and for holding my hand in the moments of total despair.